

# Non-Orthogonal Signal and System Design for Wireless Communications

**Waseem Ozan**

A thesis submitted for the degree of Doctor of Philosophy

to

**University College London**

Communication and Information Systems Research Group

Department of Electronic and Electrical Engineering

University College London

January 2020

# Statement of Originality

I, Waseem Ozan, confirm that the work presented in this thesis is my own. Where information has been derived from other sources, I confirm that this has been indicated in the thesis.

## Abstract

The thesis presents research in non-orthogonal multi-carrier signals, in which: (i) a new signal format termed truncated orthogonal frequency division multiplexing (TOFDM) is proposed to improve data rates in wireless communication systems, such as those used in mobile/cellular systems and wireless local area networks (LANs), and (ii) a new design and experimental implementation of a real-time spectrally efficient frequency division multiplexing (SEFDM) system are reported.

This research proposes a modified version of the orthogonal frequency division multiplexing (OFDM) format, obtained by truncating OFDM symbols in the time-domain. In TOFDM, subcarriers are no longer orthogonally packed in the frequency-domain as time samples are only partially transmitted, leading to improved spectral efficiency. In this work, (i) analytical expressions are derived for the newly proposed TOFDM signal, followed by (ii) interference analysis, (iii) systems design for uncoded and coded schemes, (iv) experimental implementation and (v) performance evaluation of the new proposed signal and system, with comparisons to conventional OFDM systems. Results indicate that signals can be recovered with truncated symbol transmission. Based on the TOFDM principle, a new receiving technique, termed partial symbol recovery (PSR), is designed and implemented in software defined radio (SDR), that allows efficient operation of two users for overlapping data, in wireless communication systems operating with collisions. The PSR technique is based on recovery of collision-free partial OFDM symbols, followed by the reconstruction of complete symbols to recover progressively the frames of two users suffering collisions. The system is evaluated in a testbed of 12-nodes using SDR platforms. The thesis also proposes channel estimation and equalization technique for non-orthogonal signals in 5G scenarios, using an orthogonal demodulator and zero padding. Finally, the implementation of complete SEFDM systems in real-time is investigated and described in detail.

# Impact Statement

This thesis presents contribution to the design, implementation and practical validation of non-orthogonal signals and systems, more specifically, spectrally efficient frequency division multiplexing (SEFDM) and truncated orthogonal frequency division multiplexing (TOFDM) signals and systems. Driven by increasing user density and high data rate applications, such as real-time video and audio streaming, the work in this thesis have been exploring new solutions for utilizing the spectrum more efficiently. The proposed design of SEFDM and TOFDM have the potential to make impact on future wireless communication systems, such as the new generations of 802.11 and beyond 5G systems. Thus, network operators can increase the number of subscribers by up to 60% with no need for additional spectrum license.

Over the past four years, research in this thesis summarized and documented the study of newly proposed guard interval techniques in non-orthogonal signals and systems, hence, enhance the performance of the channel estimation and equalization techniques. Such technique will impact the innovation in non-orthogonal communication systems and pave the way for new research for the construction of simple multiple-input multiple-output (MIMO) using spectrally efficient systems, which is expected to be of paramount importance in future cellular networks. Furthermore, towards the goal of achieving a full real-time SEFDM system, the work in this thesis presents the design, implementation and realization of the world first real-time SEFDM prototype. It is expected that this will impact the standardization of future wireless systems. In addition, the research has presented the proposal of a new non-orthogonal signal and system, termed TOFDM, and the proposal of a new 802.11 receiver design, for successful decoding of

colliding frames, termed partial symbol recovery (PSR). Such will impact the existing wireless communication systems research and is already being followed by researchers worldwide; for example, a group of researchers from Harbin Institute of Technology has recently reported research on TOFDM signals to enhance the security of internet-of-things (IoT) systems.

Most of the concepts presented in this thesis have been peer-reviewed for international journals and conferences. I have authored and co-authored eight papers. The equality of the work presented in this thesis have been appreciated by two awards; the first is the best paper award from the IEEE/IET International Symposium on Communication Systems, Networks and Digital Signal Processing (CSNDSP) in 2016 and the second being a finalist in an industrial wireless communication engineering impact awards, given by National Instruments in 2017.

# Acknowledgements

First, I would like to express my gratitude with sincere thanks to my supervisor Professor Izzat Darwazeh for all the great support, guidance and motivation throughout my research studies. I am grateful to Izzat for sharing all his deep knowledge and rich experience in work-field and life, from which I have learnt and benefited so much. Being your student will not only set my future career but it changed my whole life and my future accomplishments will be achieved because of you. I would also like to thank him for obtaining funding for this PhD work.

I would like to thank my collaborative supervisor Professor Kyle Jamieson from Princeton University for his constant guidance and support. I am grateful to Kyle for funding the first year of this PhD study. I would also like to thank him for giving me the opportunity to join Princeton University as a visiting student research collaborator from February to August 2018. I would like to extend my thanks to his group in Princeton, the Princeton Advanced Wireless Systems (PAWS) group, for welcoming and treating me as one of them for the whole period I spent in there. Being part of the PAWS group is an experience that I will never forget. The collaborative work has resulted in a conference and a journal publications and is introduced in Chapters 5 and 6 of this thesis.

I would like to thank my second supervisor Dr Ryan Grammenos for his help, long discussions and guidance, specifically for the guard interval techniques in SEFDM, which resulted in a journal publication and is presented in Chapter 4 of this thesis.

I would like to thank my friends and collaborators, Dr Paul Anthony Haigh, Dr Bo Tan, Dr Hedaia Ghannam and Dr Tongyang Xu, for the dis-

cussions and the collaborative work on the experimental design of SEFDM systems, which resulted in three conference publications and is introduced in Chapter 3 of this thesis. My very warm thanks to my fantastic friends Paul and Bo who are always ready to give the helping hands at all the times and without them, my PhD experience wouldn't be the same.

I am grateful to my friends Ms Amany Kassem for being an amazing lunch and coffee buddy, Dr Temitope Odedeyi for his support and prayers and for being a cheerful lunch buddy and Ms Xinyue Liu for all the support and friendly chats. Great thanks to my UCL friends and colleagues in Robert's building and MPEB 708 office for all the great memories. Many thanks for my friends in London and United Kingdom for welcoming and treating me nicely. A very warm thanks to my flatmate Demet for being a fantastic friend and for the help during this thesis writing. I am grateful to the Syriac Orthodox Church Community with their Archbishop Athanasius Toma for being my family here in London.

My four years of research were funded by UCL's Electronic and Electrical Engineering Department and for that I shall always be grateful.

Last but certainly not least, I would like to express my deepest thanks to my family who encouraged and supported me during this course of PhD studies. Many thanks to my beloved parents Hazim and Entidhar and my wonderful siblings Fr Aphrem, Yazin, Halla and Sarmad for their love, support and prayers. A very special thanks to my brother Father Aphrem for his support, prayers and taking care of me from the first day I came to the UK.

# Contents

<b>1</b>	<b>Introduction</b>	<b>22</b>
1.1	Motivation and Aims . . . . .	24
1.2	Contributions . . . . .	26
1.3	Outline . . . . .	27
1.4	Publications . . . . .	28
<b>2</b>	<b>Preliminaries of Non-Orthogonal Signals and Systems</b>	<b>32</b>
2.1	Introduction . . . . .	32
2.2	OFDM . . . . .	33
2.3	Non-Orthogonal signals and Systems . . . . .	33
2.3.1	Fast-OFDM . . . . .	34
2.3.2	MASK . . . . .	36
2.3.3	OvFDM . . . . .	37
2.3.4	HC-MCM . . . . .	37
2.3.5	Faster-Than-Nyquist . . . . .	38
2.3.6	FBMC . . . . .	39
2.3.7	UFMC . . . . .	39
2.3.8	GFDM . . . . .	40
2.4	The SEFDM Concept and Signal Model . . . . .	40
2.5	SEFDM Challenges . . . . .	42
2.5.1	Signal Generation . . . . .	42
2.5.2	Self-induced ICI characterization . . . . .	44
2.5.3	Channel Estimation . . . . .	45
2.5.4	Detection in SEFDM systems . . . . .	46

2.6	Conclusions . . . . .	53
<b>3</b>	<b>Experimental SEFDM Iterative Detection</b>	<b>55</b>
3.1	Introduction . . . . .	55
3.2	Signal Generation, System Transmitter Design and Setup . . .	56
3.2.1	SEFDM signal model . . . . .	58
3.2.2	SEFDM data and pilot symbols generation . . . . .	58
3.2.3	SEFDM systems with OFDM pilot symbols . . . . .	60
3.2.4	System transceiver and parameters . . . . .	61
3.3	Receiver Description . . . . .	61
3.3.1	Synchronization and channel estimation and equalization	62
3.3.2	Iterative detector with interference canceller . . . . .	63
3.3.3	Generation of the interference estimates . . . . .	64
3.3.4	Pipeline processing in SDR . . . . .	66
3.4	Experimental Testbed Setup and System Performance . . . . .	68
3.4.1	Testbed descriptions . . . . .	68
3.4.2	Channel estimation performance . . . . .	69
3.4.3	BER performance . . . . .	70
3.4.4	Received signal representations . . . . .	73
3.5	Interactive System Platform . . . . .	75
3.6	Conclusions . . . . .	77
<b>4</b>	<b>Zero Padding and Continuous and Conventional Cyclic Prefix: Evaluation for Non-Orthogonal Signals</b>	<b>79</b>
4.1	Introduction . . . . .	79
4.2	Guard Interval Techniques and Schemes . . . . .	80
4.3	SEFDM Signal Model . . . . .	81
4.3.1	IDFT based transmitter . . . . .	81
4.4	SEFDM with Cyclic Prefix . . . . .	83
4.4.1	Subcarrier matrix based receiver . . . . .	86
4.4.2	DFT based receiver . . . . .	87
4.4.3	Channel Estimation and Equalization in CP-SEFDM .	90
4.5	SEFDM with continuous CP . . . . .	91

4.5.1	Channel Estimation and Equalization in CCP-SEFDM	97
4.6	SEFDM with Zero Padding	98
4.6.1	Channel Estimation and Equalization in ZP-SEFDM	102
4.7	OFDM Pilot Symbols in SEFDM Systems	103
4.8	Performance Results	106
4.8.1	Guard Interval Schemes compared for system evaluation	106
4.8.2	Channel model	107
4.8.3	SEFDM signals for pilot and data symbols	107
4.8.4	OFDM pilot symbols for SEFDM systems	112
4.8.5	Comparison of the power penalty for the different guard interval schemes	113
4.9	Conclusions	115
<b>5</b>	<b>Truncated OFDM Signal and System</b>	<b>117</b>
5.1	Introduction	117
5.2	TOFDM Signal Representation	118
5.2.1	Time-domain representation	119
5.2.2	Frequency domain representation	119
5.3	TOFDM Signal Representation vs OFDM, SEFDM and FTN	121
5.4	Truncated OFDM Signal Model	124
5.4.1	Signal Model	124
5.4.2	Characterizing ICI in TOFDM System	125
5.5	Testbeds, Detection and System Performance	128
5.5.1	Uncoded TOFDM systems	128
5.5.2	Coded TOFDM systems	133
5.5.3	Error rate performance in AWGN channel.	140
5.5.4	Error rate performance in multipath wireless channel.	145
5.6	Conclusions	152
<b>6</b>	<b>Operating Interfering Wireless Networks Beyond Capacity</b>	<b>154</b>
6.1	Introduction	154
6.2	Related Work	159
6.3	802.11a Frame Structure and Construction	160

6.3.1	Preamble generation . . . . .	160
6.3.2	Data field . . . . .	165
6.4	Partial Symbol Overlap . . . . .	172
6.5	Design . . . . .	174
6.5.1	Physical layer design . . . . .	174
6.5.2	Link layer design . . . . .	184
6.5.3	Experimental parameters estimation . . . . .	188
6.6	Implementation . . . . .	192
6.6.1	Physical layer . . . . .	192
6.6.2	Link layer to transport layer . . . . .	193
6.7	Evaluation . . . . .	193
6.7.1	Methodology . . . . .	193
6.7.2	Rate region comparison . . . . .	196
6.7.3	FER measurements in link layer . . . . .	197
6.7.4	End-to-end performance . . . . .	198
6.8	Conclusions . . . . .	205
<b>7</b>	<b>Conclusions</b>	<b>207</b>
7.1	Future Work . . . . .	210
	<b>Appendices</b>	<b>213</b>
<b>A</b>	<b>SEFDM LabVIEW Code</b>	<b>214</b>
A.1	The Panel Platform . . . . .	214
A.2	The Diagram Platform . . . . .	215
A.3	Implementation of the First SEFDM 5G Transceiver Proto- type Using LabVIEW Communications System Design Suite and USRP RIO . . . . .	218
<b>B</b>	<b>Time Precoding Enabled Non-Orthogonal Frequency Divi- sion Multiplexing</b>	<b>226</b>
<b>C</b>	<b>Partial Symbol Recovery Paper</b>	<b>233</b>
	<b>References</b>	<b>249</b>

# List of Figures

2.1	OFDM spectrum of $N$ subcarriers . . . . .	34
2.2	SEFDM spectrum of $N$ subcarriers . . . . .	41
2.3	SEFDM signal generation based on single IDFT . . . . .	42
2.4	The sphere decoder tree search of BPSK constellation for 4-subcarrieris SEFDM systems . . . . .	49
3.1	Schematic block diagram of SEFDM system . . . . .	57
3.2	A resource block of the transmitted frame using SEFDM symbols	59
3.3	Conceptual illustration of subcarriers in (a) OFDM pilot symbols and (b) SEFDM symbols with $\alpha = 0.75$ . . . . .	60
3.4	A resource block of the transmitted frame using OFDM pilot symbols and SEFDM data symbols . . . . .	62
3.5	A method of producing correlation matrix . . . . .	64
3.6	Pipeline design structure of iterative decoder . . . . .	67
3.7	SEFDM transceiver test-bed setup . . . . .	69
3.8	Mean square error versus $E_b/N_0$ . . . . .	70
3.9	BER of BPSK-SEFDM using OFDM pilots . . . . .	72
3.10	BER of QPSK-SEFDM using OFDM pilots . . . . .	72
3.11	BER of 8-PSK-SEFDM using OFDM pilots . . . . .	72
3.12	Received constellations and measured spectra for $\alpha = 0.7$ . . .	74
3.13	SEFDM testbed control parameters . . . . .	76
4.1	Guard interval schemes of multicarrier systems . . . . .	80
4.2	Simplified block diagram of SEFDM transceivers with two different cyclic prefix techniques . . . . .	82
4.3	Transmitted signal structure representation for CP-SEFDM . .	83

4.4	Time samples of one CP-SEFDM and continuous CP-SEFDM symbols . . . . .	84
4.5	Received signal structure representation for CP-SEFDM . . .	85
4.6	Transmitted signal structure representation for CCP-SEFDM .	92
4.7	Received signal structure representation for CCP-SEFDM . . .	93
4.8	A simplified block diagram of ZP-SEFDM transceiver . . . . .	99
4.9	Signal structure representation for ZP-SEFDM . . . . .	100
4.10	A simplified block diagram of CP-OFDM pilot symbols transceiver	104
4.11	Frame structure. Each symbol (pilot and data symbols) in the frame has the same time duration . . . . .	108
4.12	MSE in channel estimation for different guard interval schemes in SEFDM systems . . . . .	109
4.13	BER in SEFDM system using SEFDM pilots . . . . .	111
4.14	Frame structure. The OFDM pilot symbols have longer time duration compared to SEFDM data symbols in the frame . . .	113
4.15	BER in SEFDM system using OFDM pilots . . . . .	114
4.16	Power penalty of SEFDM systems compared to OFDM systems	115
5.1	TOFDM symbols generation from OFDM symbol . . . . .	118
5.2	The spectra of OFDM and TOFDM symbols of 4-subcarriers .	120
5.3	Conceptual illustrations of OFDM, SEFDM, FTN and TOFDM in time-domain . . . . .	122
5.4	Conceptual time-frequency illustration of TOFDM and FTN when derived from an OFDM . . . . .	123
5.5	Conceptual time-frequency illustration of SEFDM when derived from an OFDM . . . . .	123
5.6	TOFDM simplified system modem. . . . .	129
5.7	BER for TOFDM system with no oversampling . . . . .	132
5.8	BER for TOFDM system with oversampling factor = 4 . . . .	132
5.9	Power penalty (at BER = $10^{-3}$ ) of different levels of truncations and oversampling to OFDM . . . . .	133
5.10	Block diagram of modified 802.11a,g transceiver using TOFDM signals . . . . .	135

5.11	The resulting signals of correlating LTF symbol and the received signal . . . . .	137
5.12	Block diagram of modified 802.11g receiver using iterative decoder. . . . .	139
5.13	Convergence BER performance of BPSK-TOFDM with various iterations using different values of $\gamma$ . . . . .	142
5.14	Convergence BER performance of QPSK-TOFDM with various iterations using different values of $\gamma$ . . . . .	143
5.15	TOFDM system performance for various values of $\gamma$ . . . . .	144
5.16	Experimental BER performance of BPSK CP-TOFDM with various iterations using different values of $\gamma$ . . . . .	147
5.17	Experimental BER performance of QPSK CP-TOFDM with various iterations using different values of $\gamma$ . . . . .	148
5.18	Experimental BER performance of BPSK ZP-TOFDM with various iterations using different values of $\gamma$ . . . . .	150
5.19	Experimental BER performance of QPSK ZP-TOFDM with various iterations using different values of $\gamma$ . . . . .	151
5.20	Power penalty of TOFDM systems compared to OFDM systems	152
6.1	Capacity region of the two-user uplink Gaussian noise interference channel . . . . .	155
6.2	PSR applies to different collision scenarios . . . . .	156
6.3	Stations 1 and 2 transmit concurrently, leading to a collision at a receiver . . . . .	156
6.4	802.11a Preamble followed by the signal OFDM symbol and multiple data OFDM symbols . . . . .	161
6.5	Inputs and outputs of the IFFT at the transmitter . . . . .	162
6.6	Constructing short training field in time-domain . . . . .	163
6.7	Correlation of a short symbol with the short training field sequence . . . . .	164
6.8	Correlation of a long symbol with the preamble . . . . .	165
6.9	Block diagram of the 802.11a transmitter . . . . .	166
6.10	Bits assignment of the SERVICE field . . . . .	166

6.11	Data field scrambler and descrambler . . . . .	168
6.12	IEEE 802.11a convolutional encoder. $T_b$ is the bit duration . .	169
6.13	BPSK and QPSK constellation bit mapping . . . . .	170
6.14	Subcarrier frequency location to the input of IFFT . . . . .	171
6.15	Heatmap of the covariance matrix that depicts the interference between neighboring subcarriers . . . . .	173
6.16	The inner loop decoder . . . . .	175
6.17	A partial and full symbol in received colliding frames . . . . .	176
6.18	A truncated partial symbol lacks certain multipath components	178
6.19	The outer loop decoding algorithm . . . . .	182
6.20	Schematic chart of Partial Symbol Recovery system . . . . .	185
6.21	Message sequence chart of intra- and inter-network collision scenarios . . . . .	187
6.22	The ability to identify a colliding user from its recent CFO and CIR . . . . .	191
6.23	Indoor experimental testbed map . . . . .	194
6.24	Rate region comparisons . . . . .	195
6.25	Average FER of all collision cases versus decoding window size of the outer loop decoder . . . . .	197
6.26	PSR Frame Error Rates Performance . . . . .	199
6.27	CDF of throughput and retransmission rate in intra-network scenario using uplink-UDP transmissions . . . . .	200
6.28	CDF of throughput and retransmission rate in inter-network scenario using bulk TCP transmissions . . . . .	203
6.29	CDF of throughput and retransmission rate in inter-network scenario using video on demand transmissions . . . . .	204
A.1	The USRP setting configurations blocks . . . . .	215
A.2	The LabVIEW code of the SEFDM transmitter . . . . .	216
A.3	The LabVIEW code of the SEFDM receiver . . . . .	217

# List of Tables

3.1	Experimental system specifications . . . . .	62
3.2	LTE EPA Fading Channel Model . . . . .	71
4.1	Channel model parameters . . . . .	107
5.1	WLAN Exponential Decay Channel Model . . . . .	136
6.1	Experimental initial CFO and CIR . . . . .	189

# Abbreviations

**4G** 4<sup>th</sup> Generation

**5G** 5<sup>th</sup> Generation

**64-QAM** 64-Quadrature Amplitude Multiplexing

**8-PSK** 8-Phase Shift Keying

**ACK** Acknowledgment

**AP** Access Point

**AWGN** Additive White Gaussian Noise

**BA** Block Acknowledgment

**BA**s Block Acknowledgments

**BCJR** Bahl, Cocke, Jelinek and Raviv

**BER** Bit Error Rate

**BER**s Bit Error Rates

**FER** Frame Error Rate

**Fast-OFDM** Fast-Orthogonal Frequency Division Multiplexing

**BPSK** Binary Phase Shift Keying

**CCP** Continuous Cyclic Prefix

---

**CDF** Cumulative Distribution Function

**CFO** Carrier Frequency Offset

**CIR** Channel Impulse Response

**CP** Cyclic Prefix

**CRC** Cyclic Redundancy Check

**CSI** Channel State Information

**D/A** Digital to Analog

**DCT** Discrete Cosine Transform

**DFT** Discrete Fourier Transform

**DMRS** Demodulation Reference Symbols

**EPA** Extended Pedestrian A

**ETSI** European Telecommunications Standards Institute

**FBMC** Filterbank Based Multicarrier

**FFT** Fast Fourier Transform

**FPGA** Field-Programmable Gate Array

**FPGAs** Field-Programmable Gate Arrays

**FSD** Fixed Sphere Decoder

**FTN** Faster-Than-Nyquist

**GFDM** Generalized Frequency Division Multiplexing

**HC-MCM** High Compaction-Multi Carrier Modulation

**IBI** Inter-Block Interference

**ICI** Inter-Carrier Interference

---

**ID** Iterative Decoder

**IDs** Iterative Decoders

**IDFT** Inverse Discrete Fourier Transform

**IDCT** Inverse Discrete Cosine Transform

**IFFT** Inverse Fast Fourier Transform

**IEEE** Institute of Electrical and Electronics Engineers

**ISI** Inter Symbol Interference

**IoT** Internet of Things

**LDPC** Low-Density Parity Check

**LTE** Long Term Evolution

**LTE-A** Long Term Evolution-Advanced

**LTF** Long Training Field

**LLR** Log-Likelihood Ratio

**LOS** Line-of-Sight

**STF** Short Training Field

**MASK** M-ary Amplitude Shift Keying

**MCM** MultiCarrier Modulation

**ML** Maximum Likelihood

**MLSD** Maximum Likelihood Sequential Detection

**MMSE** Minimum Mean Square Error

**MIMO** Multiple-In Multiple-Out

**MSE** Mean Square Error

---

**NB-IoT** Narrowband Internet-of-Things

**NI** National Instruments

**NS-3** Network Simulator-3

**NLOS** Non-Line-of-Sight

**NR** New Radio

**OQAM** Offset Quadrature Amplitude Modulation

**OFDM** Orthogonal Frequency Division Multiplexing

**OOB** Out-Of-Band

**OvFDM** Overlapped Frequency Division Multiplexing

**PAPR** Peak-to-Average Power-Ratio

**PCE** Partial Channel Estimation

**PSR** Partial Symbol Recovery

**PPR** Partial Packet Recovery

**QAM** Quadrature Amplitude Multiplexing

**QPSK** Quadrature Phase Shift Keying

**RF** Radio Frequency

**RS** Reed-Solomon

**RIO** Reconfigurable Input-Output

**SD** Sphere Decoder

**SDs** Sphere Decoders

**SDP** Semi-Definite Programming

**SDR** Software Defined Radio

---

**SDRs** Software Defined Radios

**SEFDM** Spectrally-Efficient Frequency Division Multiplexing

**SIC** Successive Interference Cancellation

**SINR** Signal-to-Interference-plus-Noise Ratio

**SNR** Signal to Noise Ratio

**TCP** Transmission Control Protocol

**TOFDM** Truncated Orthogonal Frequency Division Multiplexing

**TDL** Tapped Delay Line

**TSVD** Truncated Singular Value Decomposition

**UD-FDM** Ultra Dense-Frequency Division Multiplexing

**UDP** User Datagram Protocol

**UFMC** Universal Filter Multicarrier

**USRP** Universal Software Radio Peripheral

**WARP** Wireless Open-Access Research Platform

**WiFi** Wireless Fidelity

**ZF** Zero Forcing

**ZP** Zero Padding

# Chapter 1

## Introduction

Since the commercial deployment of 4<sup>th</sup> Generation (4G) [1] and more recently 5<sup>th</sup> Generation (5G) [2] networks, research into next generation networks (beyond 5G networks) has been developing rapidly with significant achievements [3–5]. This is due to the end user requirement for high data rates that support new media and data services. Thus, currently deployed 4G networks rates maybe insufficient to support heavy data services. In future XG networks, user demand is expected to be significantly in excess of the total network supply. As predicted in [6], the number of devices connected to the Internet by 2023 will be over three times the global population. Moreover, it is well known that radio spectrum is already heavily over subscribed, leading to high-cost premiums, and as such, new physical layer designs or modified versions of the existing ones that save spectrum are highly sought after.

The well known Orthogonal Frequency Division Multiplexing (OFDM) systems are a subset of MultiCarrier Modulation (MCM) systems, where different subcarriers maintain orthogonality by frequency separation equal to signalling rate ( $1/T$ ;  $T$  is the OFDM symbol duration) and where the data rate of each subcarrier is a fraction of the overall data rate. Orthogonality in OFDM is a crucial factor in its successful operation: loss of orthogonality leads to interference and deterioration in bit error rate [7]. Orthogonality, in time and frequency is maintained by ensuring that the spacing between

the subcarriers is equal to the inverse of the symbol rate. Consequently, this poses a constraint on the number of subcarriers that can fit into a given frequency band, for a given system. Therefore, several non-orthogonal signal formats have been introduced to provide higher spectral efficiency.

Recently a set of time- and frequency-domain techniques have been proposed to enhance spectral efficiency by deliberate violation of the orthogonality criterion in multicarrier systems. Since 2003, Spectrally-Efficient Frequency Division Multiplexing (SEFDM) signals and systems have been proposed as a means to save bandwidth, yet avoid the degradation of bit error rates, relative to OFDM [8]. Such bandwidth savings are achieved in SEFDM by decreasing the spacing between subcarriers in the frequency-domain below  $1/T$  while keeping the same data rate on each subcarrier [8]. SEFDM is a non-orthogonal scheme, which packs more subcarriers into the same spectrum as OFDM, thereby improving spectral efficiency and therefore data rates [8]. SEFDM's ability to save spectrum makes it a topic of interest, as exemplified by the great deal of work that is being carried out in this field [5, 9–14]. SEFDM is not without disadvantages though and one of the most significant disadvantages is the computational complexity requirements of the receiver [8]. In addition, SEFDM channel estimation and equalization become more challenging due to combined self-induced Inter-Carrier Interference (ICI) and multi-path effects. Therefore, different time-domain channel estimation and equalization techniques were employed in SEFDM systems to alleviate the multi-path effects [15].

Similarly, multi-stream Faster-Than-Nyquist (FTN) systems have been suggested to improve spectral efficiency by transmitting at a higher rate data than imposed by the Nyquist limit for the same bandwidth [16–18]. FTN fulfils this by signaling on each subcarrier at a rate higher than the frequency separation between two adjacent subcarriers, effectively overlapping symbols in the time-domain at the expense of a loss of orthogonality [16]. In addition, Hamamura and Tachikawa (2004), reported a non-orthogonal multicarrier system termed High Compaction-Multi Carrier Modulation (HC-MCM), based on a similar concept to SEFDM and FTN, where enhanced spectral efficiency is achieved by either reducing the subcarrier spacing or decreasing

the transmission time for OFDM symbols [19].

More recently, a new time/spectral efficient technique, termed Truncated Orthogonal Frequency Division Multiplexing (TOFDM) [20], was conceived by the author of this thesis towards the enhancement of data rates over existing systems. TOFDM is a non-orthogonal system format which modifies OFDM signals by truncating (as opposed to overlapping) the time samples of each OFDM symbol, in a way similar to what was studied in the context of assessing the spectrum of oversampled OFDM and SEFDM signals [21], where the latter can be generated by truncating the end of OFDM symbols. However, the newly proposed TOFDM technique, allows the truncation of the time samples from different locations of the OFDM symbols in the time-domain. As such, this new format is termed Truncated OFDM. Here, each OFDM time-domain symbol is truncated by a factor  $1 - \gamma$ , with minimal changes to the shape of the overall frequency spectrum. Therefore, time samples are only partially transmitted, and part of the symbol is lost before transmission. Furthermore, the fact that the TOFDM symbol time is shorter than that of an OFDM one, implies loss of orthogonality and consequently the introduction of ICI amongst the subcarriers. This TOFDM is one of the focal points of this thesis.

## 1.1 Motivation and Aims

The work in this thesis focuses on two non-orthogonal systems, SEFDM and TOFDM. Over the last 17 years, SEFDM systems have been demonstrated through many research publications and laboratory experiments. Thus far, only offline systems have been demonstrated, which simplifies the problem and avoids the complexity of system-level development at the circuit and Field-Programmable Gate Array (FPGA) level. This is due to the high computational complexity of the receiver, which is the key challenge in the realization of real-time SEFDM systems. Such computational complexity requirements are due to two main reasons: *(i)* using time-domain channel estimation and equalization in SEFDM systems leads to higher computational complexity at the receiver; and *(ii)* the decoding latency requirements, where

complex detection structures, such as Sphere Decoders (SDs) and/or Iterative Decoders (IDs) are utilized to cancel ICI and retrieve the transmitted data.

Therefore, after identifying/diagnosing the key problems, the aim is to research, design and demonstrate real-time spectrally efficient multicarrier systems and test these using Radio Frequency (RF) signals over realistic channels. To achieve this aim, three objectives are set, *(i)* to explore new methods of frequency-domain channel estimation and equalization in SEFDM systems with reduced complexity in comparison to their time-domain equivalent counterparts, *(ii)* to investigate and explore the use of different receiver architectures, of relatively low computational complexity (or low latency) with no loss in performance in comparison to conventional implementations of SEFDM systems, and *(iii)* to explore the potential of changing the OFDM signal structure itself for better spectral efficiency using new time-domain techniques. This last objective led to the development of a new type of signal termed TOFDM, which was conceived to open a new dimension for possible enhancement of data rates.

For the first two objectives, a new frequency-domain channel estimation technique, using OFDM pilots, for the SEFDM system is implemented in a Software Defined Radio (SDR) platform to tackle the computational complexity problem at the receiver, followed by a pipelined Iterative Decoder (ID) structure to reduce the latency at the receivers. Second, a new frequency-domain channel estimation and equalization using Zero Padding (ZP) with SEFDM signals are introduced, designed and implemented.

For the third objective, the thesis investigates the integration of the newly proposed TOFDM signals in existing Wireless Fidelity (WiFi) system with minimal changes at the transmitters and design TOFDM decoders at the receiver, hence, increase the data rate of existing WiFi systems. Furthermore, the design of new WiFi receivers to guarantee its successful operation in collision environments are investigated both by modelling and experimentally.

## 1.2 Contributions

This thesis documents the theoretical and practical research of the well known SEFDM systems and the newly proposed TOFDM signal and system. The new research contributions are summarized in the list below.

- **Real-time implementation of SEFDM system.**

This work was published in [C02] [C03] [C04] [OA01] [DP02] in the list of publications and appears in Chapter 3 of this thesis.

- Implemented the frequency-domain channel estimation using OFDM pilot symbols in SDR for real-time SEFDM systems.
- Developed and implemented using SDR a Pipeline design architecture for SEFDM iterative decoder to reduce the overall system detection latency and improve throughput.

- **Proposal and mathematical modelling of using zero padding in SEFDM and TOFDM systems.**

This work was published in [J01] in the list of publications and presents for ZP-SEFDM system in Chapter 4 and for ZP-TOFDM in Chapter 5.

- Proposed, designed and implemented the use of ZP instead of Cyclic Prefix (CP) and Continuous Cyclic Prefix (CCP) for SEFDM systems.
- Derived analytical expressions of channel estimation and equalization using ZP, CP and CCP for SEFDM system.
- Implemented and tested the ZP in TOFDM systems using SDR and realistic RF channels using channel emulator.

- **TOFDM design, signal modelling, interference characterization and uncoded and coded systems implementation.**

This work was published in [C05] in the list of publications and appears in Chapter 5.

- Proposed and developed the TOFDM signal and system.

- Verified and implemented the newly proposed TOFDM signal and system using SDR.
- Applied TOFDM principle and signals in the existing standard 802.11a,g system, WiFi system.
- **Proposal, design and implementation the new receiving technique termed Partial Symbol Recovery (PSR).**

This work is to be submitted as paper in [SJ01] in the list of publications (also in Appendix C) and is described in Chapter 6.

- Developed the TOFDM concept to operate the current 802.11a,g systems successfully in collision environment, thus the new proposed receiver retrieves the transmitted data of two overlapped (collided) frames.
- Presented a new technique termed PSR, which is a physical-layer and data link layer wireless receiver design technique that explicitly treats non- and partially-overlapping OFDM symbols differently from completely-overlapping OFDM symbols involved in a collision, and therefore allow signal recovery even when serious collisions occur.
- Designed and implemented the PSR receiver on the Wireless Open-Access Research Platform (WARP) SDR platform and in trace-based simulation using Network Simulator-3 (NS-3).
- Evaluated the operation of the new system using 12-nodes SDR testbed spread over two rooms in a Non-Line-of-Sight (NLOS) environment.

## 1.3 Outline

This thesis is in seven chapters organized as follows:

- **Chapter 2** gives a detailed overview of published research relating to SEFDM and other non-orthogonal signal and system.

- **Chapter 3** details the design and implementation of an experimental test-bed to evaluate the performance of SEFDM systems in real-time using frequency-domain channel estimation/equalization and iterative signal detection. Furthermore, ID pipelining is designed and implemented in SDR to reduce the overall system detection latency and improve throughput. Thus, symbols are allocated to parallel IDs that have no waiting time as they are received.
- **Chapter 4** proposes a new method for frequency-domain channel estimation and equalization for SEFDM systems, then presents numerical evaluation for channel estimation and equalization in the frequency-domain using ZP, CP and CCP.
- **Chapter 5** presents the newly proposed TOFDM signal mathematically then compares it to those of SEFDM and FTN signals. In addition, the chapter provides two system designs-uncoded and coded-using TOFDM signals. Furthermore, in this chapter detailed studies of TOFDM error rate performance in Additive White Gaussian Noise (AWGN) and multipaths channels using different values of truncation and oversampling factors.
- **Chapter 6** presents a new receiving technique and design, termed PSR, that allows efficient operation of overlapping (colliding) data in wireless communication systems, such as WiFi systems. In the chapter, evaluation of the new proposed technique is carried out in a testbed of 12-nodes using SDR platforms.
- **Chapter 7** gives conclusions for the work presented in the previous chapters, and provides some potential plans for future work.

## 1.4 Publications

The contribution of this work have been published in one journal publications, a second journal paper is under review, six publications in international conference proceedings, one online article publication, three extended

abstracts publications (one poster and two demonstration) in international conferences and two awards. The publications are listed below in reverse chronological order.

- **Journal Publications:**

[J01] – **Ozan, Waseem**, R. Grammenos, and I. Darwazeh. “Zero Padding or Cyclic Prefix: Evaluation for Non Orthogonal Signals.” *IEEE Communication Letters*. IEEE, 2020.

- **Journal Paper to be submitted:**

[SJ01] – **Ozan, Waseem**, I. Darwazeh, and K. Jamieson. “PSR: Partial Symbol Recovery to Operate Interfering Wireless Networks in Collision Environments.” *IEEE/ACM Transaction on Networking*, IEEE/ACM, 2020.

- **Conference Publications:**

[C01] – **Ozan, Waseem**, P. A. Haigh, B. Tan, and I. Darwazeh. “Time Precoding Enabled Non-Orthogonal Frequency Division Multiplexing.” In *IEEE Personal, Indoor and Mobile Radio Communications (PIMRC) 2019*.

[C02] – **Ozan, Waseem**, H. Ghannam, T. Xu, P. A. Haigh, and I. Darwazeh. “Experimental Evaluation of Channel Estimation and Equalisation in Non-Orthogonal FDM Systems.” In *2018 11th International Symposium on Communication Systems, Networks & Digital Signal Processing (CSNDSP)*, pp. 1-6. IEEE, 2018.

[C03] – **Ozan, Waseem**, P. A. Haigh, B. Tan, and I. Darwazeh. “Experimental SEFDM pipelined iterative detection architecture with improved throughput.” In *2018 IEEE 87th Vehicular Technology Conference (VTC Spring)*, pp. 1-5. IEEE, 2018.

[C04] – **Ozan, Waseem**, H. Ghannam, P. A. Haigh, and I. Darwazeh. “Experimental implementation of real-time non-orthogonal multi-carrier

systems in a realistic fading channel.” In *Radio and Wireless Symposium (RWS), 2018 IEEE*, pp. 121-124. IEEE, 2018.

[C05] – **Ozan, Waseem**, K. Jamieson, and I. Darwazeh. “Truncating and oversampling OFDM signals in white Gaussian noise channels.” *Communication Systems, Networks and Digital Signal Processing (CSNDSP), 2016 10th International Symposium on*. IEEE, 2016. (Best paper Award).

- **Other Publications:**

[O01] – S. Stainton, **Ozan, Waseem**, M. Johnston, S. Dlay, P. A. Haigh,. “Neural Network Equalisation and Symbol Detection for 802.11p V2V Communication at 5.9 GHz.” In *2020 IEEE 91st Vehicular Technology Conference (VTC Spring)*, IEEE, 2020.

- **Online Articles:**

[OA01] – **Ozan, Waseem**, R. Grammenos, H. Ghannam, P. A. Haigh, and I. Darwazeh. “Implementation of the First SEFDM 5G Transceiver Prototype Using LabVIEW Communications System Design Suite and USRP RIO.” *National Instrument*, 17 Aug. 2017, < <http://sine.ni.com/cs/app/doc/p/id/cs17492> >. (Online article). (Finalist for engineering impact award).

- **Demo and Poster Publications:**

[DP01] – Xu, T., Ghannam, H., **Ozan, W.**, & Darwazeh, I. (2018). “Demonstration of Real Time Bandwidth Compressed Signal Transmission at 2.4 GHz using Software Defined Radio (SDR).” *2018 IEEE 19th International Workshop on Signal Processing Advances in Wireless Communications*. IEEE, 2018.

[DP02] – **Ozan, Waseem**, R. Grammenos, H. Ghannam, P. A. Haigh, and I. Darwazeh. “Real-Time SEFDM Transceiver for 5G Systems and Beyond.” *Personal, Indoor, and Mobile Radio Communications (PIMRC), 2017 IEEE 28th Annual International Symposium on*. IEEE, 2017. (Extended abstract-Demo paper).

[DP03] – **Ozan, Waseem**, P. Haigh and I. Darwazeh. “Frequency Channel Estimation for Spectrally Efficient Frequency Division Multiplexing Systems.” *Wireless Communications and Networking Conference (WCNC), 2017 IEEE*. IEEE, 2017. (Extended Abstract).

- **Awards:**

[A01] – Finalist in wireless communication engineering impact awards from National Instruments in 2017.

[A02] – Best paper award at the IEEE/IET symposium on communication systems, networks and digital signal processing (CSNDSP) conference in 2016.

# Chapter 2

## Preliminaries of Non-Orthogonal Signals and Systems

### 2.1 Introduction

An SEFDM system saves bandwidth by compressing conventional OFDM subcarrier spacing beyond the orthogonality limit, thus increasing spectral efficiency. This spectral efficiency improvement translates directly into a gain in capacity, which is of paramount importance to network operators who could use this technique to save 30 to 60 percent signal bandwidth (depending on the modulation format). Hence, SEFDM becomes a timely and key technique for future beyond 5G communication systems. However, improvement in spectral efficiency comes at the expense of self-induced ICI in the SEFDM signal, which requires more sophisticated receivers (equalizers and detectors) to retrieve and decode the transmitted signals.

In this chapter, OFDM systems are briefly described in Section 2.2, then a short summary of the non-orthogonal systems is given in Section 2.3, which are candidates of beyond 5G systems. After that, the fundamental concept of SEFDM and its signal model are provided in Section 2.4, and its challenges in signal generation, channel estimation and signal recovery with all proposed

solutions are presented in Section 2.5. In addition, a brief description of Sphere Decoder (SD) and how it is applied in SEFDM systems for signal detection is detailed in Section 2.5.4.

## 2.2 OFDM

OFDM systems are a subset of the multicarrier modulation systems, where the given bandwidth is divided into several low rate orthogonal subcarriers to form an OFDM symbol that is sent over the channel [22]. In general, an OFDM signal can be expressed as:

$$x_{ofdm}(t) = \frac{1}{\sqrt{T}} \sum_{l=-\infty}^{\infty} \sum_{n=0}^{N-1} s_{l,n} \exp(j2\pi n(t - lT)\Delta f), \quad (2.1)$$

where  $s_{l,n}$  denotes the complex symbol modulated on the  $n^{th}$  subcarrier of the  $l^{th}$  OFDM symbol,  $N$  represents the number of subcarriers,  $T$  is the OFDM symbol duration,  $1/\sqrt{T}$  is a normalization factor and  $\Delta f = 1/T$  is the frequency spacing between two subcarriers as shown in Figure 2.1, which ensures orthogonality. Orthogonality in OFDM is a crucial factor for successful operation, as loss of orthogonality leads to interference, which results in deterioration in Bit Error Rate (BER) performance.

## 2.3 Non-Orthogonal signals and Systems

OFDM signals have been widely used in various existing systems, such as Long Term Evolution (LTE) [23], 802.11x [24] and 5G [3, 25]. This widely accepted paradigm of using orthogonal signals, however, has been challenged in recent times by considering the use of non-orthogonal signals to enhance efficiency and scalability [26].

A number of candidate waveform techniques are being considered for beyond 5G communications [5, 27], where these new waveform techniques can be classified into two groups according to their aim. The first group aims

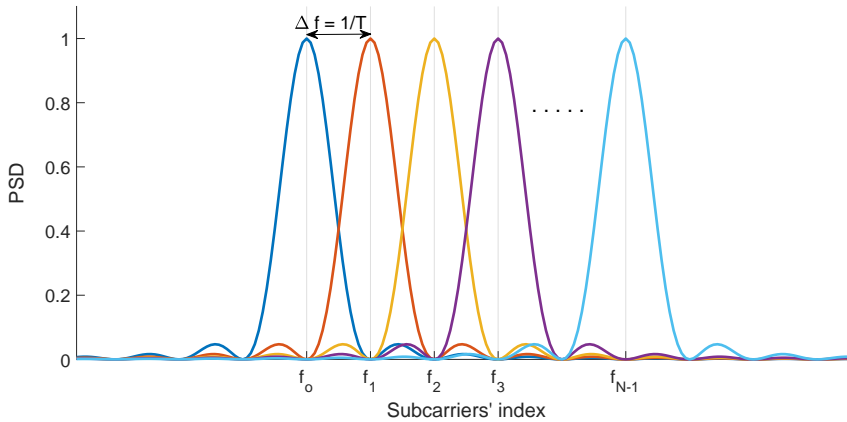


**Figure 2.1:** OFDM spectrum of  $N$  subcarriers

to either increase transmission rate by reducing the transmission time, such as FTN [13, 16] or enhancing spectral efficiency by saving signal bandwidth, such as SEFDM [28, 29] and Fast-Orthogonal Frequency Division Multiplexing (Fast-OFDM) [30]. The second group aims to reduce the out-of-band (OOB) spectral leakage, which is achieved by several methods, such as generalized frequency division multiplexing (GFDM) [31], and Filterbank Based Multicarrier (FBMC) [32] where each subcarrier is filtered.

In this section, brief introduction of non-orthogonal signals and systems are provided, which are Fast-OFDM, M-ary Amplitude Shift Keying (MASK), Overlapped Frequency Division Multiplexing (OvFDM), HC-MCM, FTN, Filterbank Based Multicarrier (FBMC), Universal Filter Multicarrier (UFMC) and Generalized Frequency Division Multiplexing (GFDM).

### 2.3.1 Fast-OFDM

Fast-OFDM [30, 33] is a subset of SEFDM. Fast-OFDM is one important and widely discussed approach, in which the spacing between subcarriers is compressed below the orthogonality limit to  $1/2T$ , where  $T$  is the symbol duration. Unlike OFDM, Fast-OFDM is a non-orthogonal scheme, which packs twice as many subcarriers into the same spectrum as OFDM, thereby doubling the spectral efficiency [30]. However, the compression in the fre-

quency-domain causes interference exclusively from the real part of the signal to the imaginary part and vice versa, thus limiting the modulation to one dimension formats, such as Binary Phase Shift Keying (BPSK) [34]. It should be noted that BPSK with Fast-OFDM has the same spectral efficiency as Quadrature Phase Shift Keying (QPSK) with OFDM, but with better power efficiency.

The continuous time Fast-OFDM signal is expressed as [34]:

$$x_{fast-ofdm}(t) = \frac{1}{\sqrt{T}} \sum_{l=-\infty}^{\infty} \sum_{n=0}^{N-1} d_{l,n} \exp\left(\frac{j2\pi n(t-lT)}{2T}\right), \quad (2.2)$$

where  $d_{l,n}$  is the one-dimensional modulating signal modulated on the  $n^{th}$  subcarrier of the  $l^{th}$  Fast-OFDM symbol,  $N$  represents the number of subcarriers,  $T$  is the Fast-OFDM symbol duration and  $1/\sqrt{T}$  is a normalization factor. Note, the factor of two is included on the numerator and denominator, to highlight the factor-of-two difference with conventional OFDM.

In order to understand the interference among the subcarriers, the cross correlation of two arbitrary subcarriers,  $m^{th}$  and  $n^{th}$ , are found as [34]:

$$\begin{aligned} c_{fast-ofdm}(m, n) &= \frac{1}{T} \int_0^T \exp\left(\frac{j\pi mt}{T}\right) \exp\left(\frac{j\pi nt}{T}\right)^* dt \\ &= \frac{1}{T} \int_0^T \exp\left(\frac{j\pi(m-n)t}{T}\right) dt \\ &= \text{sinc}(\pi(m-n)) + j \frac{\pi(m-n)}{2} \text{sinc}^2\left(\frac{\pi(m-n)}{2}\right) \end{aligned} \quad (2.3)$$

where the real and imaginary parts are given as [34]:

$$\Re(c_{fast-ofdm}(m, n)) = \begin{cases} 1, & m = n \\ 0, & m \neq n \end{cases} \quad (2.4)$$

$$\Im(c_{fast-ofdm}(m, n)) = \begin{cases} 0, & m = n \\ \frac{\pi(m-n)}{2} \text{sinc}^2\left(\frac{\pi(m-n)}{2}\right), & m \neq n \end{cases} \quad (2.5)$$

where  $(\Re)$  and  $(\Im)$  are the real and imaginary parts of the complex signal,

respectively. From (2.4), the real part of the signal is orthogonal among the subcarriers, where the cross correlation between any two subcarriers are equal to zero. However, from (2.5), it is clear that interference stemming from the real part appears on the imaginary part of the signal. Therefore, Fast-OFDM signal is limited for one dimension modulation formats.

### 2.3.2 MASK

MASK OFDM is another spectrally efficient waveform proposed in [35], which is similar to Fast-OFDM. The authors show that orthogonality can be maintained although the frequency spacing between subcarriers is equal to  $\frac{1}{2T}$ . However, this waveform is only applicable with one dimensional modulation format, such as BPSK. Therefore, the spectral efficiency of MASK is equal to that of using QPSK modulation format with OFDM signals. The MASK OFDM signal is defined as [35]:

$$x_{mask-ofdm}(t) = \sum_{n=0}^{N-1} d_n \cos \left[ \frac{2\pi nt}{2T} \right] \quad (2.6)$$

The orthogonality between the subcarriers is verified by finding the cross correlation of two subcarriers, which is given by [35]:

$$c_{mask-ofdm}(m, n) = \int_0^T \cos \left( \frac{j\pi mt}{T} \right) \cos \left( \frac{j\pi nt}{T} \right)^* dt = 0, \quad m \neq n \quad (2.7)$$

Similar to Fast-OFDM, the MASK OFDM signal saves the bandwidth by 50% in comparison to the conventional OFDM using BPSK modulation. Unlike Fast-OFDM, the MASK OFDM consists only of a real signal, where the cosine function is used for modulation. Therefore, the signal is modulated and demodulated using Inverse Discrete Cosine Transform (IDCT) and Discrete Cosine Transform (DCT), respectively. In terms of ease of implementation, Fast-OFDM is more practical because it is modulated and demodulated using Inverse Fast Fourier Transform (IFFT) and Fast Fourier Transform (FFT), respectively [36].

### 2.3.3 OvFDM

OvFDM [37], is a non-orthogonal spectrally efficient system where the fundamental concept of its signal is similar to (based on) that of SEFDM systems, however with different methods for signal generation and detection. The OvFDM signals generation process is composed of a two-stage modulation process. The first stage of OvFDM signal generator, is a pre-coding stage, which is a multiplication process between the complex data symbols and a frequency-domain overlapping matrix [37]. While the second stage, is an Inverse Discrete Fourier Transform (IDFT) process of the resulting signal of the first stage [37]. The reason of using the pre-coding stage, is to modify the complex symbols, thus the modulated signal after the IDFT process, is non-orthogonally overlapped and hence, occupies less bandwidth compared to the orthogonal signals [37]. In addition, the OvFDM system in [37], investigates the employment of CP and ZP on the system performance [37]. For signal detection at the receiver, Maximum Likelihood Sequential Detection (MLSD) is used to retrieve the transmitted data [37].

In terms of computational complexity, the OvFDM is more complex compared to SEFDM system. Where in SEFDM, the signals can be generated using a single stage transmitter, which is a single IDFT with only minor modifications to the conventional OFDM signal generation. In addition, the use of MLSD at the receiver to detect the OvFDM signals, restricts the number of subcarriers and modulation format. This is due to the exponential increase in computational complexity of the receivers with the number of subcarriers and the modulation format order.

### 2.3.4 HC-MCM

HC-MCM is another non-orthogonal multicarrier system [19], which is based on a similar concept to SEFDM and FTN, where enhanced spectral efficiency is achieved by either reducing the subcarrier spacing or decreasing the transmission time for OFDM symbols. In terms of signal generation and reception, similar techniques of those used in SEFDM systems, are applied in HC-MCM, where single IDFT is used for signal modulation. The work in

[19], focuses on finding the spectral efficiency and the minimum Euclidean distance for the HC-MCM symbols for different compression factors. For signal detection, Maximum Likelihood (ML) is used at the receiver to retrieve the transmitted data, which results in a complex system, thus, only four subcarriers were used for system evaluation. Further work on HC-MCM, *(i)* replace the conventional OFDM signals with the HC-MCM signals in order to enhance the spectral efficiency [38], *(ii)* investigate the use of continuous phase modulation with HC-MCM systems [39], and *(iii)* propose decoder similar to the sphere decoder [40], which is composed of two-stage, where the first stage provides a preliminary decision and the second stage is to make the final decision and recover the transmitted data.

### 2.3.5 Faster-Than-Nyquist

FTN, is a spectrally efficient technique that traces back to 1975 [41], in which the data symbols in the time-domain with period  $T$  are sent faster within a time period equal to  $\tau T$ , thus, the FTN symbols period is equal to  $\tau T$ , where  $\tau < 1$  is a time acceleration factor. This results in introducing Inter Symbol Interference (ISI) between the symbols in the time-domain, and therefore, the symbols are no longer orthogonal. Despite that, the signals can be sent faster by upto 25% (i.e.  $\tau = 0.802$  as derived by Mazo in [41]), than the Nyquist rate without degrading the error rate performance [16, 41]. After that, the concept of compressing the symbol in the time-domain has been extended to multicarrier systems and hence, the new system is called multi-stream FTN [42–44]. At the multi-stream FTN transmitters, two-stage FTN mapper and modulator is used [42], in a similar method to OvFDM system. The first stage, the FTN mapper, is responsible of projecting the symbols onto orthonormal basis function [43]. Thus the output of the second stage, the IFFT output, are the multi-stream FTN signals. At the receiver, an iterative decoder utilizing the Bahl, Cocke, Jelinek and Raviv (BCJR) decoder is used to recover the transmitted data [43]. The iterative decoder comprises two parts, *(i)* the outer decoder, and *(ii)* the inner decoder. The outer decoder is simply the BCJR decoder, while the inner decoder performs soft output

calculation, successive interference cancellation, and the Log-Likelihood Ratio (LLR) calculation (demapping) [43]. The hardware impenetations of this design, is reported in the work of [44].

Furthermore, the concepts of compressing the symbols in time-domain as in FTN system, and compressing the subcarriers in frequency-domain as in SEFDM, are extended to time-frequency-domain compressed multicarrier signals. This can be seen as combining two non-orthogonal systems, SEFDM and FTN, in one non-orthogonal multicarrier system termed time-frequency packing [45]. In the time-frequency packing, (*i*) the concept of compressing the subcarriers, of multicarrier systems, beyond the orthogonality limit is taken from the SEFDM system, (*ii*) while the concept of compressing the consecutive symbols in time-domain is taken from the FTN systems.

### 2.3.6 FBMC

In conventional OFDM, the signal element in the time-domain is a rectangular pulse based and hence, the modulated subcarriers have sinc shape in the frequency-domain. Therefore, the subcarriers of an OFDM signal, causes spectral leakage at neighbouring bands, Out-Of-Band (OOB) radiation, in the frequency-domain [32]. In FBMC, each subcarrier is pulse shaped individually and hence, the OOB radiation between frequency sub-bands is eliminated [32]. However, interference between the real and imaginary parts of the signal is introduced [32]. Therefore, Offset Quadrature Amplitude Modulation (OQAM) modulation format is used in FBMC system instead of the Quadrature Amplitude Multiplexing (QAM). In OQAM, the real and imaginary parts are separated, where the imaginary part of the complex signal is delayed by half the symbol duration in time.

### 2.3.7 UPMC

In FBMC, where each subcarrier is pulse shaped individually, hence, the length of the filter impulse response will be long compared to the symbols period. Typically, the filter length is four times the symbols duration [31]. Therefore, high latency will be introduced in the FBMC system. To overcome

this issue, a different multicarrier technique, termed UFMC is proposed to reduce the OOB radiation, with shorter filter impulse response compared to FBMC [46].

In UFMC, a group of subcarriers is filtered together instead of filtering each subcarrier individually [31, 46]. Therefore, the filter impulse response of UFMC is short. This means, unlike FBMC, UFMC is suitable for low latency scenarios.

### 2.3.8 GFDM

Like FBMC, each subcarrier in GFDM is filtered to result in significant reduction of the OOB radiation between the frequency sub-bands. Unlike FBMC, QAM modulation format is used in GFDM systems [31]. Thus, the self-induced interference among subcarriers due to the filtering of each subcarrier, is eliminated with interference cancellation receivers [31].

## 2.4 The SEFDM Concept and Signal Model

In SEFDM, the separation between subcarriers is reduced below the Nyquist criteria by a factor ( $\alpha$ ) as shown in Figure 2.2, where  $\alpha \leq 1$ , resulting in enhanced bandwidth utilization compared to OFDM. However, this leads to self-induced ICI in SEFDM signals, which in turn requires more sophisticated detectors to recover the transmitted data. The SEFDM signal consists of a stream of symbols, where each symbol carries  $N$  complex data symbols. Each complex symbol is modulated onto one subcarrier. Therefore, the overall continuous time-domain SEFDM signal  $\mathbf{x}_{sefdm}(t)$ , consisting of  $l$  SEFDM symbols, is expressed as [15]:

$$x_{sefdm}(t) = \frac{1}{\sqrt{T}} \sum_{l=-\infty}^{\infty} \sum_{m=0}^{N-1} s_{l,n} \exp\left(\frac{j2\pi n\alpha(t - lT)}{T}\right) \quad (2.8)$$

The key difference between OFDM (2.1) and SEFDM is the bandwidth compression factor,  $\alpha$ . SEFDM offers a bandwidth saving equal to  $((1-\alpha) \times \text{total bandwidth})$ , compared to OFDM operates at the same transmission rate.

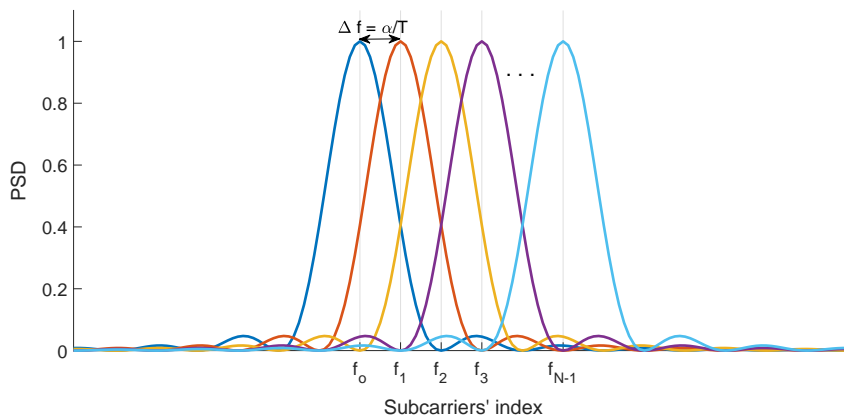


**Figure 2.2:** SEFDM spectrum of  $N$  subcarriers

Setting  $l = 1$  and considering a sampling period of  $t_s = T/Q$ , where  $Q = \rho N$  and  $\rho$  is the oversampling factor, the discrete time-sampled SEFDM data symbol is represented by

$$x_{sefdm}(k) = \frac{1}{\sqrt{Q}} \sum_{n=0}^{Q-1} s_n \exp\left(\frac{j2\pi\alpha nk}{Q}\right) \quad (2.9)$$

where  $k = [0, 1, 2, \dots, Q - 1]$  is the index of the time samples in an SEFDM symbol.

Moreover, the discrete SEFDM data symbol can be given in matrix form as:

$$\mathbf{x}_{sefdm} = \mathbf{F}\mathbf{s} \quad (2.10)$$

where  $\mathbf{x}_{sefdm}$  represents a  $Q$ -dimensional vector of a sampled SEFDM symbol in the time-domain,  $\mathbf{s}$  is an  $N$ -dimensional vector of a sampled input data signal in the frequency-domain and  $\mathbf{F}$  is a  $Q \times N$  matrix representing the sampled carrier matrix. The matrix elements of  $\mathbf{F}$  are given by  $\mathbf{F}_{k,n} = \frac{1}{\sqrt{Q}} \exp(j2\pi\alpha nk/Q)$ .

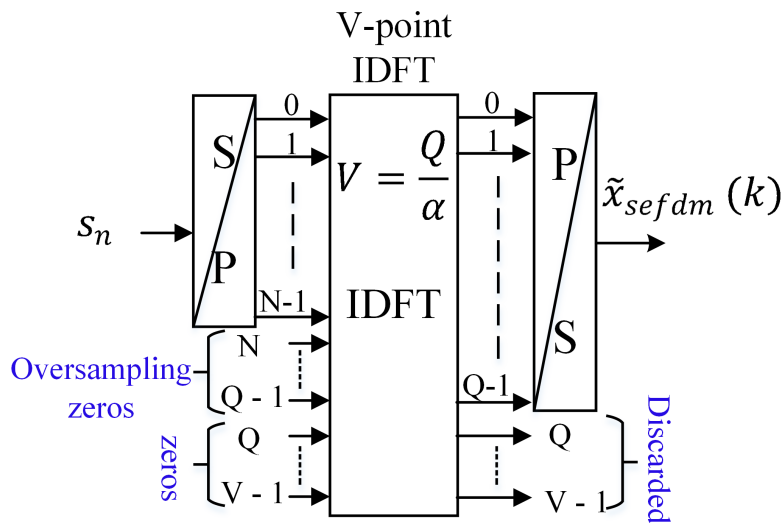


Figure 2.3: SEFDM signal generation based on single IDFT

## 2.5 SEFDM Challenges

SEFDM is not without its challenges though, since the self-induced ICI generated between the subcarriers due to the bandwidth compression, requires more sophisticated generation and recovery techniques [8].

### 2.5.1 Signal Generation

The conventional method of generating the SEFDM signals is using a bank of modulators [8], where each modulator runs at a different subcarrier frequency. However, the sensitivity of such system to frequency offsets increases with the number of subcarriers [47]. In addition, considering systems with large number of subcarriers, the modulation process becomes cumbersome [47]. Therefore, a simple method utilizing IDFT blocks is proposed in [47] to simplify the SEFDM signal generation.

#### 2.5.1.1 SEFDM generation using IDFT

The first SEFDM signal generation method is based on using an IDFT of size ( $V = \lceil Q/\alpha \rceil$ ) as shown in Figure 2.3. Where ( $\lceil * \rceil$ ) is the round function that

find the nearest integer number. Thus, the value of  $V$  has to be an integer, which restricts both  $Q$  and  $\alpha$ . Out of these  $V$  input values,  $N$  is the number of active subcarriers, while the remaining  $(V - N)$  are fed with zeros, hence, the input to the IDFT is given by:

$$\tilde{s}_n = \begin{cases} s_n & , 0 \leq n \leq N - 1 \\ 0 & , N \leq n \leq Q - 1 \\ 0 & , Q \leq n \leq V - 1 \end{cases} \quad (2.11)$$

where the zeros of size  $(Q - N)$ , in the second line of (2.11), refer to the oversampling zeros and the zeros in the third line depict the required padded zeros at the input of IDFT to generate the SEFDM signal. At the output of the IDFT, the same number of  $(V - Q) = ((1 - \alpha)/\alpha) \times Q$  samples are discarded as depicted in Figure 2.3, while the  $Q$  samples are taken forward to make up a single SEFDM symbol. The SEFDM signal expression in the new format after substituting  $(V = Q/\alpha)$  in (2.9) is given as:

$$\tilde{x}_{sefdm}(k) = \frac{1}{\sqrt{Q}} \sum_{n=0}^{V-1} \tilde{s}_n \exp\left(\frac{j2\pi nk}{V}\right) \quad (2.12)$$

where  $k = [0, 1, 2, \dots, Q - 1]$  is the index of the time samples in an SEFDM symbol.

### 2.5.1.2 SEFDM transmitters

SEFDM transmitters were designed and implemented in FPGA to prove the practicability of signal generation in SEFDM systems. In [48, 49], FPGA designs of SEFDM signal were presented, where the designs were based on the multiple IDFTs method [47].

Other works on SEFDM systems show some modifications at the point of signal generation for the purposes of reducing out-of-band- emission by filtering each subcarrier [50]; optimizing the SEFDM signal shape to enhance the spectral and energy efficiencies [9]; minimizing Peak-to-Average Power-Ratio (PAPR) using time windowing [51] or applying tone reservation method [52]; in addition, the precoding technique in [53], was introduced at the

transmitter to reduce the receiver computational complexity.

### 2.5.2 Self-induced ICI characterization

The self-induced ICI can be studied by finding the cross correlation among subcarriers. In which, the interference contribution of a subcarrier to the rest of the subcarriers in the SEFDM symbols are characterized. The work in [54], provides a full study of the ICI in the SEFDM signals and its mathematical modelling. The interference modeling is given in the correlation matrix  $\mathbf{C}$  [54], where its components can be found as:

$$\begin{aligned}
 C_{(l,n)} &= \Phi_{(l,p)}^H \Phi_{(p,n)} \\
 &= \frac{1}{Q} \sum_{p=0}^{Q-1} \exp \left[ \frac{-j2\pi\alpha p}{Q} \right] \exp \left[ \frac{j2\pi\alpha p n}{Q} \right] \\
 &= \frac{1}{Q} \sum_{p=0}^{Q-1} \exp \left[ \frac{-j2\pi\alpha(l-n)p}{Q} \right] \\
 &= \begin{cases} 1, & l = n \\ \frac{1}{Q} \sum_{p=0}^{Q-1} \exp \left[ \frac{-j2\pi\alpha(l-n)p}{Q} \right], & l \neq n \end{cases} \quad (2.13) \\
 &= \begin{cases} 1, & l = n \\ \frac{1}{Q} \left[ \frac{1 - \exp[-j\pi\alpha(l-n)]}{1 - \exp\left[\frac{-j\pi\alpha(l-n)}{Q}\right]} \right], & l \neq n \end{cases}
 \end{aligned}$$

where the  $l$  and  $n$  are the indices of the row and column of the correlation matrix. The matrix quantifies the interference contribution on the  $l^{th}$  subcarrier from its neighbouring  $n^{th}$  subcarriers. From (2.13), it can be noticed that two parameters affecting the interference coefficients in the correlation matrix are the number of subcarriers ( $Q$ ) in the SEFDM symbols and the compression factor  $\alpha$ .

### 2.5.3 Channel Estimation

SEFDM channel estimation is challenging due to the combined self-created ICI and multipath effects. In [11] and [15], channel estimation was carried out in the time-domain. It has been shown that time-domain channel estimation techniques provide a good estimate, and subsequently, a good equalization of the channel [12]. In addition, Partial Channel Estimation (PCE) is used to enhance channel estimation in the time-domain [15]. In this method, only the orthogonal subcarriers in the SEFDM signals are used for estimation and then, interpolation is used to find the channel estimate at each sub-carrier [15]. However, the computational complexity of these time-domain method, is relatively high, since time-domain estimation requires a matrix inversion operation to perform the de-convolution process needed to estimate the channel [12]. In principle, the same performance should be achievable in the frequency-domain.

Xu and Darwazeh (2017), reported that the Mean Square Error (MSE) reaches an error floor at high  $E_b/N_o$  values, when channels are estimated using SEFDM pilots with a CP in frequency-domain [12]. Furthermore, work in optical SEFDM [55] uses OFDM pilot symbols to estimate the channel. This is followed by an interpolation process of the estimated Channel State Information (CSI), which is used to compute the CSI for the compressed subcarriers in SEFDM signals. In addition, Fan *et al.*, argued that there is a gap in the design and implementation of techniques which focus specifically on effective channel estimation in non-orthogonal systems [13].

More recently, a new method utilizing OFDM symbols was used to estimate channel characteristics, where a pilot OFDM symbol is sent at the start of every frame followed by SEFDM data symbols [14,56]. The orthogonal pilot symbols have the same bandwidth as the SEFDM symbols, however, the OFDM symbols are longer in time compared to SEFDM symbols. The new designed OFDM pilot symbols, have the same number of active subcarriers and the same subcarriers location in the frequency-domain as the SEFDM symbols, hence, no interpolation is needed at the receiver. However, due to the increase in the pilot symbol duration in time-domain, modifications in

the standard resource blocks, such as LTE resource blocks, are needed. In addition, this increase in time-domain causes slight reduction in the data rate of SEFDM systems.

#### 2.5.4 Detection in SEFDM systems

Despite the self-generated ICI, the ML technique achieves the optimal error rate performance [8]. However, the computational complexity of the ML increases exponentially with the number of the subcarriers and the cardinality of modulation-mapping scheme. Linear detectors such as Zero Forcing (ZF) and Minimum Mean Square Error (MMSE) present significantly inferior error rate performances in comparison to ML detectors because of the ill-conditioning interference matrix in SEFDM systems [8]. Another detection technique termed Truncated Singular Value Decomposition (TSVD), which was reported in [57], shows superior error rate performance compared to ZF and MMSE detectors, while maintaining a fixed computational complexity for the SEFDM system. However, TSVD offers sub-optimal performance in comparison to ML detectors.

Sphere decoders, were deployed in SEFDM systems, firstly in [8], where optimum performance with lower computational complexity compared to ML is offered. However, SD suffers from variable complexity, which is dependent on system parameters (number of active subcarriers,  $N$ , and the compression factor,  $\alpha$ ), and noise level. Therefore, a Fixed Sphere Decoder (FSD) was introduced in SEFDM systems in [58], which fixes the number of visited branches in every level of the searching tree and hence, removes some of the computational complexity of the decoder. Although SD outperforms FSD in terms of error rate performance, the fixed complexity property of FSD makes it more attractive for practical implementation in hardware platforms. On the other hand, by limiting the number of node visits in the FSD, the BER performance degrades in some cases, such as for a high level of noise and also low values of  $\alpha$ . Therefore, linear detectors are used jointly with FSD to enhance the BER performance, while maintaining a similar level of computational complexity as in FSD. The linear detectors will be used to specify

how many branches will be visited at each level of the tree by calculating the initial estimate of the transmitted symbols, hence, FSD adapts its nodes visits to the noise level and  $\alpha$  factor accordingly. For example, ZF and TSVD were combined with FSD in [57], then an ID was deployed with FSD in [59] to enhance the initial estimate of the transmitted symbols, also, the work of hybrid ID-FSD was applied in [60] to detect SEFDM symbols over optical communication links.

Another detector design in [61] redefines the ML searching area into a Semi-Definite Programming (SDP) by reformulating the ML detection steps into SDP detection problem, which trades the computational complexity for performance optimality in SEFDM receivers. In addition, two-step detectors were introduced to enhance the performance of the sub-optimum detectors, such as in MMSE-ML [62], SDP-ML [61] and SDP-SD [63]. Another technique was proposed to precode the transmitted signals, hence, reduce the computational complexity at the receiver, where only the subcarriers with low Eigenvalues were decoded by ML while ZF detection was applied for the remaining subcarriers [53]. The work in [64], was proposed to exploit the machine learning base detection in SEFDM systems.

The aforementioned detector designs depict uncoded SEFDM systems, where the main targets were either to reduce the computational complexity of optimum detectors, or to improve the BER performance of sub-optimum detectors. Those detectors, imposed restrictions on choosing system parameters, such as  $\alpha$  and  $N$ , also, they were limited to low order modulations (BPSK and QPSK). Moreover, 4G was launched using OFDM as the system modulation scheme for downlink with  $N = 1200$ , up to 64-Quadrature Amplitude Multiplexing (64-QAM) with one tap equalizer. Therefore, to make SEFDM a valid modulation scheme for future generations of communication systems, the above system parameters were to be followed in the second generation of SEFDM systems [29], as explained in the next paragraph.

In the second generation of SEFDM systems, channel coding was firstly introduced in 2014 [65], where recursive convolutional coding with code rate  $R_c = 1/2$ , forward polynomial  $G1 = 1 + D + D^2$  and feedback polynomial  $G2 = 1 + D^2$ . For signal detection, an ID based on the turbo equalization

technique with interference canceller was implemented to recover the transmitted data. The fundamental idea of an ID is that the soft-decoded data with the knowledge of the correlation matrix were used to estimate the interference among subcarriers and then, subtract this interference from the original signal before being passed to the next iteration; repetition of this process enhances the estimation of the transmitted signal, however, the ID introduces processing delay in every extra iteration being processed, while providing improved BER. Where the computational complexity of each iteration of the ID processes is independent of the modulation format, number of subcarrier and the compression factor, restrictions on choosing the number of subcarriers in SEFDM symbols,  $N$ , and  $\alpha$  are relaxed. In addition, employment of different types, of channel coding in SEFDM systems were further investigated in [66–68], such as convolutional, Reed-Solomon (RS), turbo, serial concatenation and Low-Density Parity Check (LDPC) codes.

Experimental offline testbeds utilizing the turbo equalization technique with an interference canceller were implemented in SEFDM systems to evaluate the performance of Long Term Evolution-Advanced (LTE-A) like SEFDM in [12] and to evaluate SEFDM signals in radio-over-fiber scenarios at 2.4 GHz [69] and 60 GHz [70]. The experimental evaluation of the testbeds shows that SEFDM outperforms OFDM in terms of error rate performance, however, with additional fixed latency introduced by the iterative decoder. Finally, two real-time detectors were implemented in FPGAs, where the first one is a TSVD detector [71] while the second detector uses FSD, with 16 subcarriers [72].

#### 2.5.4.1 Detecting SEFDM Signal Using Sphere Decoder

The SD achieves a similar BER performance to the ML, with reduced complexity by searching for the solution among the candidate points within a predefined sphere radius, where the search is constrained by an initial radius, as long as the sphere search space of the SD is a part of the all-possible combinations symbols for the ML search space.

Figure 2.4 depicts a searching tree that demonstrates the SD operation;

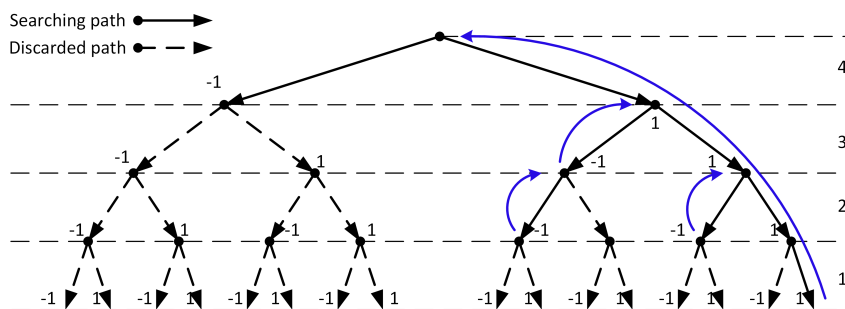


**Figure 2.4:** The sphere decoder tree search of BPSK constellation for 4-subcarriers SEFDM systems

where the size of the searching tree varies according to  $N$  and the constellation size. The number of levels is equal to  $N$  and the index present at the right side of Figure 2.4 is the index of SEFDM subcarriers. The number of branches that come out from every node at each level is equal to the cardinality of the mapping process, which is BPSK in this example that is represented by 2 points in the constellation diagram  $[-1, 1]$ . For ML decoders, the optimal solution is found after searching all the nodes in the tree, which cover all the possible combinations of the transmitted symbols. In contrast, a partial search is performed using the SD, where the nodes within a predefined sphere-space are tested, while the rest of nodes are discarded from the searching space. The solid arrows depict the nodes that appear inside the search space that is being tested. The dashed arrows illustrate the nodes that are found outside the search space, hence, excluded from the search process. The blue arrows in the diagram (backward transition) depicts that the search process at this branch is terminated and discarded with all its corresponding successors.

The initial radius determines the complexity of the SD as it specifies the search space of the SD. It is important to note that the probability of achieving the optimal result would be reduced if the initial radius has a low value, although, a reduction in computational complexity would be yielded. However, a large radius will give a better BER performance at the expense of increasing the computational complexity of the SD detector. Trade off between complexity of SD and the BER performance should be

considered. From Figure 2.4, it can be deduced that the throughput of an SEFDM system using SD for signal detection is higher than the throughput of the same system using ML, where the figure shows only 9 out of 31 points are tested using SD, while ML tests the entire searching tree.

For the SEFDM signals, the initial radius of the search space,  $g$ , is determined by finding the distance between the received symbol,  $\mathbf{r}$ , and the zero forcing estimate,  $\mathbf{s}_{zf}$ , which is found using  $\mathbf{s}_{zf} = [\mathbf{C}^{-1}\mathbf{r}]$ . The initial radius is found by the following equation [36]:

$$g = \|\mathbf{r} - \mathbf{C}\mathbf{s}_{zf}\|^2, \quad (2.14)$$

then the optimal estimation is obtained using the equation [36, 57]:

$$\mathbf{s}_{sd} = \arg \min_{\mathbf{s} \in M^N} \|\mathbf{r} - \mathbf{C}\mathbf{s}\|^2 \leq g, \quad (2.15)$$

where  $\mathbf{C}$  is the correlation matrix,  $\mathbf{s}$  is all the possible combinations of the transmitted SEFDM symbols and  $\mathbf{s}_{sd}$  is the estimated signal. In order to simplify the calculation, the norm argument in (2.15) is expanded and then  $\mathbf{p} = \mathbf{C}^{-1}\mathbf{r}$  is substituted, (2.15) is represented as [36, 57]:

$$\mathbf{s}_{sd} = \arg \min_{\mathbf{s} \in M^N} \{(\mathbf{p} - \mathbf{s})^* \mathbf{C}^* \mathbf{C} (\mathbf{p} - \mathbf{s})\} \leq g \quad (2.16)$$

where  $\mathbf{p}$  is the unconstrained ML estimate of  $\mathbf{s}$  [36].

Using Cholesky decomposition, the Euclidean distance calculation of (2.16) is simplified. The decomposition is carried out by  $chol\{\mathbf{C}^* \mathbf{C}\} = \mathbf{L}^* \mathbf{L}$  [36, 73], where  $\mathbf{L}$  is a  $N \times N$  upper triangular matrix, then (2.15) is written as [57]:

$$\mathbf{s}_{sd} = \arg \min_{\mathbf{s} \in M^N} \|\mathbf{L}(\mathbf{p} - \mathbf{s})\|^2 \leq g, \quad (2.17)$$

Due to the triangular structure of the matrix  $\mathbf{L}$ , the processes of finding the optimal solution can be divided into  $N$  steps, where each step corresponds to a dimension (a subcarrier in SEFDM signals), hence, (2.17) can

be expanded as [36]:

$$\begin{aligned}
 g &\geq (l_{N,N}(p_N - s_N))^2 \\
 &\quad + (l_{N-1,N-1}(p_{N-1} - s_{N-1}) + l_{N-1,N}(p_N - s_N))^2 \\
 &\quad + \dots
 \end{aligned} \tag{2.18}$$

where the term in the first line at the right hand, represents the expression of the level  $N$ , and the second line represents the expression of the level  $N - 1$ .

The SD algorithm tests the nodes that satisfy the constraint condition to find the best solution. The algorithm starts searching at the level  $N$  then moves down to root level in the search tree, which is the level 1. At each level, the radius will be updated and only the nodes that satisfy equation (2.17) are kept. After that, by dividing the  $N$ -dimensional hyper-sphere into  $N$  one-dimensional spheres each square term in (2.18) is easily analysed. The expression for the  $N^{th}$  term is represented by [36]:

$$l_{N,N}^2(p_N - s_N)^2 \leq g_N \tag{2.19}$$

where  $g_N = g$  at the  $N^{th}$  level. Then the search area of the  $N^{th}$  level is found from (2.19) as [36]:

$$\lceil -\frac{\sqrt{g_N}}{l_{N,N}} + p_N \rceil \leq s_N \leq \lfloor \frac{\sqrt{g_N}}{l_{N,N}} + p_N \rfloor \tag{2.20}$$

where  $\lceil \star \rceil$  and  $\lfloor \star \rfloor$  give the closest integer value that is larger and smaller from the given value, respectively; the reason of using these function is because the constellation is assumed to be with integer values. The point  $p_N$  is the center of the searching are within a circle of radius equal to  $\frac{\sqrt{g_N}}{l_{N,N}}$ , which contains the candidate solutions of  $s_N$ . Then the radius for the next level  $N - 1^{th}$  is updated in (2.21) depending on the previous level  $N^{th}$ :

$$g_{N-1} = g_N - l_{N,N}^2(p_N - s_N)^2. \tag{2.21}$$

The second line of the inequality expression of (2.18) is represented as:

$$(l_{N-1,N-1}(p_{N-1} - s_{N-1}) + l_{N-1,N}(p_N - s_N))^2 \leq g_{N-1}. \quad (2.22)$$

which yields the upper and lower bounds:

$$\begin{aligned} & \lceil -\frac{\sqrt{g_{N-1}} - l_{N-1,N}(p_N - s_N)}{l_{N-1,N-1}} + p_{N-1} \rceil \leq s_N \\ & \leq \lfloor \frac{\sqrt{g_{N-1}} - l_{N-1,N}(p_N - s_N)}{l_{N-1,N-1}} + p_{N-1} \rfloor \end{aligned} \quad (2.23)$$

After finding the possible candidate solutions in  $N^{th}$  and  $N - 1^{th}$  dimensions in (2.20) and (2.23), respectively, similar enumerations are applied to the lower levels to find the possible solutions. The processes are repeated until the last level in the search tree, which is level one. The general expressions to find the search space at the  $i^{th}$  level are written as [36]:

$$g_i = g - \sum_{j=i+1}^N l_{j,j}^2 (\zeta_j - s_j)^2 \quad (2.24)$$

$$g_{i-1} = g_i - l_{i,i}^2 (\zeta_i - s_i)^2 \quad (2.25)$$

$$\zeta_i = p_i - \sum_{j=i+1}^N \frac{l_{i,j}}{l_{i,i}} (p_j - s_j)^2 \quad (2.26)$$

where equation (2.24) and (2.25) represent the needed calculations to update the search radius at each level. Equation (2.24), depicts how to find the radius at the  $i^{th}$  level and equation (2.25) provides the needed calculation to find the radius at level  $i - 1^{th}$  out of level  $i^{th}$ . After meeting the condition in the

following equation:

$$\| \mathbf{r} - \mathbf{C}\mathbf{s} \|^2 = \sum_{i=1}^N l_{i,i}^2 (\zeta_i - s_i)^2 \leq g \quad (2.27)$$

the best solution is given as a vector of length  $N$  at the last level, which is the detected transmitted symbol [36].

## 2.6 Conclusions

This chapter aimed to provide a brief description for several multicarrier signals and systems with focus on the non-orthogonal ones. The well-known OFDM signals and systems was illustrated at the beginning of the chapter for two reasons, (i) due to its importance in current existing systems, such as 4G, 802.11x and more recently 5G, (ii) due to its role as a benchmark against which new signals and systems may be evaluated and compared. Then, the chapter carried on providing a summary of potential waveform candidates for beyond 5G systems. Most of these candidates are non-orthogonal waveforms with aim to provide enhancements over the existing OFDM signals in different sectors, such as the data rate, spectral efficiency and out-of-band leakage.

After that, SEFDM concept and signal model were presented. SEFDM is non-orthogonal signals that provides a transmission rate equal to that of the OFDM signals, however, with lower bandwidth requirements. This is achieved by compressing the frequency spacing between the subcarriers and hence, reducing the total bandwidth of the SEFDM signals. In this chapter, the SEFDM challenges in signal generation, channel estimation and signal detection with solutions were reported to date. Furthermore, the application of a SD for SEFDM signal detection has been presented.

The experimental work in SEFDM systems has been carried out using offline systems only. Therefore, the next chapter of this thesis demonstrates the design and implementation of the SEFDM experimental testbed. In addition, the chapter presents the system performance evaluation of SEFDM

system in real-time using OFDM pilot symbols for frequency-domain channel estimation and using ID for signal detection. Furthermore, the chapter demonstrates the ID pipelining design and implementation in SDR to reduce the overall system detection latency and to improve the throughput.

# Chapter 3

## Experimental SEFDM Iterative Detection

### 3.1 Introduction

One of the most significant disadvantages in SEFDM systems is the computational complexity requirements of the receiver [61], where only offline testbeds were implemented. These high computational complexity receivers are due to two main reasons: first, the channel estimation and equalization were applied in the time-domain only that requires matrix inversions, such as in [12]. Second, the high latency introduced by SEFDM decoders, where either SDs were utilized to undo the self-induced ICI [58], or IDs have been demonstrated in the literature which are relatively low complexity in comparison [65] and [10], but introduce significant latency, due to their iterative nature.

The successful employment of the orthogonal frequency-domain channel estimation in real-time that was proposed in [56, 74, 75] and introduced and discussed in Section 4.7 of this thesis, encouraged us to realize and build a complete SEFDM system in real-time. Therefore, for the first time, a pipelined ID structure is proposed to reduce the latency due to the iteration in ID, and hence increase throughput at the cost of additional computational complexity. This chapter demonstrates that, with no loss in performance in

comparison to traditional implementations of SEFDM with an ID, latency can be reduced linearly with the number of pipelined stages.

The chapter presents the following novel contribution: *(i)* proposal and design of a pipeline iterative decoder for the SEFDM systems; *(ii)* a complete real-time system implementation in SDR; and *(iii)* testing the implemented system with realistic RF fading channel model using channel emulator.

It should be noted, that the new scheme of the channel estimation that uses OFDM pilot symbols is designed by a collaborative colleague. However, the contribution in this chapter, is the implementation of the new OFDM pilot scheme for the channel estimation in SDR.

The outline of this chapter: The system transmitter specifications, frame structures and system setup are detailed in Section 3.2. In Section 3.3, a full receiver design description of the SEFDM testbed is given, which includes: *(i)* synchronization and channel estimation and equalization are provided in Section 3.3.1; *(ii)* the ID interference cancellation mechanism utilizing the interference matrix is described in Section 3.3.2; *(iv)* the correlation matrix generation and interference estimation are given in 3.3.3; *(v)* the pipeline processing of the decoder is detailed and described in Section 3.3.4. The experimental testbed setup with the fading channel models parameters and the system performance are provided in Section 3.4. The system platform parameters and their effects are given in Section 3.5 and then this chapter is concluded in Section 3.6.

## 3.2 Signal Generation, System Transmitter Design and Setup

In this section, signal generation, frame structures and system transmitter design and setup are described. Figure 3.1, sketched in blue colour, depicts the schematic block diagram of the transmitter setup. In Section 3.2.1, notes on SEFDM signal model is provided. The system transmitter design using SEFDM signals for data and pilot symbols and their frame structure design are presented in Section 3.2.2. The system transmitter utilizes SEFDM sym-

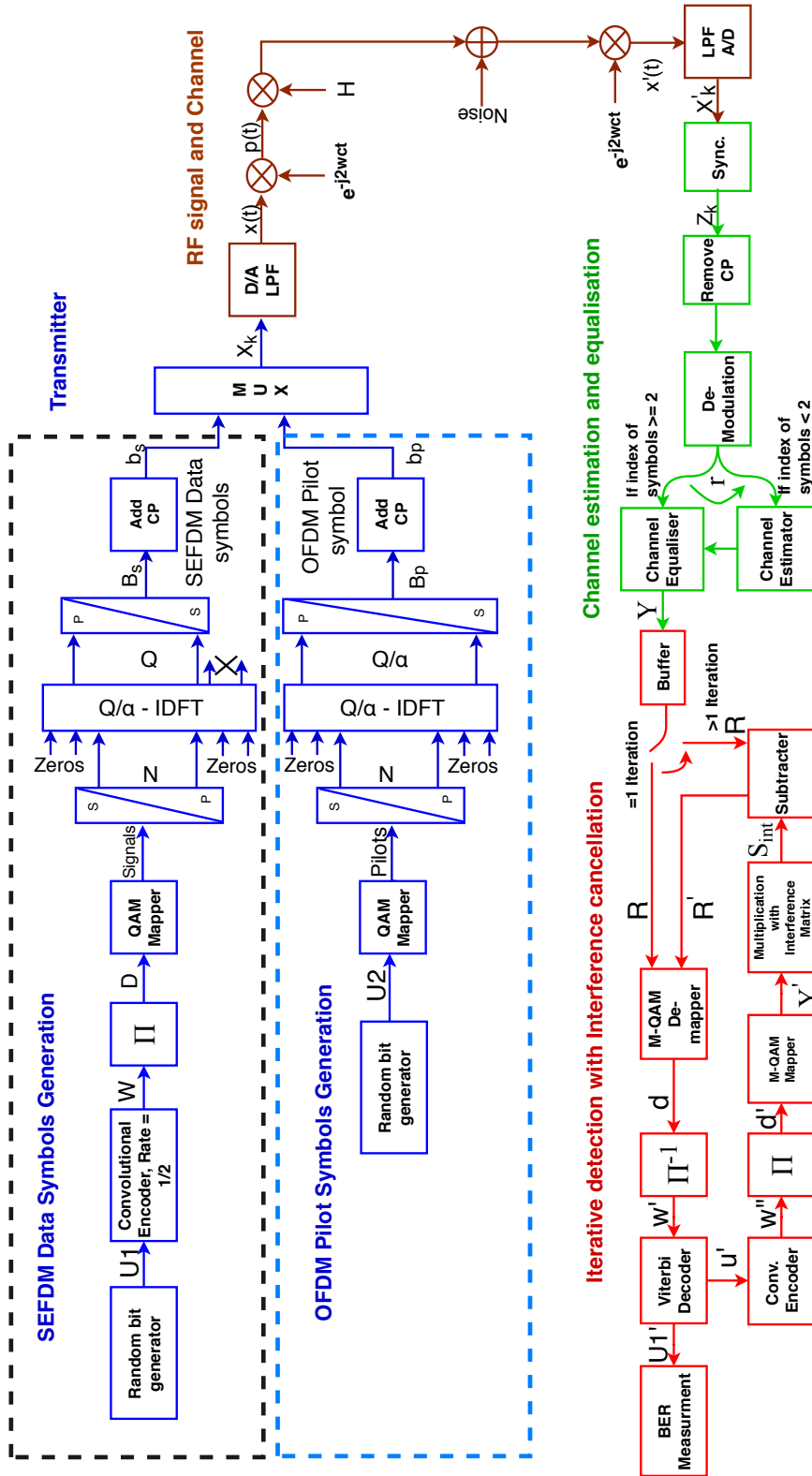


Figure 3.1: Schematic block diagram of SEFDM system

bols to carry data while using OFDM for pilot symbols, which is used for channel estimation purpose is detailed in Section 3.2.3, in addition, the subsection provides the frame structure design using the OFDM pilot symbols. At the end of this section, the system parameters are given in Section 3.2.4.

### 3.2.1 SEFDM signal model

The SEFDM signal model is described fully with mathematical representations in Section 2.4 of this thesis. In addition, Section 4.4 of this thesis provides full details of the mathematical representation and signal description of SEFDM with CP. However, this chapter provides the full description of a complete SEFDM system implementation in SDR.

### 3.2.2 SEFDM data and pilot symbols generation

In this section, the data and pilot symbols generation using SEFDM are detailed.

#### 3.2.2.1 SEFDM data symbol generation.

For the SEFDM data symbol generation, a stream of pseudorandom bits  $d$  is generated before channel coding. The experiment in this chapter, employs a recursive systematic convolutional coder with code rate  $R_c = 1/2$ , with forward polynomial  $G_1 = 1 + D + D^2$  and feedback polynomial  $G_2 = 1 + D^2$  [65]. This is followed by a block interleaver before being mapped onto the appropriate constellation. In this chapter, the system is tested using BPSK, QPSK and 8-Phase Shift Keying (8-PSK) modulation formats.

In order to generate the SEFDM symbols, the mapped data symbols,  $s$ , are divided into parallel streams by a serial-to-parallel converter. The parallel streams are fed to an IDFT of size  $Q/\alpha$ , however, only  $Q$  samples are passed to a parallel to serial process. Each  $Q$  samples constructs an SEFDM symbols in the time-domain. After that, a CP is added at the beginning of every transmitted symbol. These processes are shown in Figure 3.1 in the SEFDM symbols generation part.

### 3.2.2.2 SEFDM pilot symbols generation

A stream of pseudorandom bits is used to generate the pilot symbols for the experimental work presented in this chapter. The bits are mapped onto the appropriate modulation format. After that, the complex symbols are converted to parallel streams then fed to an IDFT to generate the SEFDM symbols in the same manner of generating the SEFDM data symbols [74].

### 3.2.2.3 Frame structure I.

For the case of using SEFDM for pilot and data symbols, the frame structure of the radio frame is similar to those of LTE, which consists of ten equally sized subframes, each of length 1 ms and consists of two time slots. In this chapter, normal CP length is considered and hence, in every time slot, there are seven symbols. A resource block of using SEFDM symbols is depicted in Figure 3.2.

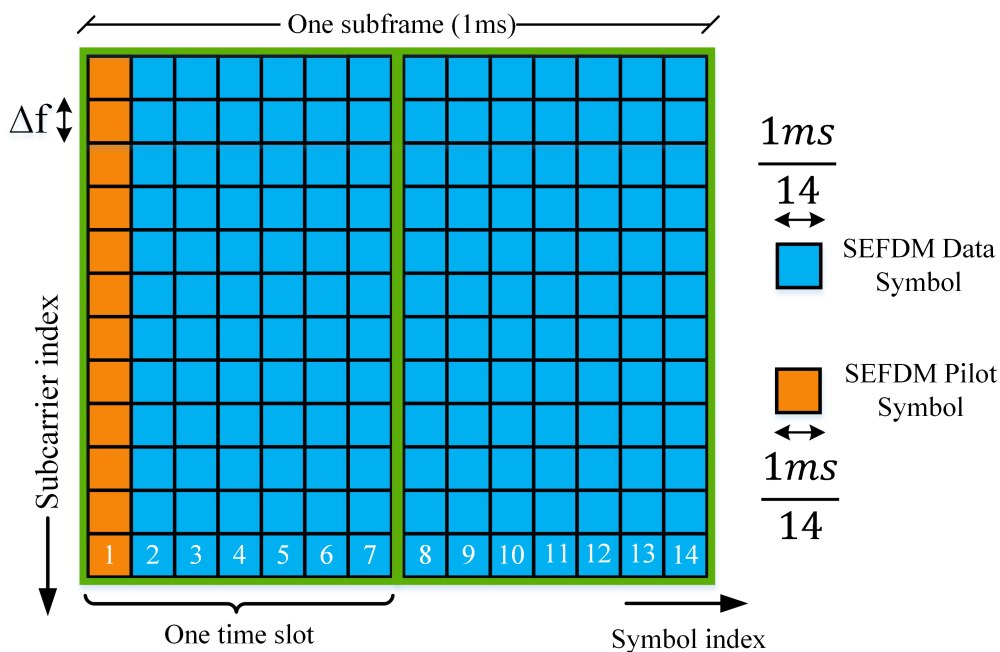


**Figure 3.2:** A resource block of the transmitted frame using SEFDM symbols

Every LTE resource block consists of 12 subcarriers and where each sub-carrier width  $\Delta f = 15$  KHz, hence the bandwidth of the LTE resource block

is 180 KHz. However, using SEFDM signals the bandwidth of each resource block is compressed by the factor  $\alpha$ , which is equal to  $180 \times \alpha$  KHz.

### 3.2.3 SEFDM systems with OFDM pilot symbols

The work in [75] proposes a new channel estimation scheme, which allows using orthogonal pilot symbols for channel estimation, while using SEFDM symbols to convey data. Hence, this pilot scheme is investigated and its performance is compared to the case of using SEFDM pilot symbols.

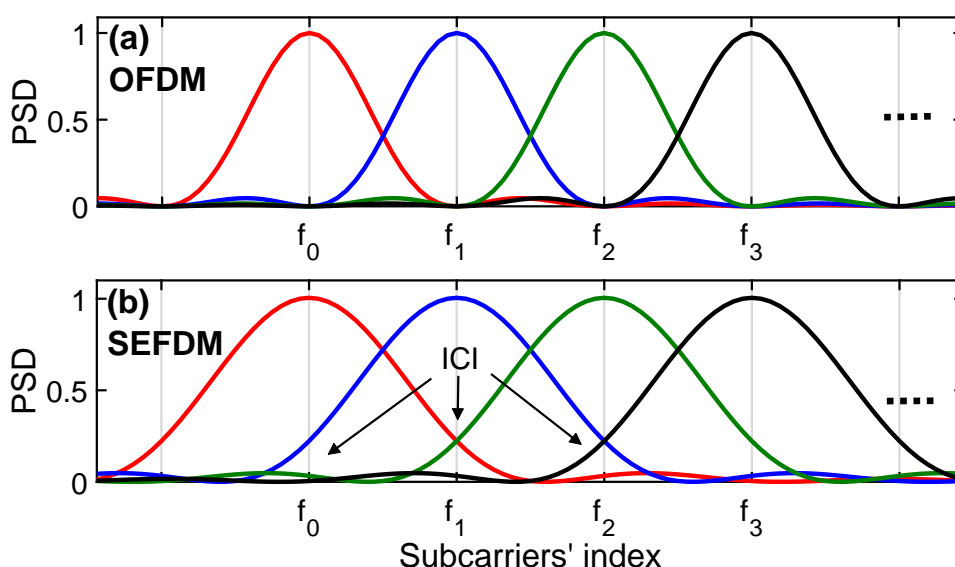


**Figure 3.3:** Conceptual illustration of subcarriers in (a) OFDM pilot symbols and (b) SEFDM symbols with  $\alpha = 0.75$

#### 3.2.3.1 OFDM pilot symbols generation

The OFDM pilot symbols are generated by passing the complex pilot symbols into an IDFT of size  $Q/\alpha$ . Then, the output time samples of the IDFT are passed to a parallel to serial process, then CP is added at the beginning of the symbols. This is depicted in Figure 3.1 in the OFDM pilot symbol generation part. Where the OFDM pilot symbols are longer in time compared to the SEFDM symbols, hence their transmission rate at each subcarrier is lower

than that of the SEFDM. Thus, the OFDM subcarriers are interference-free. A comparison of the OFDM subcarriers to the SEFDM subcarriers is depicted in Figure 3.3. From the figure, it can be noticed that the OFDM subcarriers and SEFDM subcarriers are located at the same positions and hence no interpolation process is needed to obtain the channel estimates.

### 3.2.3.2 Frame structure II

For the second frame structure using OFDM for pilot symbols while using SEFDM symbols to carry data, the number of subframes and time slots in each frame is maintained the same. However, the first symbol of each subframe is an OFDM symbol. This is at the expense of slight increase in the time duration of the pilot symbol, which is dependent on the  $\alpha$  factor. Therefore, a new frame structure should be considered [75] for each  $\alpha$ . The frame structure of the OFDM pilot symbols and SEFDM data symbols is depicted in Figure 3.4. In general, the symbols are transmitted in subframes of 14 symbols, where each frame consists of a pilot symbol followed by 13 data symbols.

### 3.2.4 System transceiver and parameters

In the final stage of the transmitter, the complex baseband signal,  $X_k$ , is fed to the aforementioned Universal Software Radio Peripheral (USRP) to perform Digital to Analog (D/A) conversion and up-conversion to the 2 GHz band. Table 3.1 depicts the system parameters of this experiment. The RF signal is transmitted through a VR5 channel emulator. Then, the signal output of the VR5 is fed to the USRP receiver to deliver the baseband digital domain signal [14].

## 3.3 Receiver Description

In this section, the receiver design including channel estimation and equalization, iterative decoding and the pipelining processing are given.

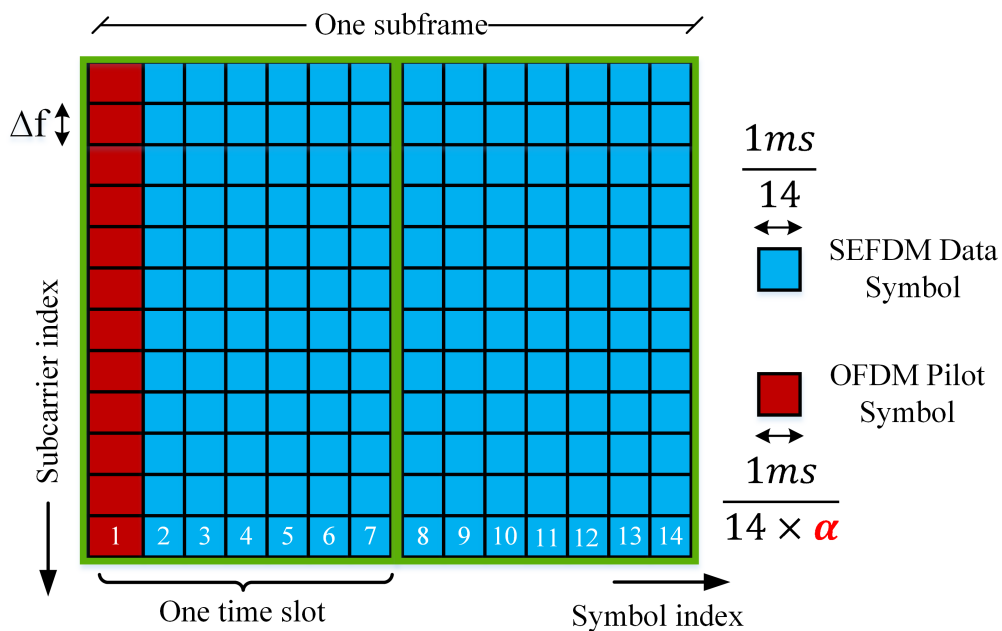


**Figure 3.4:** A resource block of the transmitted frame using OFDM pilot symbols and SEFDM data symbols

**Table 3.1:** Experimental system specifications

Parameters	Values
Centre carrier frequency	2 GHz
Sampling frequency	30.72 MHz
Signal bandwidth	18 MHz
Values of $\alpha$	1 (OFDM); 0.9; ...; 0.4
Subcarrier baseband bandwidth	15 kHz
Subcarrier spacing	$\alpha \times 15$ kHz
SEFDM symbol size	2048
Cyclic prefix	128 time samples
Modulation scheme	BPSK; QPSK; 8-PSK

### 3.3.1 Synchronization and channel estimation and equalization

A Schmidl and Cox [76] synchronization is applied in this experiment, where two identical timing sequences are added at the start of each frame to estimate the first sample of the data symbols.

Following this, the CP is removed from the received symbols and the first symbol of  $r$ , the OFDM pilot symbol is fed to a zero forcing channel estimator. Consequently, the channel estimator output with the data symbols are fed to a one-tap equalizer to mitigate the phase and amplitude distortion of the received data symbols. In this experiment, channel estimation and equalization are applied in the frequency-domain instead of the time-domain ones. This is to reduce the computational complexity required for time-domain channel estimation and equalization, and hence, providing steps towards enabling real-time SEFDM applications.

The mathematical expressions for channel estimation and equalization of SEFDM using CP are provided in Section 4.4.3. While the mathematical representation and expression of using OFDM pilot symbols for channel estimation is given in Section 4.7.

### 3.3.2 Iterative detector with interference canceller

At the detection stage, an iterative detector with an interference canceller are utilized to retrieve the data. The equalized signal,  $Y$  is de-mapped and de-interleaved before viterbi decoding. Next, the recovered decoded data in combination with the knowledge of the correlation matrix are used to estimate the interference,  $S_{int}$ , generated in SEFDM due to the compression of the subcarriers spacing in the frequency-domain. The correlation matrix contains information about the contribution of the interference from all the subcarriers to each subcarrier [54]. After subtracting the estimated interference, the signal,  $R'$  is sent to the next iteration to get an enhanced version of the estimated signal (the signal has lower level of interference); repetition of this process leads to a better signal estimates. A buffer stores the equalized symbols,  $Y$  until a specified number of iterations have been performed. Figure 3.1 depicts the interference cancellation mechanism, which is sketched with red lines.

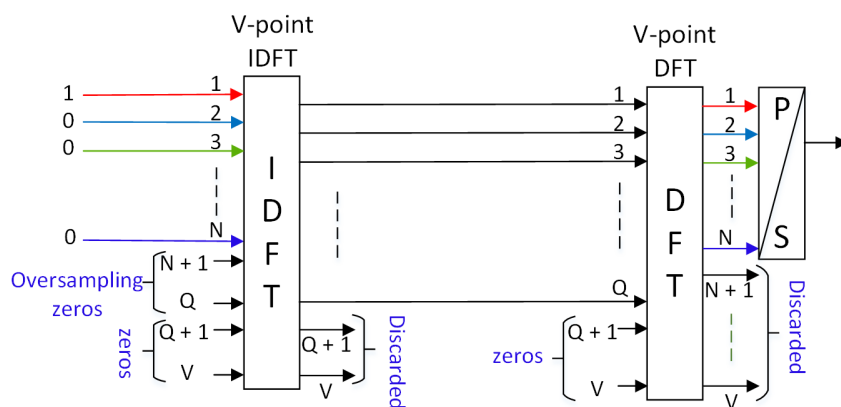


**Figure 3.5:** A method of producing correlation matrix

### 3.3.3 Generation of the interference estimates

In this system, in every iteration the interference is estimated using the decoded data with the correlation matrix, where the matrix is first calculated at the beginning of each new experiment run. In addition, the correlation matrix varies according to the following parameters: (i)  $\alpha$ , (ii) the number of subcarriers and (iii) the IDFT size. Where the system parameters in this system setup are changed on demand by a user. Hence, the correlation matrix is re-calculated whenever one parameter or more of these three parameters is changed.

#### 3.3.3.1 Generating the Correlation Matrix

The interference matrix is found in our experiment by an IDFT and Discrete Fourier Transform (DFT) as shown in Figure 3.5. The number of padded zeros at the input of the IDFT/DFT and the number of discarded samples at the output of IDFT/DFT is controlled by the compression factor,  $\alpha$ . At the input of the IDFT, the subcarrier under test with index  $i$ , where  $i = 1, 2, \dots, N$  and  $N$  is the number of active subcarriers, is fed with 1, while the rest of subcarriers are fed with zeros. This provides the level of interference contribution coming from the  $i^{th}$  subcarrier under test to the rest of active subcarriers in the system. The output of the DFT is taken to be the  $i^{th}$  row of the correlation matrix. The process is repeated  $N$  times to complete the

calculation of the correlation matrix, which is of size  $N \times N$ .

### 3.3.3.2 Interference Signal Estimation

The correlation matrix contains the interference coefficients between all active subcarriers in an SEFDM system, where the matrix coefficients change according to the compression level  $\alpha$ , the IDFT/DFT size and the number of active subcarriers, regardless of what mapping scheme is used in the system. The correlation matrix elements are given as:

$$\mathbf{C}_{(m,q)} = \begin{cases} 1, & m = q \\ \frac{1}{Q} \left[ \frac{1 - \exp[-j2\pi\alpha(m-q)]}{1 - \exp\left[\frac{-j2\pi\alpha(m-q)}{Q}\right]} \right], & m \neq q \end{cases} \quad (3.1)$$

$$= \mathbf{I} + \mathbf{\Psi}$$

where  $m = 1, \dots, N$  and  $q = 1, \dots, N$  are the row and columns indices, respectively;  $Q$  is the IDFT/DFT size. Like OFDM system, the values of the main diagonal elements of the correlation matrix is equal to one [54], which means the original data fed into every subcarrier is passed to the receiver unchanged. However, unlike OFDM system, the rest of the correlation elements, in each row of the matrix, represent the coefficients of interference contribution coming from other active subcarriers onto the desired subcarrier. Hence, the correlation matrix,  $\mathbf{C}$ , can be decomposed into two matrices; (i) a diagonal matrix,  $\mathbf{I}$ , and (ii) the interference coefficients,  $\mathbf{\Psi}$ , as given in the second line of (3.1) and the elements are given by:

$$\mathbf{\Psi}_{(m,q)} = \begin{cases} 0, & m = q \\ \frac{1}{Q} \left[ \frac{1 - \exp[-j2\pi\alpha(m-q)]}{1 - \exp\left[\frac{-j2\pi\alpha(m-q)}{Q}\right]} \right], & m \neq q \end{cases} \quad (3.2)$$

To estimate the interference that appears at each subcarrier from its neighbouring subcarriers, the matrix  $\mathbf{\Psi}$  is multiplied with the recovered,

decoded data, thus, results in the estimated interference vector. This interference estimation process, occurs in every iteration in the ID.

### 3.3.4 Pipeline processing in SDR

As described previously in section 3.3.2, the SEFDM receiver requires the ID for eliminating the inter-subcarrier interference, and one of the negative impacts of this is the introduction of a significant processing delay that limits system throughput. Therefore, in this work, a pipeline processing flow is introduced on this SDR testbed to improve the overall throughput of the ID. Pipelining is a well-known concept in real-time SDR processing [77] and FPGA processing flow design [78]. The proof of the pipeline design on the SDR platform provides a guideline for implementation on Field-Programmable Gate Arrays (FPGAs). The principle of pipeline flow design is to decompose the long processing sequence into a group of sub-modules. By allocating each sub-module with new data, the pipeline mechanism maximises efficiency of computing resources by avoiding the idle/waiting status of sub-modules. In [48] and [71], FPGA designs for SEFDM transmitter and receivers were introduced respectively, then, a pipelined architecture has been proposed for SEFDM transmitters in [49]. For the SEFDM receiver case, this work demonstrates an example pipeline flow design ID, as illustrated in Figure 3.6.

The principle for sub-module processing is to distribute evenly the processing delay to make  $\max\{\tau_i\} \leq \tau$ , where  $\tau_i$  is the processing delay of the  $i^{\text{th}}$  sub-module,  $\tau$  is the symbol duration of SEFDM. It should be noted that, the transformation of ID into a pipelined processing structure, is achieved on the iteration level rather than on each sub-iteration process. This is because (i) the main cause for the processing latency is the additional number of iterations required to decode SEFDM symbols; (ii) the processing latency of the processes inside one iteration is not evenly distributed over the processes; (iii) each iteration of ID has fixed processing delay. Therefore, each sub-module in the pipeline structure is processing a complete iteration of the ID.

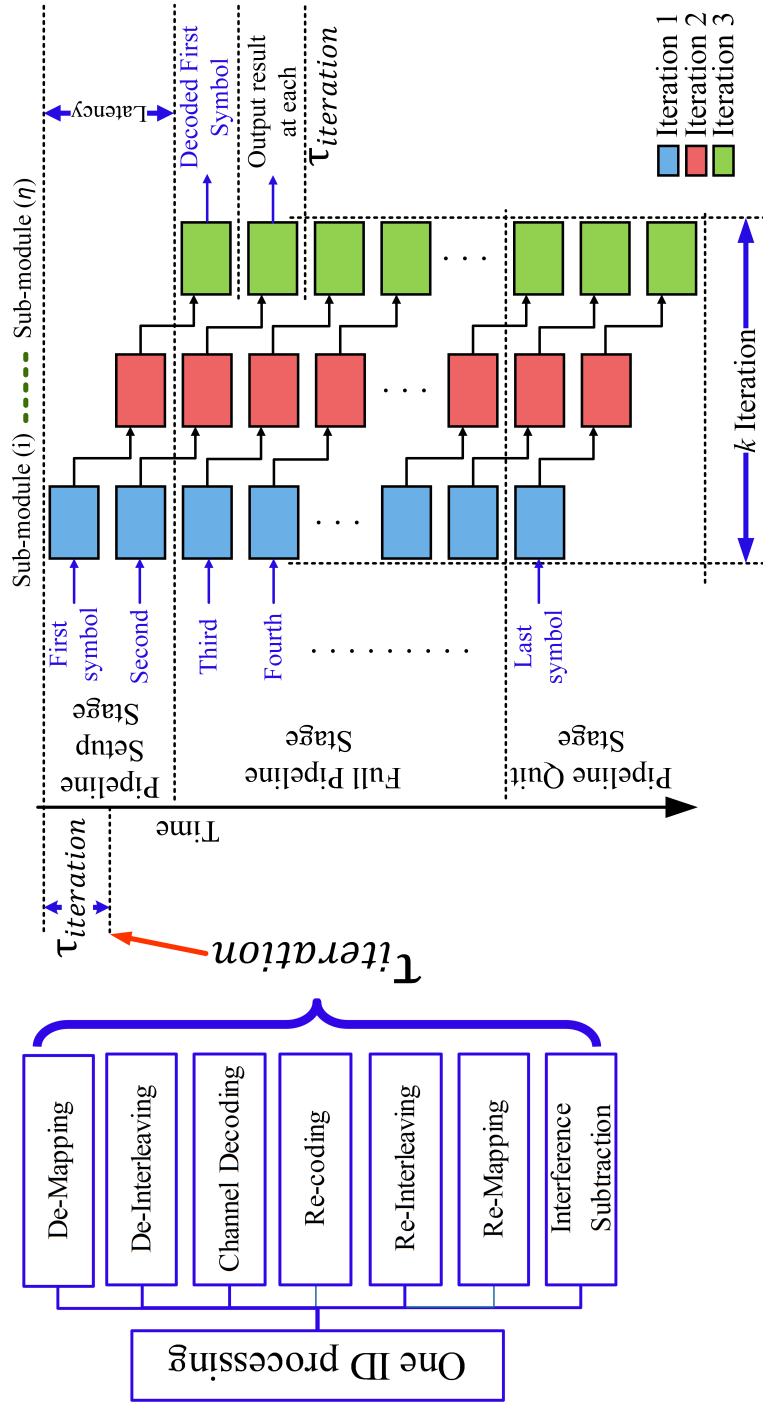


Figure 3.6: Pipeline design structure of iterative decoder

The pipeline processing can be observed in three main stages, as shown in Figure 3.6 [14]: (i) the pipeline setup stage, (ii) the full pipeline stage, and (iii) the pipeline quit stage. In the first stage, the pipeline ID decoder continue taking new received symbols until each sub-module in the pipeline design is fully loaded, however, there is no output yet. In this shown example in Figure 3.6, three sub-module are considered, where each sub-module is covering one iteration. For the full pipeline stage, Figure 3.6 shows that all the sub-modules are fully used after the pipeline setup stage. At this stage, the delay between two consecutive output from the decoder, is equal to  $\tau_{iteration}$ , which is the time required to decode one iteration. This helps to improve the system throughput significantly, up to  $\eta$  times, due to the fact that the processing delays are evenly distributed in each sub-module, where  $\eta$  is the number of sub-modules. In the final pipeline stage, where there is no further symbols to decode, the decoder starts returning to the idle state.

## 3.4 Experimental Testbed Setup and System Performance

In this section, testbed setup description is detailed in Section 3.4.1. The channel estimation evaluation using a static LTE channel model is given in Section 3.4.2. Then, the error rates performance evaluation using dynamic LTE Extended Pedestrian A (EPA) channel model are presented in Section 3.4.3. After that, a frequency spectrum of SEFDM, the constellation diagrams of the received and equalized signals and the three stages of iterative decoding are provided in Section 3.4.4.

### 3.4.1 Testbed descriptions

The software and hardware designs of the real-time experiment are presented in this section to evaluate SEFDM systems in a static LTE and a dynamic LTE EPA channel models [79]. A photograph of the experimental testbed is shown in Figure 3.7. The experimental testbed contains a

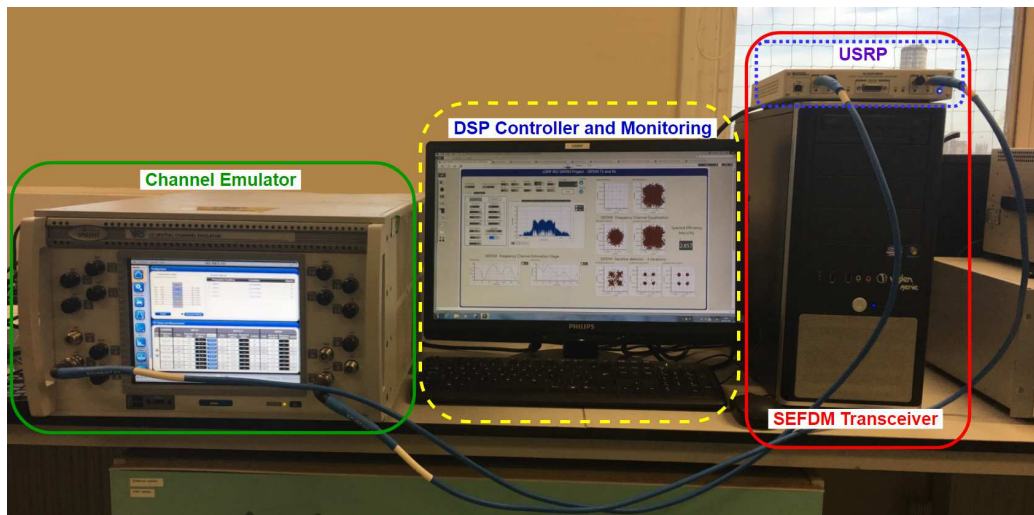


**Figure 3.7:** SEFDM transceiver test-bed setup

USRP transceivers (National Instruments (NI) USRP Reconfigurable Input-Output (RIO) N2395R) programmed using LabVIEW and a Spirent VR5 channel emulator to generate realistic LTE channels. The software design of signal generation and transmission, signal synchronisation, channel estimation and equalization, iterative signal detection and the new pipeline processing method, all developed in real-time and are detailed below.

### 3.4.2 Channel estimation performance

In this experiment, MSE performance is practically examined to evaluate the frequency-domain channel estimation performance. In this experiment, SEFDM and OFDM pilot symbols, using QPSK modulation format, are evaluated in a static channel to assess the frequency-domain channel estimation using the SDR platform. The static frequency selective channel is given as:

$$h(t) = 0.8765\delta(t) - 0.2279\delta(t - T_s) + 0.1315\delta(t - 4T_s) - 0.4032 \exp(j\pi/2)\delta(t - 7T_s). \quad (3.3)$$

where  $T_s$  is the duration of the time samples. Figure 3.8 shows the MSE performance of different compression factors ( $\alpha = 1, 0.9, 0.8, 0.7$ ). From the

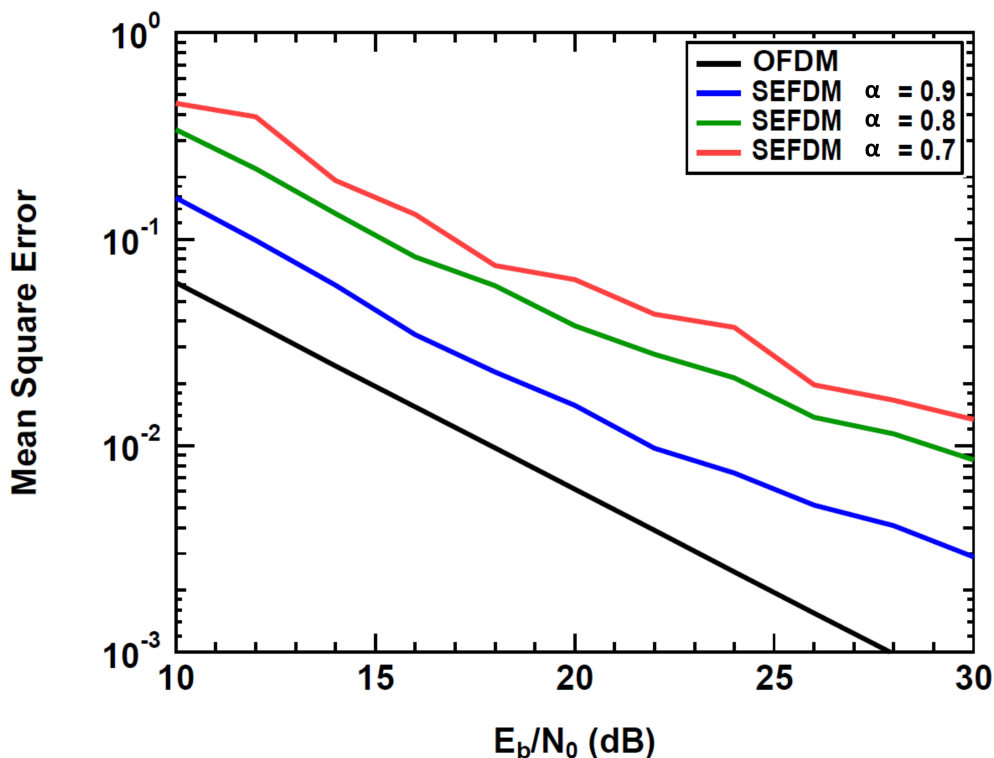


Figure 3.8: Mean square error versus  $E_b/N_0$

figure, it is clear that the frequency-domain OFDM channel estimation outperforms the SEFDM one as depicted by the lower MSE performance. This is due to the self-induced interference among the subcarriers in the SEFDM signals. Furthermore, as expected, the channel estimation accuracy degrades by decreasing  $\alpha$ , because the self-created ICI increases with decreasing  $\alpha$  factor.

### 3.4.3 BER performance

The complete SEFDM system using OFDM pilots for channel estimation, frequency-domain channel equalization and iterative decoding are evaluated with error rate performance in this section. The error rate evaluation is carried out using the SDR platform with realistic LTE RF channel model. The RF signal is transmitted through a VR5 channel emulator that has LTE EPA wireless channel model with doppler frequency of up to 5 Hz [79] and

is set using the parameters shown in Table 3.2.

**Table 3.2:** LTE EPA Fading Channel Model

Path	Relative power	Delay values
1	0.0 dB	0 ns
2	-1.0 dB	30 ns
3	-2.0 dB	70 ns
4	-3.0 dB	90 ns
5	-8.0 dB	110 ns
6	-17.2 dB	190 ns
7	-20.8 dB	410 ns

The measured BER of BPSK, QPSK and 8-PSK-SEFDM are shown in Figure 3.9, Figure 3.10 and Figure 3.11, respectively. From the figures, it is depicted that more than one iteration is needed to retrieve the transmitted data in this SEFDM system. Upon inspection, it is clear that each modulation format approaches the target BER after reaching the third iteration of ID for varying degrees of  $\alpha$ . It is also possible to infer that a higher ratio of bandwidth compression (decreasing  $\alpha$ ) is possible with a lower number of bits/symbol, since a value of  $\alpha = 0.4$  can be supported with sufficiently low BER for BPSK with a power penalty of  $\sim 2$  dB. On the other hand, for QPSK,  $\alpha = 0.7$  can be supported with approximately equivalent performance in comparison to OFDM, as the power penalty is approximately 4 dB. Finally, For 8-PSK,  $\alpha = 0.8$  is the lowest value that can be supported over the range tested, where a power penalty of 5 dB, whereas error floors are observed for  $\alpha \leq 0.7$ .

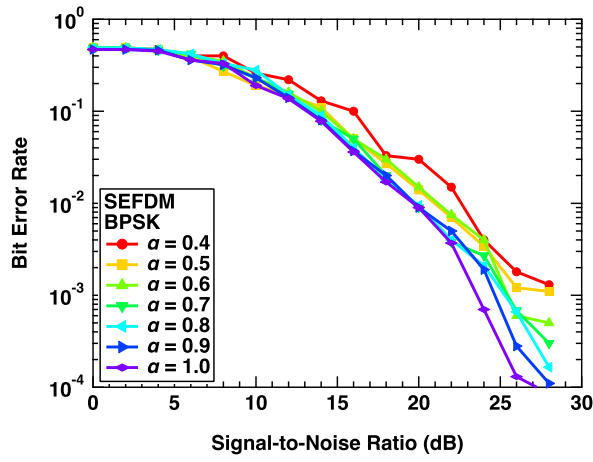


Figure 3.9: BER of BPSK-SEFDM using OFDM pilots

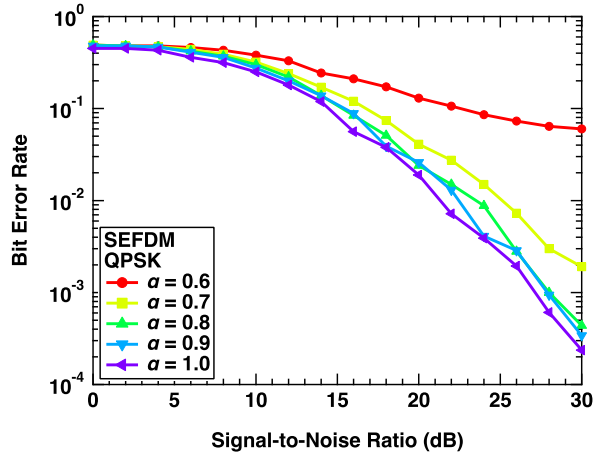


Figure 3.10: BER of QPSK-SEFDM using OFDM pilots

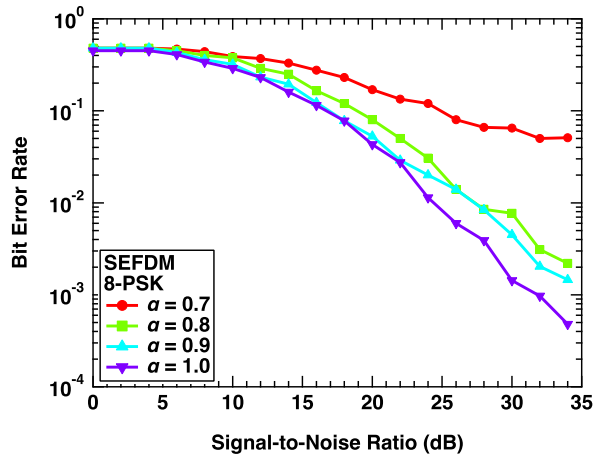
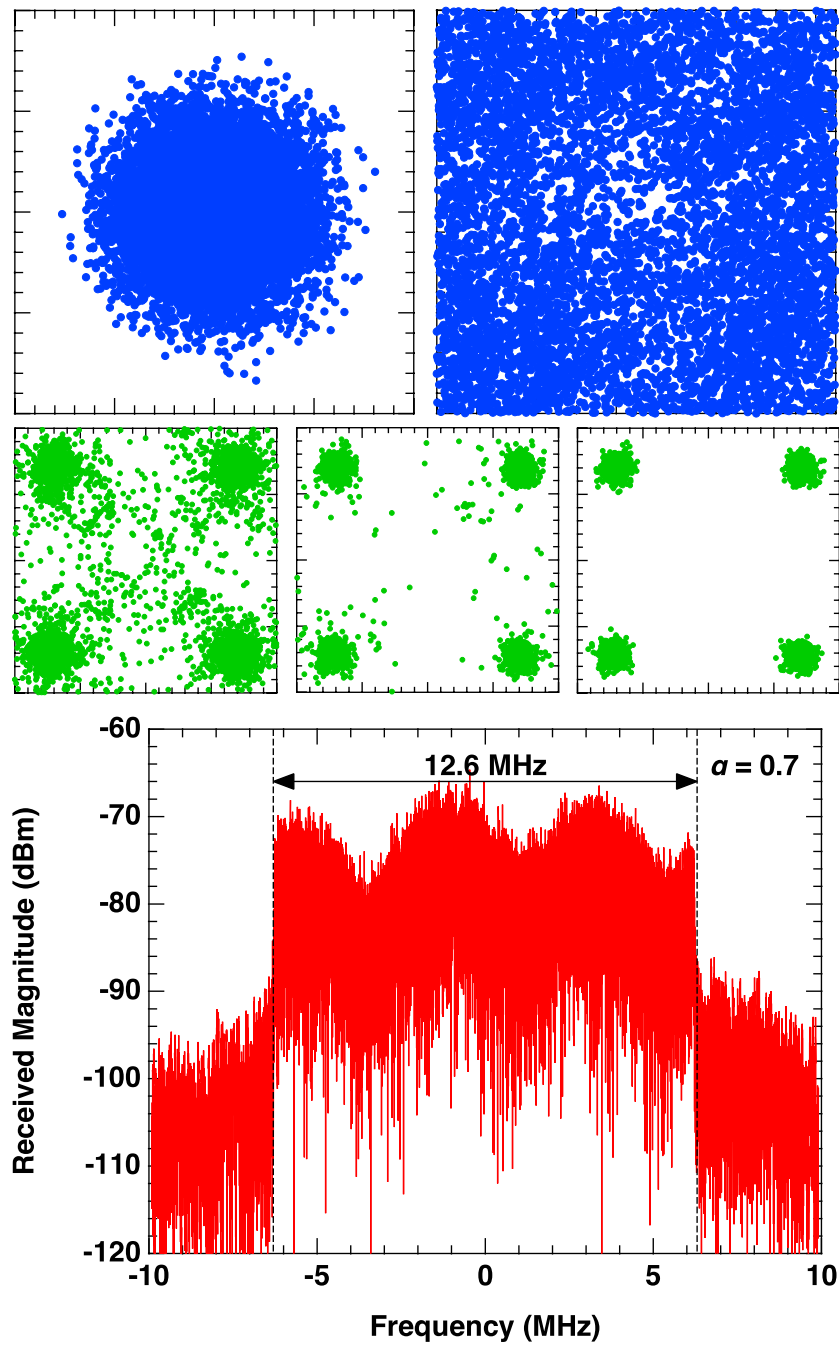


Figure 3.11: BER of 8-PSK-SEFDM using OFDM pilots

### 3.4.4 Received signal representations

In Figure 3.12, constellations for  $\alpha = 0.7$  QPSK are shown and so is the signal spectrum. The top left constellation shows the received symbols after the DFT while the top right constellation shows the same data after channel estimation and equalization. Clearly, at this stage the data cannot be recovered successfully and hence the requirement for the ID. In Figure 3.12, the progressive improvement in received signal constellation is evident as the number of iterations is increased from one (left) to three (right).

Finally, it should be noted that the transforming of the ID into a pipelined structure will increase throughput linearly, by a factor of  $\eta$ , where  $\eta$  is the number of stages in the structure. However, this comes at a cost of computational complexity, which also increases linearly with  $\eta$ .



**Figure 3.12:** Received constellations and measured spectra for  $\alpha = 0.7$ . The top left constellation shows the received symbols while the top right constellation shows the same data after equalization process. The following constellations, from left to right, represent the recovered data after the first, second and third iterations of ID

### 3.5 Interactive System Platform

In this experiment, users are able to change system parameters on demand and observe the effects. Firstly, they can select the number of subcarriers and transmission bandwidth. Other tuneable system parameters include the IDFT/DFT size, cyclic prefix size, compression factor ( $\alpha$ ) and modulation cardinality, as shown in Figure 3.13 (top left surrounded by the solid green line). Finally, a pair of antennas are used (for demonstration purposes) for transmission and reception, so users can move them and observe multipath effects on the received signal constellations and BER; in addition, several LTE static channels are provided in the code that can be dynamically selected.

Moreover, RF parameters such as centre frequency, sampling rate and signal power can be controlled, as shown in Figure 3.13 (on the left side surrounded by the dashed red line). In this work, any changes in the system parameters will be immediately self-evident visually, for example, frequency spectrum, amplitude and phase of the channel estimation, different constellation diagrams that show received, equalized and detected SEFDM symbols and the BER measurement, as shown in Figure 3.13 (on the right side surrounded by the dotted purple line). In addition, Figure 3.13 shows the frequency spectrum of the received SEFDM signal affected by the wireless fading channel and noise, where a compression factor of  $\alpha = 0.7$ , (i.e. a bandwidth saving of 30%) when QPSK-SEFDM is used. In this scenario, only 12.6 MHz is required to transmit data with the same bit rate as OFDM, which would require 18 MHz to achieve the same transmission speed. In the bottom left corner of Figure 3.13 (surrounded by a solid orange line) the detected signal after each iteration is shown. It is clear that the symbols are recovered, error free, due to the employment of the frequency-domain channel estimation and equalization in combination with an iterative detector.

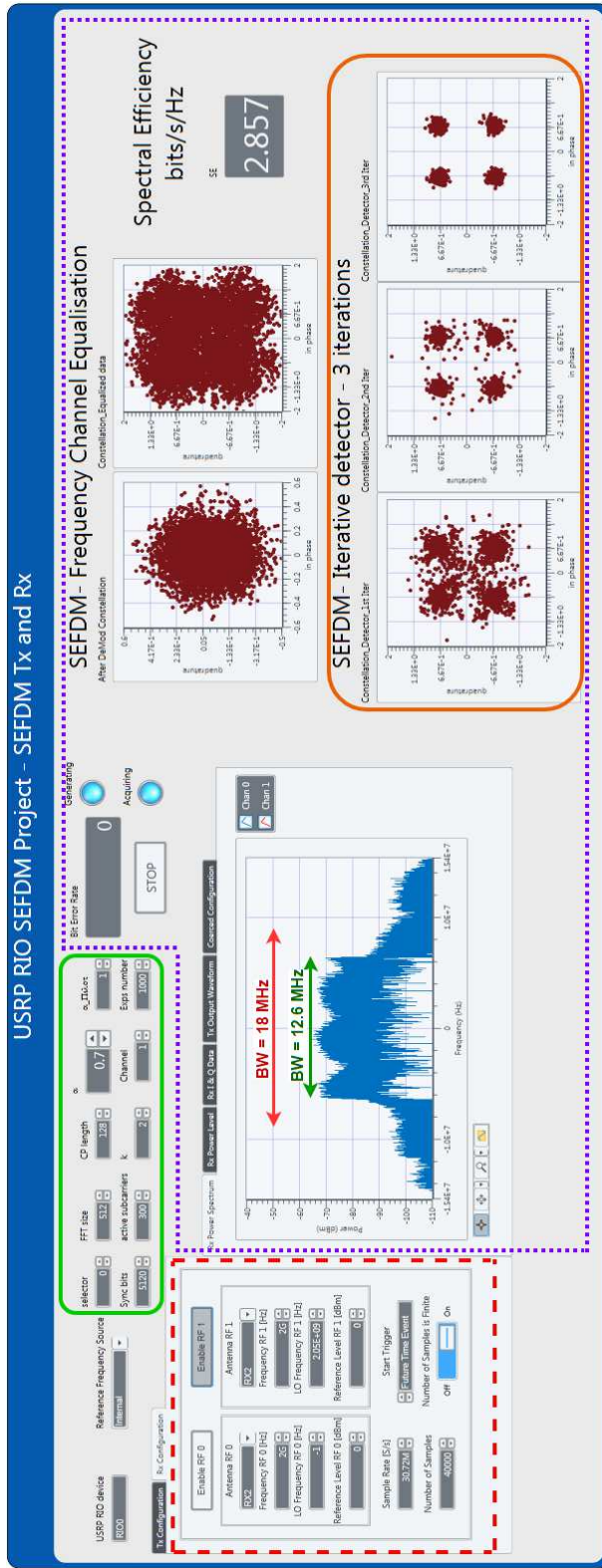


**Figure 3.13:** SEFDM testbed control parameters, constellation diagrams that show received, equalized and detected SEFDM symbols; SEFDM iterative detector showing perfect signal recovery after 3 iterations while saving 30% bandwidth  
 System spectral efficiency increases from 2 bit/s/Hz for OFDM to 2.857 for SEFDM with  $\alpha = 0.7$

## 3.6 Conclusions

In SEFDM systems, which demonstrate significant spectral efficiency gains, real-time system implementation is a challenge due to the high computational complexity introduced by the receivers. Where due to the ICI introduced by the compression in SEFDM signals, a degradation in frequency-domain channel estimation accuracy has been noticed when SEFDM pilot signal is used. Hence, during the last decade, only time-domain channel estimation and equalization were employed in SEFDM systems. However, this introduced high computational complexity and hence latency in the SEFDM receivers. Furthermore, IDs have been used to recover the SEFDM signal after processing a certain number of iterations, however, the sequential iterative process increases the processing time with the number of iterations, leading to throughput reduction. These two reasons, the time-domain channel estimation and equalization and the detection methods, have prevented the realization of a complete SEFDM system implementation in the real-time.

In this chapter, a full SEFDM system design and implementation were experimentally demonstrated. This included the experimental implementation of baseband generation, signal assembly, frequency-domain channel estimation and equalization with a pipelined iterative decoder structure. Two different pilot schemes were considered, where the first was using SEFDM symbols, while the second was using OFDM symbols. These pilot schemes were assessed with MSE performance evaluation using a static channel. From the MSE performance, the use of OFDM pilot symbols for channel estimation resulted in obtaining more accurate channel estimates in comparison to using SEFDM pilot symbols. This was at a slight expense in symbol length, which required re-designing the resource block of the standard system, such as LTE. For the complete real-time system design, OFDM pilot symbols were used for channel estimation and the system was evaluated with a dynamic LTE channel model.

In this work, on one hand, the pilot was sent as an OFDM symbol, but at a lower rate compared to SEFDM symbols. This is because in SEFDM the separation between subcarriers was reduced compared to conventional

OFDM. Therefore, the OFDM pilot was implemented in this system setup so that the frequency locations of the subcarriers equal those of SEFDM but with no ICI, which makes these pilots orthogonal. This resulted in clean pilots, allowing the use of a simple one-tap equalizer in the frequency-domain to mitigate the effect of the channel.

On the other hand, ID pipelining was designed and implemented in SDR to reduce the overall system detection latency and improve the throughput. Thus, symbols are allocated into parallel IDs that have no waiting time as they are received. The experimental findings presented in this chapter show that throughput will improve linearly with the number of the paralleled ID elements, however, hardware complexity also increases linearly with the number of ID elements.

Overall, the system design compromises become apparent through error rate performance studies. These show that for BPSK-SEFDM,  $\alpha = 0.4$  can be supported at the expense of approximately 2 dB power penalty. For the QPSK case, SEFDM symbols with  $\alpha = 0.7$  (i.e. 30% bandwidth saving) can be recovered with power penalty of close to 4 dB.

## Chapter 4

# Zero Padding and Continuous and Conventional Cyclic Prefix: Evaluation for Non-Orthogonal Signals

### 4.1 Introduction

In a classic paper published in 2002 [80], it was demonstrated that using zero padding (ZP) instead of a conventional non-zero CP for orthogonal signals, such as OFDM, can improve channel estimation and guarantee symbol recovery. This debate of using ZP or CP was revisited in 2016 for OFDM [81], yet this time considering the use of filtering or windowing to improve spectral performance required in 5G communication systems.

As mentioned in Section 2.5.3, SEFDM is a non-orthogonal multi-carrier scheme, which packs more subcarriers into the same spectrum relative to OFDM, thereby improving spectral efficiency [8] and making it a topic of current interest [9, 82]. Nevertheless, the self-created ICI inherent in SEFDM systems combined with multipath effects renders channel estimation and equalization more challenging compared to OFDM [12, 56].

Inspired by classical analyses of the received signals of multi-carrier sys-

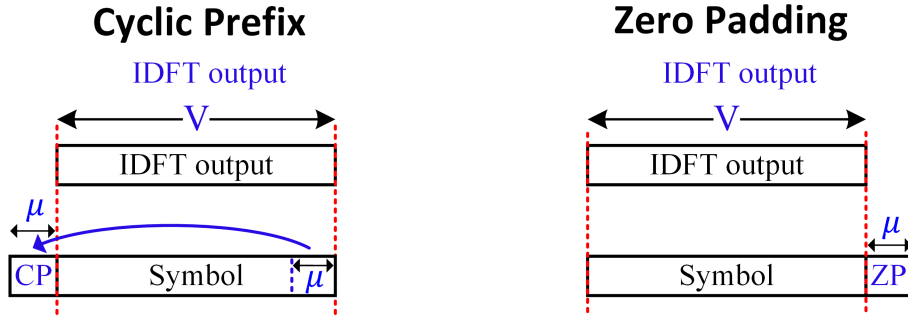


**Figure 4.1:** Guard interval schemes of multicarrier systems

tems, after traversing a multipath channel, this chapter presents the following novel contribution. First, deriving the analytical bounds of channel estimation and equalization for the following guard interval schemes in SEFDM: CP, CCP and ZP in sections 4.4, 4.5 and 4.6, respectively. Second, simulation results in Section 4.8, demonstrate that ZP-SEFDM outperforms CP-SEFDM methods, the latter reaching a non-zero error floor.

More precisely, in Section 4.4, the analytical bounds for channel estimation and equalization for CP-SEFDM are given in equations (4.19) and (4.20), respectively. While in Section 4.5 the analytical bounds of CCP-SEFDM are given in equations (4.37) and (4.38) for the same respective processes. In addition, in Section 4.6, equations (4.47) and (4.48) give the bounds of channel estimation and equalization in ZP-SEFDM.

## 4.2 Guard Interval Techniques and Schemes

In order to mitigate the effect of ISI between adjacent multi-carrier symbols (in particular OFDM) in a multipath wireless channel, a guard interval is added to every transmitted symbol in the time-domain. This guard interval attached to each symbol can be (i) a copy of parts of the symbol, such as in CP or (ii) a trail of zeros, such as in ZP. A CP is generated by copying the last  $\mu$  samples to the beginning of the symbol. On the other hand, ZP replaces the CP part by zeros attached to the end of each symbol. Figure 4.1 depicts these two guard interval schemes, CP and ZP.

### 4.3 SEFDM Signal Model

The mathematical modelling of the SEFDM signal model is provided in Section 2.4 of this thesis. In this chapter, the mathematical modelling of SEFDM starts with the matrix and vector form representation. The discrete SEFDM symbol is given in matrix form as:

$$\mathbf{x}_{sefdm} = \mathbf{F}\mathbf{s} \quad (4.1)$$

where  $\mathbf{x}_{sefdm} \in \mathbb{C}^{Q \times 1}$  is a vector of time samples representing one SEFDM symbol;  $\mathbf{F} \in \mathbb{C}^{Q \times Q}$  is the sampled non-orthogonal subcarrier matrix, which gives the mathematical representation of the SEFDM modulation process [12] and  $\mathbf{s} \in \mathbb{C}^{Q \times 1}$  is the vector of input data symbols. The matrix elements of  $\mathbf{F}$  are given by  $\mathbf{F}_{k,n} = \frac{1}{\sqrt{Q}}e^{(j2\pi\alpha nk/Q)}$ .

#### 4.3.1 IDFT based transmitter

Figure 4.2 depicts a simplified SEFDM transceiver for CP-SEFDM and continuous CP-SEFDM. It should be noted that the SEFDM symbol generation is the same for all tested guard interval techniques in SEFDM, CP-SEFDM, continuous CP-SEFDM and ZP-SEFDM. However, the guard interval (CP, continuous CP or ZP) generation varies according to the chosen guard interval type [83].

In this work, a stream of bits,  $d$ , is generated and mapped into QPSK symbols,  $\mathbf{s}$ , as shown in Figure 4.2. The latter are input to an IDFT, which is used to generate the non-orthogonal SEFDM signal; where a specified number of zeros are appended to the input of the IDFT, thus giving rise to  $V = Q/\alpha$  samples. Consequently, a  $V$ -point IDFT is required to generate the SEFDM signal of  $N$  active subcarriers, where the remaining  $V - N$  inputs are fed with zeros. Of these  $V - N$  zeros,  $(Q - N)$  zeros are introduced due to the oversampling ratio,  $\rho$ . The remaining  $(V - Q)$  zeros which are added to the input of the IDFT depend on the level of bandwidth compression applied. The same number of  $(V - Q)$  samples are discarded at the output of the IDFT, while the  $Q$  samples that are taken forward make up a single

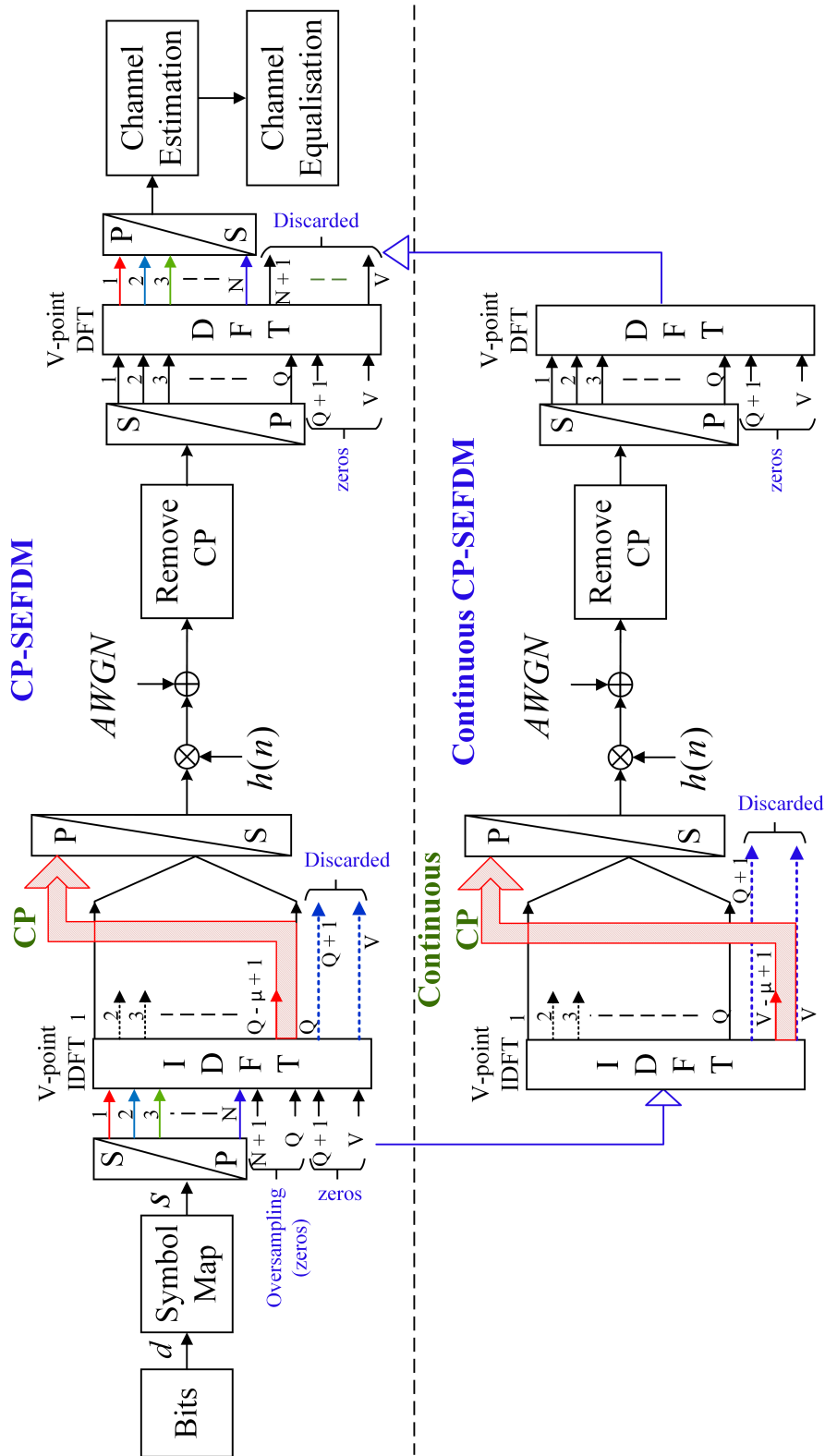
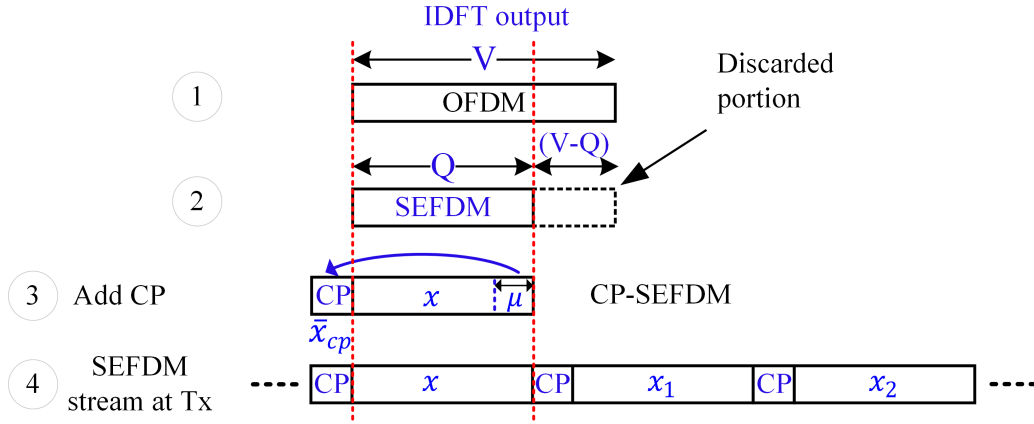


Figure 4.2: Simplified block diagram of SEFDM transceivers with two different cyclic prefix techniques



**Figure 4.3:** Transmitted signal structure representation for CP-SEFDM

SEFDM symbol. Figure 4.2 illustrates the IDFT based transmitter with the input symbols to the IDFT. In addition, steps 1 and 2 of Figure 4.3 depict the IDFT output, the discarded part and the SEFDM symbol.

## 4.4 SEFDM with Cyclic Prefix

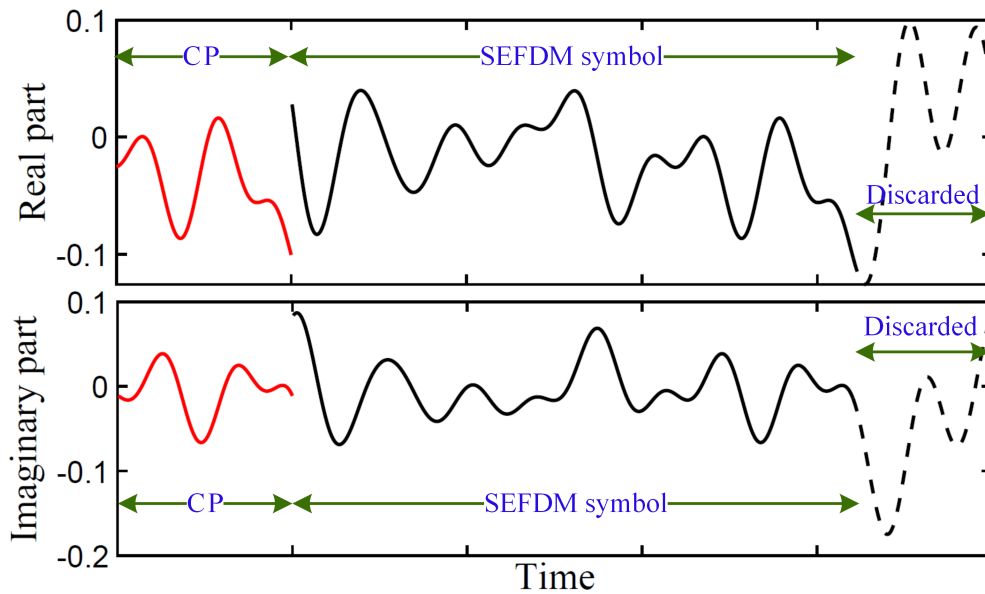
In this section, mathematical analyses of the received CP-SEFDM symbols are derived using *(i)* subcarrier matrix based receiver; and *(ii)* DFT based receiver. After that, the analytical bounds of channel estimation and equalization using CP-SEFDM symbols are obtained.

Step 3 of Figure 4.3, depicts the generation of a conventional CP-SEFDM symbol. In which, the last  $\mu \in \mathbb{N}$  samples of an SEFDM symbol,  $\bar{x}_{cp} \in \mathbb{C}^{\mu \times 1}$ , are added to the beginning of each transmitted SEFDM symbol, hence giving:

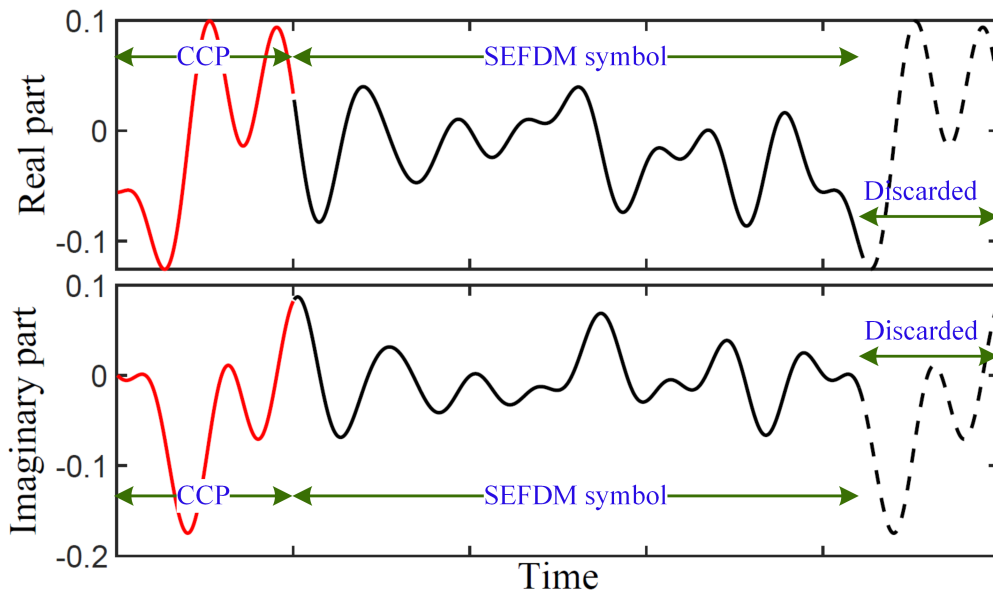
$$\mathbf{x}_{cp} = \begin{bmatrix} \bar{x}_{cp} \\ \mathbf{x}_{sefdm} \end{bmatrix} \quad (4.2)$$

where  $\mathbf{x}_{cp} \in \mathbb{C}^{(Q+\mu) \times 1}$  is the CP-SEFDM symbol. Unlike CP-OFDM symbols, CP-SEFDM symbols have phase discontinuity between the CP part and the SEFDM symbol, as shown in Figure 4.4(a).

The CP-SEFDM symbol is transmitted through a wireless frequency selective channel with channel impulse response (CIR)  $\mathbf{h} = [h_0, h_1, \dots, h_\mu] \in$



(a) Conventional CP-SEFDM



(b) Continuous CP-SEFDM

**Figure 4.4:** Time samples of one CP-SEFDM and continuous CP-SEFDM symbols. The curves with red colour are the guard interval part while the black parts are the IDFT output. The solid-black curves are the SEFDM symbols and the dashed-black curves are the discarded samples at the output of the IDFT

$\mathbb{C}^{(\mu+1)\times 1}$ . The mathematical representation of the received CP-SEFDM after traversing a multipath channel,  $\mathbf{y}_{cp} \in \mathbb{C}^{(Q+2\mu)\times 1}$ , is given in a linear convolution process of the CP-SEFDM symbol with the CIR as:

$$\mathbf{y}_{cp} = \mathbf{h} * \mathbf{x}_{cp} = \begin{bmatrix} \bar{\mathbf{y}}_{cp} \\ \mathbf{y} \\ \mathbf{y}_{isi} \end{bmatrix} \quad (4.3)$$

where the three signal parts,  $\bar{\mathbf{y}}_{cp}$ ,  $\mathbf{y}$  and  $\mathbf{y}_{isi}$ , are depicted in Figure 4.5;  $\bar{\mathbf{y}}_{cp} \in \mathbb{C}^{\mu \times 1}$  is the CP part that is affected by the ISI components stemming from the previous SEFDM symbol and hence it is ignored at the receiver;  $\mathbf{y} \in \mathbb{C}^{Q \times 1}$  is the received SEFDM symbol that is passed to the detection stage;  $\mathbf{y}_{isi} \in \mathbb{C}^{\mu \times 1}$  represents the ISI components that are added to the succeeding SEFDM symbol and  $(*)$  denotes a linear convolution process.

At the receiver, the symbols will arrive distorted by the channel and contaminated with AWGN. The use of a CP at the beginning of a symbol results in the channel impulse response being modelled as a circulant convolution matrix,  $\mathbf{H}_{cp} \in \mathbb{C}^{Q \times Q}$  [84]. Thus, the received SEFDM symbol,  $\mathbf{y}$ , is represented as:

$$\mathbf{y} = \mathbf{H}_{cp} \mathbf{x}_{sefdm} + \mathbf{z} = \mathbf{H}_{cp} \mathbf{F} \mathbf{s} + \mathbf{z} \quad (4.4)$$

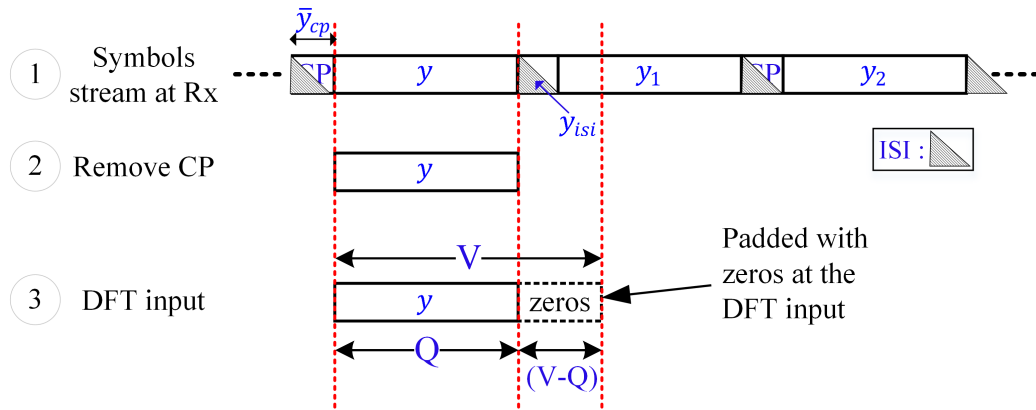


**Figure 4.5:** Received signal structure representation for CP-SEFDM

where  $\mathbf{z} \in \mathbb{C}^{Q \times 1}$  is the AWGN noise vector and  $\mathbf{H}_{cp}$  is given as:

$$\mathbf{H}_{cp} = \begin{bmatrix} h_0 & 0 & \dots & \dots & 0 & h_\mu & \dots & h_1 \\ h_1 & h_0 & \ddots & & & \ddots & \ddots & \vdots \\ \vdots & h_1 & \ddots & \ddots & & & \ddots & h_\mu \\ h_\mu & \vdots & \ddots & \ddots & \ddots & & & 0 \\ 0 & h_\mu & \ddots & \ddots & h_0 & \ddots & & \vdots \\ \vdots & \ddots & \ddots & \ddots & h_1 & \ddots & \ddots & \vdots \\ \vdots & & \ddots & \ddots & \vdots & \ddots & h_0 & 0 \\ 0 & \dots & \dots & 0 & h_\mu & \vdots & h_1 & h_0 \end{bmatrix} \quad (4.5)$$

The eigenvalue decomposition of the channel matrix,  $\mathbf{H}_{cp}$ , is given as [84, 85]:

$$\mathbf{H}_{cp} = \mathbf{M}_{cp} \mathbf{\Lambda}_{cp} \mathbf{M}_{cp}^H \quad (4.6)$$

where  $\mathbf{\Lambda}_{cp} = \text{diag}\{\lambda_0, \dots, \lambda_{Q-1}\} \in \mathbb{C}^{Q \times Q}$  and  $\lambda_i$  is the  $i$ th eigenvalue of  $\mathbf{H}_{cp}$ , while  $\mathbf{M}_{cp}$  and  $\mathbf{M}_{cp}^H \in \mathbb{C}^{Q \times Q}$  are unitary matrices, where  $\mathbf{M}_{cp}^H$  has rows that are the eigenvectors of  $\mathbf{H}_{cp}$  and  $[\cdot]^H$  denotes the conjugate transpose operation. Every eigenvector,  $\mathbf{e}_v \in \mathbb{C}^{1 \times Q}$ , of  $\mathbf{H}_{cp}$  is given as [85]:

$$e_v(l) = \frac{1}{\sqrt{Q}} \{W_Q^{0l}, W_Q^{1l}, \dots, W_Q^{(Q-1)l}\}, l = 0, \dots, Q-1 \quad (4.7)$$

where  $l \in \mathbb{Z}$  is the row index of  $\mathbf{H}_{cp}$  and  $W_Q = e^{-j2\pi/Q} \in \mathbb{C}$ . From (4.7), it can be shown [85] that  $\mathbf{M}_{cp}^H$  is a DFT matrix.

#### 4.4.1 Subcarrier matrix based receiver

The demodulated SEFDM signal,  $\mathbf{r}_{cp}$ , using the transpose conjugate of the non-orthogonal carrier matrix,  $\mathbf{F}^H$ , is expressed in matrix form as:

$$\begin{aligned} \mathbf{r}_{cp} &= \mathbf{F}^H \mathbf{y} = \mathbf{F}^H [\mathbf{H}_{cp} \mathbf{x}_{sef dm} + \mathbf{z}] \\ &= \mathbf{F}^H [\mathbf{H}_{cp} \mathbf{F} \mathbf{s} + \mathbf{z}] = \mathbf{F}^H [\mathbf{M}_{cp} \mathbf{\Lambda}_{cp} \mathbf{M}_{cp}^H \mathbf{F} \mathbf{s} + \mathbf{z}] \\ &= \mathbf{F}^H \mathbf{M}_{cp} \mathbf{\Lambda}_{cp} \mathbf{M}_{cp}^H \mathbf{F} \mathbf{s} + \mathbf{F}^H \mathbf{z} = \mathbf{A} \mathbf{\Lambda}_{cp} \mathbf{B} \mathbf{s} + \mathbf{F}^H \mathbf{z} \end{aligned} \quad (4.8)$$

where the components of the  $m^{\text{th}}$  row and  $n^{\text{th}}$  column of the matrices  $\mathbf{A} = \mathbf{F}^H \mathbf{M}_{cp}$  and  $\mathbf{B} = \mathbf{M}_{cp}^H \mathbf{F}$  can be found as:

$$\mathbf{A}[m, n] = \frac{1}{Q} \sum_{k=0}^{Q-1} e^{(-j2\pi\alpha mk/Q)} e^{(j2\pi nk/Q)} = \frac{1}{Q} \left[ \frac{1-e^{-j2\pi(\alpha m-n)}}{1-e^{-j2\pi(\alpha m-n)/Q}} \right] \quad (4.9)$$

where  $k, m$  and  $n = 0, \dots, Q-1 \in \mathbb{Z}$ . The derivation of (4.9) is based on a sum of geometric series:  $\sum_{k=0}^{Q-1} r^k = \frac{1-r^Q}{1-r}$ . Following the same method applied in (4.9), the components of matrix  $\mathbf{B}$  are found as:

$$\mathbf{B}[m, n] = \frac{1}{Q} \sum_{k=0}^{Q-1} e^{(-j2\pi mk/Q)} e^{(j2\pi\alpha nk/Q)} = \frac{1}{Q} \left[ \frac{1-e^{-j2\pi(m-\alpha n)}}{1-e^{-j2\pi(m-\alpha n)/Q}} \right] \quad (4.10)$$

When  $\alpha = 1$ , the signals are OFDM and hence  $\mathbf{A}$  and  $\mathbf{B}$  are identity matrices so (4.8) becomes:

$$\mathbf{r}_{cp} = \mathbf{\Lambda}_{cp} \mathbf{s} + \mathbf{F}^H \mathbf{z} \quad (4.11)$$

which shows that the multipath channel is decomposed into a set of  $Q$  orthogonal subchannels. On the contrary, we recall that in SEFDM,  $\alpha < 1$ , which implies that  $\mathbf{A}$  and  $\mathbf{B}$  are no longer identity matrices. Thus, the wideband channel cannot be decomposed into independent narrowband subchannels.

In order to find the analytical bounds for channel estimation and equalization in CP-SEFDM systems, this work proposes the use of an orthogonal DFT based demodulator at the receiver to recover the data symbols.

#### 4.4.2 DFT based receiver

Each received SEFDM symbol is appended with zeros to length  $V = Q/\alpha$  before the symbol is fed to a  $V$ -point DFT, as shown in Figure 4.2 and step

3 of Figure 4.5. Assuming that  $Q/\alpha \in \mathbb{N}$ , then (4.4) may be re-written as:

$$\begin{aligned} \begin{bmatrix} \mathbf{y} \\ \mathbf{0}_{(V-Q) \times 1} \end{bmatrix} &= \begin{bmatrix} \mathbf{H}_{cp}, & \mathbf{0}_{Q \times (V-Q)} \\ \mathbf{0}_{(V-Q) \times Q}, & \mathbf{0}_{(V-Q) \times (V-Q)} \end{bmatrix} \begin{bmatrix} \mathbf{F} \\ \mathbf{0}_{(V-Q) \times Q} \end{bmatrix} \mathbf{s} \\ &+ \begin{bmatrix} \mathbf{z} \\ \mathbf{0}_{(V-Q) \times 1} \end{bmatrix} \\ \tilde{\mathbf{y}} &= \tilde{\mathbf{H}}_{cp} \tilde{\mathbf{F}} \mathbf{s} + \tilde{\mathbf{z}} = \tilde{\mathbf{H}}_{cp} \tilde{\mathbf{x}}_{sefdm} + \tilde{\mathbf{z}} \end{aligned} \quad (4.12)$$

where  $\tilde{\mathbf{y}} \in \mathbb{C}^{V \times 1}$ ,  $\tilde{\mathbf{H}}_{cp} \in \mathbb{C}^{V \times V}$ ,  $\tilde{\mathbf{F}} \in \mathbb{C}^{V \times Q}$ ,  $\tilde{\mathbf{x}}_{sefdm} \in \mathbb{C}^{V \times 1}$  and  $\tilde{\mathbf{z}} \in \mathbb{C}^{V \times 1}$  are the zero appended versions of the received SEFDM symbol, channel matrix, subcarrier matrix, transmitted SEFDM symbol and AWGN noise vector, respectively.

The appended channel matrix,  $\tilde{\mathbf{H}}_{cp}$ , is no longer circulant and thus cannot be decomposed. This matrix is expressed as:

$$\tilde{\mathbf{H}}_{cp} = \begin{bmatrix} h_0 & 0 & \dots & 0 & h_\mu & \dots & h_1 & 0 & \dots & 0 \\ h_1 & h_0 & \ddots & & \ddots & \ddots & \vdots & \vdots & & \vdots \\ \vdots & h_1 & \ddots & \ddots & & \ddots & h_\mu & \vdots & & \vdots \\ h_\mu & \vdots & \ddots & h_0 & \ddots & & \ddots & \vdots & & \vdots \\ 0 & h_\mu & \ddots & h_1 & \ddots & \ddots & & 0 & & \vdots \\ \vdots & \ddots & \ddots & \vdots & \ddots & \ddots & \ddots & & & \vdots \\ \vdots & & \ddots & h_\mu & \dots & h_1 & h_0 & 0 & & \vdots \\ \vdots & & & 0 & \dots & \dots & \dots & 0 & & \vdots \\ \vdots & & & & & & & & & \vdots \\ 0 & \dots & \dots & \dots & \dots & 0 & \dots & \dots & \dots & 0 \end{bmatrix} \quad (4.13)$$

Following a similar approach to that outlined in [86],  $\tilde{\mathbf{H}}_{cp}$  can be constructed from three  $V \times V$  matrices as:

$$\tilde{\mathbf{H}}_{cp} = \mathbf{H}_{cp1} + \mathbf{H}_{cp2} - \mathbf{H}_{cp3} \quad (4.14)$$

where  $\mathbf{H}_{cp1} \in \mathbb{C}^{V \times V}$  is the desired circulant matrix having tap coefficient

vectors  $\mathbf{h}^T = [h_0, \dots, h_\mu]$ , while  $\mathbf{H}_{cp2} \in \mathbb{C}^{V \times V}$  and  $\mathbf{H}_{cp3} \in \mathbb{C}^{V \times V}$  represent the missing and unwanted elements in the appended channel matrix,  $\tilde{\mathbf{H}}_{cp}$ , respectively. The elements of  $\mathbf{H}_{cp2}$  and  $\mathbf{H}_{cp3}$  are given as:

$$\mathbf{H}_{cp2} = \begin{bmatrix} 0 & \dots & 0 & h_\mu & \dots & h_1 & 0 & \dots & 0 \\ \vdots & & & \ddots & \ddots & \vdots & \vdots & & \vdots \\ \vdots & & & & \ddots & h_\mu & \vdots & & 0 \\ \vdots & & & & & \ddots & 0 & & 0 \\ \vdots & & & & & & \ddots & \ddots & \vdots \\ 0 & \dots & 0 & 0 \end{bmatrix} \quad (4.15)$$

$$\mathbf{H}_{cp3} = \begin{bmatrix} 0 & \dots & \dots & \dots & \dots & 0 & h_\mu & \dots & h_1 \\ \vdots & & & & & & \ddots & \ddots & \vdots \\ 0 & & & & & & & \ddots & h_\mu \\ \vdots & \ddots & 0 & \dots & \dots & 0 & \dots & \dots & 0 \\ \vdots & & \ddots & h_\mu & \dots & h_1 & h_0 & \ddots & \vdots \\ \vdots & & & \ddots & h_\mu & \vdots & h_1 & h_0 & 0 \\ 0 & \dots & \dots & \dots & 0 & h_\mu & \vdots & h_1 & h_0 \end{bmatrix} \quad (4.16)$$

The eigenvalue decomposition of  $\mathbf{H}_{cp1}$  is given as:

$$\mathbf{H}_{cp1} = \mathbf{M}\mathbf{\Lambda}\mathbf{M}^H \quad (4.17)$$

Applying the concept from (4.7),  $\mathbf{\Phi}^H = \mathbf{M}^H$ , where  $\mathbf{\Phi}^H$  is a DFT matrix of size  $V \times V$  [85]. The demodulated CP-SEFDM signal,  $\tilde{\mathbf{r}}_{cp}$ , is thereby

expressed in matrix form as:

$$\begin{aligned}
\tilde{\mathbf{r}}_{cp} &= \Phi^H \tilde{\mathbf{y}} = \Phi^H [\mathbf{H}_{cp1} \tilde{\mathbf{x}}_{sefdm} + \mathbf{H}_{cp2} \tilde{\mathbf{x}}_{sefdm} - \mathbf{H}_{cp3} \tilde{\mathbf{x}}_{sefdm} + \tilde{\mathbf{z}}] \\
&= \Phi^H [\mathbf{M} \Lambda \mathbf{M}^H \tilde{\mathbf{x}}_{sefdm} + \mathbf{H}_{cp2} \tilde{\mathbf{x}}_{sefdm} - \mathbf{H}_{cp3} \tilde{\mathbf{x}}_{sefdm} + \tilde{\mathbf{z}}] \\
&= \Phi^H \mathbf{M} \Lambda \mathbf{M}^H \tilde{\mathbf{F}} \mathbf{s} + \Phi^H \mathbf{H}_{cp2} \tilde{\mathbf{x}}_{sefdm} - \Phi^H \mathbf{H}_{cp3} \tilde{\mathbf{x}}_{sefdm} + \Phi^H \tilde{\mathbf{z}} \\
&= \mathbf{M}^H \mathbf{M} \Lambda \mathbf{M}^H \tilde{\mathbf{F}} \mathbf{s} + \Phi^H \mathbf{H}_{cp2} \tilde{\mathbf{x}}_{sefdm} - \Phi^H \mathbf{H}_{cp3} \tilde{\mathbf{x}}_{sefdm} + \Phi^H \tilde{\mathbf{z}} \\
&= \Lambda \Gamma \mathbf{s} + \Phi^H \mathbf{H}_{cp2} \tilde{\mathbf{x}}_{sefdm} - \Phi^H \mathbf{H}_{cp3} \tilde{\mathbf{x}}_{sefdm} + \Phi^H \tilde{\mathbf{z}} \\
&= \lambda \tilde{\mathbf{s}} + \Phi^H \mathbf{H}_{cp2} \tilde{\mathbf{x}}_{sefdm} - \Phi^H \mathbf{H}_{cp3} \tilde{\mathbf{x}}_{sefdm} + \Phi^H \tilde{\mathbf{z}}
\end{aligned} \tag{4.18}$$

where  $\Lambda$  is the diagonal matrix of the narrowband subchannel gains, whose diagonal elements given in the vector  $\lambda \in \mathbb{C}^{V \times 1}$ ;  $\tilde{\mathbf{s}} = \Gamma \mathbf{s}$  is the expected received SEFDM symbol when no multipath or noise channels are present,  $\mathbf{M}^H \mathbf{M}$  is equal to an identity matrix, and  $\Gamma = \mathbf{M}^H \tilde{\mathbf{F}} \in \mathbb{C}^{V \times Q}$  is the SEFDM correlation matrix, which quantifies the interference contribution to each subcarrier from its neighbouring subcarriers [12]. It should be evident that even in the absence of noise, the demodulated CP-SEFDM signal would comprise interference components from the missing and unwanted matrices,  $\mathbf{H}_{cp2}$  and  $\mathbf{H}_{cp3}$ .

### 4.4.3 Channel Estimation and Equalization in CP-SEFDM

The analytical bound of channel estimation for CP-SEFDM is found using zero forcing (ZF) and it is given by:

$$\begin{aligned}
\hat{\lambda} &= \tilde{\mathbf{r}}_{cp} / \tilde{\mathbf{s}} = (\lambda \tilde{\mathbf{s}} + \Phi^H \mathbf{H}_{cp2} \tilde{\mathbf{x}}_{sefdm} - \Phi^H \mathbf{H}_{cp3} \tilde{\mathbf{x}}_{sefdm} + \Phi^H \tilde{\mathbf{z}}) / \tilde{\mathbf{s}} \\
&= \underbrace{\lambda}_1 + \underbrace{\Phi^H \mathbf{H}_{cp2} \tilde{\mathbf{x}}_{sefdm} / \tilde{\mathbf{s}}}_2 - \underbrace{\Phi^H \mathbf{H}_{cp3} \tilde{\mathbf{x}}_{sefdm} / \tilde{\mathbf{s}}}_3 + \underbrace{\Phi^H \tilde{\mathbf{z}} / \tilde{\mathbf{s}}}_4
\end{aligned} \tag{4.19}$$

where part 1 represents the subchannel gain estimated at each subcarrier, parts 2 and 3 are the added interference to each subcarrier due to the multipath channel effects, and part 4 corresponds to the noise signal.

The analytical bound of channel equalization for CP-SEFDM is found

using a one-tap equalizer and it is given as:

$$\begin{aligned}\hat{\mathbf{r}}_{cp} &= \tilde{\mathbf{r}}_{cp}/\lambda = (\lambda\tilde{\mathbf{s}} + \Phi^H \mathbf{H}_{cp2} \tilde{\mathbf{x}}_{sefdm} - \Phi^H \mathbf{H}_{cp3} \tilde{\mathbf{x}}_{sefdm} + \Phi^H \tilde{\mathbf{z}})/\lambda \\ &= \underbrace{\tilde{\mathbf{s}}}_1 + \underbrace{\Phi^H \mathbf{H}_{cp2} \tilde{\mathbf{x}}_{sefdm}/\lambda}_2 - \underbrace{\Phi^H \mathbf{H}_{cp3} \tilde{\mathbf{x}}_{sefdm}/\lambda}_3 + \underbrace{\Phi^H \tilde{\mathbf{z}}/\lambda}_4\end{aligned}\quad (4.20)$$

where part 1 is the desired signal, which in turn is contaminated with interference (parts 2 and 3) and noise (part 4). The reason of using  $\lambda$  in (4.20) instead of  $\hat{\lambda}$  is to depict the analytical bound of channel equalization without considering channel estimation impairments.

## 4.5 SEFDM with continuous CP

The work in [75], proposes a different method of generating the CP part termed CCP. The lower diagram of Figure 4.2 depicts a simplified block diagram of the CCP-SEFDM transceiver. Unlike the conventional CP-SEFDM, the new method maintains the phase continuity between the CP and the SEFDM symbols, as shown in Figure 4.4(b). The CCP part ( $\bar{\mathbf{x}}_{ccp}$ ) is generated by copying the last  $\mu$  samples of the IDFT output before being discarded in SEFDM symbols generation, as shown in Figure 4.6.

A CCP-SEFDM symbol,  $\mathbf{x}_{ccp} \in \mathbb{C}^{(Q+\mu) \times 1}$ , is given in the following equation and its parts are shown in Figure 4.6.

$$\mathbf{x}_{ccp} = \begin{bmatrix} \bar{\mathbf{x}}_{ccp} \\ \mathbf{x}_{sefdm} \end{bmatrix}\quad (4.21)$$

The CCP-SEFDM symbol after traversing a multipath wireless channel,  $\mathbf{y}_{ccp}$ , is given by:

$$\mathbf{y}_{ccp} = \mathbf{h} * \mathbf{x}_{ccp} = \mathbf{H}_{ccp} \mathbf{x}_{ccp}\quad (4.22)$$

where  $\mathbf{H}_{ccp} \in \mathbb{C}^{(Q+2\mu) \times (Q+\mu)}$  is the channel matrix representation of the linear

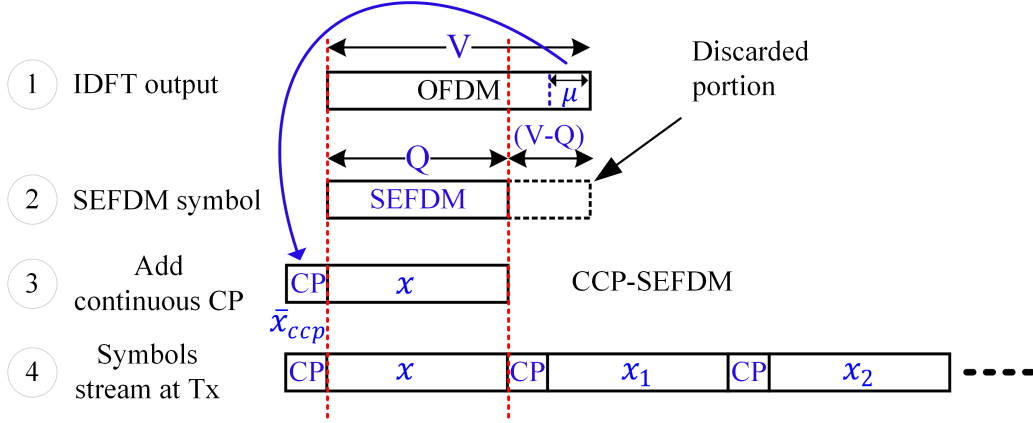


**Figure 4.6:** Transmitted signal structure representation for CCP-SEFDM

convolution process and it is given by:

$$\mathbf{H}_{ccp} = \begin{bmatrix} h_0 & 0 & \dots & \dots & \dots & 0 \\ h_1 & h_0 & \ddots & & & \vdots \\ \vdots & h_1 & \ddots & \ddots & & \vdots \\ h_\mu & \vdots & \ddots & h_0 & \ddots & \vdots \\ 0 & h_\mu & \ddots & h_1 & \ddots & 0 \\ \vdots & \ddots & \ddots & \vdots & \ddots & h_0 \\ \vdots & & \ddots & h_\mu & \ddots & h_1 \\ \vdots & & & \ddots & \ddots & \vdots \\ 0 & \dots & \dots & \dots & 0 & h_\mu \end{bmatrix}_{(Q+2\mu) \times (Q+\mu)} \quad (4.23)$$

The  $\mathbf{y}_{ccp}$  can be represented in matrix form as:

$$\mathbf{y}_{ccp} = \begin{bmatrix} \mathbf{H}_{ccp1} \\ \mathbf{H}_{ccp2} \\ \mathbf{H}_{ccp3} \end{bmatrix} \mathbf{x}_{ccp} = \begin{bmatrix} \bar{\mathbf{y}}_{ccp} \\ \mathbf{y}_c \\ \mathbf{y}_{c_{isi}} \end{bmatrix} \quad (4.24)$$

where  $\bar{\mathbf{y}}_{ccp} \in \mathbb{C}^{\mu \times 1}$  is the CCP part that is affected by the ISI components, hence it is neglected at the receiver;  $\mathbf{y}_c \in \mathbb{C}^{Q \times 1}$  is the received SEFDM symbol

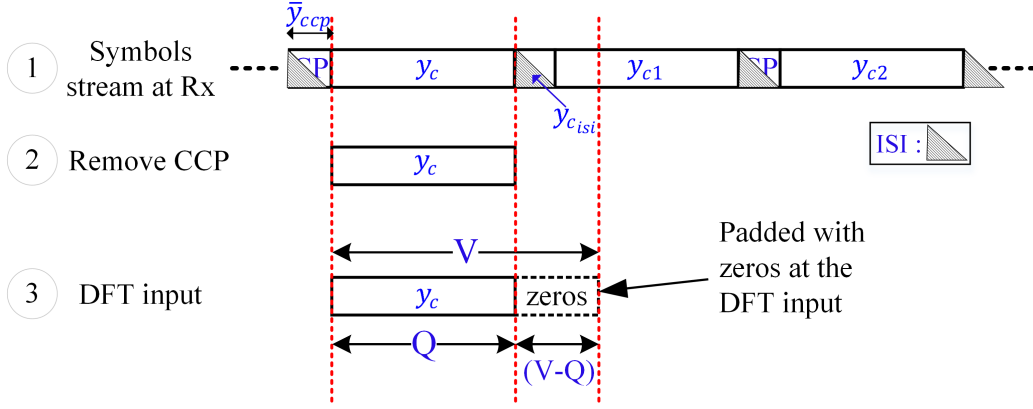


**Figure 4.7:** Received signal structure representation for CCP-SEFDM

before being passed to the demodulation stage;  $\mathbf{y}_{cisi} \in \mathbb{C}^{\mu \times 1}$  represents the ISI components that are added to the succeeding SEFDM symbol. The signal parts,  $\bar{\mathbf{y}}_{ccp}$ ,  $\mathbf{y}_c$  and  $\mathbf{y}_{cisi}$ , are depicted in Figure 4.7. The matrix  $\mathbf{H}_{ccp}$  can be partitioned into three parts, (i) an upper part  $\mathbf{H}_{ccp1} \in \mathbb{C}^{\mu \times (Q+\mu)}$ , (ii) a middle part  $\mathbf{H}_{ccp2} \in \mathbb{C}^{Q \times (Q+\mu)}$  and (iii) a lower part  $\mathbf{H}_{ccp3} \in \mathbb{C}^{\mu \times (Q+\mu)}$ , which are given as:

$$\mathbf{H}_{ccp1} = \begin{bmatrix} h_0 & 0 & \dots & \dots & \dots & \dots & \dots & \dots & 0 \\ h_1 & h_0 & \ddots & & & & & & \vdots \\ \vdots & \ddots & \ddots & \ddots & & & & & \vdots \\ h_{\mu-2} & \ddots & \ddots & h_0 & \ddots & & & & \vdots \\ h_{\mu-1} & h_{\mu-2} & \dots & h_1 & h_0 & 0 & \dots & \dots & 0 \end{bmatrix}_{\mu \times (Q+\mu)} \quad (4.25)$$

$$\mathbf{H}_{ccp2} = \begin{bmatrix} h_\mu & h_{\mu-1} & \dots & h_0 & 0 & \dots & \dots & \dots & 0 \\ 0 & h_\mu & \ddots & \ddots & h_0 & \ddots & & & \vdots \\ \vdots & 0 & \ddots & \ddots & \ddots & \ddots & \ddots & & \vdots \\ \vdots & & \ddots & \ddots & \ddots & \ddots & \ddots & \ddots & \vdots \\ \vdots & & & 0 & h_\mu & \dots & \dots & h_0 & \ddots \\ \vdots & & & & \ddots & \ddots & \ddots & \ddots & 0 \\ 0 & \dots & \dots & \dots & \dots & 0 & h_\mu & \dots & h_0 \end{bmatrix}_{Q \times (Q+\mu)} \quad (4.26)$$

$$\mathbf{H}_{ccp3} = \begin{bmatrix} 0 & \dots & \dots & \dots & 0 & h_\mu & \dots & \dots & \dots & h_1 \\ \vdots & & & & & \ddots & \ddots & \vdots & \ddots & h_2 \\ \vdots & & & & & & \ddots & h_\mu & \ddots & \vdots \\ \vdots & & & & & & & \ddots & \ddots & \vdots \\ 0 & \dots & 0 & h_\mu \end{bmatrix}_{\mu \times (Q+\mu)} \quad (4.27)$$

As mentioned earlier, out of the three parts in Equation 4.24,  $\mathbf{y}_c$  is the part that is desired at the receiver, which is the SEFDM symbol. The  $\mathbf{y}_c$  part can be further analyzed as:

$$\mathbf{y}_c = \mathbf{H}_{ccp2} \mathbf{x}_{ccp} = \begin{bmatrix} \mathbf{H}_{ccp2a} & \mathbf{H}_{ccp2b} \end{bmatrix} \begin{bmatrix} \bar{\mathbf{x}}_{ccp} \\ \mathbf{x}_{sefdm} \end{bmatrix} = \underbrace{\mathbf{H}_{ccp2a} \bar{\mathbf{x}}_{ccp}}_1 + \underbrace{\mathbf{H}_{ccp2b} \mathbf{x}_{sefdm}}_2 \quad (4.28)$$

where term 1 represents the multipath components stemming from the CCP part, while the term 2 represents the SEFDM symbol after traversing a wireless multipath channel. The matrices  $\mathbf{H}_{ccp2a}$  and  $\mathbf{H}_{ccp2b}$  are given by:

$$\mathbf{H}_{ccp2a} = \begin{bmatrix} h_\mu & \dots & h_1 \\ 0 & \ddots & \ddots \\ \vdots & \ddots & h_\mu \\ \vdots & & \vdots \\ \vdots & & \vdots \\ \vdots & & \vdots \\ 0 & \dots & 0 \end{bmatrix}_{Q \times \mu} \quad (4.29)$$

and

$$\mathbf{H}_{ccp2b} = \begin{bmatrix} h_0 & 0 & \dots & \dots & \dots & \dots & 0 \\ \vdots & h_0 & \ddots & & & & \vdots \\ \vdots & \ddots & \ddots & \ddots & & & \vdots \\ h_\mu & \ddots & \ddots & \ddots & \ddots & & \vdots \\ 0 & h_\mu & \dots & \dots & h_0 & \ddots & \vdots \\ \vdots & \ddots & \ddots & \ddots & \ddots & \ddots & 0 \\ 0 & \dots & 0 & h_\mu & \dots & \dots & h_0 \end{bmatrix}_{Q \times Q} \quad (4.30)$$

At the receiver, the SEFDM symbol,  $\mathbf{y}_c$ , is contaminated with AWGN noise and wireless multipath channel effects. Hence, the received symbol,  $\mathbf{y}_{c_{rx}}$ , can be written as:

$$\mathbf{y}_{c_{rx}} = \mathbf{y}_c + \mathbf{z}_c = \mathbf{H}_{ccp2a} \bar{\mathbf{x}}_{ccp} + \mathbf{H}_{ccp2b} \mathbf{x}_{sefdm} + \mathbf{z}_c \quad (4.31)$$

Each SEFDM symbol is zero padded to length  $V = Q/\alpha$  before it is fed to the DFT process. The received SEFDM symbol may then be re-written as:

$$\begin{aligned} \begin{bmatrix} \mathbf{y}_{c_{rx}} \\ \mathbf{0}_{(V-Q) \times 1} \end{bmatrix} &= \begin{bmatrix} \mathbf{H}_{ccp2a}, & \mathbf{0}_{Q \times (V-\mu)} \\ \mathbf{0}_{(V-Q) \times \mu}, & \mathbf{0}_{(V-Q) \times (V-\mu)} \end{bmatrix} \begin{bmatrix} \bar{\mathbf{x}}_{ccp} \\ \mathbf{0}_{(V-\mu) \times 1} \end{bmatrix} \\ &+ \begin{bmatrix} \mathbf{H}_{ccp2b}, & \mathbf{0}_{Q \times (V-Q)} \\ \mathbf{0}_{(V-Q) \times Q}, & \mathbf{0}_{(V-Q) \times (V-Q)} \end{bmatrix} \begin{bmatrix} \mathbf{F} \\ \mathbf{0}_{(V-Q) \times Q} \end{bmatrix} \mathbf{s} + \begin{bmatrix} \mathbf{z}_c \\ \mathbf{0}_{(V-Q) \times 1} \end{bmatrix} \\ \tilde{\mathbf{y}}_{c_{rx}} &= \underbrace{\tilde{\mathbf{H}}_{ccp2a} \tilde{\tilde{\mathbf{x}}}_{ccp}}_1 + \underbrace{\tilde{\mathbf{H}}_{ccp2b} \tilde{\mathbf{F}} \mathbf{s}}_2 + \underbrace{\tilde{\mathbf{z}}_c}_3 = \tilde{\mathbf{H}}_{ccp2a} \tilde{\tilde{\mathbf{x}}}_{ccp} + \tilde{\mathbf{H}}_{ccp2b} \tilde{\tilde{\mathbf{x}}}_{sefdm} + \tilde{\mathbf{z}}_c \end{aligned} \quad (4.32)$$

where only part 1 is the desired signal, while parts 2 and 3 are the interfering and noise parts. Yet, the matrix  $\tilde{\mathbf{H}}_{ccp2b}$  is not a circulant matrix and thus cannot be decomposed using eigenvalue decomposition. Following a similar method of [86] the matrix can be constructed of two matrices as:

$$\tilde{\mathbf{H}}_{ccp2b} = \mathbf{H}_{ccp2b1} - \mathbf{H}_{ccp2b2} \quad (4.33)$$

where  $\mathbf{H}_{ccp2b1} \in \mathbb{C}^{V \times V}$  is a circulant matrix having the tap coefficient vector  $\mathbf{h}^T = [h_0, \dots, h_\mu]$ , while  $\mathbf{H}_{ccp2b2} \in \mathbb{C}^{V \times V}$  represents the missing elements in the  $\tilde{\mathbf{H}}_{ccp2b}$  matrix. The elements of  $\mathbf{H}_{ccp2b2}$  are given by:

$$\mathbf{H}_{ccp2b2} = \begin{bmatrix} 0 & \dots & \dots & \dots & \dots & 0 & h_\mu & \dots & h_1 \\ \vdots & & & & & & \ddots & \ddots & \vdots \\ 0 & & & & & & & \ddots & h_\mu \\ \vdots & \ddots & 0 & \dots & \dots & 0 & \dots & \dots & 0 \\ \vdots & & \ddots & h_\mu & \dots & h_1 & h_0 & \ddots & \vdots \\ \vdots & & & \ddots & h_\mu & \vdots & h_1 & h_0 & 0 \\ 0 & \dots & \dots & \dots & 0 & h_\mu & \vdots & h_1 & h_0 \end{bmatrix}_{V \times V} \quad (4.34)$$

The eigenvalue decomposition of  $\mathbf{H}_{ccp2b1}$  is given by:

$$\mathbf{H}_{ccp2b1} = \mathbf{M}_{ccp} \mathbf{\Lambda}_{ccp} \mathbf{M}_{ccp}^H \quad (4.35)$$

where  $\Phi^H = \mathbf{M}^H$ .

The demodulated CCP-SEFDM signal,  $\tilde{\mathbf{r}}_{ccp}$ , is thereby expressed as:

$$\begin{aligned} \mathbf{r}_{ccp} &= \Phi^H \tilde{\mathbf{y}}_{c_{rx}} = \Phi^H [\tilde{\mathbf{H}}_{ccp2a} \tilde{\mathbf{x}}_{ccp} + \tilde{\mathbf{H}}_{ccp2b} \tilde{\mathbf{x}}_{sefdm} + \tilde{\mathbf{z}}_c] \\ &= \Phi^H [\tilde{\mathbf{H}}_{ccp2a} \tilde{\mathbf{x}}_{ccp} + \mathbf{H}_{ccp2b1} \tilde{\mathbf{x}}_{sefdm} - \mathbf{H}_{ccp2b2} \tilde{\mathbf{x}}_{sefdm} + \tilde{\mathbf{z}}_c] \\ &= \Phi^H [\tilde{\mathbf{H}}_{ccp2a} \tilde{\mathbf{x}}_{ccp} + \mathbf{M}_{ccp} \mathbf{\Lambda}_{ccp} \mathbf{M}_{ccp}^H \tilde{\mathbf{x}}_{sefdm} - \mathbf{H}_{ccp2b2} \tilde{\mathbf{x}}_{sefdm} + \tilde{\mathbf{z}}_c] \\ &= \Phi^H \tilde{\mathbf{H}}_{ccp2a} \tilde{\mathbf{x}}_{ccp} + \Phi^H \mathbf{M}_{ccp} \mathbf{\Lambda}_{ccp} \mathbf{M}_{ccp}^H \tilde{\mathbf{x}}_{sefdm} - \Phi^H \mathbf{H}_{ccp2b2} \tilde{\mathbf{x}}_{sefdm} + \Phi^H \tilde{\mathbf{z}}_c \\ &= \Phi^H \tilde{\mathbf{H}}_{ccp2a} \tilde{\mathbf{x}}_{ccp} + \mathbf{M}^H \mathbf{M}_{ccp} \mathbf{\Lambda}_{ccp} \mathbf{M}_{ccp}^H \tilde{\mathbf{F}} \mathbf{s} - \Phi^H \mathbf{H}_{ccp2b2} \tilde{\mathbf{x}}_{sefdm} + \Phi^H \tilde{\mathbf{z}}_c \\ &= \Phi^H \tilde{\mathbf{H}}_{ccp2a} \tilde{\mathbf{x}}_{ccp} + \mathbf{\Lambda}_{ccp} \mathbf{\Gamma} \mathbf{s} - \Phi^H \mathbf{H}_{ccp2b2} \tilde{\mathbf{x}}_{sefdm} + \Phi^H \tilde{\mathbf{z}}_c \\ &= \Phi^H \tilde{\mathbf{H}}_{ccp2a} \tilde{\mathbf{x}}_{ccp} + \lambda_{ccp} \tilde{\mathbf{s}} - \Phi^H \mathbf{H}_{ccp2b2} \tilde{\mathbf{x}}_{sefdm} + \Phi^H \tilde{\mathbf{z}}_c \end{aligned} \quad (4.36)$$

### 4.5.1 Channel Estimation and Equalization in CCP-SEFDM

Using zero forcing for channel estimation, the analytical bound of channel estimation for CCP-SEFDM is found as:

$$\begin{aligned}\hat{\lambda}_{ccp} &= \mathbf{r}_{ccp}/\tilde{\mathbf{s}} = (\Phi^H \tilde{\mathbf{H}}_{ccp2a} \tilde{\mathbf{x}}_{ccp} + \lambda_{ccp}\tilde{\mathbf{s}} - \Phi^H \mathbf{H}_{ccp2b2} \tilde{\mathbf{x}}_{sefdm} + \Phi^H \tilde{\mathbf{z}}_c)/\tilde{\mathbf{s}} \\ &= \underbrace{\lambda_{ccp}}_1 + \underbrace{\Phi^H \tilde{\mathbf{H}}_{ccp2a} \tilde{\mathbf{x}}_{ccp}/\tilde{\mathbf{s}}}_2 - \underbrace{\Phi^H \mathbf{H}_{ccp2b2} \tilde{\mathbf{x}}_{sefdm}/\tilde{\mathbf{s}}}_3 + \underbrace{\Phi^H \tilde{\mathbf{z}}_c/\tilde{\mathbf{s}}}_4\end{aligned}\quad (4.37)$$

where part 1 represents the subchannel gain estimated at each subcarrier, parts 2 and 3 are the added interference to each subcarrier due to the multipath channel effects, and part 4 corresponds to the noise signal.

The analytical bound of channel equalization for CCP-SEFDM using a one-tap equalizer is given as:

$$\begin{aligned}\hat{\mathbf{r}}_{ccp} &= \mathbf{r}_{ccp}/\lambda_{ccp} = (\Phi^H \tilde{\mathbf{H}}_{ccp2a} \tilde{\mathbf{x}}_{ccp} + \lambda_{ccp}\tilde{\mathbf{s}} - \Phi^H \mathbf{H}_{ccp2b2} \tilde{\mathbf{x}}_{sefdm} + \Phi^H \tilde{\mathbf{z}}_c)/\lambda_{ccp} \\ &= \underbrace{\tilde{\mathbf{s}}}_1 + \underbrace{\Phi^H \tilde{\mathbf{H}}_{ccp2a} \tilde{\mathbf{x}}_{ccp}/\lambda_{ccp}}_2 - \underbrace{\Phi^H \mathbf{H}_{ccp2b2} \tilde{\mathbf{x}}_{sefdm}/\lambda_{ccp}}_3 + \underbrace{\Phi^H \tilde{\mathbf{z}}_c/\lambda_{ccp}}_4\end{aligned}\quad (4.38)$$

where part 1 is the desired signal, which in turn is contaminated with interference in parts 2 and 3, and noise in part 4. The reason of using  $\lambda_{ccp}$  in (4.38) instead of  $\hat{\lambda}_{ccp}$  is to depict the analytical bound of channel equalization without considering channel estimation impairments.

It should be noted that in order to fulfill the circular convolution criterion, two conditions must be obeyed. First, the signal plus the CP portion must be continuous in phase when they are transmitted through the wireless fading channel. Second, the input samples to the DFT should form a periodic signal. These two conditions are met in CP-OFDM signals. However, in CP-SEFDM signals, there is a discontinuity in phase between the CP portion and the SEFDM symbol [75]. In addition, after removing the CP or the

CCP portion at the receiver, the SEFDM symbols are padded with zeros at the input of the DFT, which in turn yields a non-periodic signal in the time-domain, hence introducing additional interference to the subcarriers in the frequency-domain. As a result of the aforementioned reasons, inaccurate channel estimation and equalization occurs in CP-SEFDM and CCP-SEFDM systems.

## 4.6 SEFDM with Zero Padding

Figure 4.8 illustrates the ZP-SEFDM system. Here, each transmitted SEFDM symbol,  $\mathbf{x}$ , is padded with zeros instead of appending a CP at the beginning of the SEFDM symbol. The transmitted SEFDM symbol may then be shown as in steps 3 and 4 of Figure 4.9 and represented as:

$$\mathbf{x}_{zp} = \begin{bmatrix} \mathbf{x}_{sefdm} \\ \mathbf{0}_{\mu \times 1} \end{bmatrix} \quad (4.39)$$

The ZP-SEFDM symbol after traversing a multipath wireless channel,  $\mathbf{y}_{sym}$ , is given by:

$$\mathbf{y}_{sym} = \mathbf{h} * \mathbf{x}_{zp} = \begin{bmatrix} \tilde{\mathbf{y}} \\ \bar{\mathbf{y}}_{zp} \\ \mathbf{0}_{\mu \times 1} \end{bmatrix} \quad (4.40)$$

where  $\tilde{\mathbf{y}} \in \mathbb{C}^{Q \times 1}$  is the SEFDM symbol affected by the multipath and AWGN channels,  $\bar{\mathbf{y}}_{zp} \in \mathbb{C}^{\mu \times 1}$  is the ZP part that contains the energy spillage arising from ISI, and the  $\mathbf{0}_{\mu \times 1}$  represents the zeros that result from convolving the CIR and the zeros in the ZP part, and which are added to the succeeding symbol. The received signal parts are shown in step 5 of Figure 4.9. Thus, at the receiver, the received ZP-SEFDM symbol,  $\tilde{\mathbf{y}}$ , and its ZP part,  $\bar{\mathbf{y}}_{zp}$ , can be represented as:

$$\mathbf{y}_{zp} = \mathbf{h} * \mathbf{x}_{sefdm} + \mathbf{z}_{zp} = \begin{bmatrix} \tilde{\mathbf{y}} \\ \bar{\mathbf{y}}_{zp} \end{bmatrix} \quad (4.41)$$

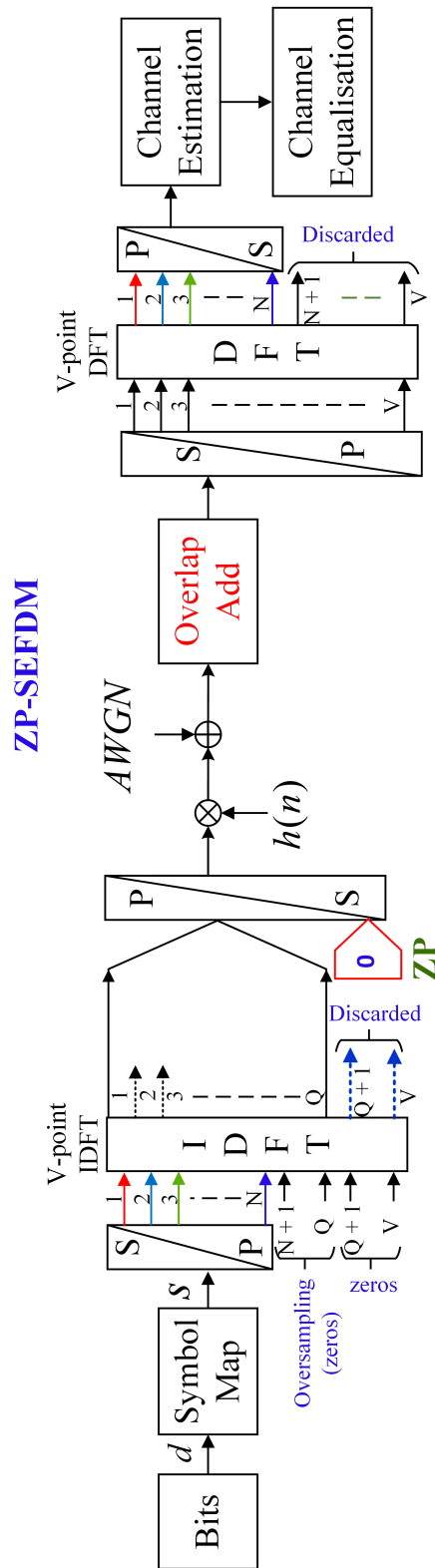
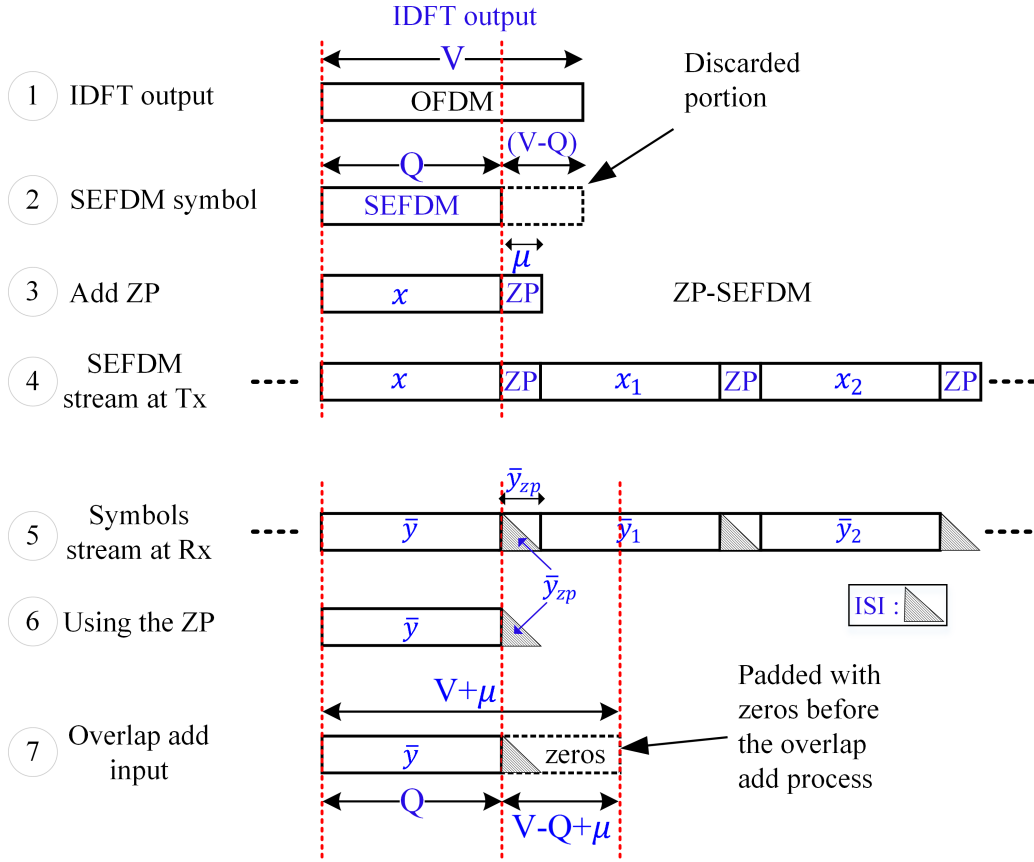


Figure 4.8: A simplified block diagram of ZP-SEFDM transceiver



**Figure 4.9:** Signal structure representation for ZP-SEFDM

where  $\mathbf{y}_{zp} \in \mathbb{C}^{(Q+\mu) \times 1}$  is the received symbol with the ZP part,  $\mathbf{h} \in \mathbb{C}^{\mu \times 1}$  is the CIR,  $\mathbf{x}_{sefdm} \in \mathbb{C}^{Q \times 1}$  is the transmitted SEFDM symbol and  $\mathbf{z}_{zp} \in \mathbb{C}^{(Q+\mu) \times 1}$  is the AWGN noise vector.

To determine the circulant channel matrix in ZP-SEFDM, the received SEFDM symbol, in which the ZP part carries ISI, is padded with zeros to length  $V + \mu$ , as shown in step 7 of Figure 4.9, where  $V = Q/\alpha$ , and expressed in matrix form as:

$$\tilde{\mathbf{y}}_{zp} = \begin{bmatrix} \mathbf{y}_{zp} \\ \mathbf{0}_{(V-Q) \times 1} \end{bmatrix} = \begin{bmatrix} \mathbf{h} * \mathbf{x}_{sefdm} + \mathbf{z}_{zp} \\ \mathbf{0}_{(V-Q) \times 1} \end{bmatrix} = \mathbf{h} * \tilde{\mathbf{x}}_{sefdm} + \tilde{\mathbf{z}}_{zp} \quad (4.42)$$

where  $\tilde{\mathbf{x}}_{sefdm}$  and  $\tilde{\mathbf{z}}_{zp}$  are the padded versions of  $\mathbf{x}_{sefdm}$  and  $\mathbf{z}_{zp}$ , to length  $V$

and  $V + \mu$ , respectively. Equation (4.42) can be further analyzed as:

$$\begin{aligned}\tilde{\mathbf{y}}_{zp} &= \mathbf{H}_{zp}\tilde{\mathbf{x}}_{sefdm} + \mathbf{z}_{zp} = \mathbf{H}_{zp} \begin{bmatrix} \mathbf{x}_{sefdm} \\ \mathbf{0}_{(V-Q)\times 1} \end{bmatrix} + \begin{bmatrix} \mathbf{z}_{zp} \\ \mathbf{0}_{(V-Q)\times 1} \end{bmatrix} \\ &= \mathbf{H}_{zp} \begin{bmatrix} \mathbf{F} \\ \mathbf{0}_{(V-Q)\times Q} \end{bmatrix} \mathbf{s} + \tilde{\mathbf{z}}_{zp} = \mathbf{H}_{zp}\tilde{\mathbf{F}}\mathbf{s} + \tilde{\mathbf{z}}_{zp}\end{aligned}\quad (4.43)$$

where  $\tilde{\mathbf{y}}_{zp} \in \mathbb{C}^{(V+\mu)\times 1}$ ,  $\mathbf{H}_{zp} \in \mathbb{C}^{(V+\mu)\times V}$ ,  $\tilde{\mathbf{F}} \in \mathbb{C}^{V\times Q}$ ,  $\mathbf{s} \in \mathbb{C}^{Q\times 1}$  and  $\tilde{\mathbf{z}}_{zp} \in \mathbb{C}^{(V+\mu)\times 1}$ . The channel matrix  $\mathbf{H}_{zp}$  is represented as:

$$\mathbf{H}_{zp} = \begin{bmatrix} h_0 & 0 & \dots & \dots & \dots & 0 \\ h_1 & h_0 & \ddots & & & \vdots \\ \vdots & h_1 & \ddots & \ddots & & \vdots \\ h_\mu & \vdots & \ddots & h_0 & \ddots & \vdots \\ 0 & h_\mu & \ddots & h_1 & \ddots & 0 \\ \vdots & \ddots & \ddots & \vdots & \ddots & h_0 \\ \vdots & & \ddots & h_\mu & \ddots & h_1 \\ \vdots & & & \ddots & \ddots & \vdots \\ 0 & \dots & \dots & \dots & 0 & h_\mu \end{bmatrix}\quad (4.44)$$

In order to convert the channel matrix into a circulant matrix, this work adapts and uses the overlap-add method of block convolution described in [80]. In which, the received SEFDM symbol plus the ZP part are combined before being fed into a DFT. The overlap-add method starts by splitting the received SEFDM vector  $\tilde{\mathbf{y}}_{zp}$  into two parts. The upper part  $\mathbf{y}_u = \mathbf{H}_u\tilde{\mathbf{x}}_{sefdm} + \mathbf{z}_u \in \mathbb{C}^{V\times 1}$  and the lower part  $\mathbf{y}_l = \mathbf{H}_l\tilde{\mathbf{x}}_{sefdm} + \mathbf{z}_l \in \mathbb{C}^{\mu\times 1}$ , where  $\mathbf{H}_u \in \mathbb{C}^{V\times V}$  and  $\mathbf{H}_l \in \mathbb{C}^{\mu\times V}$  correspond to the upper and lower partitions of  $\mathbf{H}_{zp}$ , respectively. We append  $\mathbf{y}_l$  with  $V - \mu$  zeros to be the same size as  $\mathbf{y}_u$  and

then we add the result to  $\mathbf{y}_u$ . Hence, (4.43) can be formed as:

$$\begin{aligned}\mathbf{y}_V &= \mathbf{y}_u + \begin{bmatrix} \mathbf{y}_l \\ \mathbf{0}_{(V-\mu) \times 1} \end{bmatrix} \\ &= \left( \mathbf{H}_u + \begin{bmatrix} \mathbf{H}_l \\ \mathbf{0}_{(V-\mu) \times V} \end{bmatrix} \right) \tilde{\mathbf{x}}_{sefdm} + \mathbf{z}_v = \tilde{\mathbf{H}}_{zp} \tilde{\mathbf{x}}_{sefdm} + \mathbf{z}_v\end{aligned}\quad (4.45)$$

where  $\tilde{\mathbf{H}}_{zp}$  is a  $V \times V$  circulant matrix and hence its eigenvalue decomposition is  $\tilde{\mathbf{H}}_{zp} = \mathbf{M}\mathbf{\Lambda}_{zp}\mathbf{M}^H$  with  $\mathbf{\Phi}^H = \mathbf{M}^H$ .

Feeding  $\mathbf{y}_V$  to the  $V$ -point DFT,  $\mathbf{\Phi}^H$ , yields the demodulated ZP-SEFDM signal as:

$$\begin{aligned}\mathbf{r}_{zp} &= \mathbf{\Phi}^H \mathbf{y}_V = \mathbf{\Phi}^H \left( \tilde{\mathbf{H}}_{zp} \tilde{\mathbf{x}}_{sefdm} + \mathbf{z}_v \right) = \mathbf{\Phi}^H \mathbf{M}\mathbf{\Lambda}_{zp}\mathbf{M}^H \tilde{\mathbf{F}}\mathbf{s} + \mathbf{\Phi}^H \tilde{\mathbf{z}}_{zp} \\ &= \mathbf{M}_{zp}^H \mathbf{M}\mathbf{\Lambda}_{zp}\mathbf{M}^H \tilde{\mathbf{F}}\mathbf{s} + \mathbf{\Phi}^H \tilde{\mathbf{z}}_{zp} = \mathbf{\Lambda}_{zp}\mathbf{\Gamma}\mathbf{s} + \tilde{\mathbf{z}}_{\Phi} = \lambda_{zp}\tilde{\mathbf{s}} + \tilde{\mathbf{z}}_{\Phi}\end{aligned}\quad (4.46)$$

where  $\lambda_{zp}$  is the subchannel gains vector and  $\tilde{\mathbf{z}}_{\Phi}$  is the  $V \times 1$  AWGN noise vector. Equation (4.46)-analogous to (4.11) for OFDM systems-provides evidence that using ZP instead of a CP in SEFDM allows the decomposition of the wideband multipath channel into independent narrowband channels.

### 4.6.1 Channel Estimation and Equalization in ZP-SEFDM

The analytical bound of estimated channel characteristics for ZP-SEFDM are given by:

$$\hat{\lambda}_{zp} = \mathbf{r}_{zp}/\tilde{\mathbf{s}} = (\lambda_{zp}\tilde{\mathbf{s}} + \tilde{\mathbf{z}}_{\Phi})/\tilde{\mathbf{s}} = \underbrace{\lambda_{zp}}_1 + \underbrace{\tilde{\mathbf{z}}_{\Phi}/\tilde{\mathbf{s}}}_2\quad (4.47)$$

where  $\lambda_{zp}$  (part 1) describes the estimated flat channel gains associated with each subcarrier while part 2 corresponds to the noise vector. Equation (4.47) shows that there is no self-created ICI enhancement between the subcarriers.

The analytical bound of the equalizer for ZP-SEFDM is given as:

$$\begin{aligned}\hat{\mathbf{r}}_{zp} &= \mathbf{r}_{zp}/\lambda_{zp} \\ &= (\lambda_{zp}\tilde{\mathbf{s}} + \tilde{\mathbf{z}}_{\Phi})/\lambda_{zp} = \underbrace{\tilde{\mathbf{s}}}_1 + \underbrace{\tilde{\mathbf{z}}_{\Phi}/\lambda_{zp}}_2\end{aligned}\quad (4.48)$$

Unlike the cases of CP-SEFDM equation of (4.20) and CCP-SEFDM equation of (4.38), equation (4.48) demonstrates that equalizing the channel effects in ZP-SEFDM signals, does not lead to additional interference between the subchannels. Hence, simple equalization methods, such as a one-tap equalizer, can be performed without additional interference coming from the CP and CCP parts. Thus, ZP-SEFDM outperforms CP techniques in SEFDM systems with respect to obtaining accurate channel characteristics and equalizing the channel effects.

## 4.7 OFDM Pilot Symbols in SEFDM Systems

The work in [75] proposes to use orthogonal pilot symbol for obtaining channel estimates in the frequency-domain. This leads to no self-induced ICI among the subcarriers and hence, the channel estimation performance using OFDM pilot symbols is more accurate compared to using SEFDM pilot symbols. A schematic block diagram of pilot OFDM symbols transceiver is depicted in Figure 4.10. The input complex pilot symbols that are fed into the IDFT are given as:

$$s_{ofdm}(q) = \begin{cases} p_{ofdm}(q), & 0 \leq q < N \\ 0, & N \leq q < Q/\alpha - 1 \end{cases}\quad (4.49)$$

Each pilot symbol of  $s_{ofdm}$  is modulated onto one subcarrier. The discrete-

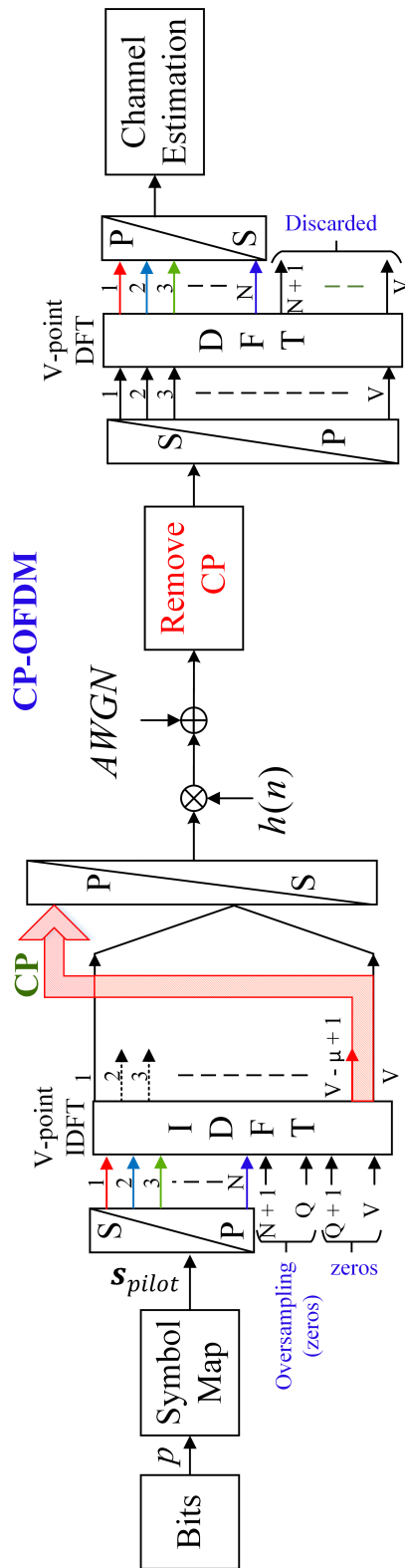


Figure 4.10: A simplified block diagram of CP-OFDM pilot symbols transceiver

time OFDM symbol vector of size  $V = Q/\alpha$  is given by:

$$x_{ofdm}(b) = \frac{1}{\sqrt{V}} \sum_{q=0}^{V-1} s_{ofdm} e^{(j2\pi qb/V)} \quad (4.50)$$

where  $b = [0, \dots, V-1] \in \mathbb{Z}$  is the time sample index and  $q \in \mathbb{Z}$  is the subcarrier index. The discrete OFDM symbol may be written in matrix form as:

$$\mathbf{x}_{ofdm} = \mathbf{\Phi}_{ofdm} \mathbf{s}_{ofdm} \quad (4.51)$$

where  $\mathbf{x}_{ofdm} \in \mathbb{C}^{V \times 1}$  is a vector of time-domain samples of an OFDM symbol;  $\mathbf{\Phi}_{ofdm} \in \mathbb{C}^{V \times V}$  is the sampled IDFT matrix used in the OFDM modulation process and  $\mathbf{s}_{ofdm} \in \mathbb{C}^{V \times 1}$  is the vector of input data symbols.

The received pilot symbols are distorted by the channel and contaminated with AWGN noise. As mentioned before, the use of a CP at the beginning of the symbols results in modelling the channel matrix as a circulant matrix. The received OFDM pilot symbols are represented as:

$$\mathbf{y}_{ofdm} = \mathbf{H}_{ofdm} \mathbf{x}_{ofdm} + \mathbf{z}_{ofdm} = \mathbf{H}_{ofdm} \mathbf{\Phi}_{ofdm} \mathbf{s}_{ofdm} + \mathbf{z}_{ofdm} \quad (4.52)$$

where  $\mathbf{z}_{ofdm} \in \mathbb{C}^{V \times 1}$  is the AWGN noise vector. The eigenvalue decomposition of the channel matrix,  $\mathbf{H}_{ofdm}$ , is given as [84, 85]:

$$\mathbf{H}_{ofdm} = \mathbf{M}_{ofdm} \mathbf{\Lambda}_{ofdm} \mathbf{M}_{ofdm}^H \quad (4.53)$$

The received pilot OFDM symbols are demodulated using a DFT process, thus the symbols are represented as:

$$\begin{aligned} \mathbf{r}_{ofdm} &= \mathbf{\Phi}_{ofdm}^H \mathbf{y}_{ofdm} = \mathbf{\Phi}_{ofdm}^H [\mathbf{H}_{ofdm} \mathbf{x}_{ofdm} + \mathbf{z}_{ofdm}] \\ &= \mathbf{\Phi}_{ofdm}^H [\mathbf{M}_{ofdm} \mathbf{\Lambda}_{ofdm} \mathbf{M}_{ofdm}^H \mathbf{x}_{ofdm} + \mathbf{z}_{ofdm}] \\ &= \mathbf{\Phi}_{ofdm}^H \mathbf{M}_{ofdm} \mathbf{\Lambda}_{ofdm} \mathbf{M}_{ofdm}^H \mathbf{\Phi}_{ofdm} \mathbf{s}_{ofdm} + \mathbf{\Phi}_{ofdm}^H \mathbf{z}_{ofdm} \\ &= \mathbf{M}_{ofdm}^H \mathbf{M}_{ofdm} \mathbf{\Lambda}_{ofdm} \mathbf{M}_{ofdm}^H \mathbf{M}_{ofdm} \mathbf{s}_{ofdm} + \mathbf{\Phi}_{ofdm}^H \mathbf{z}_{ofdm} \\ &= \mathbf{\Lambda}_{ofdm} \mathbf{s}_{ofdm} + \mathbf{\Phi}_{ofdm}^H \mathbf{z}_{ofdm} \\ &= \lambda_{ofdm} \mathbf{s}_{ofdm} + \mathbf{z}_{\Phi ofdm} \end{aligned} \quad (4.54)$$

The channel estimate at each subcarrier is found using the zero forcing method, which is given as:

$$\hat{\lambda}_{ofdm} = \mathbf{r}_{ofdm} / \mathbf{s}_{ofdm} = (\lambda_{ofdm} \mathbf{s}_{ofdm} + \mathbf{z}_{\Phi ofdm}) / \mathbf{s}_{ofdm} = \underbrace{\lambda_{ofdm}}_1 + \underbrace{\mathbf{z}_{\Phi ofdm} / \mathbf{s}_{ofdm}}_2 \quad (4.55)$$

where  $\lambda_{ofdm}$  (part 1) represents the estimated channel gains at each subcarrier while part 2 corresponds to the noise vector.

## 4.8 Performance Results

System parameters in the simulations are carried out based on the Narrowband Internet-of-Things (NB-IoT) standard [87]. The NB-IoT system parameters are appropriately modified to accommodate the bandwidth compression factors ranging between  $\alpha = 0.5 - 0.9$  [88]. The number of active subcarriers is  $N = 12$  data subcarriers and the modulation format is QPSK.

### 4.8.1 Guard Interval Schemes compared for system evaluation

To comprehensively evaluate the channel estimation and equalization of the different guard interval techniques in SEFDM systems, two frame structures are used in this work; (i) using SEFDM symbols for both pilot and data symbols; and (ii) using OFDM symbols as pilots, followed by SEFDM symbols to carry data.

Three guard interval schemes for use in SEFDM systems are evaluated in this work, which are: (i) CP-SEFDM, (ii) CCP-SEFDM, and (iii) ZP-SEFDM. The system performance of the three schemes is evaluated with the following metrics:

- **MSE**, which is used to evaluate the accuracy of channel estimation using different pilot signals for different SEFDM schemes.

**Table 4.1:** Channel model parameters

<i>Parameters</i>	<i>Value</i>
Channel delay profile	TDL-D
Delay spread	300 ns
Maximum Doppler shift	111.2 Hz
K-factor	7 dB

- **BER**, this to evaluate the effect of the channel estimation and equalization on the error rate performance of SEFDM systems. The BER is determined after the detection stage for CP-OFDM, CP-SEFDM, CCP-SEFDM and ZP-SEFDM.

### 4.8.2 Channel model

The signals are sent over a Tapped Delay Line (TDL) 5G channel model of type (D) [89]. The channel is defined in the European Telecommunications Standards Institute (ETSI) standards [89] and it represents a Line-of-Sight (LOS) channel model. Hence, the first tap follows a Ricean distribution with a K-factor = 7 dB, while the rest of the taps follow a Rayleigh distribution. The taps delays and power values are given in Table 7.7.2-4 of the standards in [89]. The channel model parameters are given in Table 4.1 [75].

### 4.8.3 SEFDM signals for pilot and data symbols

The frame structure is similar to that of LTE [1] where every radio frame of length 10 ms consists of ten equally sized subframes, each of which contains  $2 \times 0.5$  ms time slots. In every time slot, there are seven SEFDM symbols. Of these seven symbols, one carries a pilot (the first symbol in the time slot) that is used for channel estimation and the other six symbols carry data signals. The SEFDM pilot symbols used in this test are the Demodulation Reference Symbols (DMRS), where the DMRS are designed for channel estimation and power measurement in the 5G New Radio (NR) [90]. Figure 4.11 depicts the frame structure used in this simulation evaluation.

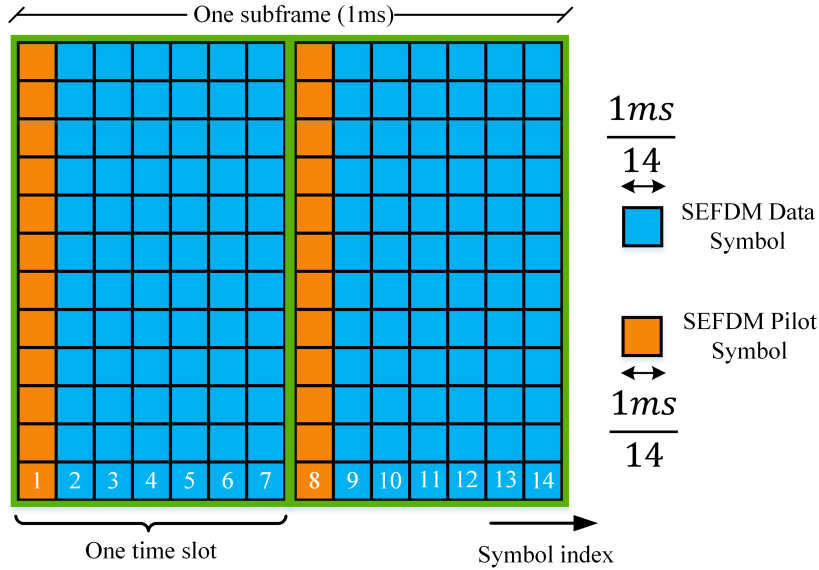


**Figure 4.11:** Frame structure. Each symbol (pilot and data symbols) in the frame has the same time duration

#### 4.8.3.1 MSE in channel estimation

The MSE is given by [12]:

$$\text{MSE} = \mathbb{E} \left\{ [\lambda - \hat{\lambda}]^{\mathbf{H}} [\lambda - \hat{\lambda}] \right\} \quad (4.56)$$

where  $\lambda$  is the real gain of the channel under evaluation and  $\hat{\lambda}$  is the estimated channel gain at the receiver. From Figure 4.12, it is evident that the MSE of the channel estimation in CP-SEFDM and continuous CP-SEFDM eventually reaches a non-zero error floor for any value of  $\alpha < 1$ , as corroborated in Equations 4.19 and 4.37, respectively. On the contrary, the MSE for the ZP method monotonically decreases with increased  $E_b/N_o$ , which agrees with our mathematical findings in (4.47).

#### 4.8.3.2 BER performance

BER is the chosen figure-of-merit to evaluate the distortion in the complex received SEFDM signal that affects signal reliability and error rate, where impairments are introduced by many factors, such as noise and multipath

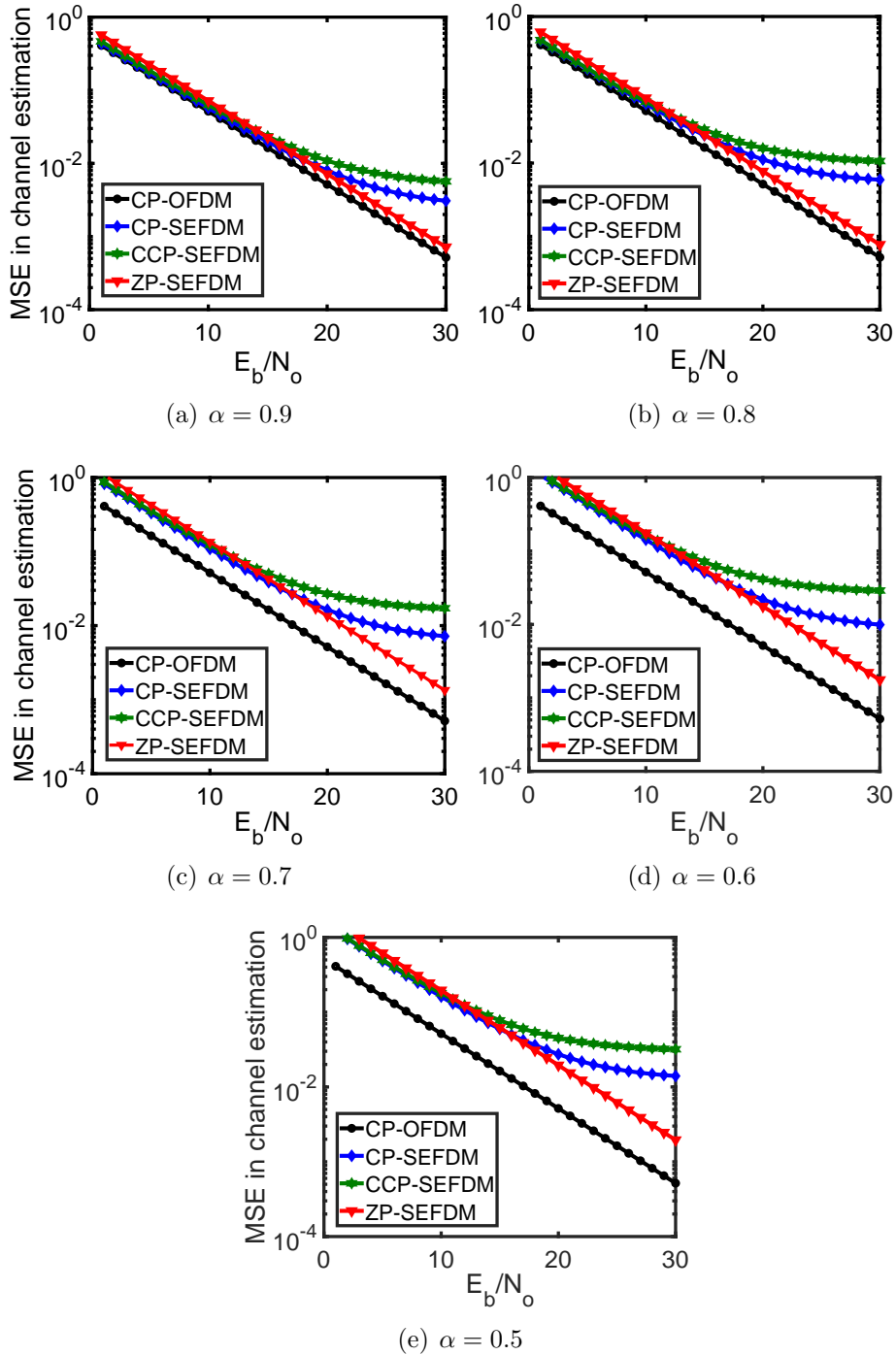


**Figure 4.12:** MSE in channel estimation for CP-OFDM, CP-SEFDM, CCP-SEFDM and ZP-SEFDM using DMRS pilot signal and tested in LOS TDL-D channel model for different bandwidth compression factors

channel effects.

After the equalization process, the complex symbols are detected using a SD, which utilizes the correlation matrix to decode the transmitted SEFDM symbol. Figure 4.13 depicts the BER performance using SEFDM for data and pilot symbols. It is evident that ZP-SEFDM outperforms CP-SEFDM and CCP-SEFDM. ZP-SEFDM has lower BER values because the narrow-band subchannels are orthogonal to each other, as determined in (4.48). In addition, the figure shows that, unlike ZP-SEFDM, the CP-SEFDM and CCP-SEFDM BER curves diverge and reach a non-zero error floor for all values of  $\alpha$ . As expected, Figure 4.13 shows that higher spectral efficiencies (lower  $\alpha$  values) come at the expense of signal deterioration, which is apparent in terms of worse BER values due to higher levels of self-created ICI.

However, the error rate performance of SEFDM systems is still very high compared to OFDM systems. To further investigate the cause of this error rate degradation, a different pilot symbol scheme is considered for SEFDM systems. Specifically, the SEFDM pilot symbols are replaced with OFDM pilot symbols as suggested in [75], where the OFDM pilot symbols have the same subcarrier spacing, however, a lower data rate. This is subject of the next subsection.

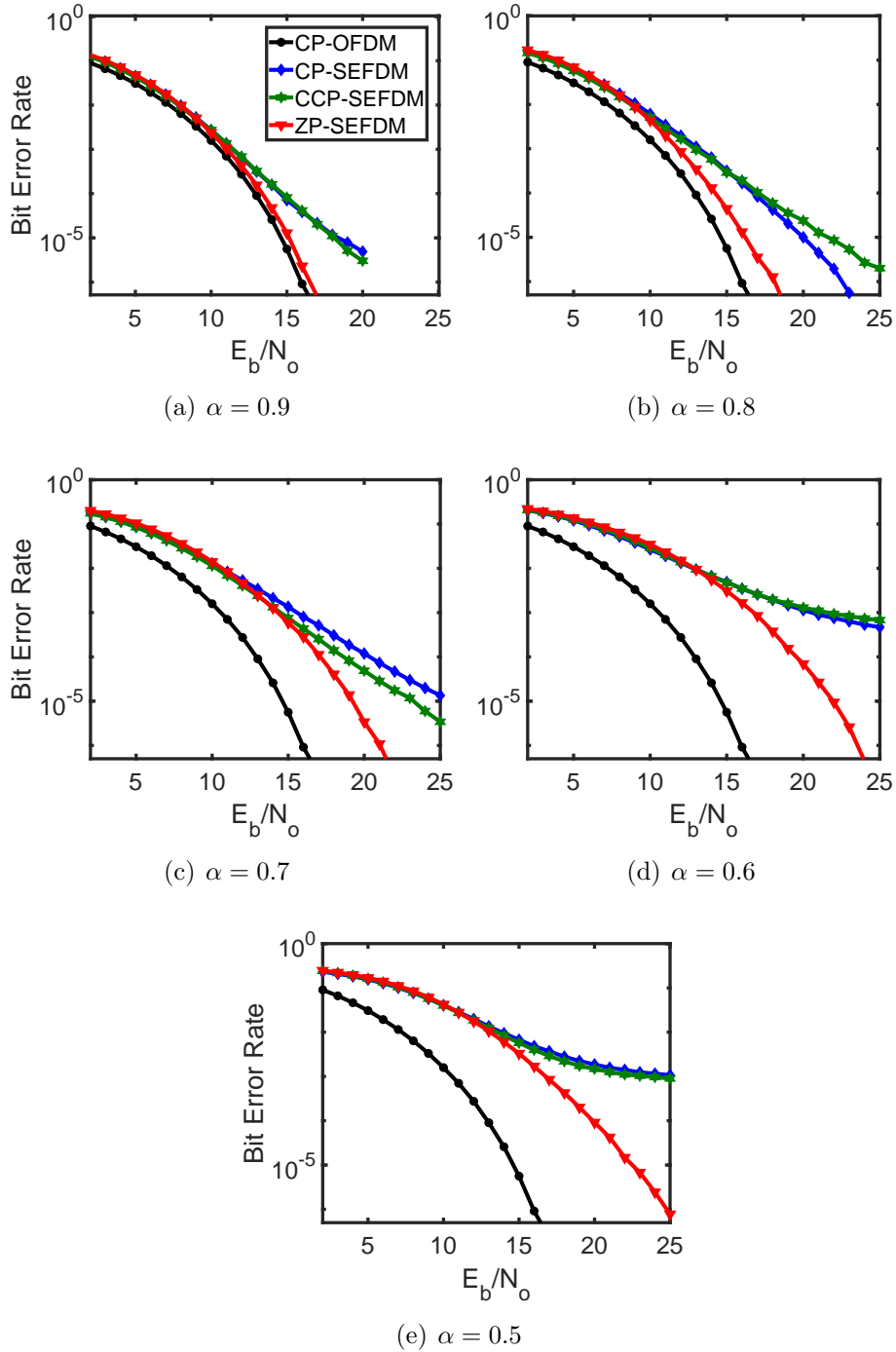


**Figure 4.13:** BER in SEFDM system using SEFDM pilots for CP-OFDM, CP-SEFDM, CCP-SEFDM and ZP-SEFDM using LOS TDL-D channel model and for different bandwidth compression factors

#### 4.8.4 OFDM pilot symbols for SEFDM systems

The work in [56] and [75] propose to use OFDM pilot symbols for channel estimation purposes for CP-SEFDM and CCP-SEFDM, respectively. A similar frame structure design as that in [75] is followed in this work. Figure 4.14 illustrates the frame structure of the new scheme of using OFDM for pilot symbols. In this work, and for the first time, the ZP scheme is proposed to be used for SEFDM data symbols, however, the pilot symbols are OFDM symbols. The new system proposal is predicted to enhance the error rate performance. This is because ZP-SEFDM has better equalization performance according to the findings in Equation 4.48. To support and verify this claim, the BER is used for systems evaluation of (i) CP-SEFDM; (ii) CCP-SEFDM; and (iii) ZP-SEFDM for data symbols, with OFDM pilot symbols being used for channel estimation.

Figure 4.15 shows the BER performance of the three different systems and for various values of  $\alpha$ . From the results, it is evident that the error rate performance of using ZP-SEFDM for data symbols, outperforms the cases of using the cyclic prefix schemes with SEFDM for data symbols. It should be noted that, this agrees with the analytical bounds finding of channel equalization given in equations 4.20, 4.38 and 4.48 for CP-SEFDM, CCP-SEFDM and ZP-SEFDM, respectively.

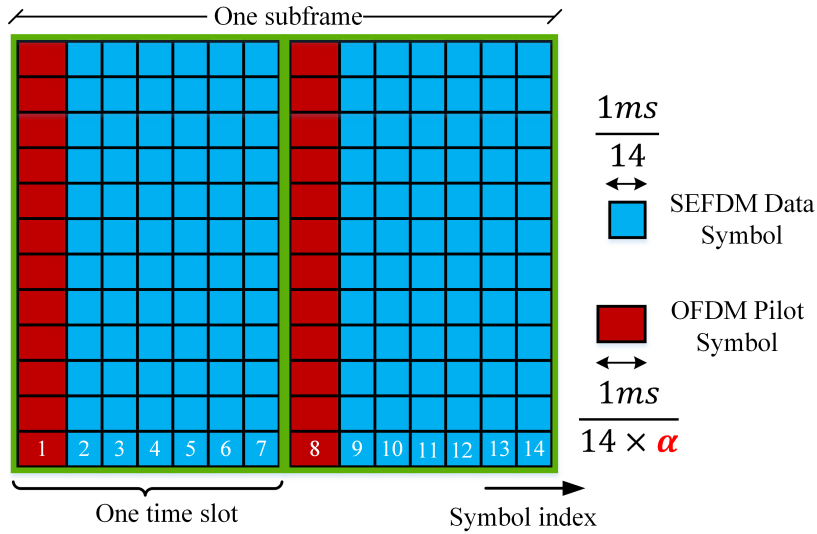


**Figure 4.14:** Frame structure. The OFDM pilot symbols have longer time duration compared to SEFDM data symbols in the frame

#### 4.8.5 Comparison of the power penalty for the different guard interval schemes

To further illustrate the difference in error rate performance of CP-SEFDM, CCP-SEFDM and ZP-SEFDM. The power penalty, defined as the  $E_b/N_o$  difference between OFDM and the three different SEFDM (CP-SEFDM, CCP-SEFDM and ZP-SEFDM) systems, is measured in (dB) at a BER =  $10^{-4}$  and is shown in Figure 4.16. The upper figure (4.16(a)) shows the power penalty when SEFDM pilot symbols are used for channel estimation, while the lower figure (4.16(b)) indicates the case of using OFDM pilot symbols. For different values of  $\alpha$ , the power penalty is increased with the decrease of  $\alpha$  (and concurrent increase in spectral efficiency), which is due to the higher level of interference introduced between subcarriers. In addition, Figure 4.16, indicates that ZP-SEFDM outperforms CP-SEFDM and CCP-SEFDM with the two channel estimation methods used in this test and for all values of  $\alpha$ . The CP-SEFDM and CCP-SEFDM BER curves stop at  $\alpha = 0.7$  in Figure 4.16(a) and  $\alpha = 0.6$  in Figure 4.16(a), because the BER performance reaches error rate higher than  $10^{-4}$  for  $\alpha < 0.7$  and  $\alpha < 0.6$ , respectively.

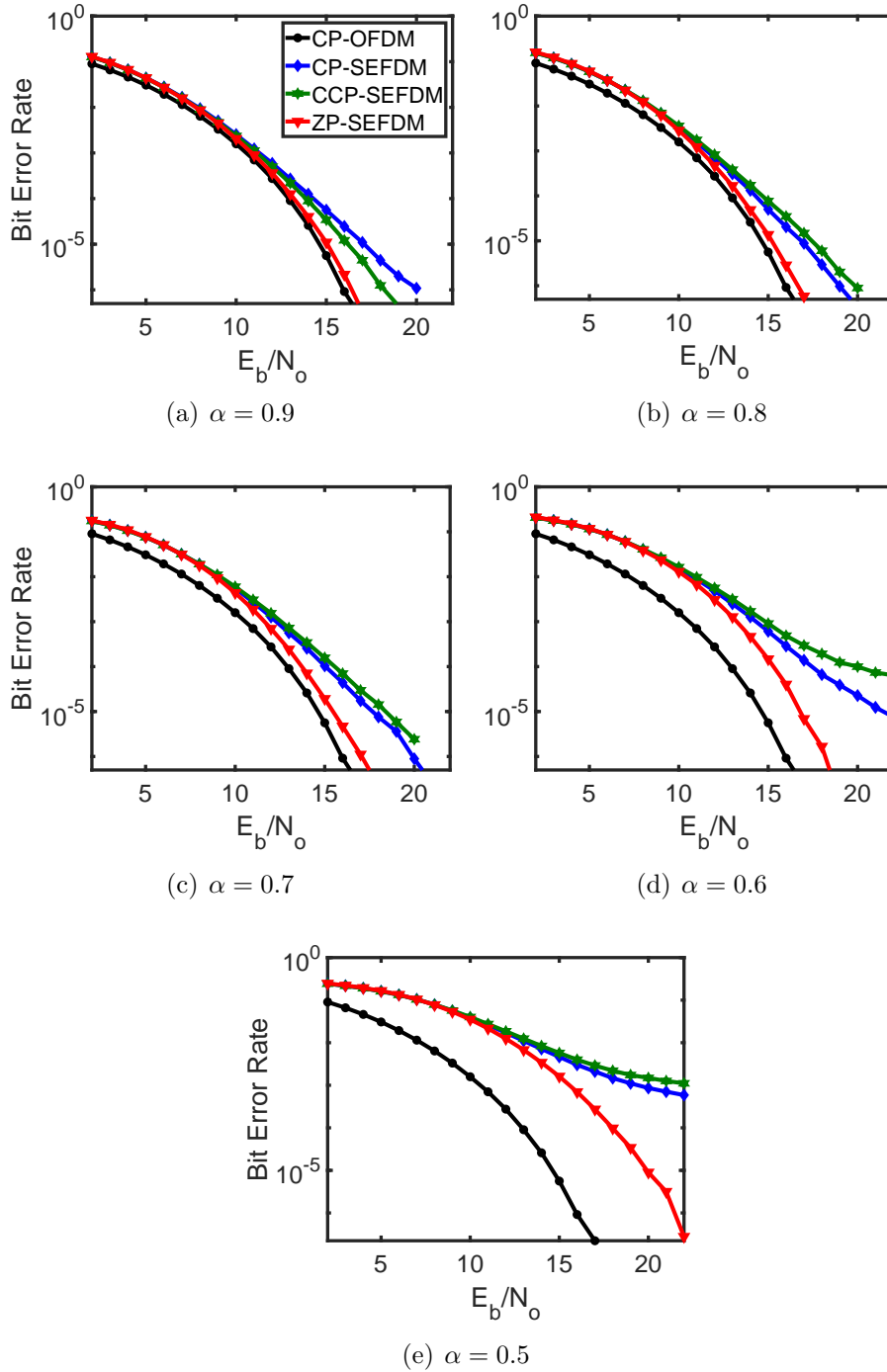
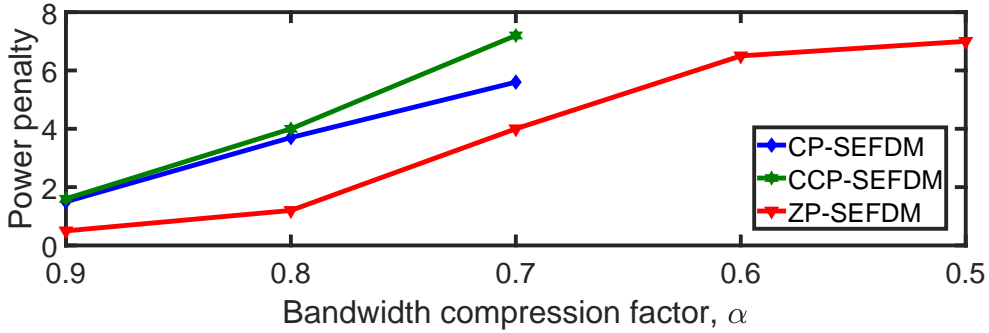
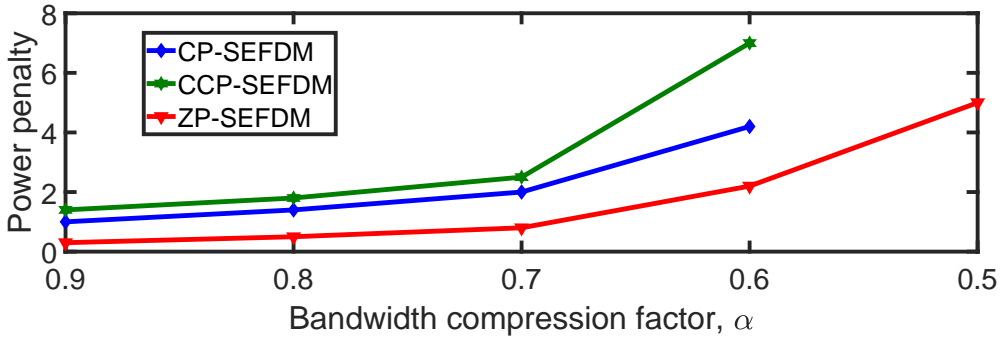


**Figure 4.15:** BER in SEFDM system using OFDM pilots for CP-OFDM, CP-SEFDM, CCP-SEFDM and ZP-SEFDM using LOS TDL-D channel model and for different bandwidth compression factors



(a) SEFDM pilot symbols for channel estimation



(b) OFDM pilot symbols for channel estimation

**Figure 4.16:** Power penalty (at  $\text{BER} = 10^{-4}$ ) between OFDM and CP-SEFDM, CCP-SEFDM and ZP-SEFDM systems. (a) shows the power penalty for the case of using SEFDM pilot symbols. (b) indicates the power penalty for the case of using OFDM pilot symbols

## 4.9 Conclusions

In multicarrier systems, the total rate of the signal is divided into a set of smaller rates which are transmitted over subcarriers. This signal is transmitted to the receiver through a medium with a multipath wideband channel. In OFDM systems, using CP with OFDM symbols and using an IDFT and a DFT at the transmitter and receiver, respectively, allows the wideband channel to be divided into a set of orthogonal narrowband sub-channels. Each of which, is associated with a subcarrier of the multicarrier OFDM signals. Therefore, channel estimation and equalization of the amplitude and phase distortion, due to the multipath channels, occur individually at each subcar-

rier.

In addition to the signal distortion caused by multipath channels, non-orthogonal multi-carrier systems, such as SEFDM, also suffer from self-induced ICI. Therefore, the work demonstrated in this chapter provides a full study and investigation of using two existing guard interval techniques, CP and CCP. In addition, this work introduced a novel channel estimation and equalization technique employing an orthogonal DFT-based demodulator in conjunction with ZP. Moreover, the chapter provided the analytical expressions of channel estimation and equalization in CP-SEFDM, CCP-SEFDM and ZP-SEFDM for the first time, where such work has not been done in any previous work for SEFDM systems. The simulation results presented in this chapter show that, ZP-SEFDM can offer over one order of magnitude improvement in MSE performance at high  $E_b/N_o$  values compared to CP-SEFDM with commensurate improvement in BER for the received signal.

Furthermore, this chapter provided a study of using CP-OFDM pilot symbols for channel estimation while using SEFDM for data symbols. The use of the three guard interval techniques (CP, CCP and ZP) with SEFDM signals were evaluated. From the results presented here, using ZP with SEFDM for data symbols, outperforms the other guard interval techniques in SEFDM systems.

# Chapter 5

## Truncated OFDM Signal and System

### 5.1 Introduction

The research in this chapter reports a new non-orthogonal signal format which modifies OFDM signals by truncating the end of each OFDM symbol. As such, this new format is termed TOFDM. Here, each OFDM time-domain symbol is truncated by a factor  $(1 - \gamma)$  to generate the TOFDM signal. Therefore, time samples are only partially transmitted and part of the symbol is discarded at transmission. Furthermore, the fact that the TOFDM symbol time is shorter than that of an OFDM one, implies loss of orthogonality and consequently the introduction of ICI amongst the subcarriers.

The work in this chapter focuses on studying the newly proposed TOFDM signal. Hence, the new signal representation in time and frequency is provided in Section 5.2. Then, a comparison of TOFDM with other similar spectrally efficient techniques is given in Section 5.3. After that, analytical representation, interference characterization and modelling of the TOFDM signal are given in details in Section 5.4. Then, two complete TOFDM systems are designed, implemented and described in Section 5.5. The first (provided in Section 5.5.1), is an uncoded system that uses a SD at the receiver, which in turn, utilizes the interference knowledge to retrieve the transmit-

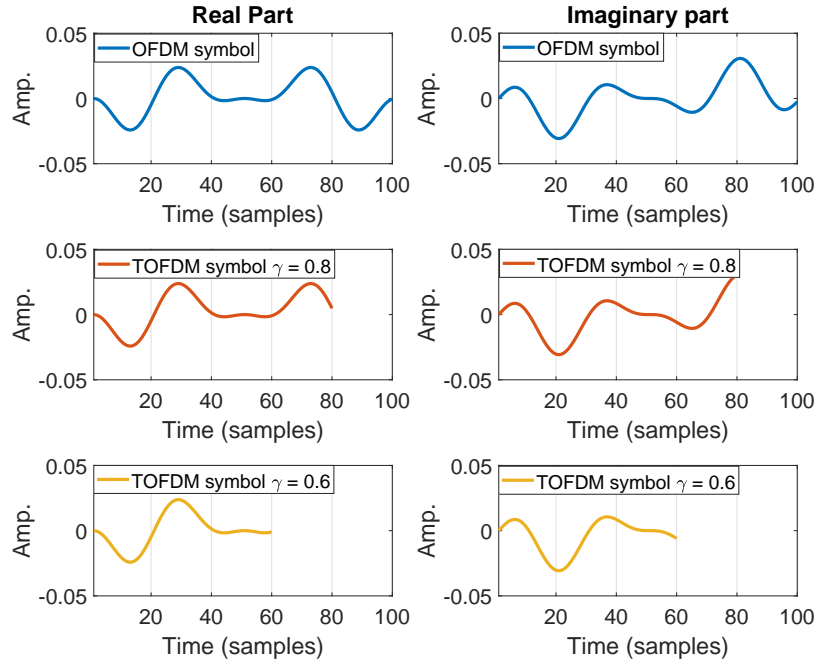


**Figure 5.1:** TOFDM symbols generation from OFDM symbol

ted data. The parameters that affect the error performance and complexity of this system are studied and evaluated in simulation. The second system is a coded system (provided in Section 5.5.2), which is modified version of the standard IEEE 802.11a,g, where the OFDM signals are replaced with TOFDM ones. A new iterative decoder for the proposed system is designed and then implemented in (i) Matlab simulation to evaluate the system performance using AWGN channels, and (ii) SDR, where the system is evaluated in realistic RF environments using USRP and channel emulator.

## 5.2 TOFDM Signal Representation

In this section, time and frequency representation of OFDM and TOFDM are detailed.

### 5.2.1 Time-domain representation

As mentioned earlier, each OFDM symbol is truncated in the time-domain to generate the TOFDM symbol, which means the duration of a TOFDM symbol,  $T_{tofdm}$ , is shorter than that of an OFDM symbol,  $T_{ofdm}$ , by a factor  $\gamma \leq 1$ . The relation between the TOFDM and OFDM symbols duration is given as:

$$T_{tofdm} = \gamma T_{ofdm} \quad (5.1)$$

In TOFDM systems, only a  $\gamma T_{ofdm}$  duration of the OFDM symbols is sent while the remaining  $(1 - \gamma)T_{ofdm}$  is discarded at the transmitter. When  $\gamma = 1$ , the symbol is an OFDM one, whereas lesser values of  $\gamma$  achieve different truncations. A smaller value of  $\gamma$  offers a greater spectral efficiency in the time-domain. This implies that more data can be sent over the same frequency bandwidth. Figure 5.1, shows how two TOFDM symbols with different truncation levels,  $\gamma = 0.8$  and  $\gamma = 0.6$ , are generated from OFDM by truncating 20% and 40%, respectively. In addition, the subsequent TOFDM symbol comes earlier in time by  $(1 - \gamma)$  because of the truncation in the preceding symbol. Thus, five TOFDM symbols, using  $\gamma = 0.8$ , may be sent in the same time period as four OFDM ones, utilizing the same signal bandwidth.

### 5.2.2 Frequency domain representation

In OFDM signals, the frequency spacing between two adjacent subcarriers,  $\Delta f$ , is given as:

$$\Delta f = \frac{f_s}{Q_i} \quad (5.2)$$

where  $f_s$  is the sampling frequency and  $Q_i$  is the number of input bins to the IDFT in the frequency domain. The subcarrier width, of an OFDM symbol, in the frequency domain,  $\delta f$ , is given as:

$$\delta f = \frac{1}{T_{ofdm}} = \frac{1}{QT_s} = \frac{f_s}{Q} \quad (5.3)$$

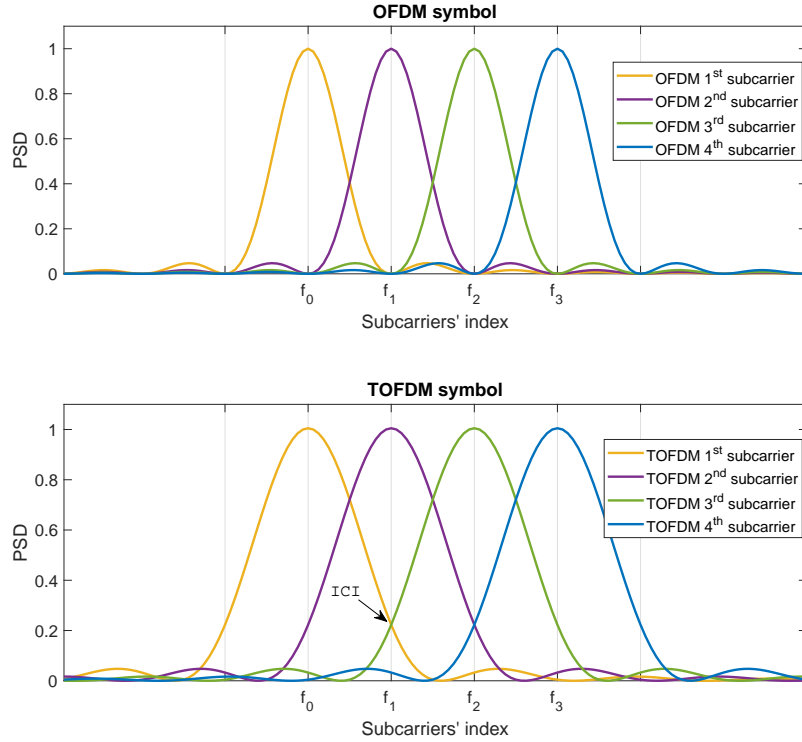


**Figure 5.2:** The spectra of OFDM and TOFDM symbols of 4-subcarriers

where  $Q$  is the number of time samples in an OFDM symbol and  $T_s$  is the time samples period.

Orthogonality between subcarriers in OFDM, as shown in the upper part of Figure 5.2, is maintained by ensuring that the spacing between the subcarriers equals the inverse of the symbol period. Thus, the number of input bins to the IDFT, is equal to the number of time samples in an OFDM symbol and hence,  $\Delta f = \delta f$ .

In TOFDM systems, like OFDM systems, the number of input bins to the IDFT,  $Q_i$ , and the sampling frequency are maintained the same. Thus, the frequency spacing between two adjacent subcarriers is defined as  $\Delta f = \frac{f_s}{Q_i} = \frac{1}{T_{ofdm}}$ , which is equal to that of the OFDM signals. Nevertheless, the TOFDM symbol duration is not equal to the reciprocal of the frequency spacing between the subcarriers ( $\Delta f$ ). Where the subcarriers

width in TOFDM,  $\delta f_{tofdm}$ , is given by:

$$\delta f_{tofdm} = \frac{1}{T_{tofdm}} = \frac{1}{\gamma Q T_s} = \frac{f_s}{\gamma Q} \quad (5.4)$$

where the  $\delta f_{tofdm}$  is inversely proportional with the value of the truncation factor,  $\gamma$ . This means, the generated TOFDM signal is not orthogonal, where the transmission rate of each subcarrier, in comparison with OFDM signal, is higher as depicted in Figure 5.2.

### **5.3 TOFDM Signal Representation vs OFDM, SEFDM and FTN**

Figures 5.3, 5.4 and 5.5 present conceptual illustrations of the time- and frequency- domain of OFDM, SEFDM, TOFDM and FTN signals. In Figure 5.3, it is clear that OFDM and SEFDM symbols are sent with the same symbol duration, while FTN transmits overlapped symbols. OFDM systems transmit orthogonal symbols in time and frequency, while SEFDM systems transmit more data by relaxing the spacing between the subcarriers in the frequency-domain, which means the bandwidth of these systems is narrower than OFDM despite having no difference in the time duration of SEFDM and OFDM symbols. FTN systems send more data over the same bandwidth than in OFDM by transmitting symbols faster than the Nyquist limit. This allows more symbols to be sent in a shorter time, equivalently saving bandwidth. However, due to transmission at a higher rate, the FTN signal will overlap and produce interference.

On the other hand, TOFDM sends partial samples of the OFDM symbol, although TOFDM has the same symbol duration as FTN, the features of these symbols are totally different as explained earlier. However, truncation in the time-domain can lead to lost information and interference generation between subcarriers. In Figure 5.4, the frequency spacing between the subcarriers of OFDM, TOFDM and FTN signals are the same, which means all the subcarriers are positioned at the same frequencies when TOFDM sig-

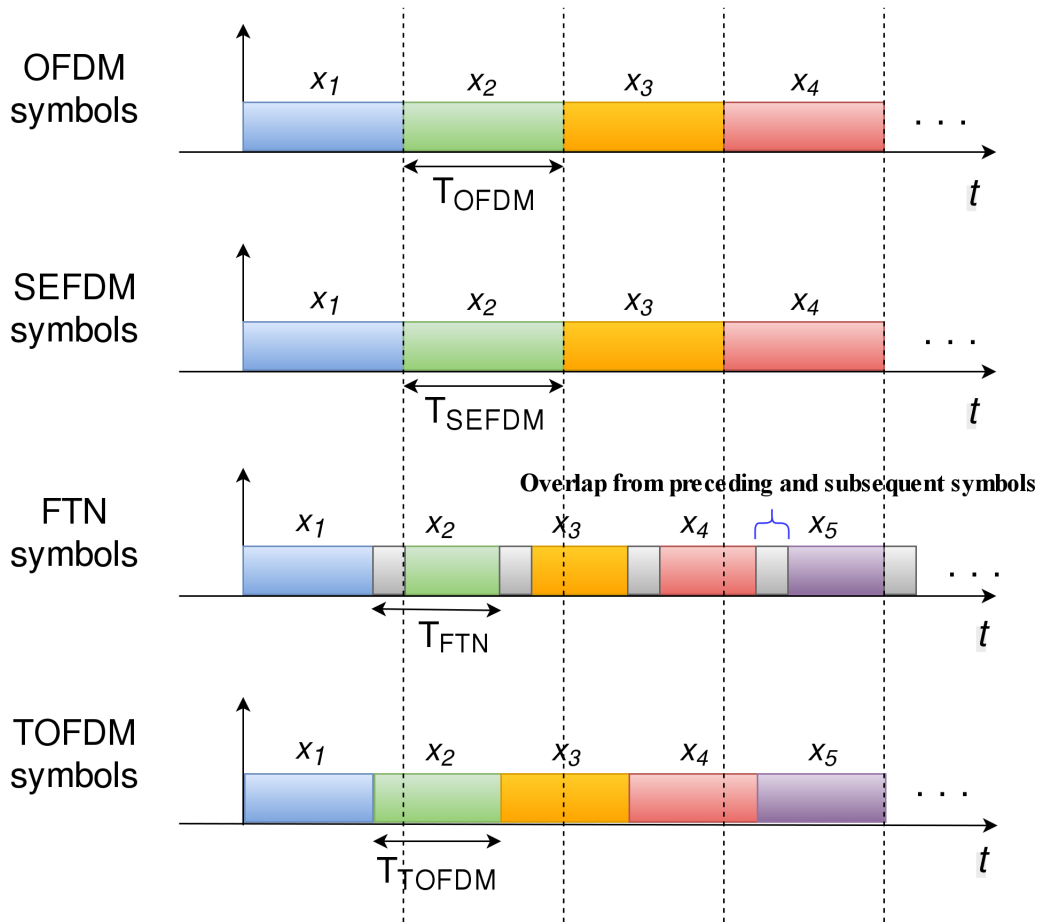


**Figure 5.3:** Conceptual illustrations of OFDM, SEFDM, FTN and TOFDM in time-domain where the compression factor for FTN and TOFDM is  $\gamma = 0.8$

nals are generated. However, the symbol durations of TOFDM and FTN are shorter in the time-domain, which implies that the transmission rate is higher. In addition, because the symbol becomes shorter, the bandwidth of each subcarrier becomes wider; the signals are changed to be non-orthogonal, which leads to interference in the system.

In Figure 5.5, OFDM, TOFDM and FTN have the same frequency spacing while SEFDM has a compressed bandwidth. The bandwidth savings in SEFDM are been accomplished by compressing the spacing in the frequency-domain between subcarriers. It can be noticed that SEFDM has the same symbol duration (width in the figure) as OFDM.

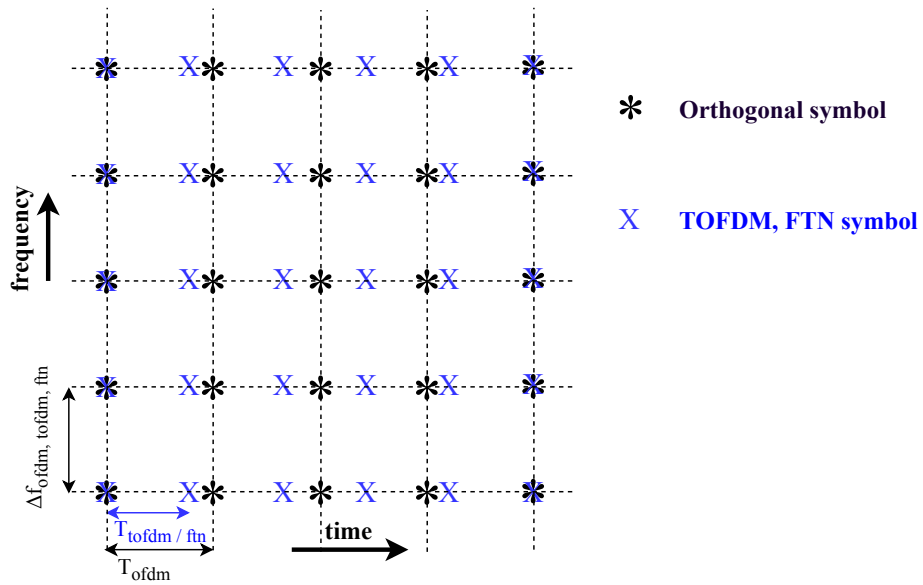


Figure 5.4: Conceptual time-frequency illustration of TOFDM and FTN when derived from an OFDM

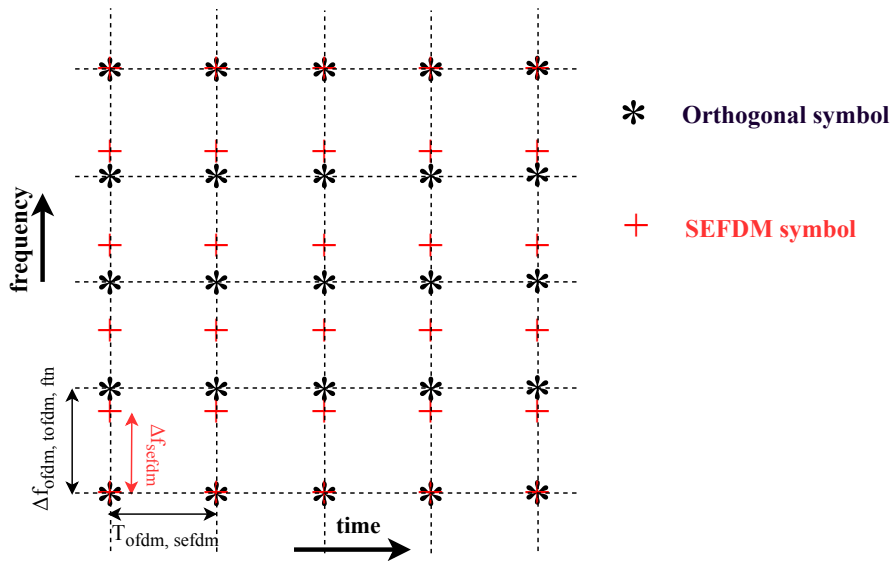


Figure 5.5: Conceptual time-frequency illustration of SEFDM when derived from an OFDM

## 5.4 Truncated OFDM Signal Model

This section describes the basic signal model for TOFDM signals and characterizes the self-induced ICI in TOFDM signals.

### 5.4.1 Signal Model

A TOFDM symbol  $\mathbf{x}(t)$  is generated by multiplexing a vector of  $N$  inputs of a complex signal denoted as  $\mathbf{s}$  onto parallel subcarriers, in a similar way to OFDM but with a time truncation factor,  $\gamma$ , as :

$$\mathbf{x}(t) = \frac{1}{\sqrt{T_{tofdm}}} \sum_{l=-\infty}^{\infty} \sum_{n=0}^{N-1} \mathbf{s}_{l,n} \exp\left(\frac{j2\pi n(t - l\gamma T_{ofdm})}{T_{ofdm}}\right), \quad (5.5)$$

Defining  $T_{tofdm}$  as the TOFDM symbol duration as  $T_{tofdm} = \gamma T_{ofdm}$ , (5.5) can also be represented as:

$$\mathbf{x}(t) = \frac{1}{\sqrt{T_{tofdm}}} \sum_{l=-\infty}^{\infty} \sum_{n=0}^{N-1} \mathbf{s}_{l,n} \exp\left(\frac{j2\pi n(t - lT_{tofdm})}{T_{ofdm}}\right), \quad (5.6)$$

where  $\mathbf{s}_{l,n}$  denotes the data symbol modulated on the  $n^{th}$  subcarrier and  $l^{th}$  TOFDM symbol,  $N$  represents the number of the subcarrier and  $1/\sqrt{T_{tofdm}}$  is a normalization factor.

By sampling one TOFDM symbol with sample period  $T_{ofdm}/Q$ , where  $Q = \rho N$  and  $\rho \geq 1$  is the oversampling rate, in case of  $\rho = 1$  the sampling process satisfies the Nyquist frequency rule. The signal is padded with zeros in the frequency domain to increase the number of samples in the time-domain while maintaining the bandwidth in the frequency domain. A discrete TOFDM symbol is expressed as [54]:

$$\mathbf{x}(k) = \frac{1}{\sqrt{\gamma Q}} \sum_{n=0}^{Q-1} \mathbf{s}_n \exp\left(\frac{j2\pi nk}{Q}\right), \quad (5.7)$$

where  $k$  is the index of the time sample of the TOFDM symbol for the range

$0 \leq k \leq \gamma Q - 1$ . Equation (5.7) depicts the process of modulating the input data onto different subcarriers in a TOFDM symbol and it is represented in matrix form as [54]:

$$\mathbf{x} = \mathbf{\Phi} \mathbf{s}. \quad (5.8)$$

$\mathbf{x} = [x_0, x_1, \dots, x_{\gamma Q-1}]^T$  represents a  $\gamma Q$ -dimensional vector that is a sampled TOFDM symbol in the time-domain,  $\mathbf{s} = [s_0, s_1, \dots, s_{Q-1}]^T$  is an  $Q$ -dimensional vector that is a sampled input data in the frequency domain. The symbol  $\mathbf{\Phi}$  signifies the sampled carrier matrix;  $\mathbf{\Phi}$  is a  $\gamma Q \times Q$  two-dimensional matrix. The elements of the  $\mathbf{\Phi}$  matrix are given as:

$$\Phi_{k,n} = \frac{1}{\sqrt{\gamma Q}} \exp(j2\pi nk/Q) \quad (5.9)$$

where  $0 \leq n \leq Q - 1$  and  $0 \leq k \leq \gamma Q - 1$ . The symbol  $[.]^T$  refers to a matrix or alternatively a vector transpose.

### 5.4.2 Characterizing ICI in TOFDM System

A similar method of analysis to that developed for SEFDM in [54] is followed here. Sampling the subcarriers of a TOFDM symbol results in the carrier matrix, denoted as  $\mathbf{\Phi}$ , which represents the mathematical function of a sampled bank of modulators:

$$\mathbf{\Phi} = \frac{1}{\sqrt{\gamma Q}} \begin{bmatrix} 1 & 1 & 1 & \dots & 1 \\ 1 & e^{j\frac{2\pi}{Q}} & e^{j\frac{4\pi}{Q}} & \dots & e^{j\frac{2\pi(Q-1)}{Q}} \\ \vdots & \vdots & \vdots & \ddots & \vdots \\ 1 & e^{j\frac{2\pi(\gamma Q-1)}{Q}} & e^{j\frac{4\pi(\gamma Q-1)}{Q}} & \dots & e^{j\frac{2\pi(\gamma Q-1)(Q-1)}{Q}} \end{bmatrix}_{\gamma Q \times Q}. \quad (5.10)$$

In order to study and understand the ICI in a TOFDM system, the cross correlation matrix, denoted as  $\mathbf{C}$ , is now evaluated. A discrete representation of the signal is assumed in this chapter, as this allows the study of truncation and oversampling effects on generated signal and detection properties. A similar method to that reported in [54] is followed.

The cross correlation measures the degree to which two signals are correlated. Assuming that the two discrete TOFDM sub-carriers are  $e^{\frac{2\pi km}{Q}}$  and  $e^{\frac{2\pi kn}{Q}}$ , the cross correlation  $\mathbf{C}[m, n]$  of two arbitrary subcarriers  $m$  and  $n$  in a TOFDM signal may be represented by:

$$\begin{aligned}\mathbf{C}[m, n] &= \frac{1}{\gamma Q} \sum_{k=0}^{\gamma Q-1} \exp\left(\frac{-j2\pi mk}{Q}\right) \exp\left(\frac{j2\pi nk}{Q}\right) \\ &= \frac{1}{\gamma Q} \sum_{k=0}^{\gamma Q-1} \exp\left(\frac{-j2\pi(m-n)k}{Q}\right) \\ &= \frac{1}{\gamma Q} \left[ \frac{1 - e^{-j2\pi(m-n)\gamma}}{1 - e^{-\frac{j2\pi(m-n)}{Q}}}\right],\end{aligned}\tag{5.11}$$

where  $k = 0, \dots, (\gamma Q - 1)$ , and  $Q$  is the number of samples per subcarrier, and the  $(m - n)$  represents the subcarriers index distance, that is the index distance between a subcarrier  $m$  to subcarrier  $n$ . Therefore, each correlation coefficient  $\mathbf{C}[m, n]$  in (5.11) above is an interference-coefficient between two subcarriers. Since the condition of orthogonality between all subcarriers is violated, each subcarrier contributes some level of interference to produce the overall ICI in the signal.

The derivation of the third line of (5.11) is based on the sum of geometric series:  $\sum_{k=0}^{Q-1} r^k = \frac{1-r^Q}{1-r}$ . The correlation matrix  $\mathbf{C}$ , given in (5.12) below, is the interference matrix, whose elements are those derived in (5.11), define the interference between all subcarriers as well as the relative value of each subcarrier:

$$\mathbf{C} = \frac{1}{\gamma Q} \begin{bmatrix} \gamma Q & \frac{1 - e^{j2\pi\gamma}}{1 - e^{\frac{j2\pi}{Q}}} & \cdots & \frac{1 - e^{j2\pi(Q-1)\gamma}}{1 - e^{\frac{j2\pi(Q-1)}{Q}}} \\ \frac{1 - e^{-j2\pi\gamma}}{1 - e^{-\frac{j2\pi}{Q}}} & \gamma Q & \cdots & \frac{1 - e^{j2\pi(Q-2)\gamma}}{1 - e^{\frac{j2\pi(Q-2)}{Q}}} \\ \vdots & \vdots & \ddots & \vdots \\ \frac{1 - e^{-j2\pi(Q-1)\gamma}}{1 - e^{-\frac{j2\pi(Q-1)}{Q}}} & \frac{1 - e^{-j2\pi(Q-2)\gamma}}{1 - e^{-\frac{j2\pi(Q-2)}{Q}}} & \cdots & \gamma Q \end{bmatrix}_{Q \times Q} \quad (5.12)$$

The correlation matrix  $\mathbf{C}$  is a Toeplitz [91] and Hermitian  $Q \times Q$  matrix and its elements are given by:

$$\mathbf{C}[m, n] = \frac{1}{\gamma Q} \begin{bmatrix} \gamma Q & , m = n \\ \frac{1 - e^{-j2\pi(m-n)\gamma}}{1 - e^{-\frac{j2\pi(m-n)}{Q}}} & , m \neq n \end{bmatrix} \quad (5.13)$$

It is evident that the non-diagonal elements in the matrix  $\mathbf{C}$  are non-zero indicating the self-ICI in TOFDM. The correlation matrix is used to estimate the interference among the subcarriers. Although only partial data is transmitted and the rest is discarded, the receiver has the ability to retrieve the data by estimating the removed part of the symbol by using the correlation matrix. Examination of (5.11) shows that the correlation matrix can be found by using subcarrier matrix as they are directly related by:

$$\mathbf{C} = \mathbf{\Phi}^* \times \mathbf{\Phi} \quad (5.14)$$

where  $[\cdot]^*$  is the Hermitian transpose operation. Equation (5.14) shows that the correlation matrix  $\mathbf{C}$  can be generated easily by using the carrier matrix  $\mathbf{\Phi}$ , where the latter can be found by knowing the truncation and the

oversampling factors.

## 5.5 Testbeds, Detection and System Performance

In this section, uncoded and coded TOFDM systems are designed, implemented and then their performance is evaluated. The two designs involve signal generation, reception and decoding, and data recovery. For the first system, the uncoded system, which is given in Section 5.5.1, SD is used to retrieve the transmitted data bits utilizing the correlation matrix (the interference matrix). The system decoder is evaluated by testing the BER in simulations. On the other hand, for the coded systems, an iterative decoder is designed specifically for TOFDM systems, which is based on successive interference cancellation. Furthermore, the TOFDM coded systems are designed using two guard interval schemes, (i) ZP and (ii) CP. The coded systems are designed, implemented and evaluated in simulations and realistic RF testbeds as described in Section 5.5.2.

### 5.5.1 Uncoded TOFDM systems

In this section, the uncoded TOFDM transceiver is described in Section 5.5.1.1, while the signal detection is given in Section 5.5.1.2, and the system performance is evaluated in Section 5.5.1.3.

#### 5.5.1.1 Signal generation and reception

Figure 5.6 illustrates a basic block diagram for the TOFDM system model used in this study. The figure sketches a simple time-domain representation of TOFDM transmitted symbols, showing partial transmission for the samples, as the blue coloured samples are not transmitted. Simply, OFDM symbols are generated and then truncated before transmission. The transmitted TOFDM signal,  $\mathbf{x}(t)$ , is contaminated with AWGN signal,  $\mathbf{z}(t)$ , to give the received

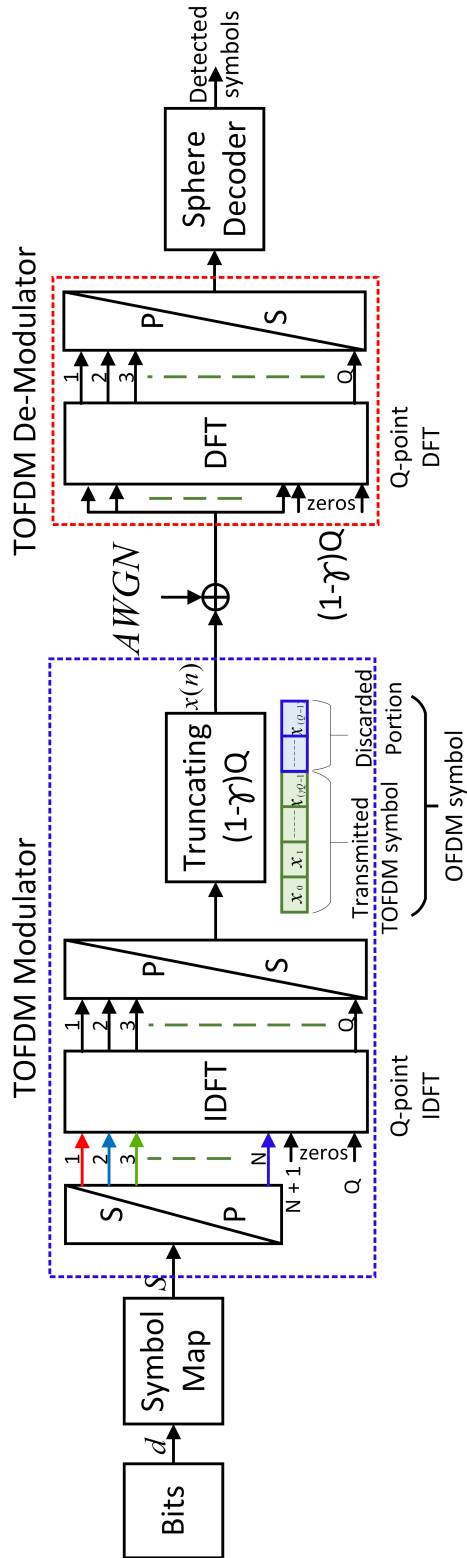


Figure 5.6: TOFDM simplified system modem.

signal  $\mathbf{y}(t)$ , as:

$$\mathbf{y}(t) = \mathbf{x}(t) + \mathbf{z}(t). \quad (5.15)$$

At the receiver, the duration of the symbol at each modulator is shorter by the factor  $\gamma$ , relative to the original OFDM symbol. Note that  $\gamma Q$  is equal to the number of the transmitted samples per TOFDM symbol. The received TOFDM signal is fed into a DFT of size  $Q$  to demodulate the received signal. Where the number of TOFDM time samples in each symbol is smaller than the number of input bins to the DFT. Hence, the last  $(1 - \gamma)Q$  bins are fed with zeros as shown in Figure 5.6. The discrete form of the received signal is expressed as:

$$\mathbf{r}(n) = \frac{1}{\sqrt{\gamma Q}} \sum_{k=0}^{\gamma Q-1} \mathbf{x}_k \exp\left(\frac{-j2\pi nk}{Q}\right) + \mathbf{z}_c(k), \quad (5.16)$$

where  $n = 0, \dots, Q - 1$ ,  $x_n$  is the transmitted signal,  $\mathbf{r}$  is the received signal after demodulation and  $\mathbf{z}_c$  is a  $Q \times 1$  vector of AWGN samples correlated with the conjugate subcarriers.

### 5.5.1.2 Signal Detection

The detection techniques followed in this section is similar to those applied to SEFDM in [92]. The demodulated signal is fed to a SD to detect the signal. The mathematical representation for the SD is expressed as:

$$\mathbf{s}_{sd} = \arg \min_{\mathbf{s} \in M^Q, \|\mathbf{r} - \mathbf{C}\mathbf{s}\|^2 \leq g} \|\mathbf{r} - \mathbf{C}\mathbf{s}\|^2, \quad (5.17)$$

where  $\mathbf{s}_{sd}$  is the estimated signal,  $M^Q$  is all the possible combinations for the transmitted TOFDM symbols,  $M$  is the cardinality of the constellation diagram,  $g$  is the radius of the hypersphere search area that is centered at the vector  $\mathbf{r}$ , and  $\mathbf{s}$  is the vector that has the highest probability of being transmitted. The latter is found by finding the minimum Euclidean distance from all the possible vector combinations which take place inside the multi-

dimensional hypersphere searching area. In other words, by using a SD we can detect the received signal by estimating the truncated portion of every TOFDM symbol, enabling recovery of the intended signal. In addition, the SD tests a subset of the all possible combinations of transmitted symbols, which means it enjoys improved computational efficiency over a ML detector, which compares the received symbol with the all possible combinations of the transmitted TOFDM symbols.

### 5.5.1.3 Uncoded system performance

The TOFDM system is tested using ten subcarriers, QPSK modulation format and different truncation factors  $\gamma = 0.9, 0.8, 0.7$  and  $0.6$ , for different values of oversampling. A smaller value of  $\gamma$  allows the system to transmit fewer samples and gives a higher spectral efficiency. In this study, two oversampling values (1 and 4) are used in the simulations, where higher values of oversampling will result in lower levels of aliasing, leading to better Bit Error Rates (BERs). Figures 5.7 and 5.8 show the error performance for two values of oversampling factor  $\rho = 1$  and  $4$ , respectively, without and with different level of truncation.

The power penalty, defined as  $E_b/N_o$  difference between OFDM and TOFDM systems, is measured at  $\text{BER} = 10^{-3}$  in Figure 5.9. It should be noted that by truncating 20% of samples, TOFDM shows identical performance to OFDM. With further samples truncation up to 30%, therefore higher interference, 1 dB power penalty is observed. Due to the improved spectral efficiency, such power penalty may be tolerated. The figure also demonstrates the effect of oversampling on power penalty. For high truncation factors such as 0.9 and 0.8, the oversampling has no clear effect. For lower truncation factors, therefore higher interference, the power penalty is reduced with the increase of oversampling factors due to improved signal resolutions.

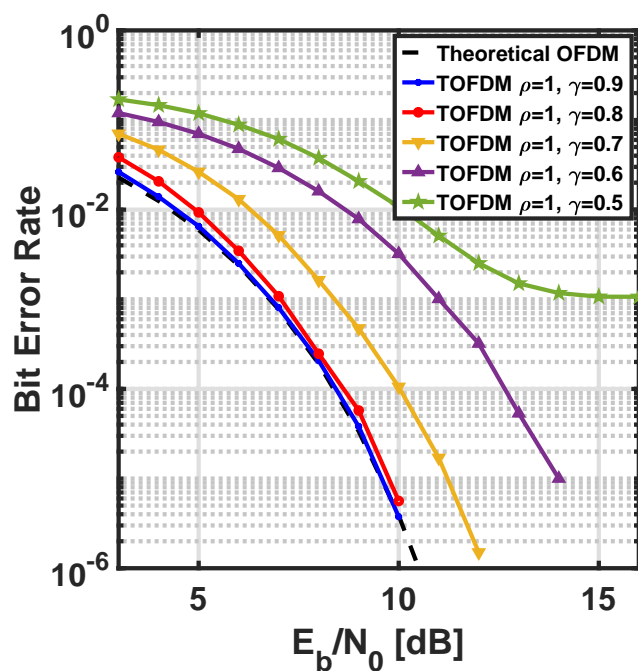


Figure 5.7: BER for TOFDM system with no oversampling

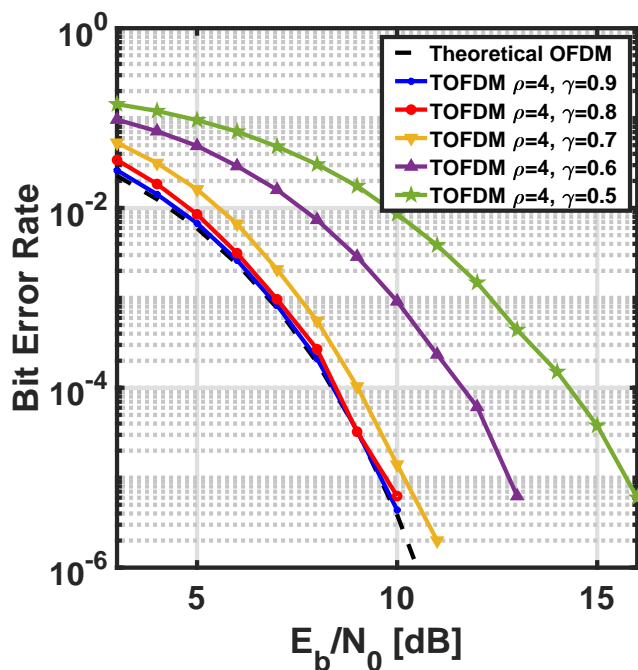
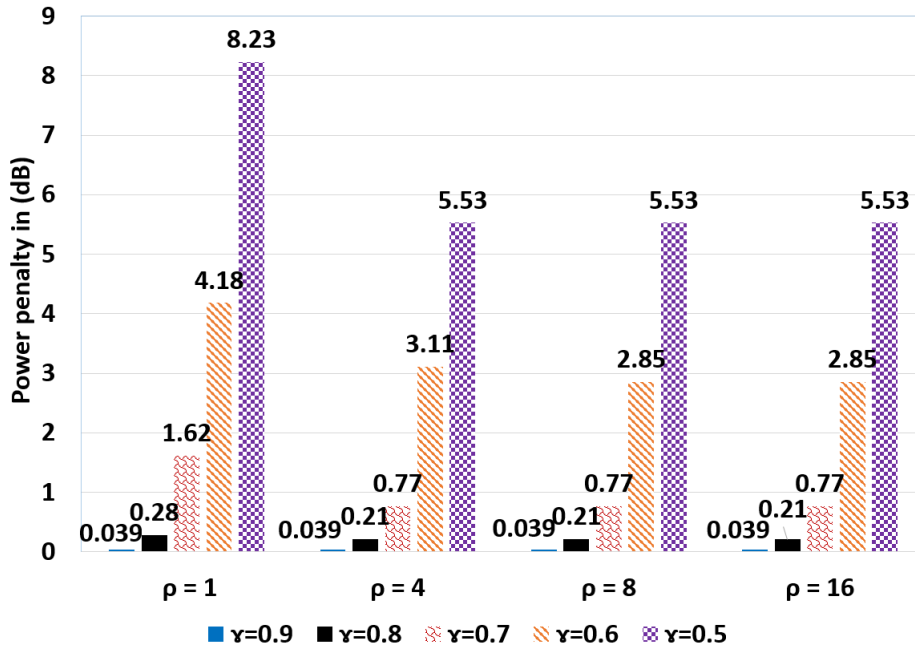


Figure 5.8: BER for TOFDM system with oversampling factor = 4



**Figure 5.9:** Power penalty (at  $\text{BER} = 10^{-3}$ ) of different levels of truncations and oversampling to OFDM

### 5.5.2 Coded TOFDM systems

This section presents the design, implementation and system performance of a new TOFDM system with channel coding. The new proposed system employs channel coding (convolutional coding is used in this chapter) at the transmitter and iterative soft decoder at the receiver. This system is built on top of the Institute of Electrical and Electronics Engineers (IEEE) 802.11g, which is achieved by modifying the transmitter to send TOFDM signals instead of OFDM signals. As a result, the symbol transmission is reduced in comparison to the conventional OFDM system and hence enhance the system data rate. At the receiver, a new iterative decoder is designed using the soft-output data and the knowledge of the interference coefficients given in the correlation matrix to cancel the interference among the subcarriers in TOFDM symbols. The new system is first evaluated in AWGN channels using computer simulations. After that, the system is built in an experimental testbed using USRP for RF signal generation and reception. Then,

the system is evaluated using realistic channel models generated in a channel emulator. Furthermore, in addition to using the conventional CP in TOFDM systems, TOFDM system using ZP as a guard interval, is designed and implemented. The transmitter, receiver and decoder design, and the system performance of the new coded TOFDM system are given in the following subsections.

### 5.5.2.1 Transmission

At the transmitter, a pseudorandom binary sequence is generated, which is then scrambled using the IEEE 802.11a,g scrambler, which is a 127-bit frame-synchronous scrambler [24][93]. Then, the scrambled bits are encoded by convolutional encoder with code rate  $R_c = 1/2$ . The convolutional encoder is the industry-standard encoder with the first polynomial  $g_0 = 133_8$  and the second polynomial  $g_1 = 171_8$ . After that, the encoded bits are interleaved and mapped into BPSK and QPSK and then fed into serial to parallel converter. Next, the symbols are fed into IFFT, resulting in the generation of OFDM symbols. Each OFDM symbol consists of  $Q$  samples in the time-domain. Not all the samples are transmitted, where only part of the samples of length  $\gamma Q$ , are passed and the rest are discarded. After that, CP or ZP is attached to each TOFDM symbol before being transmitted in frames. In this system evaluation, each frame consists of a preamble and 50 data symbols. It should be noted that, the preamble used in this test and study, is the same as the IEEE 802.11a,g preamble, where full OFDM symbols are sent. This is to guarantee accurate time synchronization, and Carrier Frequency Offset (CFO) and channel estimation. The preamble generation is described in Section 6.3.1 of the next chapter in this thesis.

The upper part of Figure 5.10 depicts the block diagram of modified 802.11a transmitter using TOFDM signals. The scrambler, convolutional encoder, interleaver, mapper and the modulation process using IFFT are the same as the IEEE 802.11a,g standard [24][93], which are given in Section 6.3 of the next chapter in this thesis.

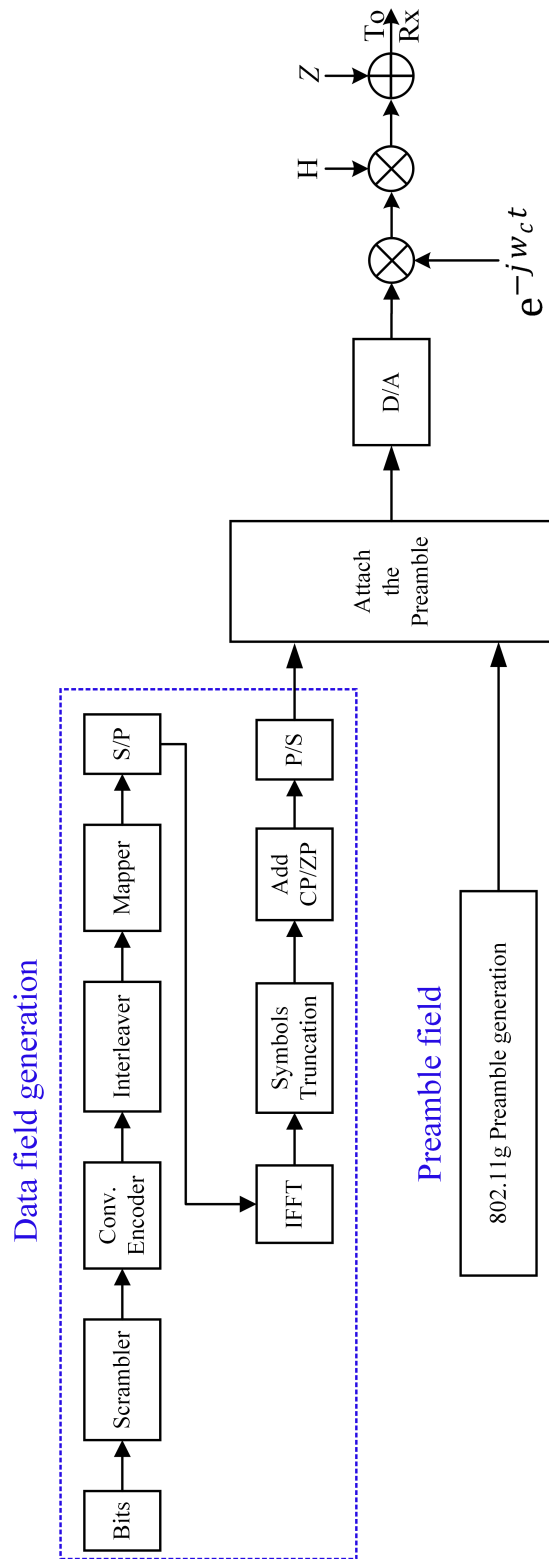


Figure 5.10: Block diagram of modified 802.11a,g transceiver using TOFDM signals

### 5.5.2.2 Channel model description

The RF frames are transmitted over a mobile environment implemented using a Spirent VR5 channel emulator. The wireless channel model is the built-in wireless LAN-exponential decay 802.11a,g, with user terminal velocity of 50 km/hour. The channel paths follow Rayleigh distribution and their delays and power values parameters are given in the following table.

**Table 5.1:** WLAN Exponential Decay Channel Model

Path	Relative power	Delay values
1	0.0 dB	0 $\mu$ s
2	-2.1 dB	0.0125 $\mu$ s
3	-4.2 dB	0.025 $\mu$ s
4	-6.3 dB	0.0375 $\mu$ s
5	-8.4 dB	0.05 $\mu$ s
6	-10.5 dB	0.0625 $\mu$ s
7	-12.7 dB	0.075 $\mu$ s
8	-14.8 dB	0.0875 $\mu$ s
9	-16.9 dB	0.1 $\mu$ s
10	-19.0 dB	0.1125 $\mu$ s
11	-21.1 dB	0.125 $\mu$ s
12	-23.2 dB	0.1375 $\mu$ s
13	-25.3 dB	0.15 $\mu$ s
14	-27.4 dB	0.1625 $\mu$ s
15	-29.5 dB	0.175 $\mu$ s

### 5.5.2.3 Signal recovery

At the receiver, time synchronization, CFO estimation and compensation, channel estimation and equalization, and an iterative detector with an interference canceller are utilized to retrieve the data.

**5.5.2.3.1 Synchronization, and CFO estimation and compensation.** In order to find the starting time sample of each frame, the Long Training Field (LTF) symbol is correlated with the received signal. As mentioned in Section 6.3.1.2 of this thesis, two peaks are expected to result from

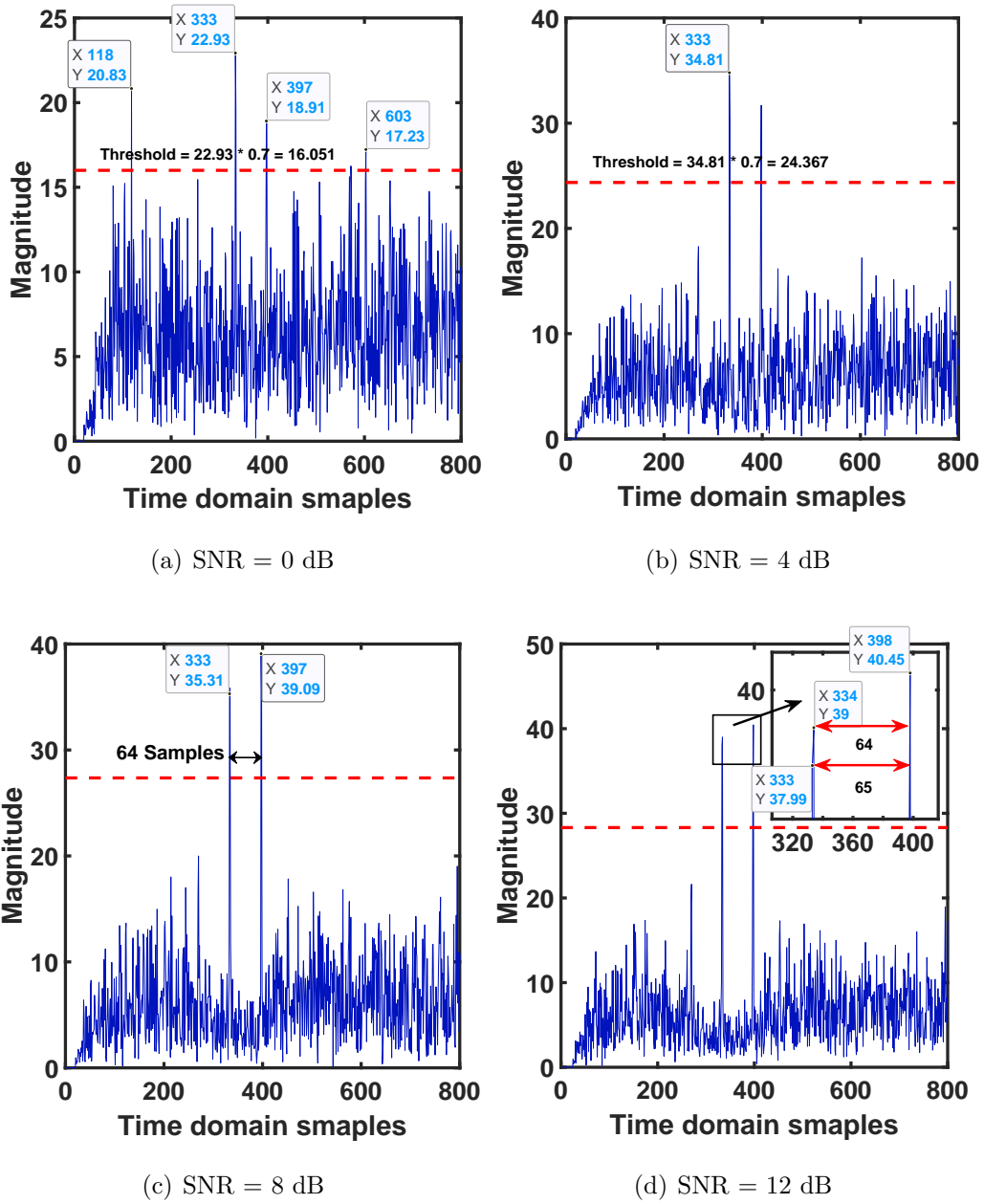


Figure 5.11: The resulting signals of correlating LTF symbol and the received signal

the correlation process between the LTF symbol and the preamble signal. Figure 5.11 shows the resulting signal of the correlation between the LTF symbol and received signal after traversing a multipath channel and being contaminated with AWGN noise in the channel emulator, for different value of Signal to Noise Ratio (SNR). The mechanism of finding the first received time sample of the frames, are described in the following steps: (i) correlate the LTF symbol with the received signal, (ii) find the highest resulting peak, (iii) multiply the amplitude of the highest peak with 0.7 then set the resulting value as a threshold bar (the red dashed-lines of Figure 5.11 represent the threshold bar), (iv) search for other peaks above the threshold bar, (v) identify the earliest two peaks appear in time, that are above the threshold bar and have 64 time samples difference in between, and (vi) the first peak of the two found peaks identifies the beginning of the LTF symbols in the preamble signal, which comes straight before the data symbols. It should be noted that the multiplication with 0.7 value is set after intensive number of experimental runs. For the case when no peaks are found, the frame is dropped and not counted/considered in the BER measurement.

For CFO estimation, the same mechanism that is given in Section 6.5.3.4 of this thesis is followed. While for CFO compensation, the process is given in Section 6.5.3.5.

**5.5.2.3.2 Signal demodulation.** After finding the starting time sample of the received frame, the FFT is used to perform signal demodulation. For the scenario of using CP in TOFDM symbols, the CP part is removed at the receiver and the TOFDM symbol is passed to the FFT. While for the scenario of using ZP, the TOFDM symbol and the ZP part are combined using the overlap-add mechanism designed for non-orthogonal signals and then fed into the FFT. The design of the overlap-add technique is similar to that of SEFDM systems provided in Section 4.6 of this thesis.

**5.5.2.3.3 Channel estimation and equalization** The experimental work and study presented in this chapter, use the two LTF symbols of the preamble signal for channel estimation. The full description of the process,

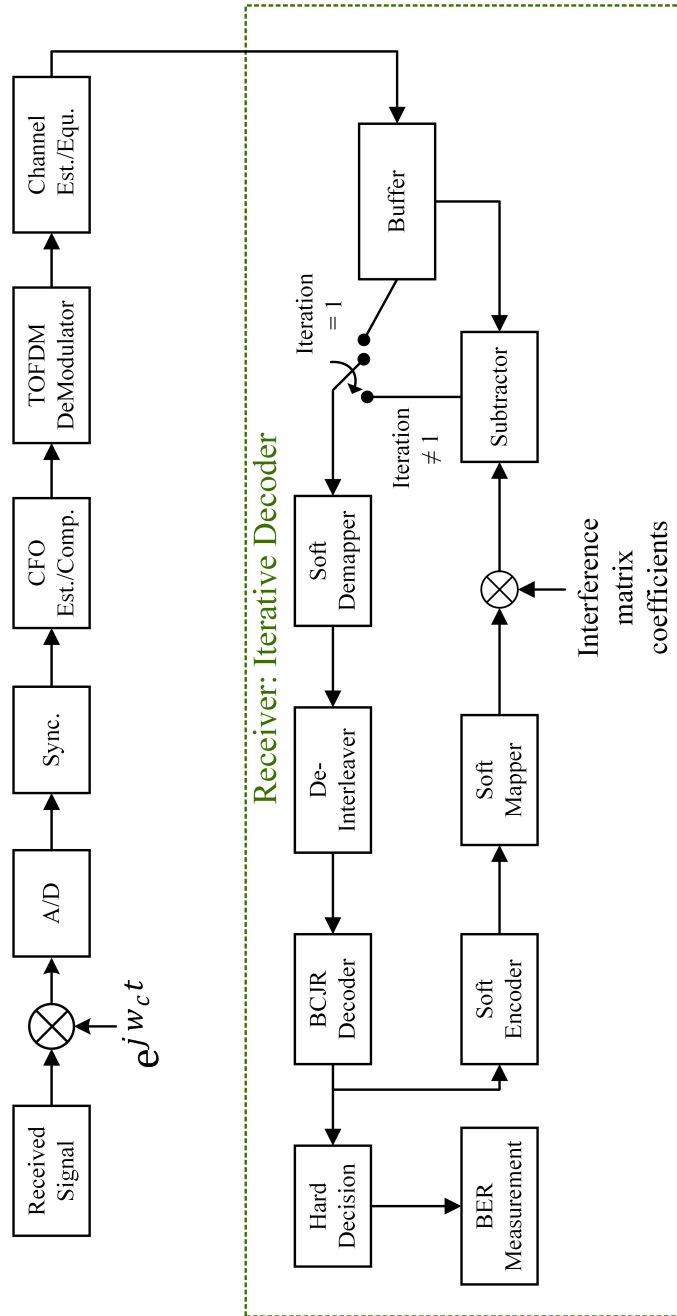


Figure 5.12: Block diagram of modified 802.11g receiver using iterative decoder.

is provided in Section 6.5.3.3. Zero forcing channel equalization is applied, which occurs in the frequency-domain.

**5.5.2.3.4 Iterative decoder.** Figure 5.12, depicts the block diagram of the modified 802.11a,g receiver, which uses iterative decoder to recover the data carried in TOFDM signals. In general, the interference between subcarriers is estimated and subtracted in every iteration from the original equalized signal before passing the signal to the next iteration.

The equalized data is passed into a soft demapper, where its output expressed in the LLR form. The sign of LLR value indicates the sign of the bits and its magnitude determines the reliability of the sign of the demapped bit. The LLR bits are then deinterleaved and decoded using BCJR [94] decoder, where its output is in the LLR form too. The decoded bits are encoded again using soft encoder and its output bits are mapped with soft mapper. The interference is estimated by multiplying the soft symbol with the interference coefficient matrix, which identify the interference contribution between the subcarriers. The estimated interference is subtracted from the received demodulated signal before being passed to the next iteration. Repetition of this process leads to better interference estimate and consequently, better estimate of the transmitted data. The lower part of Figure 5.12 depicts the iterative decoding process.

### 5.5.3 Error rate performance in AWGN channel.

In this section, error rates performance of simulation TOFDM systems with channel coding are provided. The numerical BER performance of BPSK and QPSK of TOFDM system is examined using AWGN channel and shown in Figures 5.13 and 5.14, respectively. The figures indicate the BER performance of various truncation levels ( $\gamma$  values) using ten decoding iterations for each truncation level. Using BPSK modulation format, the system approaches the target BER after reaching the second iteration (of the ID) for  $\gamma \geq 0.5$ . While for  $\gamma = 0.4$  (60% truncation), six iterations are needed to reach the target BER with slight performance degradation. In terms of data

rate enhancement, this means that up to 100% and 150% data rate improvement can be achieved using two and six iterations of ID, respectively. This at the expense of power penalty of less than 0.2 dB in comparison to OFDM system. However,  $\gamma = 0.4$  is the lowest value that can be supported over the range tested, whereas error floor is observed for  $\gamma = 0.3$  for all the iterations of ID. On the other hand, for QPSK,  $\gamma = 0.9, 0.8$  and  $0.7$  can be used with approximately equivalent performance compared to OFDM system, as the power penalty is within 0.2 dB. This can be achieved by two, three and six iterations of ID for the respective  $\gamma$  values. Nevertheless, the BER performance degrades significantly for  $\gamma \leq 0.6$ . In general, the numerical results of using BPSK and QPSK indicate that a higher number of iterations is needed with a higher order modulation used in the TOFDM system. To summarise the results, Figure 5.15 depict the number of iterations of ID needed for each  $\gamma$  value, thus the BER remains stable, where no further BER enhancement to be observed.

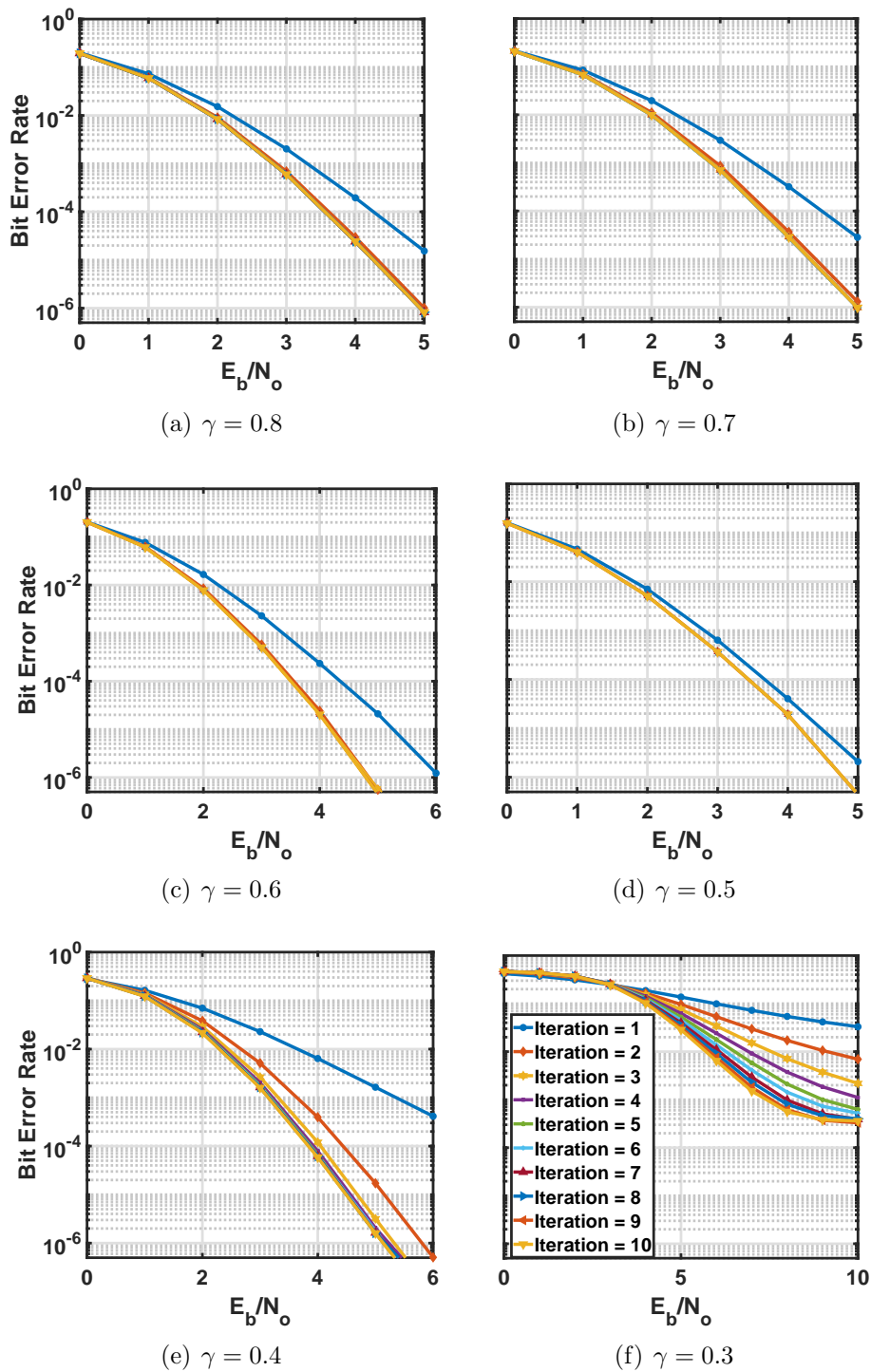


Figure 5.13: Convergence BER performance of BPSK-TOFDM with various iterations using different values of  $\gamma$

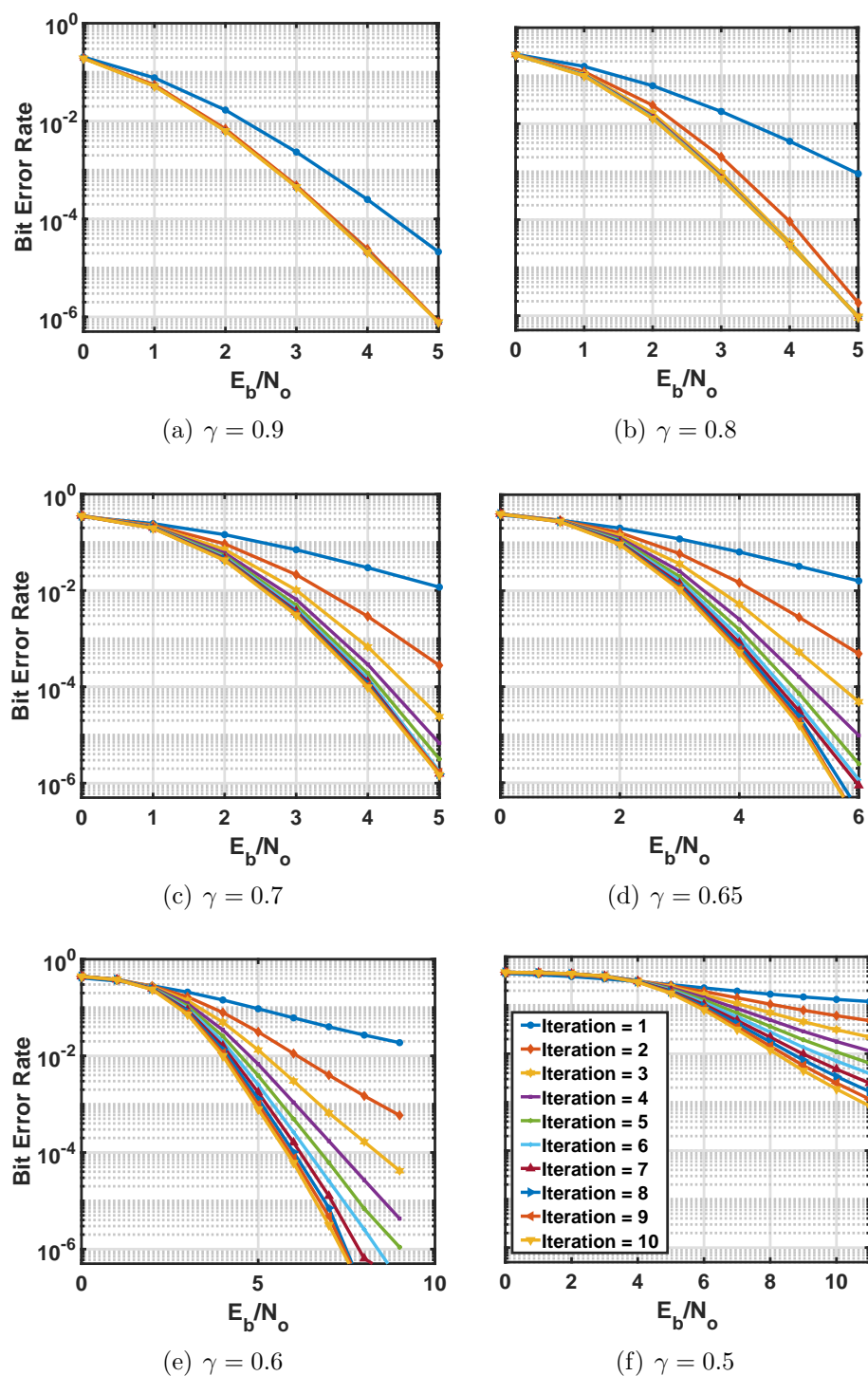
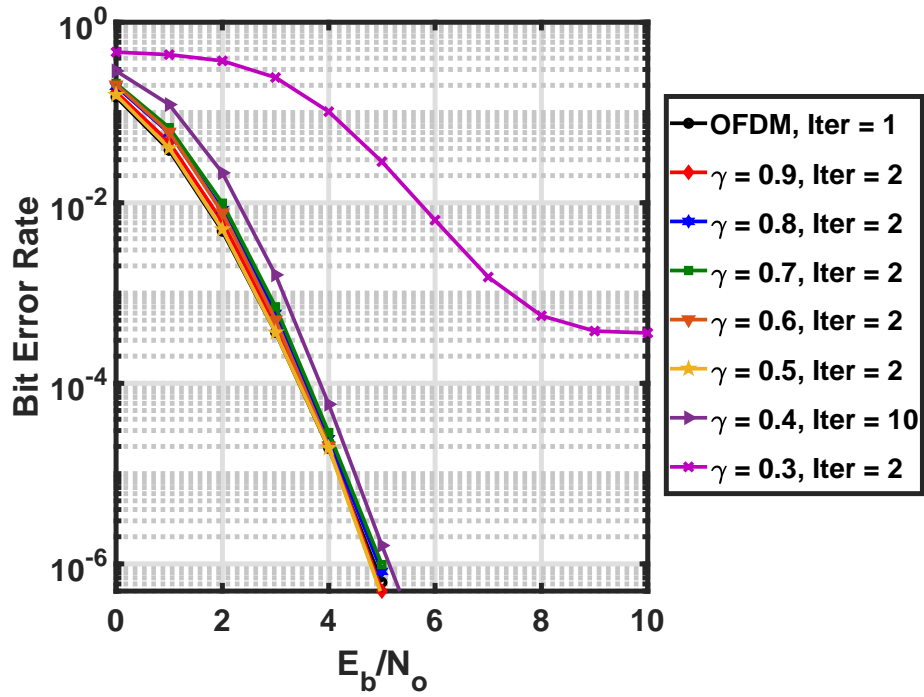
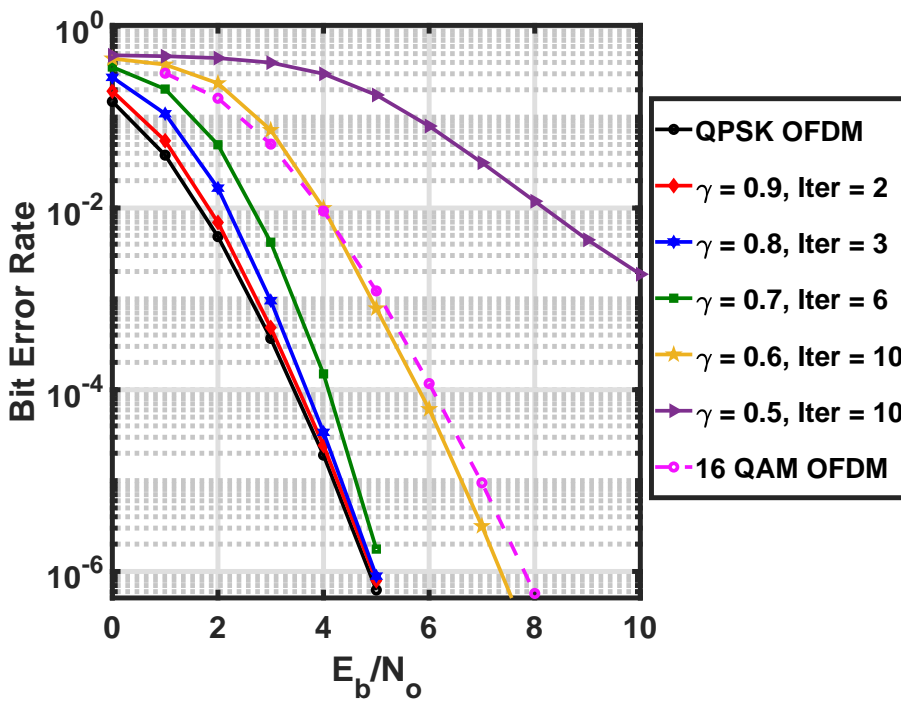


Figure 5.14: Convergence BER performance of QPSK-TOFDM with various iterations using different values of  $\gamma$



(a) BPSK



(b) QPSK

Figure 5.15: TOFDM system performance for various values of  $\gamma$

#### 5.5.4 Error rate performance in multipath wireless channel.

In this section, error rates performance of the modified 802.11g using TOFDM signals are presented and compared to the conventional 802.11g, where OFDM signals are used. The new TOFDM systems are evaluated using two guard interval techniques, CP and ZP using different values of truncation factor for two modulation formats, BPSK and QPSK. The multipath channel model used in this experimental evaluation is the wireless LAN-exponential decay 802.11a,g, which is described in Section 5.5.2.2.

##### 5.5.4.1 Channel estimation and equalization for TOFDM

Following the channel estimation technique of 802.11a,g, the two LTF symbols of the preamble signal are used estimate the channel characteristics at each subcarrier in the frequency-domain, which fully described in Section 6.5.3.3. Inspired by the all channel estimation work in SEFDM systems and by the work presented in chapter 4 of this thesis, the symbols in the preamble signal are OFDM ones. This means the preamble signal for the TOFDM systems are the same as that of the 802.11a,g OFDM systems. This is due to the fact that using OFDM pilot symbols for channel estimation provides more accurate estimates of the channels compared to using non-orthogonal pilot symbols. Furthermore, due to the fact that the sub-carriers location of OFDM and TOFDM signals, in the frequency-domain, are the same, hence no interpolation process is required to find the channel estimates for TOFDM signals.

For channel equalization, the conventional zero forcing technique is used to equalize the effect of the multipath channel on the received signals. In order to study the error rates performance of using different guard interval (CP and ZP) on the channel equalization performance in TOFDM systems, CP-TOFDM and ZP-TOFDM are evaluated here.

#### 5.5.4.2 TOFDM with cyclic prefix

Figures 5.16 and 5.17, show the error rate performance of CP-TOFDM using BPSK and QPSK modulations, respectively. Using BPSK for CP-TOFDM, there is no clear BER enhancement beyond the first iteration for the truncation factor values between  $\gamma = 0.9$  and  $0.5$ ; while two iterations are needed for  $\gamma = 0.4$ . This is not the case when QPSK modulation format is used, where a minimum of two iterations are required for the TOFDM systems to reach their optimum BER performance. In general, using lower  $\gamma$  value in TOFDM systems requires higher number of iterations to retrieve the transmitted data.

In terms of error rate performance in multipath channels, the power penalty gap between the BER performance of TOFDM and OFDM systems is higher than that observed in AWGN channels of Figures 5.13 and 5.14. This could be due to degradation in channel estimation and equalization performance and hence degrades the TOFDM decoding performance. However, orthogonal symbols are used to obtain the channel estimates at each subcarriers as mentioned in the previous subsection. Thus, the accuracy of channel estimation for TOFDM and OFDM systems are the same. This could narrow down the cause of the performance degradation in multipath channels to the equalization process accuracy. Therefore, to enhance the equalization performance accuracy, similar technique of using ZP instead of CP that is proposed by the author and presented in chapter 4 of this thesis, is followed in here. The BER results of ZP-TOFDM is shown and evaluated in the next subsection.

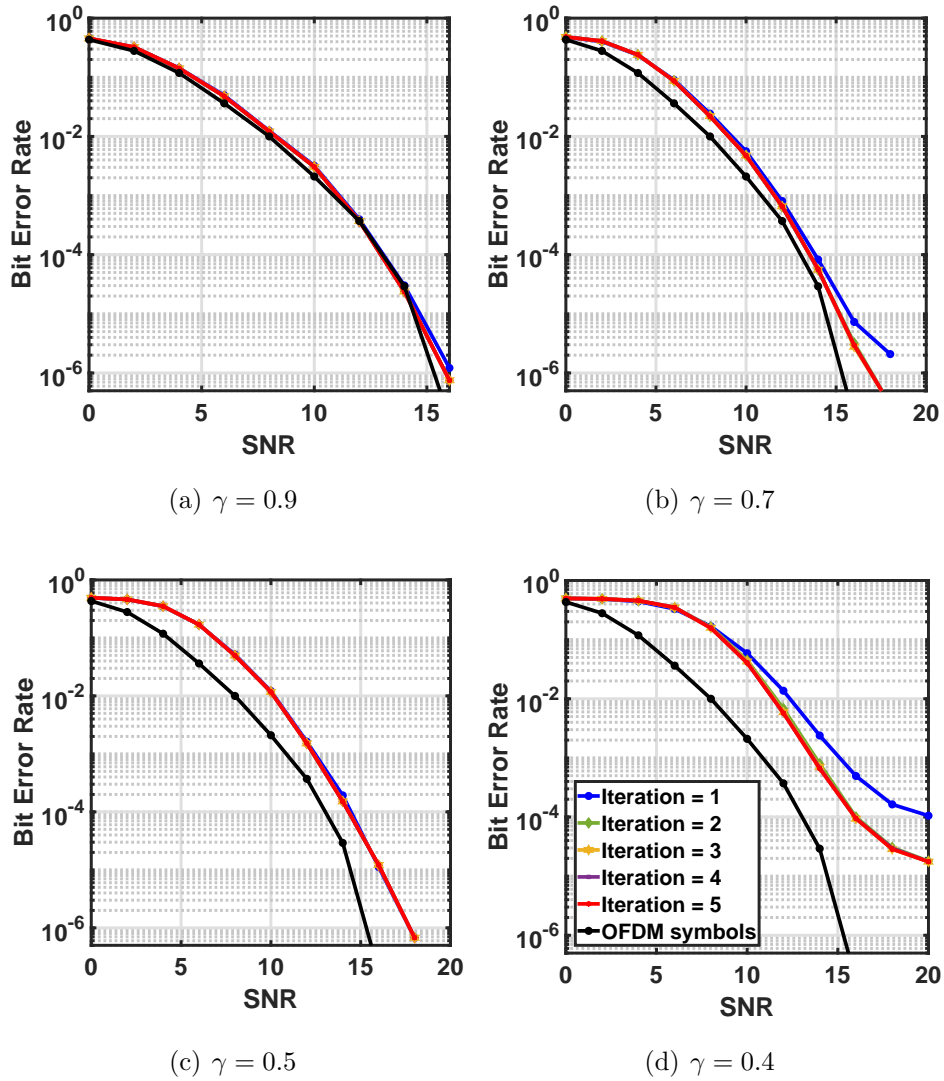


**Figure 5.16:** Experimental BER performance of BPSK CP-TOFDM with various iterations using different values of  $\gamma$

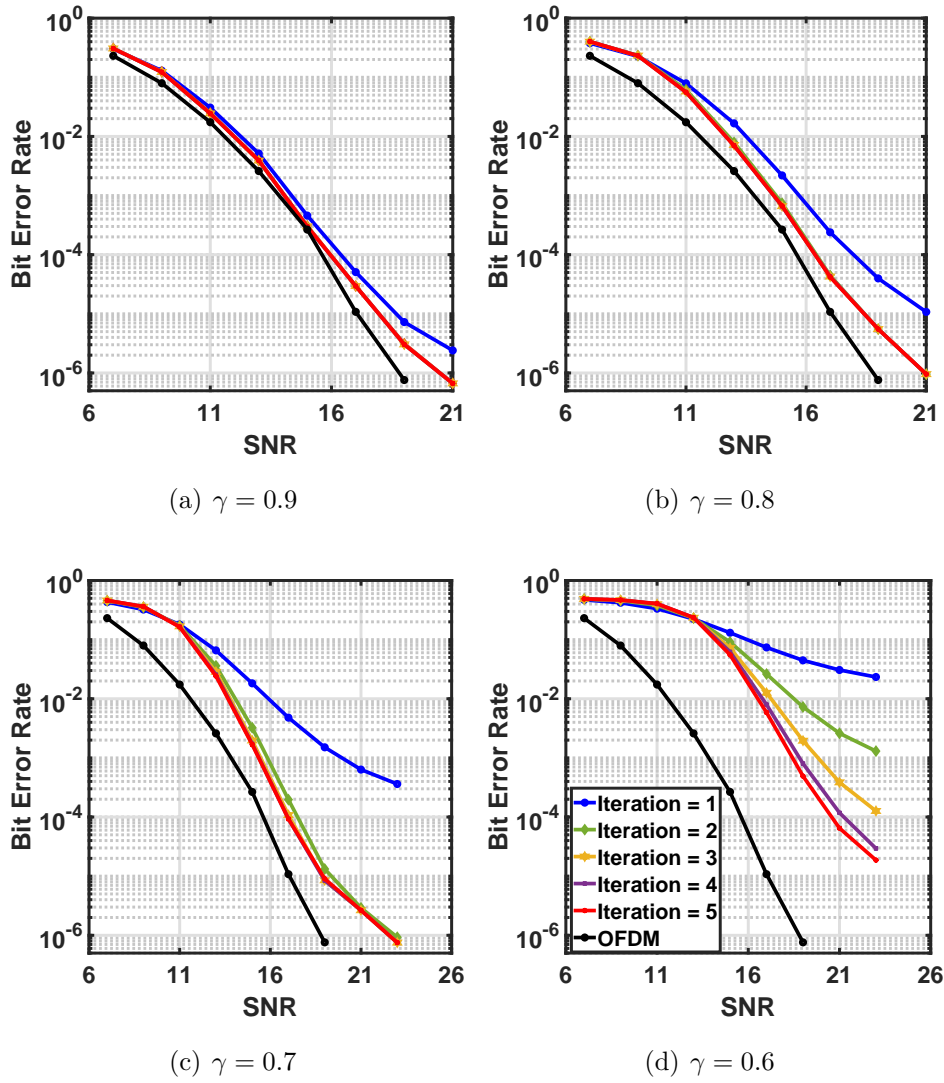


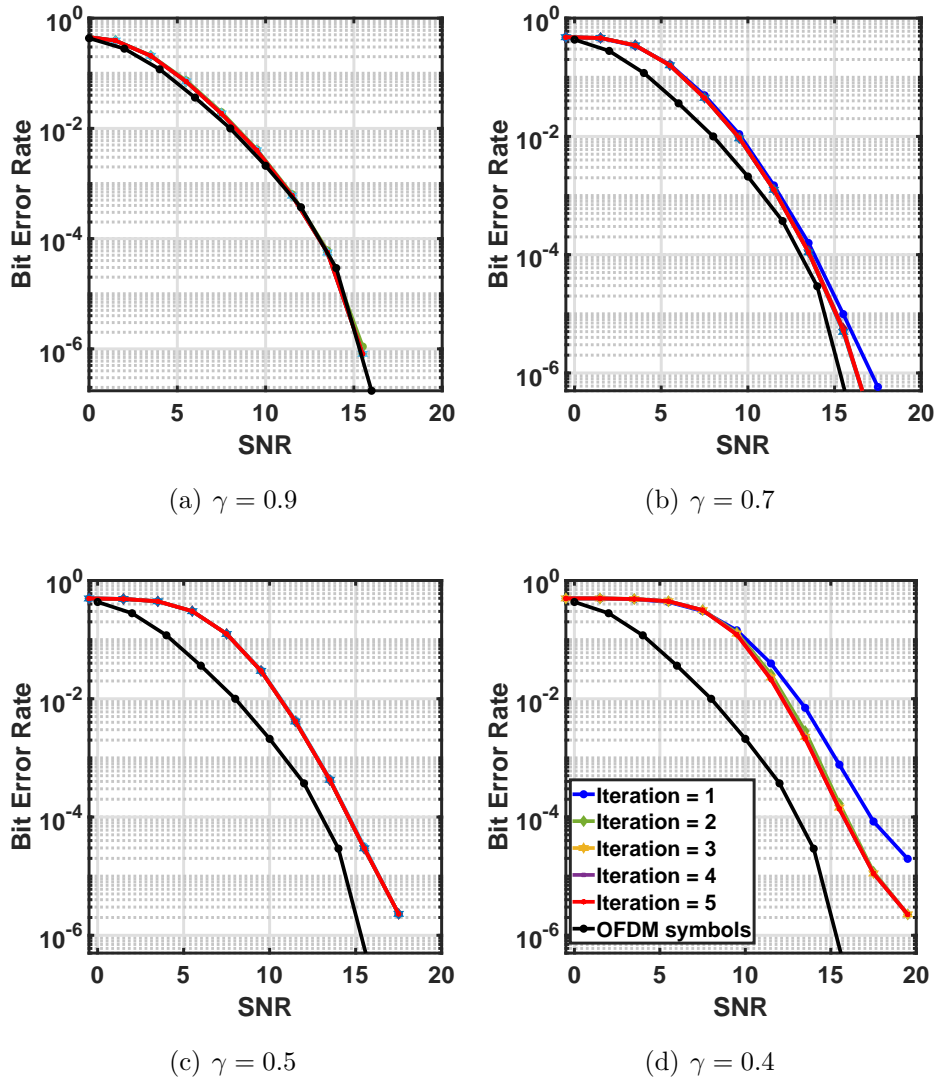
Figure 5.17: Experimental BER performance of QPSK CP-TOFDM with various iterations using different values of  $\gamma$

### 5.5.4.3 TOFDM with zero padding with power penalty evaluation

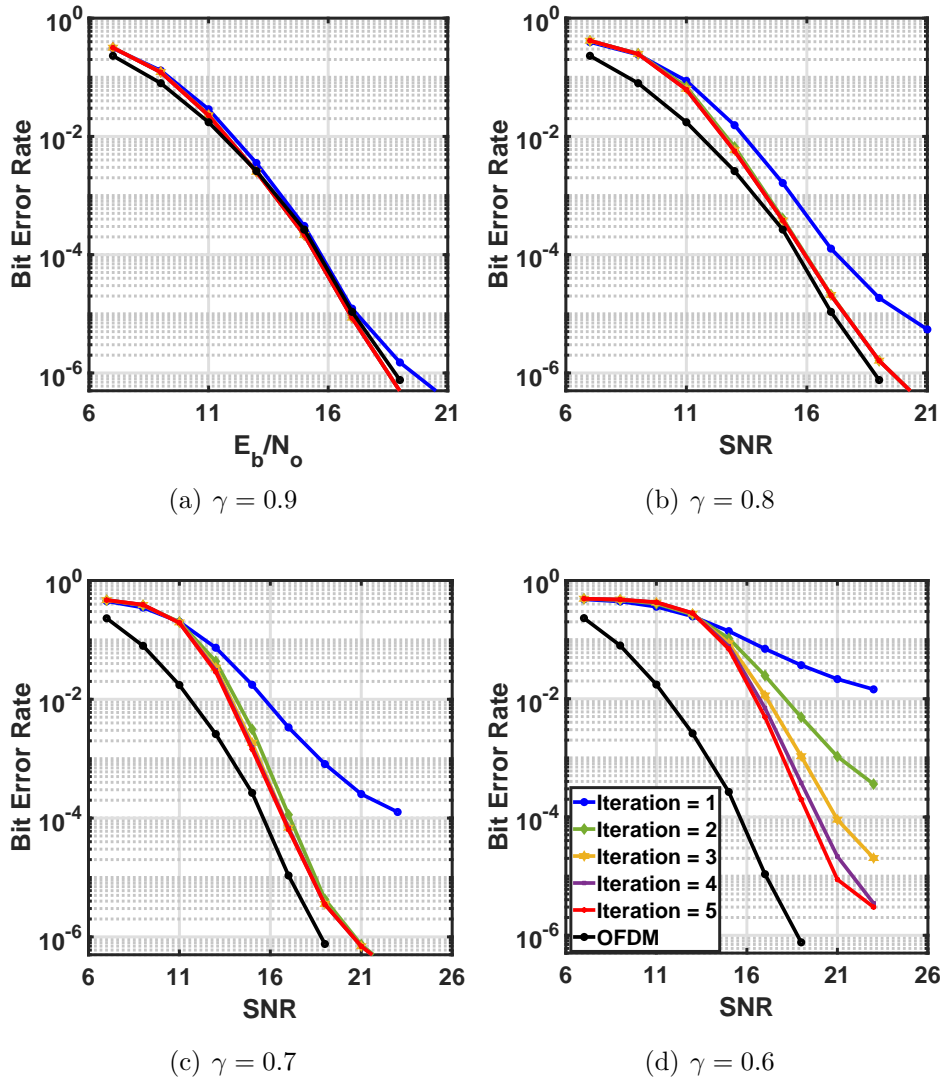
The error rates performance of ZP-TOFDM are evaluated in this section as depicted in Figures 5.18 and 5.19 for BPSK and QPSK modulations, respectively. In general, the BER results depict that more than one decoding iteration is required to retrieve the transmitted data. The error rate performance of TOFDM systems shows that improved spectral efficiency can be achieved by truncating the signal (partial transmission of the signal) at the transmitter. Yet, this is at the expense of power penalty in the system performance, which is the difference in power between OFDM and TOFDM systems.

Figure 5.20, depicts the power penalty between CP-TOFDM and ZP-TOFDM, and CP-OFDM, measured at  $\text{BER} = 10^{-4}$  and  $10^{-5}$  for BPSK and QPSK modulation formats. The arrows appear in the figures indicate that the BER performance reaches a non-zero error floor. Using BPSK in TOFDM systems, 100% data rate enhancement (using  $\gamma = 0.5$ ) can be achieved with approximately 1.5 dB power penalty in comparison to OFDM systems. While using QPSK, upto 42% data rate enhancement ( $\gamma = 0.7$ ) can be achieved with about 1 dB power penalty using ZP-TOFDM. Furthermore, for  $\gamma = 0.9$ , which is about 11% data rate improvement, no power penalty is observed in the measured BER for ZP-TOFDM compared to OFDM.

For the guard interval scheme evaluation, the error rate performance of using ZP-TOFDM systems, slightly outperforms that of using CP-TOFDM systems for most of the tested cases (different truncation factors and modulation format); while similar or same performance is achieved for the rest of the tested cases. These results agrees with the mathematical findings of the equalization expressions using ZP and CP, presented in equations 4.48 and 4.20 respectively, where using ZP in non-orthogonal signals, enhances the equalization process and hence, leads to BER performance improvements. Furthermore, the results show that using ZP in TOFDM systems has clearer enhancement in higher modulation order, such as  $\text{BER} = 10^{-4}$  in this example, and for lower error rate regions ( $\text{BER} < 10^{-5}$ ) where about 1 dB power penalty enhancement is observed in Figure 5.20(d).



**Figure 5.18:** Experimental BER performance of BPSK ZP-TOFDM with various iterations using different values of  $\gamma$



**Figure 5.19:** Experimental BER performance of QPSK ZP-TOFDM with various iterations using different values of  $\gamma$

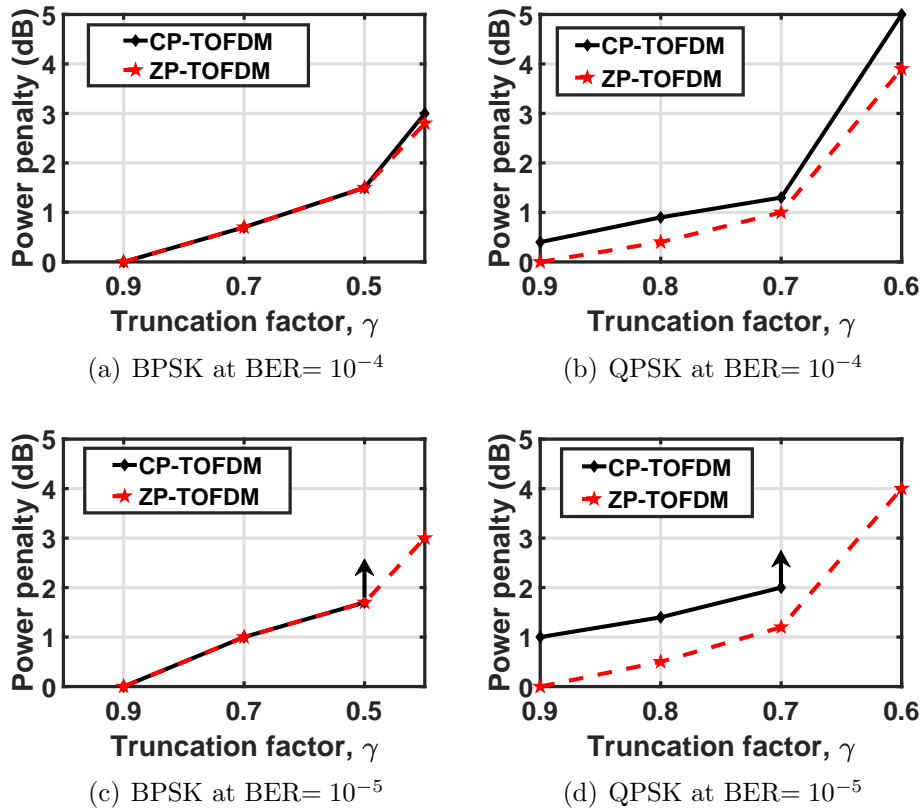


Figure 5.20: Power penalty of TOFDM systems compared to OFDM systems

## 5.6 Conclusions

This chapter introduced a new modified version of the OFDM signal by truncating the OFDM symbols in time. Where the new signal is shorter in time, hence, the width of the subcarriers in the frequency domain increases. Hence, the new signal is no longer orthogonal and thus interference is introduced among the subcarriers. Therefore, this chapter provided a study on the new non-orthogonal signal properties in frequency and time-domain. Then, the new signal characteristics were compared with other similar non-orthogonal signals and systems that aim to enhance the spectral efficiency. After that, a mathematical modelling of the signal was presented and a study and modelling of the inter carrier interference were provided.

In addition, this chapter presented design, implementation and perfor-

mance evaluation of two full TOFDM systems. The first system is the uncoded TOFDM system, which aimed to study the new TOFDM signals for different system parameters, such as oversampling and truncation factors. The second system is an enhanced 802.11g system, where TOFDM is used instead of the conventional OFDM signals and hence, the new system provides data rate improvement. Furthermore, a study on whether to use CP or ZP with the new TOFDM signal, was examined and evaluated. The performance evaluation of the new signals, were studied in computer simulation using AWGN channels and with experimental SDR testbed using USRP and channel emulator. The reported results show that TOFDM improves the data rate by sending partial symbols, yet allows detection with a small deterioration of error rates.

# Chapter 6

## Operating Interfering Wireless Networks Beyond Capacity

### 6.1 Introduction

In densely populated urban areas, wireless networks that exist in unlicensed spectrum (such as 802.11) routinely contend with vast numbers of users operating nearby, causing uncontrolled amounts of interference, with transmissions overlapping in both time and frequency. While medium access protocols can avoid some collisions, packet collisions due to hidden terminal nodes and inter-network collisions are still prevalent and harm throughput [95]. Roughly speaking, the likelihood of a bit error is positively correlated with the Signal-to-Interference-plus-Noise Ratio (SINR), measured at the receiver. The result is that in such unplanned networks, problems of interference from neighboring networks combine with the problems of range and reliability these networks already experience, resulting in degradation of application performance.

From an information-theoretic standpoint Ahlswede [96] and Liao [97] characterized the *capacity region* of the general multiple access channel, i.e., the set of tuples (each entry in the tuple containing the rate of each user) such that there exists a receiver design that achieves an arbitrarily low bit error rate provided that the users transmit at rates within that set. Figure 6.1

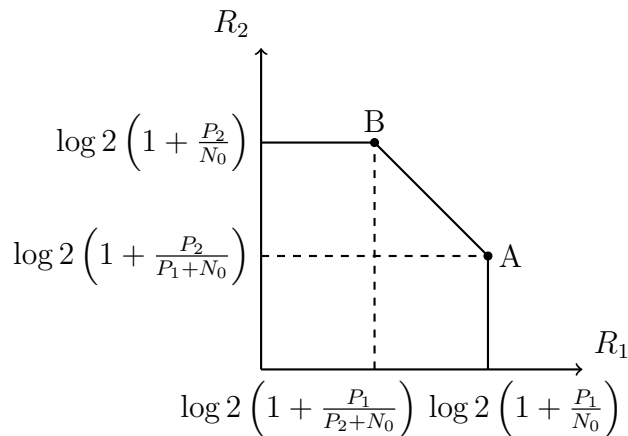


**Figure 6.1:** Capacity region of the two-user uplink Gaussian noise interference channel

shows the capacity region for the two-user uplink Gaussian noise channel [98]. This line of work proved that in such a channel, the rate of each user cannot exceed the Shannon capacity of interference-free links (leading to the constraints that  $R_{1,2} < \log(1 + P_{1,2}/N_0)$ , where  $P_{1,2}$  are the transmit powers of users one and two respectively, and  $N_0$  is the Gaussian noise power) and that the total rate cannot exceed the Shannon capacity of a Gaussian noise channel with power equal to the sum of the two users' powers.

The receiver that achieves Pareto-optimal points in the capacity region is the *successive interference cancellation* receiver [98], which achieves point A or B in the capacity region by first treating one transmission as noise while decoding the other transmission, then re-modulating and subtracting the first transmission from the received signal.

For years, work in this area took the above model—which treats every bit in two interfering transmissions equally—as the best fit to the reality of interfering data transmissions in wireless networks. Thus, this concept of capacity was treated as a given for single antenna communication and effort instead expended in other promising directions to increase capacity (such as the use of multiple antennas), which is surveyed in Section 6.2.

However, in practical unplanned wireless networks, such as 802.11 there are many opportunities for collisions both within (Figure 6.2 (A)) and be-

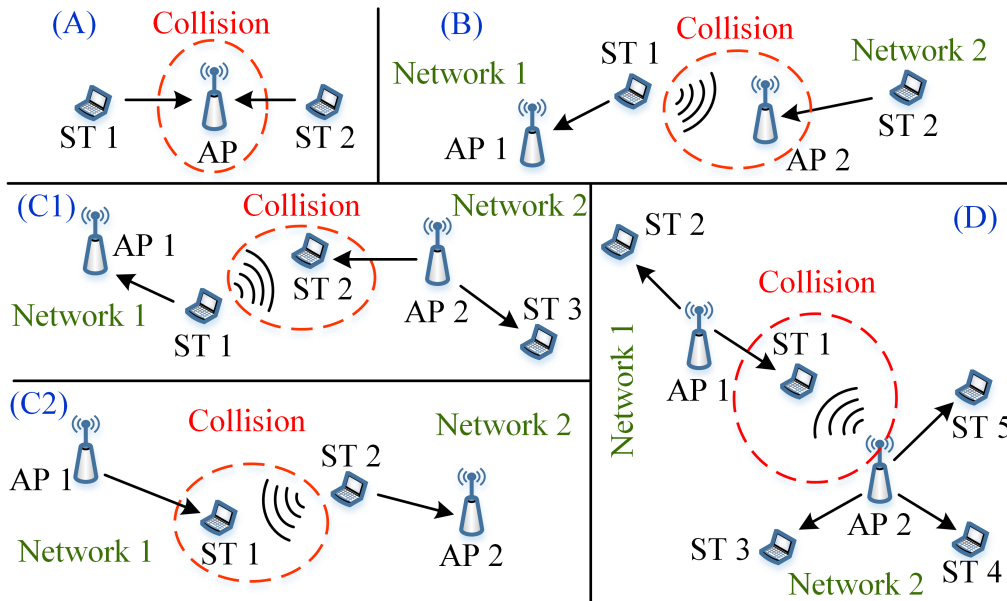


**Figure 6.2:** PSR applies to different collision scenarios. The scenario (A) is hidden terminal nodes which causes collisions within a network; the scenarios (B, C1, C2 and D) depict the inter-network collision scenarios that occur in two existing neighbouring networks. The nodes surrounded with dashed line are the nodes that experience collisions

tween (Figure 6.2 (B–D)) networks. The insight of this work begins with the observation that in a practical unplanned wireless network such as 802.11, or uncoordinated mobile cellular networks, the interference channel model is not necessarily exhaustively applicable to every bit in the colliding packets, as Figure 6.3 illustrates. From two colliding packet transmissions, it can be

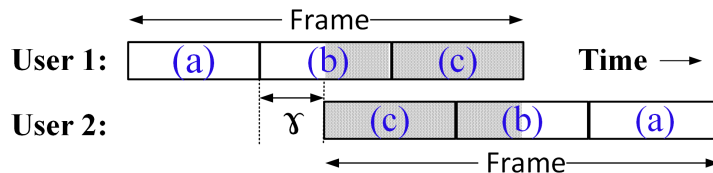


**Figure 6.3:** Stations 1 and 2 transmit concurrently, leading to a collision at a receiver. Different data symbols experience differing degrees of overlap (a)–(c)

noted that (a) a head of some data symbols “in the clear” of the collision,

(b) two partially-overlapping symbols of each colliding packet, and finally (c) the remainder of the wholly-overlapping symbols in the body of the packet overlap. Crucially, out of these three regions of packet data involved in the collision, region (c) and the collided part of region (b) are subject to the Ahlswede-Liao capacity region. Therefore, there is an opportunity to tailor a receiver to operate beyond the capacity region by utilizing the collision-free part of region (b) to fully recover region (b), then exploiting that to decode and recover region (c). Achieving this, however, requires that two challenges be overcome:

1. First, for the symbols in region (b) that are partially overlapped by interference, a decode attempt on just the interference-free region of these symbols results in interference across different OFDM subcarriers in frequency. While the SD [99, 100] can take this interference into account, it quickly becomes computationally prohibitive as the number of OFDM subcarriers increases past 20 or so, and so there is a need to develop a computationally-efficient receiver whose performance approaches that of the SD.
2. Second, channel coding is employed with the symbol-by-symbol modulation shown in Figure 6.3, and this channel coding spreads information across the symbols in time, blurring the boundaries between the three regions noted above. Thus any receiver that leverages this regions observation for increased capacity must be co-designed with the channel coding in use.

The work in this chapter presents a new technique termed PSR, a physical-layer and data link layer wireless receiver design that explicitly treats non- and partially-overlapping OFDM symbols differently from completely-overlapping OFDM symbols involved in a collision. The PSR algorithm first decodes the non-overlapping part of one user's overlapping OFDM symbol sent from one of the users, using a novel *interference modeling* step that models and cancels the intercarrier interference that results from truncation of the OFDM symbol in time. This design also applies the SD to small

blocks of OFDM subcarriers in order to precisely cancel this intercarrier interference, while relying on linear methods to cancel the interference across blocks, thus bounding the computational complexity required by SD utilization in the design. Furthermore, the design jointly integrates the functions of intercarrier interference cancellation, channel equalization, CFO and phase offset compensation, and ISI mitigation, co-designing this functionality with the remainder of the system. This functionality comprises the *inner loop decoder*, which is described fully in Section 6.5.1.1.

After using the inner loop decoder to make an estimate of the interference-free portion of an OFDM symbol, PSR remodulates the resulting bits to a full-length OFDM symbol and cancels the interference from the originally received signal, allowing it to make a decoding attempt on a complete symbol lacking interference from the other user, provided the partially-received symbol was decoded correctly: this allows for a *window* of two symbols to be decoded jointly, and another symbol from the first user to be rendered interference-free. This process continues, expanding the window until the number of bit errors falls to an error floor (determined by power and noise levels, and modulation/coding rates) that are determined empirically. The window then slides along the entire length of the collision, comprising the *outer loop decoder* of the PSR decoding algorithm. This algorithm adapts, with minor modification, to various collision patterns resulting from different lengths of colliding frames.

The outline of this chapter: The related work is discussed in Section 6.2. The physical layer frame structure specifications, which follow the standard 802.11, are detailed in Section 6.3. In Section 6.4, the self-induced interference characterization of the partial symbols is analyzed. The design of physical and data link layers are provided in Section 6.5. This is followed by Section 6.6, which presents the PSR physical layer implementation in SDR and the PSR link layer to transport layer implementation in NS-3. The PSR system evaluation of rate region comparison, frame error rate and end-to-end performance are given in Section 6.7.

## 6.2 Related Work

A prior work on exploiting packet overlaps in Partial Packet Recovery (PPR) [101] aims to recover the collision free part of colliding packets but does not attempt to recover their colliding parts, hence it requires retransmission and suffers reduced throughput. Other work for decoding collisions from hidden terminal nodes, termed Zigzag Decoding [95], requires two successive collisions of the same packets. In contrast, PSR is the first work the author is aware of, besides the classical Successive Interference Cancellation (SIC) algorithm (against which PSR is benchmarked in §6.7), that recovers full packets from a single collision and requires no retransmission to operate.

*FTN Modulation.* Most data transmission is linear: the result of summing a sequence of pulses. These pulses are almost always orthogonal (i.e., invisible) to each other, meaning that if the current symbol is viewed at a symbol duration later in time, it is zero—this is the *Nyquist criterion* [102]. If the criterion is not met, the pulses interfere, but in 1975 Mazo showed that for a simple linear modulation the data pulses could in fact be compressed in time by a multiplicative factor of 0.802 [41], a speedup of approximately 25%, without a loss in performance. Follow-on work has generalized this concept to OFDM modulation, compressing the OFDM signal in frequency [8, 54, 92] and both time and frequency [103–105]. Partial Symbol Recovery’s inner partial OFDM symbol decoder can be viewed as a type of FTN modulation that differs from previous work because of its time truncation. Partial Symbol Recovery leverages a refined version of the TOFDM decoder [20] for its inner partial OFDM symbol decoder, but builds atop TOFDM to develop the outer decoder in its entirety.

Prior work on FTN modulations largely focused on receiver methods for detection that are more computationally efficient than the SD [106], such as semidefinite programming [107] and fixed-complexity methods [108]. Other work on Shannon capacity has expanded the concept to include delay and outage probability [109], but does not address the concept of partial overlap that is exploited in this work.

Massive Multiple-In Multiple-Out (MIMO) base stations [110–114] lever-

age large numbers of antennas to increase spectral efficiency. Interference alignment [115] (IA) techniques use multiple antennas to align different interfering transmissions, and have been realized in both wireless LAN [116,117] and cellular [118] settings.

Bit rate adaptation based on acknowledgements [119,120] and SINR [121–124] and rateless codes [125–133] attempts to maximize utilization of individual links, but still does not exploit the partial overlap concept. Other influential link-centric approaches include full-duplex wireless links [134–137], which are also independent of Partial Symbol Recovery’s contribution.

## 6.3 802.11a Frame Structure and Construction

In 802.11a, the physical frames consist of three parts, preamble, signal field and data field. The first part is the preamble field, which carries well known data for all 802.11a systems that is used for carrier frequency offset estimation, time synchronisation and channel estimation. This is followed by the signal field, which is used to carry the rate and frame length information. The last part of the physical frame is the data field, which carries the message information (user data).

However, in the PSR system implementation, the frame structure consists only of the preamble and data field. This is because the rate and length of the colliding frames are predefined in the experimental testbed. Detailed description of the preamble and data field is given in the following subsections.

### 6.3.1 Preamble generation

The preamble field consists of two parts, (*i*) the Short Training Field (STF) and (*ii*) the LTF. The STF is used for coarse carrier frequency offset estimation and to find the initial time synchronisation [24][93]. On the other hand, the LTF is used for fine carrier frequency offset estimation, accurate time synchronisation and to find the channel estimate [24][93]. Figure 6.4 depicts the preamble structure.

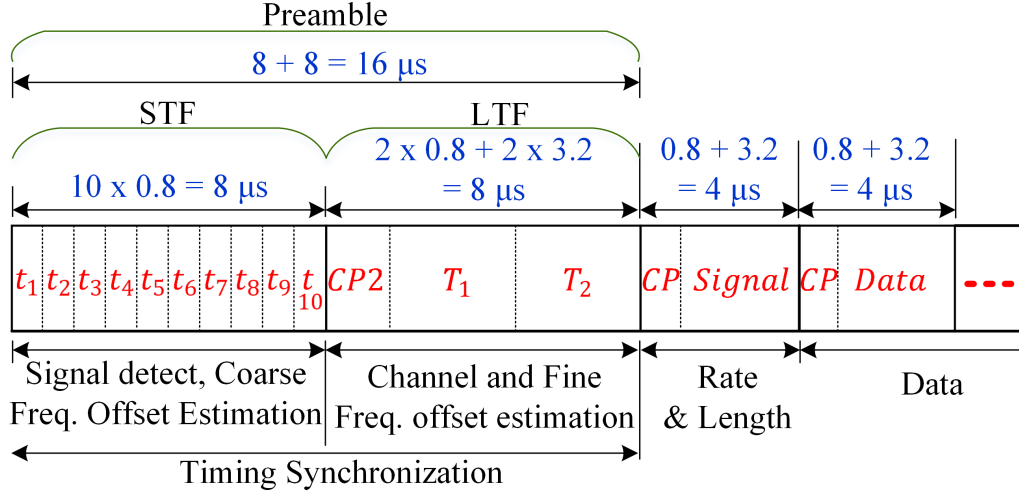


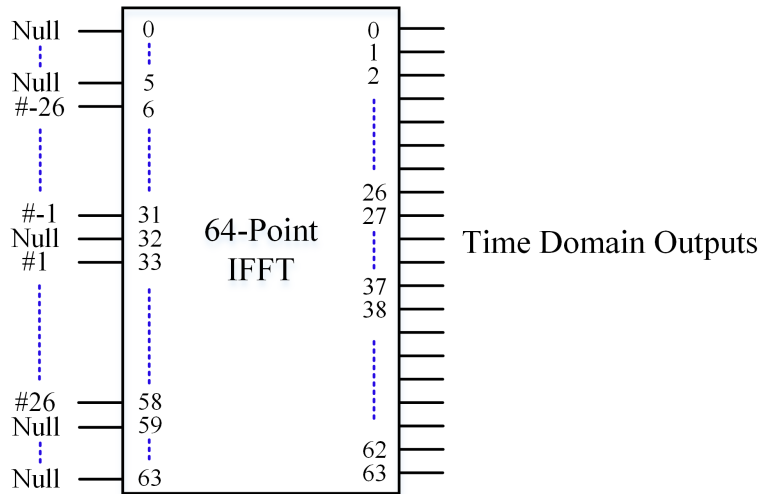
**Figure 6.4:** 802.11a Preamble followed by the signal OFDM symbol and multiple data OFDM symbols. The  $t_1, t_2, \dots, t_{10}$  denote the short training symbols, while the  $T_1$  and  $T_2$  are the long training symbols

### 6.3.1.1 Short training field

The time-domain signal of the STF is composed of ten short repeated symbols of length  $0.8 \mu\text{s}$  each, hence the STF is  $8 \mu\text{s}$  in length, as shown in Figure 6.4. In the frequency-domain, the STF is defined in the 802.11a standards [93] by a sequence given as:

$$\begin{aligned} \mathbf{S}_{STF} = \sqrt{13/6} \times \{ & 0, 0, 1 + j, 0, 0, 0, -1 - j, 0, 0, 0, 1 + j, 0, 0, 0, -1 - j, 0, 0, \\ & 0, -1 - j, 0, 0, 0, 1 + j, 0, 0, 0, 0, 0, 0, 0, -1 - j, 0, 0, 0, -1 - j, \\ & 0, 0, 0, 1 + j, 0, 0 \} \end{aligned} \quad (6.1)$$

where the multiplication with a factor of  $\sqrt{13/6}$  is to normalize the power of the generated OFDM symbol. The sequence is padded with zeros to length 64 and then fed into a 64-point IFFT. Figure 6.5 shows the location of the frequency-domain sequence to the input of the IFFT, where the input subcarriers locations are the numbers  $[-26, -25, \dots, -1, 0, 1, \dots, 26]$ . The OFDM symbol utilizes 12 subcarriers out of 52 active subcarriers. The resulting time-domain OFDM symbol at the output of the IFFT is shown in



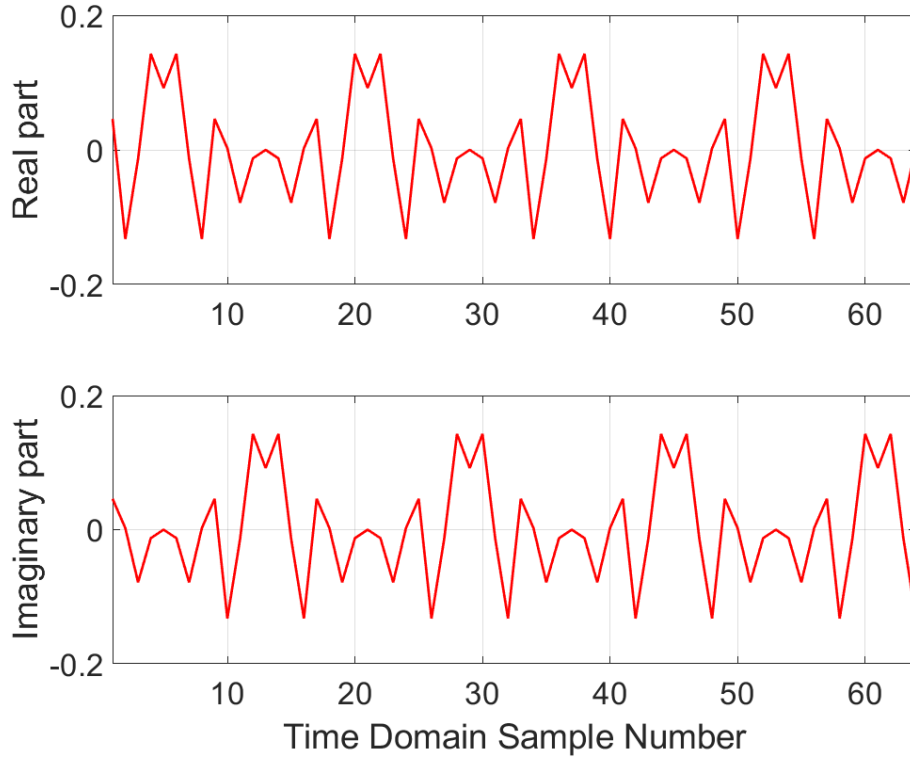
**Figure 6.5:** Inputs and outputs of the IFFT at the transmitter

Figure 6.6.

In this system design, the sampling rate is chosen equal to 20 Msamples/second, hence each OFDM symbol has duration of  $3.2 \mu s$ . The OFDM symbol has a pattern that repeats four times ( $0.8 \mu s$  periodicity), as shown in Figure 6.6. Where the STF is  $8 \mu s$  in length, therefore, the OFDM symbol is repeated two and a half times to generate the STF signal in the time-domain.

Figure 6.7 depicts the cross correlation between the STF and a short training symbol. It is clear that the STF sequence has good correlation properties, where the separation between the correlation peaks and its side-lobes is approximately 10 dB [24]. In addition, the sequence was chosen to have a low PAPR, hence, its properties are not harmed by an overloaded analogue front end [24].

The STF sequence may be used in various services, firstly, its correlation peaks can be used for initial time estimate in the time-domain [24][93]. Second, it may be used to indicate a frame detection, whereby the resulting correlation peak of the correlation between a received short symbol and a previous symbol, in the STF, is higher than a threshold [93]. Third, it may be used for automatic gain control (AGC) [93]. Finally, the STF is used for initial carrier frequency offset estimation, where the phase difference between



**Figure 6.6:** Constructing short training field in time-domain

two samples in two sequential short symbols in STF (separated by  $0.8 \mu s$ ), can be used to find the frequency offset. This allows a carrier frequency offset estimate of up to  $\pm 1/0.8 \mu s/2 = \pm 625$  KHz [24].

### 6.3.1.2 Long training field

The LTF is  $8 \mu s$  in length. In the time-domain, the LTF is composed of  $1.6 \mu s$  cyclic prefix followed by two repeated  $3.2 \mu s$  OFDM symbol. The cyclic prefix in the LTF is generated by copying the second half of the OFDM symbol and attach it to the beginning of the two repeated OFDM symbols. The long OFDM training symbol is generated using a 64-point IFFT. The frequency-domain input sequence to the IFFT is defined in 802.11a standard

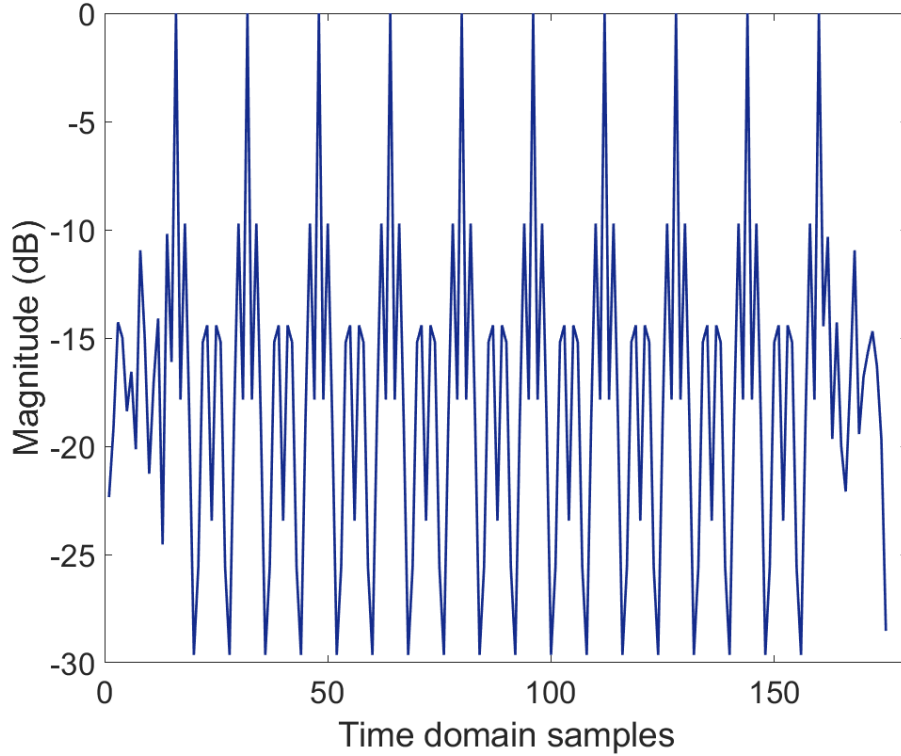


**Figure 6.7:** Correlation of a short symbol with the short training field sequence

as:

$$\begin{aligned} \mathbf{S}_{LTF} = \{ & 1, 1, -1, -1, 1, 1, -1, 1, -1, 1, 1, 1, 1, 1, 1, -1, -1, 1, 1, -1, 1, -1, 1, 1, 1, \\ & 1, 0, 1, -1, -1, 1, 1, -1, 1, -1, 1, -1, -1, -1, -1, -1, 1, 1, -1, -1, 1, -1, 1, \\ & -1, 1, 1, 1, 1 \} \end{aligned} \quad (6.2)$$

where the sequence consists of 52 subcarriers carrying either  $-1$  or  $1$ , and the  $0$  in the middle refers to the subcarrier at DC. The numbering of the active subcarrier locations to the input of the IFFT is  $[-26, -25, \dots, -1, 0, 1, \dots, 26]$  (see Figure 6.5).

Figure 6.8 illustrates the cross correlation between the preamble and a long training OFDM symbol, with a sampling rate of 20 Msamples/s. The resulting peaks after the correlation process may be used to find a more

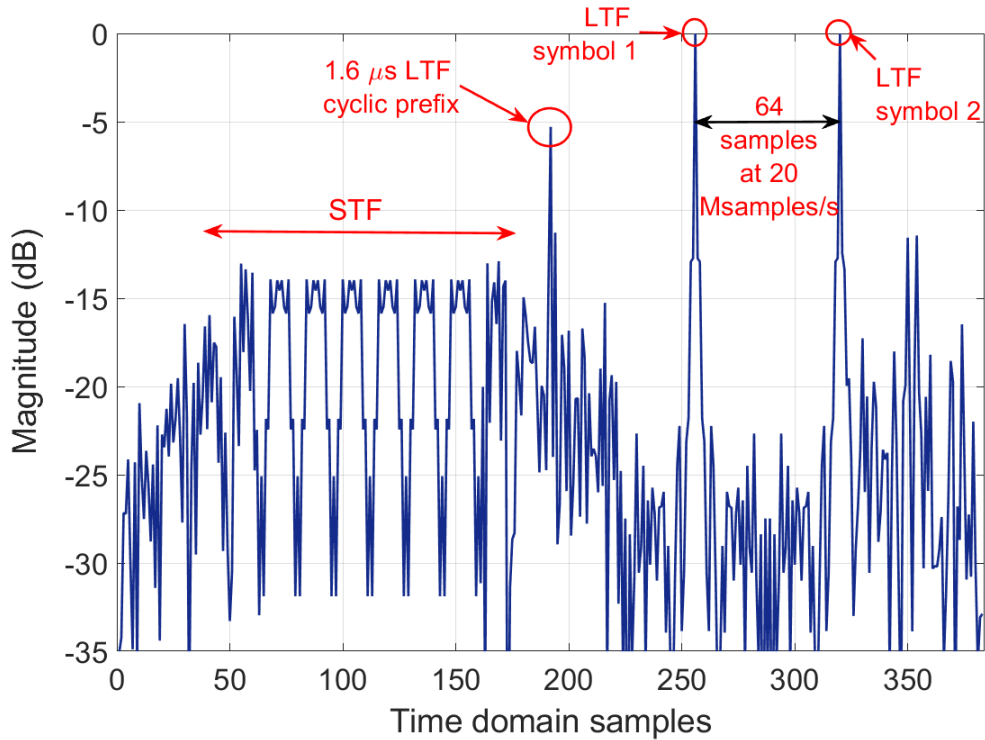


**Figure 6.8:** Correlation of a long symbol with the preamble

accurate starting time estimate [24]. In LTF, any two repeated samples in time are separated by  $3.2 \mu s$ , which is higher than the time separation of STF ( $0.8 \mu s$ ) [24]. Therefore, the difference in phase between these two samples leads to more accurate estimation of frequency offset. The frequency offset is estimated up to  $\pm 1/3.2 \mu s/2 = \pm 156.25$  KHz [24]. In addition, the LTF is used for channel estimation.

### 6.3.2 Data field

In this section, the processes of generating the data field from the bits level to the modulated OFDM symbols are detailed. The data field is composed of service, message bits, tail bits and padded bits (if needed as described in the next subsections). The data field transmitter is shown in Figure 6.9.

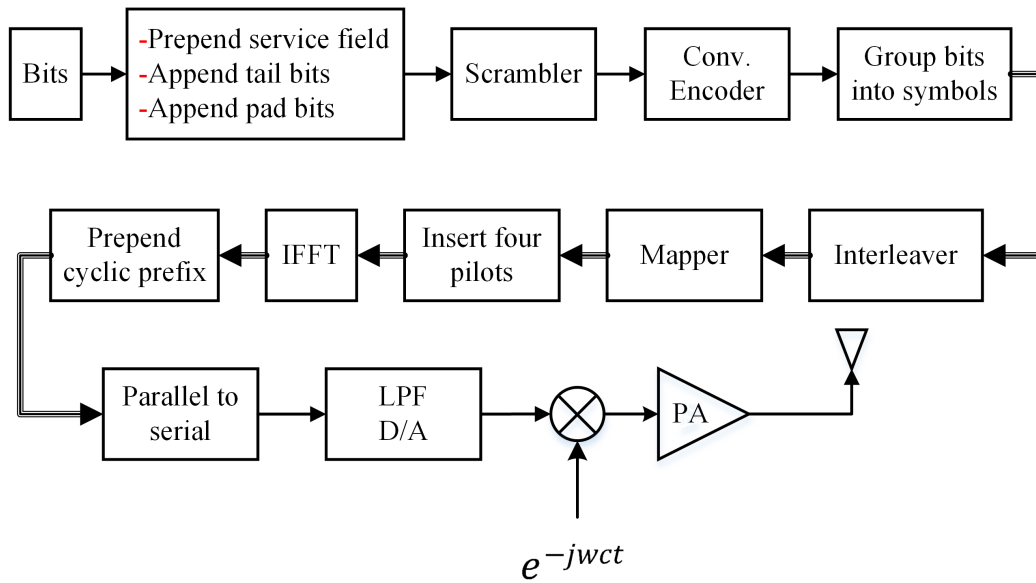


Figure 6.9: Block diagram of the 802.11a transmitter

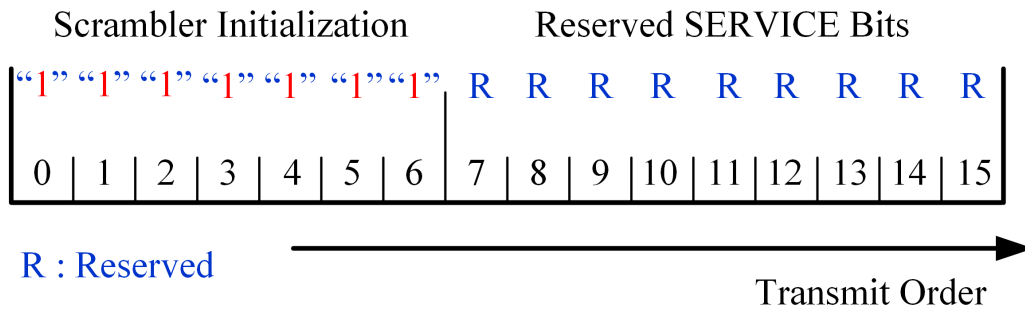


Figure 6.10: Bits assignment of the SERVICE field

### 6.3.2.1 Service field

The service field has 16 bits, where the bits 0-6 are used to carry the initial state of the scrambler, the rest of the bits are reserved for future services. All the reserved bits are set to zeros. Figure 6.10 shows the service field bits as given in IEEE 802.11a standard [93].

### 6.3.2.2 Tail bits

The tail bits are six zeros attached to the end of the data field. The purpose of these bits is to allow the convolutional encoder to rest its value to the zero state. After the scrambling process, these six zero bits becomes non-zero bits, hence, the scrambled bits are replaced with six zero bits.

### 6.3.2.3 Pad bits

The number of bits in the data field must be multiple the number of coded bit in an OFDM symbol ( $N_{CBPS}$ ). Therefore, the message bits are extended to be multiple the number of data bits in an OFDM symbol ( $N_{DBPS}$ ). The number of zero padded bits,  $N_{pad}$ , are calculated from the message length,  $M_{length}$ , as following. Firstly, the highest number of OFDM symbol can be created using the message data is found as [93]:

$$N_{sym} = \lceil (16 + 8 \times M_{length} + 6) / N_{DBPS} \rceil \quad (6.3)$$

where  $M_{length}$  is measured in octet and the  $\lceil * \rceil$  is the ceiling function that finds the nearest integer value which is greater than the given value. Second, the number of the data bits that needed to create the  $N_{sym}$  OFDM symbols is given as [93]:

$$N_{data} = N_{sym} \times N_{DBPS} \quad (6.4)$$

After that, the number of zero padded bits is given as [93]:

$$N_{pad} = N_{data} - (16 + 8 \times M_{length} + 6) \quad (6.5)$$

These bits are passed with the service, message and tail bits into the scrambling process.

### 6.3.2.4 Scrambler

The data field is passed to a length-127-frame-synchronous scrambler [93]. The scrambler block diagram is illustrated in Figure 6.11 and its polynomial

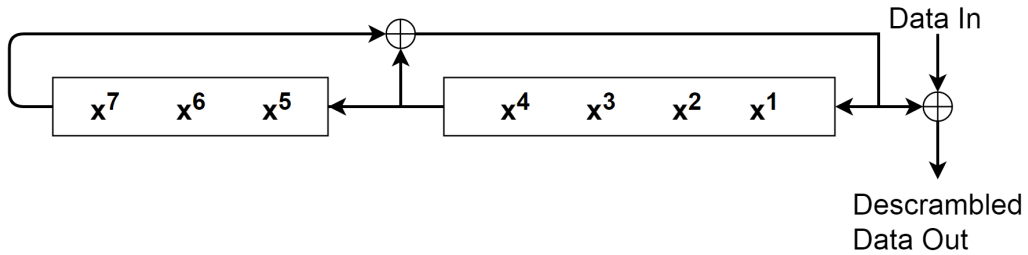


**Figure 6.11:** Data field scrambler and descrambler

is given as [93]:

$$G_{scr}(x) = x^7 + x^4 + 1 \quad (6.6)$$

This polynomial generates a repeatedly sequence of 127 bits length. In the case of the initial state is set to all ones, the resulting output is the following sequence that is given as: 00001110 11110010 11001001 00000010 00100110 00101110 10110110 00001100 11010100 11100111 10110100 00101010 11111010 01010001 10111000 11111111. In practice, the initial state of the scrambler is a pseudo random non-zero bits, which is used at the transmitter to scramble the data and at the receiver to descramble the received data. As mentioned in Section 6.3.2.1, the scrambler initial state is sent to the receiver in the service field symbol.

### 6.3.2.5 Convolutional encoder

After the data field bits is being scrambled, the bits are encoded using convolutional encoder with code rate  $R_c = 1/2$ , constraint length equal to 7 and using the industry-standard generator polynomials,  $g_0 = 133_8$  and  $g_1 = 171_8$  as shown in Figure 6.12 [93].

### 6.3.2.6 Data interleaver

The coded data bits are grouped with  $N_{CBPS}$  bits in each group and passed to the interleaving process (see Figure 6.9). The interleaver has two stage permutations, the first permutation is to ensure that all the adjacent coded bits are mapped onto non-adjacent subcarriers in an OFDM symbol. This to reduce the effect of the frequency selective channel. The purpose of the

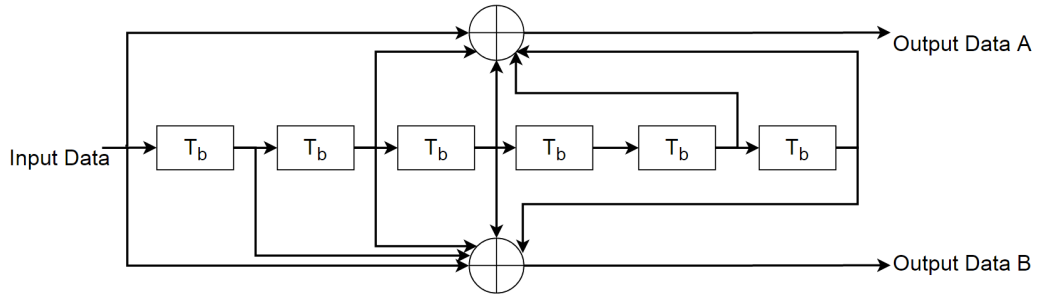


**Figure 6.12:** IEEE 802.11a convolutional encoder.  $T_b$  is the bit duration

second permutation is ensure that the bits mapping of adjacent coded bits are distributed over less and more significant bits of the constellation mapping. This avoids the long string of bits are mapped onto low reliability bits (the low significant bits) of the constellation.

The first permutation of the interleaver is defined by [93]:

$$l = (N_{CBPS}/16)(k \bmod 16) + \lfloor k/16 \rfloor, \quad k = 0, 1, \dots, N_{CBPS} - 1 \quad (6.7)$$

where  $l = [0, 1, \dots, N_{CBPS} - 1]$  is the bits index after the first permutation,  $k$  is the bits index before the first permutation,  $\lfloor * \rfloor$  is the floor function, which returns the nearest integer number less than the argument value and  $\bmod$  is the modulo function.

The second permutation is defined by [93]:

$$m = c \times \lfloor l/c \rfloor + (l + N_{CBPS} - \lfloor 16 \times l/N_{CBPS} \rfloor) \bmod c \quad (6.8)$$

The value of  $c$  is determined according to the value of  $N_{CBPS}$  as:

$$c = \lceil N_{CBPS}/2 \rceil \quad (6.9)$$

### 6.3.2.7 Subcarriers modulation mapping

The encoded and interleaved data bits are mapped using BPSK and QPSK. The data mapping is performed using Gray-coded constellation mapping, which is illustrated in Figure 6.13.

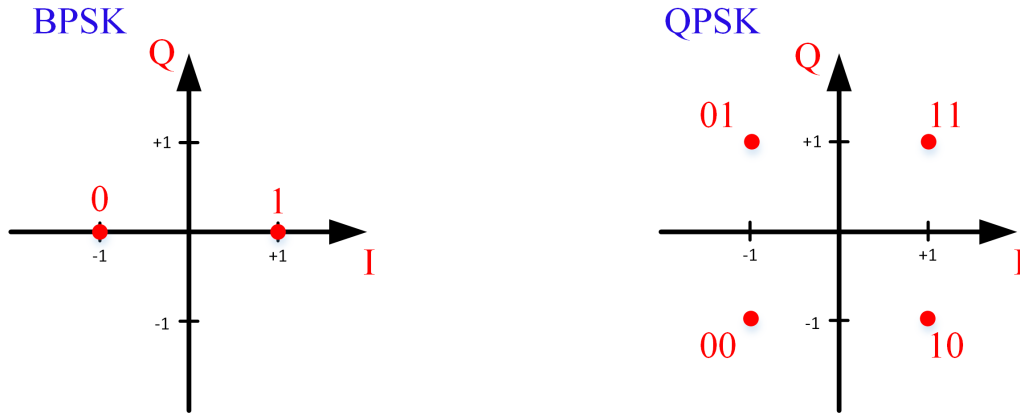


Figure 6.13: BPSK and QPSK constellation bit mapping

### 6.3.2.8 Pilot subcarriers

In each OFDM symbol, four subcarriers out of the 52 subcarriers are used to carry pilot signals. This allows the receiver to robust the residual frequency offset and phase offset after frequency offset correction. The pilot signals are located on subcarriers -21, -7, 7 and 21 to the input of IFFT (see Figure 6.5). The pilot subcarriers elements are generated by performing cyclic extension to the following 127 elements sequence that is given by [93]:

$$\begin{aligned}
 \mathbf{s}_{pilot} = \{ & 1, 1, 1, 1, \quad -1, -1, -1, 1, \quad -1, -1, -1, -1, \quad 1, 1, -1, 1, \quad -1, -1, 1, 1, \\
 & -1, 1, 1, -1, \quad 1, 1, -1, 1, \quad 1, -1, -1, 1, \quad 1, 1, -1, 1, \quad -1, -1, -1, 1, \\
 & -1, 1, -1, -1, \quad 1, -1, -1, 1, \quad 1, 1, 1, 1, \quad -1, -1, 1, 1, \quad -1, -1, 1, -1, \\
 & 1, -1, 1, 1, \quad -1, -1, -1, 1, \quad 1, -1, -1, -1, \quad -1, 1, -1, -1, \quad 1, -1, 1, 1, \\
 & 1, 1, -1, 1, \quad -1, 1, -1, 1, \quad -1, -1, -1, -1, \quad -1, 1, -1, 1, \quad 1, -1, 1, -1, \\
 & 1, 1, 1, -1, \quad -1, 1, -1, -1, \quad -1, 1, 1, 1, \quad -1, -1, -1, -1, \quad -1, -1, -1 \}
 \end{aligned}
 \tag{6.10}$$

Each four bits are used in an OFDM symbol. The sequence can be generated using the scrambling function illustrated in Figure 6.11 when the initial state is set to all ones, and after replacing all the "1" values with "-1" and the "0" values with "1".

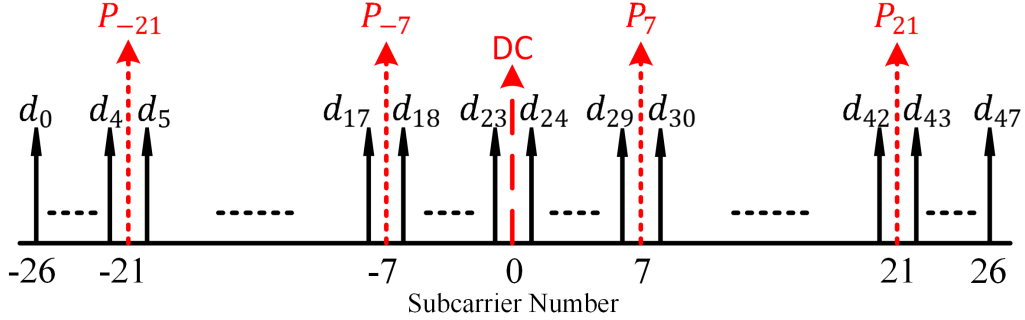


**Figure 6.14:** Subcarrier frequency location to the input of IFFT

### 6.3.2.9 OFDM modulation

The serial complex data stream is passed into serial to parallel function of size  $N = 48$ , which is the number of data subcarriers at the input of IFFT. The data subcarriers ( $d$ ), pilot subcarriers ( $s_{pilot}$ ) and the zero DC locations are illustrated in Figure 6.14, these are padded with zeros to length  $Q = 64$  and fed into the IFFT. Hence, The input data symbols that are fed into the OFDM modulation process are given as:

$$s_n = \begin{cases} 0, & 0 \leq n < 5 \ \& \ 59 \leq n < 63 \ \& \ n = 32 \\ s_{pilot}, & n = [11, 25, 39, 53] \\ d, & elsewhere \end{cases} \quad (6.11)$$

The continuous time-domain OFDM signal,  $x(t)$ , consisting of  $m$  OFDM symbols, is represented as:

$$x(t) = \frac{1}{\sqrt{T}} \sum_{m=-\infty}^{\infty} \sum_{n=0}^{Q-1} s_{m,n} \exp \left[ \frac{j2\pi n(t - mT)}{T} \right] \quad (6.12)$$

where  $T = 3.2$  is the period of an OFDM symbol,  $s_{m,n}$  is the complex symbol modulated on the  $n^{th}$  subcarrier belonging to the  $m^{th}$  OFDM symbol. In discrete time-domain, an OFDM symbol can be represented as follows:

$$x(k) = \frac{1}{\sqrt{Q}} \sum_{n=0}^{Q-1} s_n \exp \left[ \frac{j2\pi nk}{Q} \right] \quad (6.13)$$

The discrete OFDM symbol may be represented in matrix form as:

$$X = \mathbf{F}S \quad (6.14)$$

where  $X$  is the  $Q$ -dimensional vector of a sampled OFDM symbol in the time-domain,  $\mathbf{F}$  is the sampled IFFT matrix of size  $Q \times Q$ .

### 6.3.2.10 Cyclic prefix

Using a sampling rate at 20 Msamples/s, the last 16 samples in time-domain (CP part) are copied and added to the beginning of each OFDM symbol. This CP part acts as a guard interval between consecutive OFDM symbols in order to eliminate or alleviate the effect of ISI.

In the final stage of the transmitter, the complete physical frame is filtered then passed into digital-to-analogue converter before the up-conversion stage, which is running by a local oscillator at 5 GHz. The signal generation is depicted in Figure 6.9.

### 6.3.2.11 802.11a receiver

In general, the 802.11a receiver decodes the collision-free received frames and retrieve their data. However, when collisions are present, the 802.11a receivers fail to recover the data and hence frame re-transmission is required. The rest of this chapter focuses on the design and evaluation of a new 802.11 receiver that specifically targets the parts of data symbols that experience no interference during a frame collision.

## 6.4 Partial Symbol Overlap

In this section, the predictable interference characterization between OFDM subcarriers that occurs when the receiver observes just the beginning fraction  $\gamma$  of an OFDM symbol, in time. This *partial symbol* can be analyzed by the IFFT as:

$$x_{\text{partial}}(m) = \frac{1}{\sqrt{\gamma Q}} \sum_{l=0}^{Q-1} d_l \exp\left(\frac{j2\pi lm}{Q}\right) \quad (6.15)$$

where  $m = [0, 1, \dots, \gamma Q - 1]$  is the index of the time samples and  $l$  is the subcarrier index;  $d_l$  is the complex input data;  $Q$  is the size of the IFFT, used to generate the signal;  $\gamma Q$  is the number of time samples in a partial symbol, where  $\gamma \leq 1$  is the fractional symbol proportion observed. In an OFDM, each time sample is observed as a summation of sampled input symbols, each modulated on an individual complex subcarrier. This observation is significant because a symbol may be decoded even when only a fraction of its time samples has been received [20].

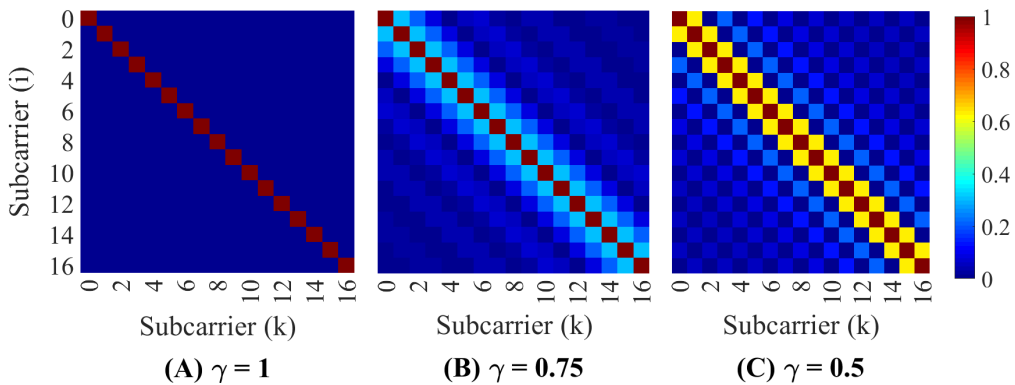


**Figure 6.15:** Heatmap of the covariance matrix that depicts the interference between neighboring subcarriers. (A) is for orthogonal symbols; (B) and (C) are for partial symbols with  $\gamma = 0.75$  and  $0.5$ , respectively

Orthogonality in time and frequency in OFDM (i.e.  $T = 1/\Delta f$ , where  $T$  is the symbol period and  $\Delta f$  is the subcarrier separation), is a crucial factor in its successful operation. However, should this condition be violated, i.e. the observed symbol period  $< T$ , orthogonality is violated and ICI is introduced. The analytical description of the self-induced ICI of the partial symbols, is given by the covariance matrix ( $\mathbf{\Gamma}$ ), which quantifies the interference contribution on each subcarrier from its neighboring subcarriers [20]. To visualize the effect of ICI on the received partial symbols, Figure 6.15 (A) shows that all the subcarriers are orthogonal with zero ICI while (B) and (C) in the same figure show that the ICI caused on a desired subcarrier (on the main diagonal) stems from the neighboring subcarriers (on the secondary diagonals) when  $\gamma$  is smaller than 1.

The covariance matrix components can be found as:

$$\begin{aligned}
 \mathbf{\Gamma}_{(l,n)} &= \mathbf{F}_{(l,m)}^H \mathbf{F}_{(m,n)} \\
 &= \frac{1}{\gamma Q} \sum_{m=0}^{\gamma Q-1} \exp \left[ \frac{-j2\pi lm}{Q} \right] \exp \left[ \frac{j2\pi mn}{Q} \right] \\
 &= \begin{cases} 1, & l = n \\ \frac{1}{\gamma Q} \left[ \frac{1 - \exp[-j2\pi(l-n)\gamma]}{1 - \exp\left[\frac{-j2\pi(l-n)}{Q}\right]} \right], & l \neq n \end{cases} \quad (6.16)
 \end{aligned}$$

where  $\mathbf{\Gamma} \in \mathbb{C}^{Q \times Q}$  is the covariance matrix,  $(\cdot)^H$  is the transpose conjugate operation. The final derivation in (6.16) is based on the sum of geometric series:  $\sum_{k=0}^{Q-1} r^k = \frac{1-r^Q}{1-r}$ . From (6.16), it should be noted that the covariance matrix coefficients change according to the duration of the partial symbol, which is identified by the  $\gamma$  factor.

## 6.5 Design

PSR is implemented jointly in the physical and data link layers. In this section, the physical layer (L1) design of PSR is discussed in Section 6.5.1; the data link layer (L2) design is described in Section 6.5.2, and Section 6.5.3 addresses experimental design considerations for key system parameters.

### 6.5.1 Physical layer design

PSR uses the 802.11a standard for preamble and data generation in the physical frame. The modifications to the current existing physical layer involve adding the PSR decoder design and a triggering mechanism to a current 802.11 receiver. The PSR decoder is a nested-loop decoder, consisting of (i) an *inner loop decoder* and (ii) an *outer loop decoder*. The inner loop decoder is designed to decode a partial symbol and recover its full symbol as explained next in Section 6.5.1.1. The outer loop decoder is designed to cancel users interference, and to constrain error propagation between symbols in a user frame. Its design is detailed in Section 6.5.1.2.

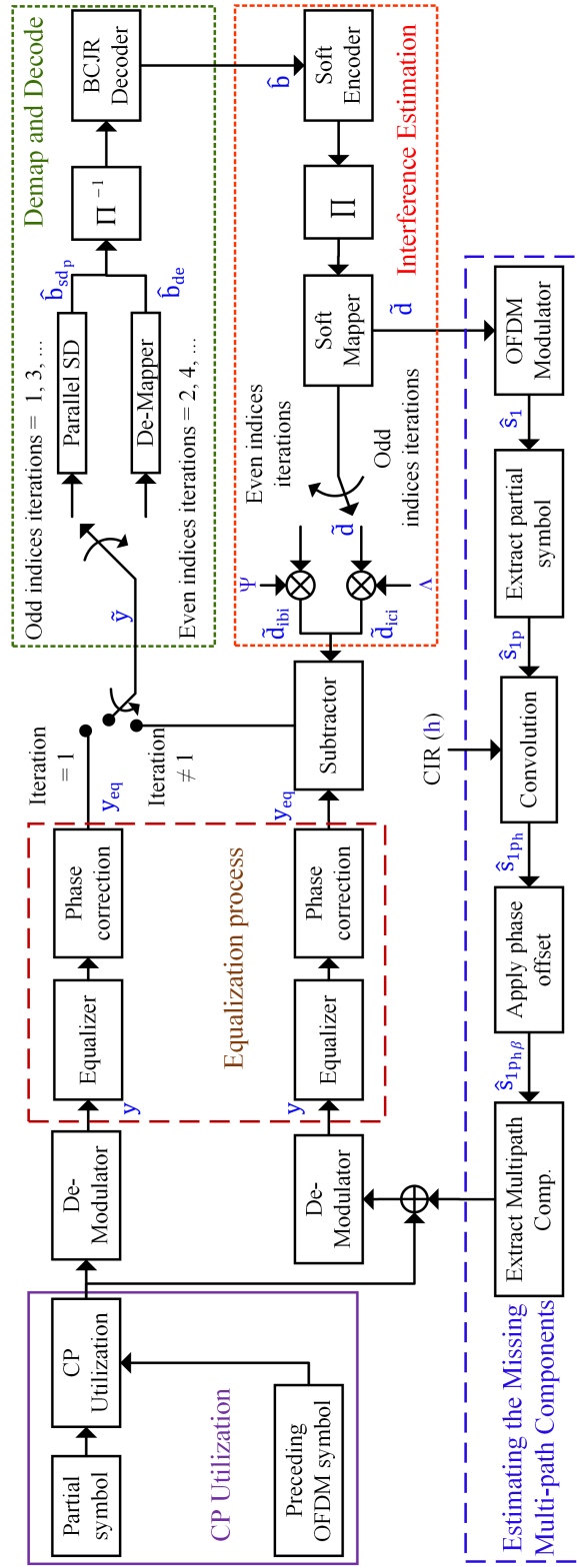


**Figure 6.16:** The inner loop decoder: Eliminates ISI and uses information in the CP then: equalizes and phase corrects; recovers the bits from partial symbols; re-encodes the symbols to estimate and subtract the self-induced inter-carrier interference of the original signal before being passed to the next iteration

### 6.5.1.1 Inner loop decoder

The inner loop decoder is divided into two steps; (i) ISI cancellation and CP part utilization; and (ii) joint iterative decoder. Figure 6.16 depicts the entire decoding processes of the inner loop decoder.

**6.5.1.1.1 ISI cancellation and CP part utilization.** In the 802.11a frame, each OFDM symbol starts with a CP, which is generated by copying the last  $\mu$  samples of a symbol to the start of the symbol (see Figure 6.17), and is used to mitigate the ISI stemming from the prior OFDM symbol and reduce sensitivity to symbol timing estimation error. Hence, in conventional 802.11a systems, the CP is discarded at the receiver because it is distorted with ISI and carries redundant data.

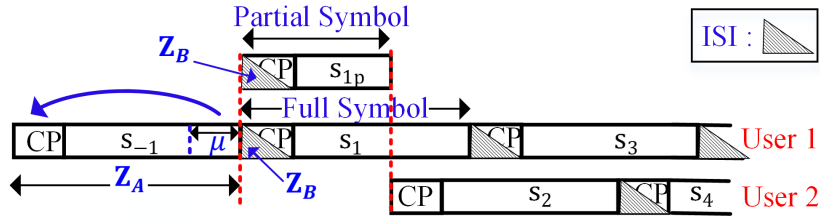


**Figure 6.17:** A partial and full symbol in received colliding frames. The partial symbol,  $\mathbf{s}_{1p}$ , consists of a CP and a part of a symbol. Symbols with odd indices belong to user 1 and the symbols with even indices belong to user 2. Each CP is contaminated with ISI

In the PSR receiver, each collision-free partial symbol consists of a CP portion and a part of the OFDM symbol, as shown in Figure 6.17. When the tail of the symbol is overlapped by the other user, as in  $\mathbf{s}_{1p}$ , the receiver uses the CP in the decoding process to compensate for the portion lost due to the collision. However, the CP in the partial symbol ( $\mathbf{s}_{1p} \in \mathbb{C}^{(\gamma Q) \times 1}$ ) is contaminated with ISI coming from the preceding symbol ( $\hat{\mathbf{s}}_{-1} \in \mathbb{C}^{Q \times 1}$ ), hence, the ISI is estimated and subtract it from the partial symbol. This is achieved by convolving the Channel Impulse Response (CIR),  $\mathbf{h} \in \mathbb{C}^{(\mu+1) \times 1}$ ,

with  $\hat{\mathbf{s}}_{-1}$ , as:

$$\mathbf{z}_{-1} = \mathbf{h} * \hat{\mathbf{s}}_{-1} = \begin{cases} \mathbf{z}_{\mathbf{A}}, & 1 \leq k \leq Q \\ \mathbf{z}_{\mathbf{B}}, & Q + 1 \leq k \leq Q + \mu \end{cases} \quad (6.17)$$

where  $\mathbf{z}_{-1} \in \mathbb{C}^{(Q+\mu) \times 1}$  is the symbol after the convolution process, and  $(*)$  is the convolution process. The  $\mathbf{z}_{\mathbf{A}}$  part is the preceding symbol after traversing the multipath channel, and the  $\mathbf{z}_{\mathbf{B}}$  part is the ISI components, as shown in Figure 6.17. Next, the ISI ( $\mathbf{z}_{\mathbf{B}}$ ) is subtracted from the partial symbol,  $\mathbf{s}_{1\mathbf{p}}$  before being passed to the joint iterative decoder.

**6.5.1.1.2 Joint iterative decoder.** The received partial symbols suffer from (i) multipath effects from the wireless channel; (ii) phase offsets; and (iii) the self-induced ICI between the subcarriers, which is created when the tail part is lost in the overlap with the other user. The receiver is designed to jointly equalize channel effects and the phase offset, and then to cancel the self-induced ICI, thus recovering the overall data from the partially received symbols.

**Partial symbol equalization and phase compensation.** The self-induced interference between the partial symbol subcarriers is combined with the multipath effects and the phase offset. Therefore, partial symbol equalization and phase compensation become more challenging. To illustrate, Figure 6.18 depicts a comparison a received partial symbol with what such symbol would "hypothetically" be after traversing a multipath wireless channel. The missing multipath components, in received partial symbols, result in increased interference levels and consequently inaccurate equalization and phase correction. Dealing with this problem requires the estimation of the missing multipath components and then adding the estimates to the partial symbols (the dashed-blue line box of Figure 6.16 depicts the processes). The process requires knowledge of two key parameters; namely the CIR and phase offset, the estimation of these is detailed in Section 6.5.3.5. Two stages are required, firstly, the recovered partial symbol 1,  $\hat{\mathbf{s}}_{1\mathbf{p}}$ , at the end of every

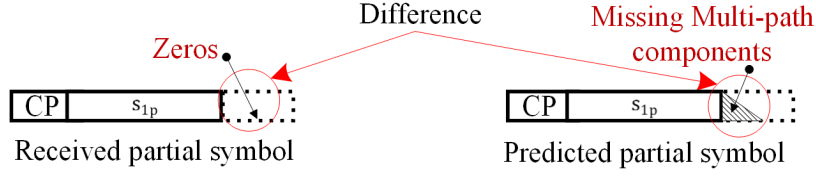


**Figure 6.18:** A truncated partial symbol lacks certain multipath components. The triangle depicts these estimated, missing multipath components

iteration is convolved with the CIR:

$$\hat{\mathbf{s}}_{1\mathbf{p}_h} = \mathbf{h} * \hat{\mathbf{s}}_{1\mathbf{p}} \quad (6.18)$$

where  $\hat{\mathbf{s}}_{1\mathbf{p}_h}$  is the estimated partial symbol 1 with channel effects. Secondly, the effects of the phase offset is added to the resulting signal from the first step:

$$\hat{\mathbf{s}}_{1\mathbf{p}_h\beta} = \hat{\mathbf{s}}_{1\mathbf{p}_h} \cdot e^{-j\beta_1}, \quad (6.19)$$

where  $\hat{\mathbf{s}}_{1\mathbf{p}_h\beta}$  is the estimated partial symbol 1 after applying phase offset ( $\beta_1$ ). The last  $\mu$  samples of the resulting signal represent the required multipath components, which are added to the partial symbol before being passed to the next iteration. Finally, the partial symbol is passed to the equalization and phase compensation processes of the next iteration (the dashed-brown part of Figure 6.16 depicts the processes). Repetition of this process during the joint channel equalization, phase compensation and decoding iterations, leads to a better estimate of the missing multipath components and hence, improves the equalization and phase compensation.

**The self-induced interference cancellation mechanism.** As mentioned earlier in Section 6.4, that the self-created interference between sub-carriers is characterized and modelled in the covariance matrix,  $\mathbf{\Gamma}$ . This covariance matrix is used in a SD [138] [139], to retrieve the data of a partial symbol. The SD mathematical representation is given as:

$$\hat{\mathbf{b}}_{\text{sd}} = \arg \min_{\mathbf{d} \in M^N, \|\tilde{\mathbf{y}} - \mathbf{\Gamma}\mathbf{d}\|^2 \leq g} \|\tilde{\mathbf{y}} - \mathbf{\Gamma}\mathbf{d}\|^2 \quad (6.20)$$

where  $\hat{\mathbf{b}}_{\text{sd}} \in \mathbb{C}^{Q \times 1}$  is the estimated data bits vector in the partial symbol,  $M^N$  is the number of all possible signal combinations in a symbol,  $M$  is the cardinality of the constellation diagram,  $N$  is the number of subcarriers and  $g$  is the radius of the hypersphere search area that is centered at  $\tilde{\mathbf{y}} \in \mathbb{C}^{Q \times 1}$  which is the demodulated partial symbol after equalization and phase compensation,  $\mathbf{d} \in \mathbb{C}^{Q \times 1}$  is the complex input data vector that has the highest probability of being transmitted. The latter is found by finding the minimum Euclidean distance from all the possible vector combinations which take place inside the multi-dimensional hypersphere searching area. This results in data recovery of the partial symbol.

It should be noted that using a single SD, to recover the data in all subcarriers, leads to high computational complexity, hence, the method of [140] is adapted, in which the subcarriers are divided into sets of blocks, each is operated on by a smaller SD. For 802.11a signals, there is a natural division into such blocks and separation of these (5 blocks) by the four pilot subcarriers, which are placed between the data subcarriers (see Figure 6.14) [93]. Thus, the interference of the known pilot tones onto subcarrier blocks is measured and cancelled by subtraction from each subset at the receiver.

Nevertheless, the interference from subcarriers in one block to adjacent blocks, Inter-Block Interference (IBI), has also to be considered. Therefore, in this design, the iterations with odd indices eliminate ICI within a block of subcarriers, steps **(A)** and **(B)** of this section; while the iterations with even indices eliminate the IBI among the blocks, steps **(C)** and **(D)**. Furthermore, the interference cancellation mechanism in a single iteration is divided into two main steps, first, demap and decode the partial symbol to recover its data in soft form, as described in steps **(A)** and **(C)** (the dashed-green line box of Figure 6.16). Second, estimate and subtract the interference in the partial symbol, which is given in steps **(B)** and **(D)** (the dotted-red line box of Figure 6.16).

**(A) Step one of the odd indices iterations.** In order to recover the data in each block of subcarriers, the covariance matrix of each block is used in a small-size SD set following equation (6.20). The output of the small-size SD set ( $\hat{\mathbf{b}}_{\text{sd}_p}$ ) is given as LLR values, where the sign of LLR values indicates

the sign of the bits and its magnitude determines the reliability of the bits. After that, the output of all the subcarriers is de-interleaved and decoded using soft-output BCJR decoder [94] (see Figure 6.16).

**(B) Step two of the odd indices iterations.** The soft-output bits ( $\hat{\mathbf{b}}$ ) are encoded using soft-encoder where its output bits are interleaved and mapped ( $\tilde{\mathbf{d}}$ ). Then, the ICI in each block ( $\tilde{\mathbf{d}}_{\text{ici}}$ ) is estimated and subtracted. Where the covariance matrix characterizes the data and the ICI in the partial symbols, hence, it can be decomposed into two matrices as:

$$\mathbf{\Gamma} = \mathbf{I} + \mathbf{\Lambda} \quad (6.21)$$

where  $\mathbf{I}$  is an identity matrix that represents the data coefficients matrix and the  $\mathbf{\Lambda}$  is the ICI coefficients matrix of each block. Now, using  $\tilde{\mathbf{d}}$ , and the self-induced ICI coefficients matrix,  $\mathbf{\Lambda}$  of each block, the ICI is found as:

$$\tilde{\mathbf{d}}_{\text{ici}} = \mathbf{\Lambda} \tilde{\mathbf{d}} \quad (6.22)$$

After that, the ICI components are subtracted from the equalized partial symbol ( $\mathbf{y}_{\text{eq}}$ ) before the symbol being passed to the next iteration (see Figure 6.16).

**(C) Step one of the even indices iterations.** After cancelling the interference within the blocks in the odd indices iterations, here in the even indices iterations, the decoder cancels the IBI among the blocks. To achieve this, the received signal from the previous iteration is fed to a soft-output demapper, which translates the distorted received constellation into LLR values ( $\hat{\mathbf{b}}_{\text{de}}$ ). Then, the output is de-interleaved and decoded using soft-output BCJR to get soft-bits,  $\hat{\mathbf{b}}$ .

In order to quantify the interference between the blocks, we derive the interference matrix using equation (6.16). Thus, the IBI interference matrix

is given as:

$$\begin{aligned} \mathbf{\Gamma}_{\mathbf{IBI}(l,n)} &= \begin{cases} 1, & l = n \\ 0, & l \neq n \ \& \\ & N_1 \leq l \leq N_2, \\ & N_1 \leq n \leq N_2 \end{cases} \quad (6.23) \\ &= \frac{1}{\gamma Q} \left[ \frac{1 - \exp[-j2\pi(l-n)\gamma]}{1 - \exp\left[\frac{-j2\pi(l-n)}{Q}\right]} \right], \quad \text{else} \\ &= \mathbf{I}_{\mathbf{IBI}} + \mathbf{\Psi} \end{aligned}$$

where  $l = n = [0, 1, \dots, Q - 1]$  are the subcarriers indices,  $N_1$  is the index of the first subcarrier in a block, while  $N_2$  is the index of the last subcarrier in a block,  $\mathbf{I}_{\mathbf{IBI}} \in \mathbb{C}^{Q \times Q}$  is an identity matrix and the matrix  $\mathbf{\Psi} \in \mathbb{C}^{Q \times Q}$  is the interference coefficients matrix.

**(D) Step two of the even indices iterations.** In this step, we find and subtract the interference between the blocks. To achieve this, the  $\hat{\mathbf{b}}$  from step (C) are encoded and interleaved to get  $\tilde{\mathbf{d}}$ , as shown in Figure 6.16. Then, the latter is multiplied with the IBI coefficient matrix,  $\mathbf{\Psi}$ , to estimate the IBI components, as:

$$\tilde{\mathbf{d}}_{\mathbf{ibi}} = \mathbf{\Psi} \tilde{\mathbf{d}} \quad (6.24)$$

After that, the IBI is estimated and subtracted before the symbol is being passed to the next iteration. Repetition of these processes results in decoding enhancement efficiency.

### 6.5.1.2 Outer loop decoder

Figure 6.19 illustrates the operation of the outer loop decoder. Starting with the received ( $R_x$ ) signal, distorted by interference from user 2, and comprises the two overlapped signals of the two users; each one of these signals is composed of a set of OFDM symbols, represented by the numbered elementary rectangles in the figure, where those with odd indices belong to user 1. The partial symbol 1 ( $\mathbf{s}_{1p}$ ) of user 1 is the collision-free partial symbol, while the rest of the symbols (of both users) are overlapped interfered

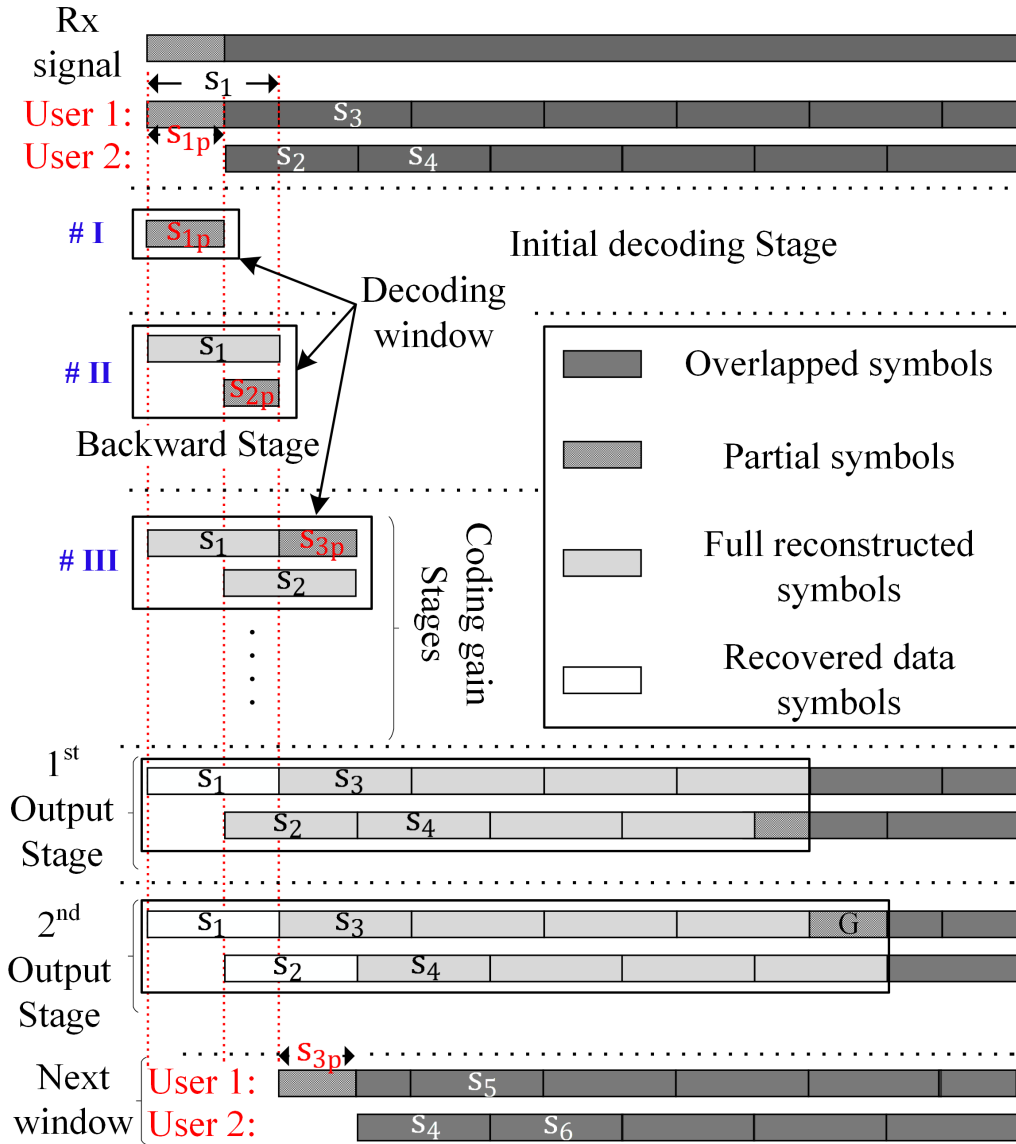


**Figure 6.19:** The outer loop decoding algorithm. The algorithm uses the inner loop decoder to recover the data in the collision-free portion of symbol 1 in the first stage. Then, the algorithm increases the decoding window size in every additional stage up to stage  $G$  in this example, where decisions on symbol 1 and 2 are made. After that, the decoding algorithm starts a fresh decoding window from symbol 3. The symbols with odd indices belong to user 1 and the ones with even indices belong to user 2

symbols. The role of the outer decoder is to follow the inner decoder, which has already recovered the data of  $\mathbf{s}_{1p}$ , to reconstruct a full symbol 1 ( $\mathbf{s}_1$ ). Then, the outer decoder acts on  $\mathbf{s}_1$  and the rest of the symbols, so that all symbols are recovered even those with severe interference.

The outer loop operation starts with a decoding window of length equal to one symbol as shown in Figure 6.19 in step #**I**. Then, the decoding window size is increased linearly, with the number of stages, until it reaches the size of  $G$  symbols. For this work, the value of  $G$  was selected empirically following an extensive number of experiments (Section 6.7.3). The outer loop decoding algorithm operates to detect data only of the first two symbols in the window of size  $G$ . After that, these two symbols are subtracted from the received overlapped signal and the result is passed to the next decoding window.

**6.5.1.2.1 Initial stage of decoding** Here, the outer loop decoder uses the inner loop (described in Section 6.5.1.1) to decode the partial symbol,  $\mathbf{s}_{1p}$ . After that, the outer loop fully reconstructs  $\mathbf{s}_1$ .

**6.5.1.2.2 Backward stage of decoding** The decoding window is set to two, where  $\mathbf{s}_1$  and the partial symbol 2 ( $\mathbf{s}_{2p}$ ) are part of the decoding process (stage #**II** in Figure 6.19). This stage is divided into five steps: (i) the outer loop implements basic interference cancellation by subtracting the reconstructed  $\mathbf{s}_1$  from the received signal to estimate  $\mathbf{s}_{2p}$ ; (ii) in a manner similar to that of the initial decoding stage, the receiver decodes  $\mathbf{s}_{2p}$  using the inner loop, then reconstructs the full symbol 2 ( $\mathbf{s}_2$ ); (iii) next,  $\mathbf{s}_2$  is subtracted from the received signal to get  $\mathbf{s}_1$  without interference; (iv) then  $\mathbf{s}_1$  is fully decoded to recover its data and then reconstructed to yield a received  $\mathbf{s}_1$ , as if there were no interference; finally, (v) the outer loop repeats the first and second steps to reconstruct an interference-free version of  $\mathbf{s}_2$  to be passed to the next stage.

The reason for stage #**II** is that the partial decoder results in higher error rates relative to a conventional OFDM decoder, because partial symbols contain fewer samples, which means each has lower energy than the full symbol. Therefore, stage #**II** cancels the interference effects of  $\mathbf{s}_{2p}$  to obtain

a full interference-free symbol,  $\mathbf{s}_1$ , yielding a better error rate performance.

It should be noted that the partial symbol length of user 1 ( $\mathbf{s}_{1p}$  in stage #I in Figure 6.19) is different to the partial symbol length of user 2 ( $\mathbf{s}_{2p}$  in stage #II in Figure 6.19), where the duration of the partial symbols of the two users in total is equal to the duration of a full symbol.

**6.5.1.2.3 Middle (coding gain) stages of decoding** In the same way as the backward stage, the decoding window increases its size by one symbol for every additional stage until the stage preceding the hard decision, in which, all the symbols in the decoding window are full symbols except for the last symbol, which is the partial symbol. For instance, when the decoding window size is equal to six symbols, there will be five full symbols and one partial symbol. Through these stages, the symbols of each user go through the appropriate convolutional decoder, to increase the coding gain.

**6.5.1.2.4 Hard decision on symbol 1** The outer loop decoder gives the first output, which is the recovered data of  $\mathbf{s}_1$ .

**6.5.1.2.5 Final stage of decoding** The PSR decoder produces the second output that is the recovered data of  $\mathbf{s}_2$ .

**6.5.1.2.6 Reset the decoding window** Recovered  $\mathbf{s}_1$  and  $\mathbf{s}_2$  are subtracted completely from the overlapped received signal before being passed to the next decoding window, also of size  $G$ . The above processes are repeated again but now starting with a fresh decoding window, of size equal to one, to decode partial symbol 3 ( $\mathbf{s}_{3p}$ ) and ending with a decoding of full symbols 3 and 4 ( $\mathbf{s}_3$  and  $\mathbf{s}_4$ , respectively). This carry on to the end of the frame, making hard decision on two symbols only per decoding window.

## 6.5.2 Link layer design

In the current 802.11 receivers, the receiving station transmits an Acknowledgment (ACK) after a data frame is successfully decoded and passes the Cyclic Redundancy Check (CRC), as shown in Figure 6.20. Otherwise, the received

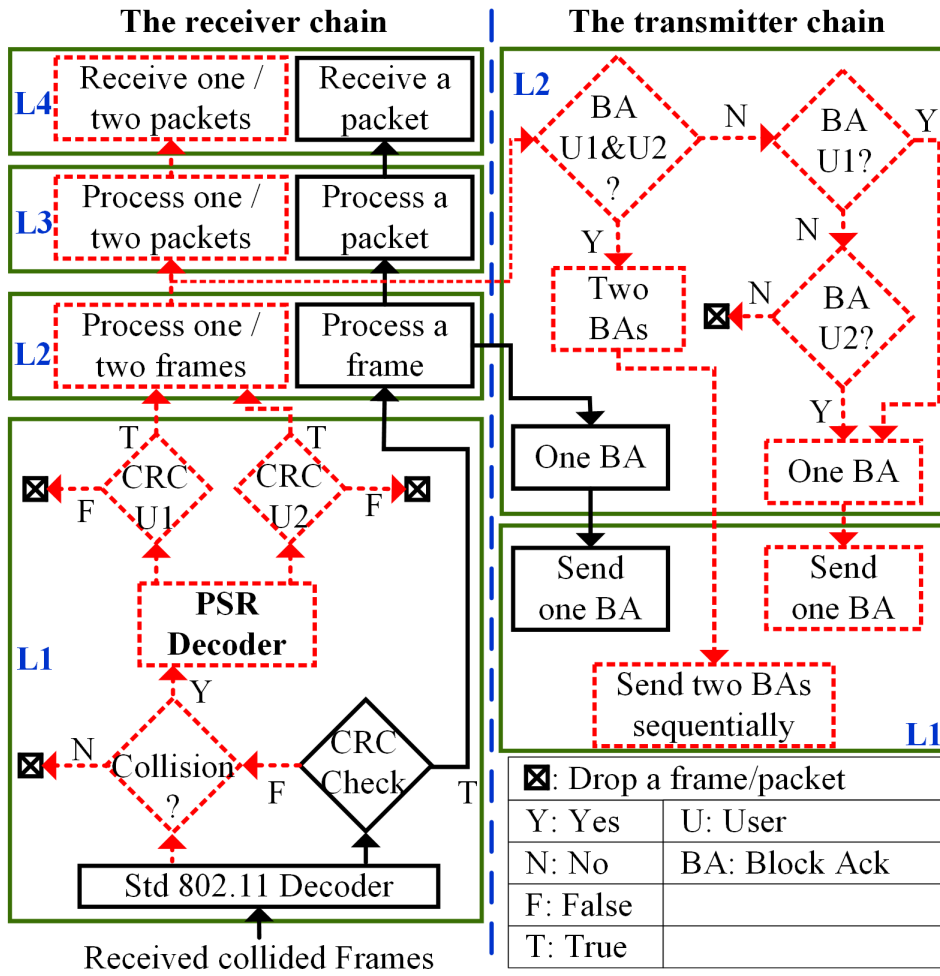


**Figure 6.20:** Schematic chart of PSR system. The solid-black lines depict the existing 802.11 receivers, while the dot-red lines represent the additional PSR functions in each layer. U 1 and U 2 are user 1 and user 2, respectively

frame is dropped and no ACK is sent. The solid-black lines of Figure 6.20 depict this process, in existing 802.11 receivers. On the other hand, the new receiver design modifies the data link layer by adding a new acknowledgment scheme, which allows the receiving station to acknowledge successfully recovered frames of the two users, as shown by the added dotted-red blocks in Figure 6.20. In this system design, delayed Block Acknowledgment (BA) mechanism is used from 802.11n to delay sending the BA to the transmitting users until PSR fully decodes the two colliding frames. This is because one of the colliding users could finish transmitting data frames while the other user has not yet completed its transmission.

Decoding overlapped frames necessitates two different designs; (i) for intra-network collision (the scenario in Figure 6.2 (A) and (B)) and (ii) for collisions in two co-existing networks (the scenarios in Figure 6.2 (C)). It should be noted that, at the physical layer, the two designs are identical.

### 6.5.2.1 Intra-network collisions

When two users are transmitting concurrently, the receiving station of the two users decodes the overlapping data frames using PSR as explained in Section 6.5.1. However, the acknowledgment mechanism differs according to whether the collisions occur (i) between data frames of two users or (ii) between data and control frames.

**Collision between data frames of two users.** Figure 6.21 (A) depicts the operation of the AP using standard 802.11 and PSR receivers. The 802.11 receiver sends a BA indicating indices of successfully recovered frames. On the other hand, after successful recovery of the overlapping frames using PSR, the AP sends two separate Block Acknowledgments (BAs), one for each user. Each BA indicates the indices of the recovered frames of each transmitter, as shown in Figure 6.21 (A).

**Collision of data frames with control frames.** In this case, exemplified by Figure 6.21 (B), user 2 sends control frames to the AP, which collides and hence no ACK is received. Then user 2 re-sends the control frame after a random wait, in the worst case and under heavy traffic from user 1, further

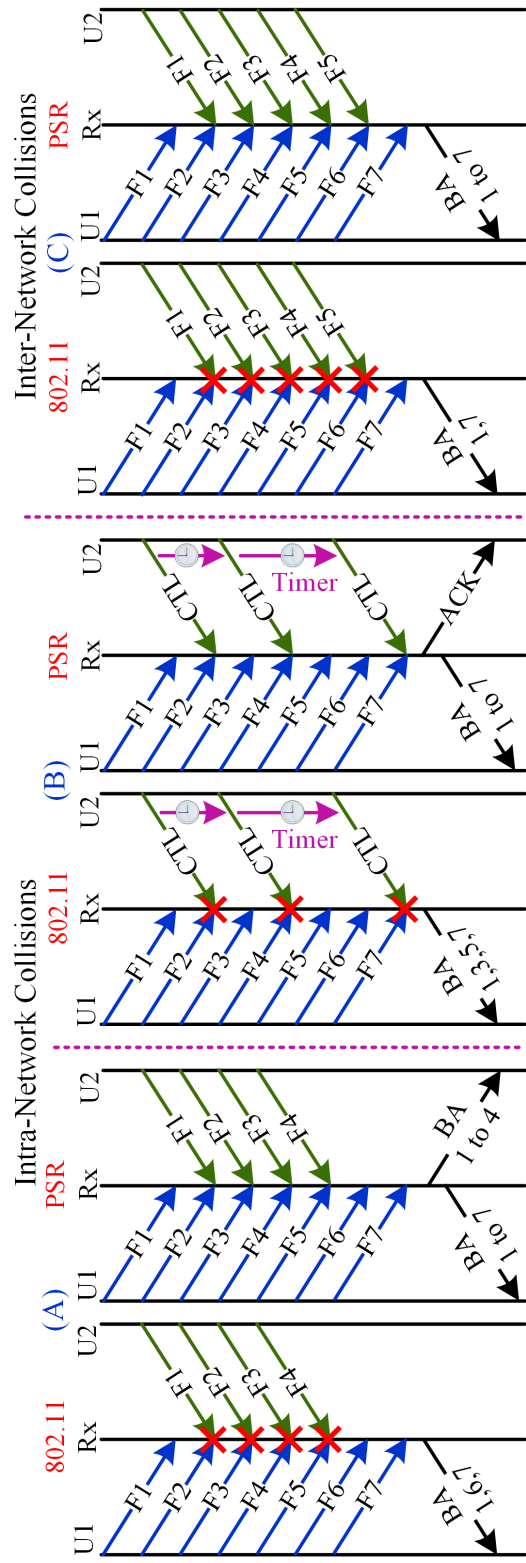


**Figure 6.21:** Message sequence chart of intra- and inter-network collision scenarios. User 1 and user 2 cause collisions at the receiving station when they have concurrent transmissions. (A) collisions of data frames of two users at the AP; (B) collisions between data and control frames at the AP; (C) collisions are the inter-network collision scenario. The character F refers to the data frames, while the CTL refers to the control frames

collisions may occur. In the 802.11 receiver, the affected data frames of user 1 are dropped and a single BA is sent for the recovered frames. In contrast, for the PSR case, overlapped frames are recovered for both users and the receiver waits until no transmission is detected, then an ACK is sent for the control of user 2 and a BA for the data frames of user 1.

### **6.5.2.2 Inter-network collisions**

In this case of inter-network scenarios, the overlapped frames at the recipient station have different destination addresses. Therefore, after decoding the overlapped frames, the receiving station only takes the frames that have its address in the destination field. Hence, sending only a single BA after a complete reception. Figure 6.21 (C) depicts the process of sending a single BA. The advantage of using PSR over standard 802.11 receivers, is the ability to recover overlapped frames. This enhances the throughput and reduces the retransmission rate.

## **6.5.3 Experimental parameters estimation**

### **6.5.3.1 Collision detection**

In this work, a technique similar to Zigzag Decoding [95] is followed, where the known preamble is correlated with the received signal. When the two preambles are properly aligned, a correlation peak results. A single incoming frame results in a single correlation peak at the start of that frame. The generation of a second peak within the duration of the first frame indicates that a colliding/interfering frame is present, since the second peak is a result of correlation with the colliding frame's preamble. This identifies the cause of CRC failure as a collision and hence the receiving station activates PSR to decode the colliding frames.

### **6.5.3.2 $\gamma$ estimation**

It is important to find the value of  $\gamma$ , defined in Section 6.4, and hence the inter-carrier interference levels as these are required for the detection process

**Table 6.1:** Experimental initial CFO and CIR

<i>Station Identification</i>	<i>CFO</i>	<i>CIR</i>
Station 1	$CFO_1$	$CIR_1$
Station 2	$CFO_2$	$CIR_2$
$\vdots$	$\vdots$	$\vdots$
Station N	$CFO_N$	$CIR_N$

in the inner loop as explained in Section 6.4 and Section 6.5.1.1.  $\gamma$  can simply be estimated (see Figure 6.3) by finding the time delay between the starting sample, of the colliding user transmission using the first correlation peak, and the second correlation peak.

### 6.5.3.3 CIR estimation

The LTF symbols are used for channel estimation. This is achieved by performing FFT on each long OFDM symbol, then the subcarriers of the two symbols are averaged to reduce the noise [24]. After that, the averaged subcarriers data are divided over the known transmitted sequence (the frequency-domain LTF sequence given in Equation 6.2) to find an estimate of the channel at each subcarrier. Then, the CIR is found by performing IFFT on the estimated frequency channel response. This method is applied for the collision-free frame reception and also for the scenarios where a preamble is received in the collision-free region (region **(a)** in Figure 6.3). For example, the preamble of user 1 is received in the collision-free region, hence, it is used to estimate CIR for user 1.

In each receiving station in the PSR testbed, the estimated CIR is stored with the associated transmitting station user identification, as shown in Table 6.1. Thus allowing the receiving station to have an initial estimate of the channel for the colliding user (user 2). This is because the colliding user preamble is distorted in the collision (overlapped with user 1 frame), further details is given in Section 6.5.3.5.

#### 6.5.3.4 CFO and phase offset estimation

It is almost impossible to have two radios that generate the exact carrier frequency. Therefore, the difference in frequency between the transmitting radio and receiving radio devices causes CFO. The CFO is estimated at the receiver using the two long OFDM symbol (the LTF signal) in the preamble signal. The conjugate of the first received long OFDM symbol is multiplied with the second symbol then the phase of the multiplication result is averaged and divided over  $2\pi$  to find the CFO in Hz. The process is given by [141]:

$$\delta f = \frac{1}{2 * \pi * Q} \times \sum_{m=0}^{Q-1} \angle \mathbf{s}_{ltf}^*(m) \mathbf{s}_{ltf}(m + Q) \quad (6.25)$$

where  $Q = 64$  samples in the time-domain.

The residual CFO in the received signal due to error in estimating the CFO will result in a phase offset, which is estimated using the pilot subcarriers inserted in 802.11 OFDM symbols. This is achieved by performing FFT to a received OFDM data symbol, after which the four pilot subcarriers samples are divided over the known transmitted pilot subcarriers. After that, the phase offsets at the four subcarriers is measured and averaged to find the phase offset ( $\beta$ ) for that OFDM symbol, the process is given as [141]:

$$\beta = \frac{1}{4} \times \sum_{m=0}^3 \angle(\mathbf{p}_{rx} / \mathbf{p}_{tx}) \quad (6.26)$$

The details of the pilot subcarriers and their locations in the OFDM symbols are given in Section 6.3.2.8.

#### 6.5.3.5 User identification, CFO, and CIR estimation and compensation

The received signals are distorted by the wireless multipath channels and the CFO effects and contaminated with AWGN noise. In order to mitigate the multipath channel and CFO effects, the receiving station estimates the CIR and CFO for each user. In 802.11 standards, such is estimated using the

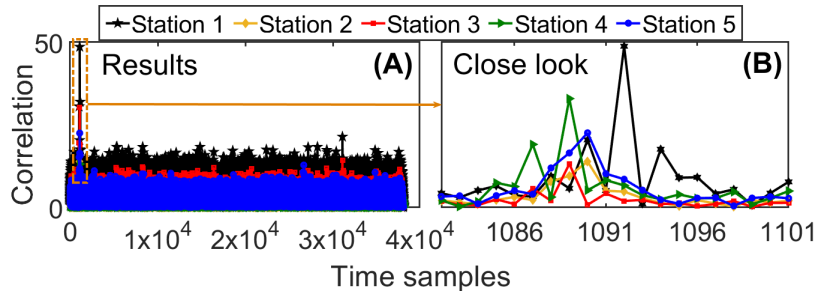


**Figure 6.22:** Our technique ability to identify a colliding user from its recent CFO and CIR. (B) shows that station 1 has the highest peak, which indicates the colliding user

received preamble attached to each frame.

**Colliding user identification and initial CFO and CIR.** For user 1, the CIR and CFO are estimated using its preamble signal, which is received within the collision-free region. Unfortunately, this can not be done for user 2, since its received preamble is corrupted by the collision with the signal of user 1. To resolve this problem, a new technique is introduced to define the colliding user identification, and the corresponding CIR and CFO. The technique, implemented in two stages, is based on the premise that the combination of CIR and CFO for each station will be unique. The first stage, the receiving station keeps a record of user identifications and associated most recent CIR and CFO of users stations in its vicinity, whenever user data is received with no collision. The second stage is to define which set of CIR and CFO is the correct match to the colliding user. To achieve this, the decoder sequentially convolves all the saved CIR with the known preamble signal and then applies CFO. After that, the decoder correlates the resulting convolution values with the received signal and compares the results of all correlation processes. This comparison identifies the colliding station identification through its most recent CFO and CIR, which are used as an initial estimate to decode the signal of the colliding user. Figure 6.22 shows the correlation values resulting from using five saved pairs of CFO and CIR measured in the experimental testbed. The result with highest peak represents the right CFO and CIR of the colliding station, which is station 1 in this example.

**Updating CFO and CIR information.** After identifying the initial CFO and CIR information as mentioned earlier, the decoder uses this information to decode the colliding signal until the preamble of the user 2 (the colliding signal) is fully recovered. Then, the extracted/recovered preamble signal of user 2 is used to get a new estimate of the CFO and CIR.

**CFO compensation.** We correct CFO for a partial symbol before it is passed to the inner loop decoder by applying a frequency shift to the signal in the time-domain:

$$\mathbf{s}_{\mathbf{x}\mathbf{p}} = \mathbf{s}_{\mathbf{x}\mathbf{p}_{\text{cfo}}} \cdot e^{-j2\pi\delta f n} \quad (6.27)$$

where  $\mathbf{s}_{\mathbf{x}\mathbf{p}}$  and  $\mathbf{s}_{\mathbf{x}\mathbf{p}_{\text{cfo}}}$  are the partial symbol (with sub index  $\mathbf{x}$ ) after and before compensating CFO, respectively, and the exponential term represents the applied correction of the frequency shift,  $\delta f$ , which is estimated using the preamble, and  $n$  the time index from the beginning of the frame.

## 6.6 Implementation

The 802.11 devices for both transmitters and receivers are WARP V3 devices Software Defined Radios (SDRs). The WARP devices operate on channel 17 at 5660 MHz and use TP-link antennas with 5 dB gain. We set the sampling rate in the WARP device to be 20 MHz. The WARP devices connect to a Linksys SE4008 WRT 8-port gigabit Ethernet switch through Ethernet cables.

### 6.6.1 Physical layer

The SDR testbed is driven by MATLAB R2017b for 802.11a signal generation, following the 802.11a OFDM physical frame structure. A 64-point IFFT generates the symbols, and uses 48 inputs for data, 4 for pilots and the rest are padded with zeros. A preamble is attached at the beginning of each frame.

Automatic gain control is applied to the received signals, then the received overlapped signal is saved to disk to be processed in off-line decoding. The

PSR and SIC decoders are written in Matlab. The decoders save the decoded bits to disk for performance evaluation.

### **6.6.2 Link layer to transport layer**

We build the network topology scenario shown in Figure 6.23 in NS-3 [142] with the 802.11n standard system specifications. First, we evaluate standard 802.11, in which an ACK is sent to the transmitter only when a frame is decoded correctly. On the other hand, SIC and PSR are built on top of 802.11n, and so act exactly as 802.11n unless there is a collision, in which case, the frame that could not be decoded by the 802.11n receiver is examined to detect if it experiences collision event as explained in Section 6.5.3.1. When a collision event is detected, trace driven data of the decoder under evaluation (either SIC or PSR), which contains details of the decoding performance, is used by the receiver to make a decision on the success or otherwise of frame decoding. The use of NS-3 in our evaluations, is to achieve almost real life collision environment where transmissions are not synchronized, the frame length is variable and the  $\gamma$  variable is not set.

## **6.7 Evaluation**

In this section, the PSR system is evaluated versus the 802.11 and SIC systems. In Section 6.7.1 we describe the methodology and in Section 6.7.2 we evaluate the PSR versus SIC in terms of rate region. Experimental evaluation of the PSR system in the link layer is given in Section 6.7.3 and of the end-to-end throughput performance of the transport layer in Section 6.7.4.

### **6.7.1 Methodology**

PSR is evaluated with 12-nodes using the SDRs testbed. Physically, each node is a WARP device connected to a computer. The network topology, shown in Figure 6.23, contains both non-line-of-sight and line-of-sight links.

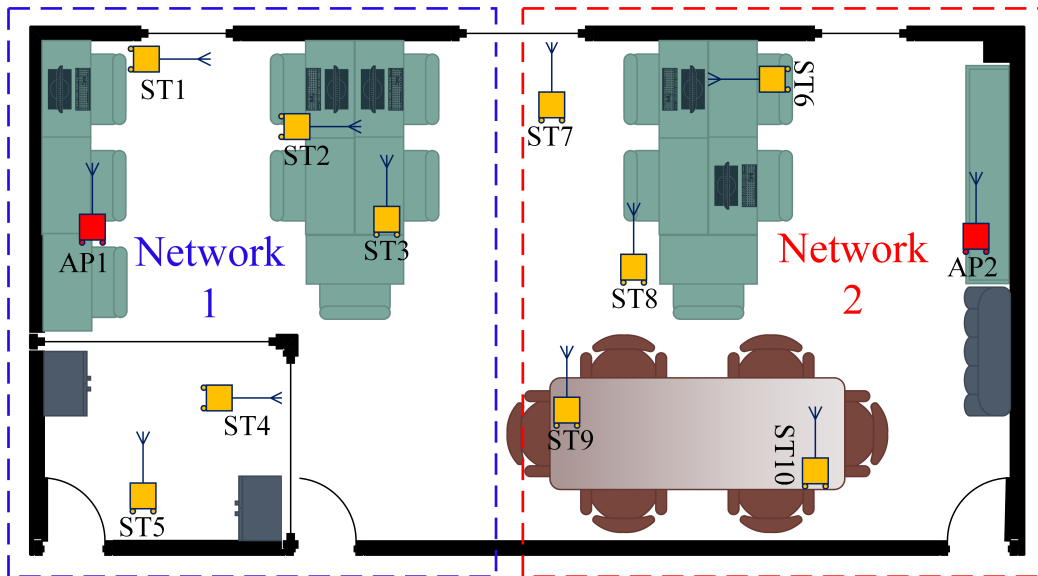


**Figure 6.23:** Indoor experimental testbed map. The testbed consists of ten nodes operate as user stations and two nodes operate as APs. The nodes are distributed across two rooms for two networks in non-line-of-sight and line-of-sight indoor environment

### 6.7.1.1 Experimental collision traces

In our application, the focus of this work is on decoding two 802.11 frames that have collided. Two nodes simultaneously transmit data to another node to intentionally cause a collision. For example, ST 1 and ST 2, shown in Figure 6.23, both transmit data to AP 1, and the received collision data are saved in files to be decoded later. Four different experimental runs are carried out to collect collided frames. First, frame transmissions from two network 1 stations to AP 1, where network 1 contains the stations shown in Figure 6.23. Second, frame transmissions from two network 2 stations to AP 2, where network 2 contains the stations shown in Figure 6.23. Third, frame transmissions from AP 1 and a network 2 station to a network 1 station to cause a collision at the latter. Finally, transmission from AP 2 and a station from network 1 to a station in network 2, to cause a collision at the latter.

For each experimental run, the experiment parameters are varied, such as modulation format (BPSK and QPSK) and experiments are run for ten

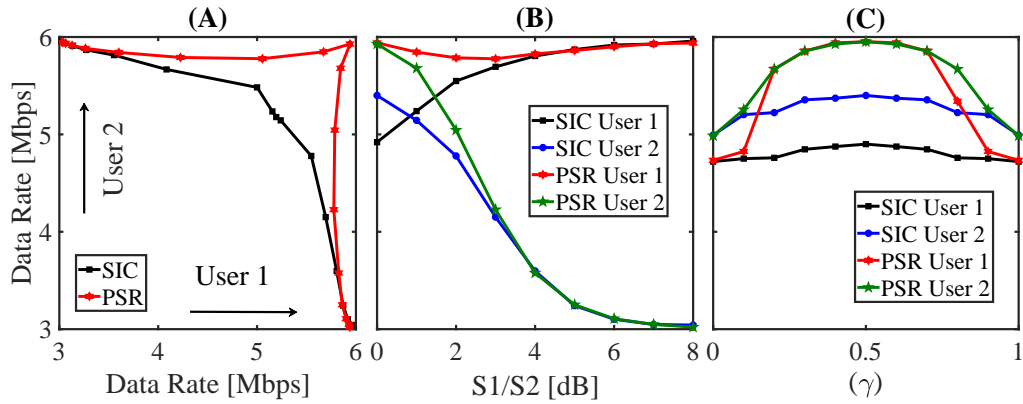


**Figure 6.24:** Rate region comparisons. (A) the rate region of the two user uplink AWGN channel. (B) The data rate of user 1 and 2 using SIC and PSR. (C) Rate performance versus different values of  $\gamma$

values of the fractional overlap,  $\gamma = 0, 0.1, \dots, 0.9$ . In each experiment, 600 physical frames are sent from two nodes which results in 600 collision traces that are collected at the receiver. Every frame carries 12,000 bits (1,500 bytes).

### 6.7.1.2 Schemes compared for end-to-end evaluation

Using the 12-node testbed and the trace driven simulations, three schemes end-to-end are evaluated: (i) PSR, (ii) SIC, and (iii) 802.11n. The evaluation is carried out with the following metrics:

- **Frame Error Rate (FER)**, which is the percentage of incorrectly decoded frames to the total and where a frame is considered successfully decoded if it passes the CRC.
- **Throughput**, this is the data throughput-per-second measured at the transport layer.
- **Frame retransmission rate**, this is the number of physical frame retransmissions-per-second measured at L2.

### 6.7.2 Rate region comparison

In this section, the rate region of the two users uplink AWGN channel is compared in MATLAB simulation, using SIC and PSR. The current maximum rate region of two users scenario can be achieved using SIC receivers, as shown in Figure 6.24 (A). The maximum rate of a user in this rate region is constrained by the rate of the other user who shares the same link. This is because a SIC decoder considers the interfering signal of a user as noise in order to decode the signal of the other user. Interestingly, this role does not apply to the PSR system. This is because the PSR exploits the collision-free partial symbol to bootstrap the colliding frames in a collisions, where such a partial symbol is not constrained by the rate of the interfering user.

To investigate further how the PSR decoder can "break" the rate region, we provide the rate performance of the two users versus the difference between their signal powers, as depicted in Figure 6.24 (B), the rate performance is compared to the SIC decoder. As expected, using SIC decoder, the rate of a user decreases as the power difference between the two received signals decreases. On the other hand, the PSR decoder outperforms the SIC decoder, where the rate performance of a user is maintained almost the same no matter what is the difference in power between the two received signals.

However, the performance of the PSR is not without limitation, where the PSR decoder depends on the duration of the partial symbols in time; such duration is represented by the  $\gamma$  ratio factor, defined in Section 6.4. Figure 6.24 (C), shows the rate performance of the two users using the PSR and the SIC decoders versus different values of  $\gamma$ . The figure shows that the PSR performance outperforms the SIC decoder for most of the  $\gamma$  values and then converges to the SIC performance level at the edges of  $\gamma$  values. Moreover, from the figure, we note that the PSR performance is constrained by the lowest value of  $\gamma$ , this is because the shorter the period the partial symbols have, the fewer time samples used and hence lower amount of energy per symbol leading to more errors and hence lower rate.

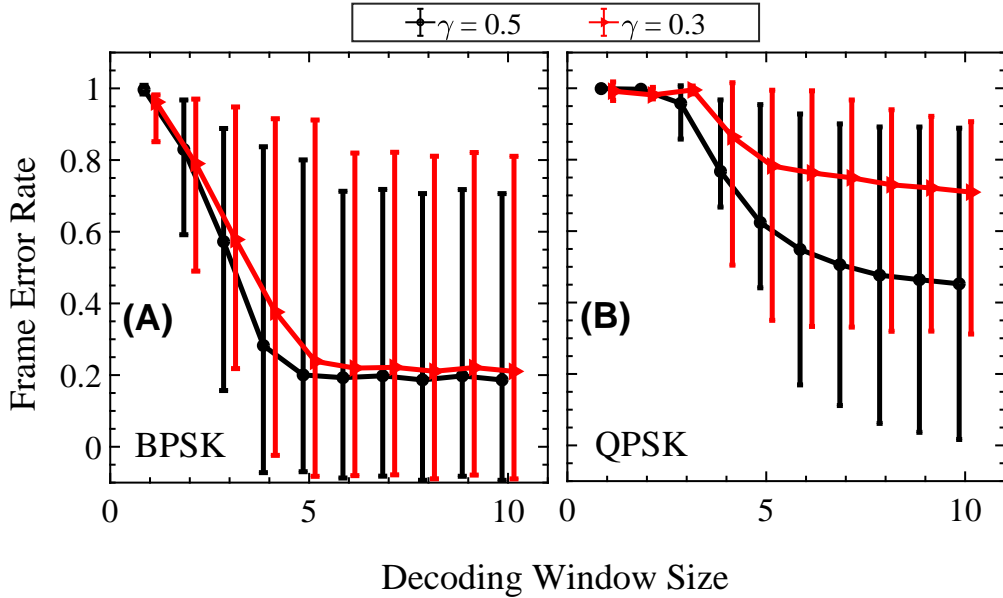


**Figure 6.25:** Average FER of all collision cases versus decoding window size of the outer loop decoder. Maximum and minimum FER values, due to variation of channel conditions and noise, indicated by the vertical lines. (A) using BPSK modulation; (B) using QPSK modulation

### 6.7.3 FER measurements in link layer

In this section, PSR is evaluated in terms of FER performance using all permutations of two nodes transmitting simultaneously to another node (this is called collision cases). In total the experimental indoor testbed, shown in Figure 6.23, provides 45 collision cases. The evaluation metrics are (i) FER versus the decoding window size of the outer loop decoder, described in §6.5.1.2; (ii) FER versus different values of  $\gamma$ ; and (iii) the Cumulative Distribution Function (CDF) of the FER for PSR and compared to SIC for all the collision cases.

**Performance evaluation of the outer loop decoder.** Figure 6.25 shows the FER performance of different stages of the outer loop decoder. In this experiment, the decoding window size is set to  $G = 10$ ,  $G$  defined in Section 6.5.1.2. Each marker point in the curve represents the average FER

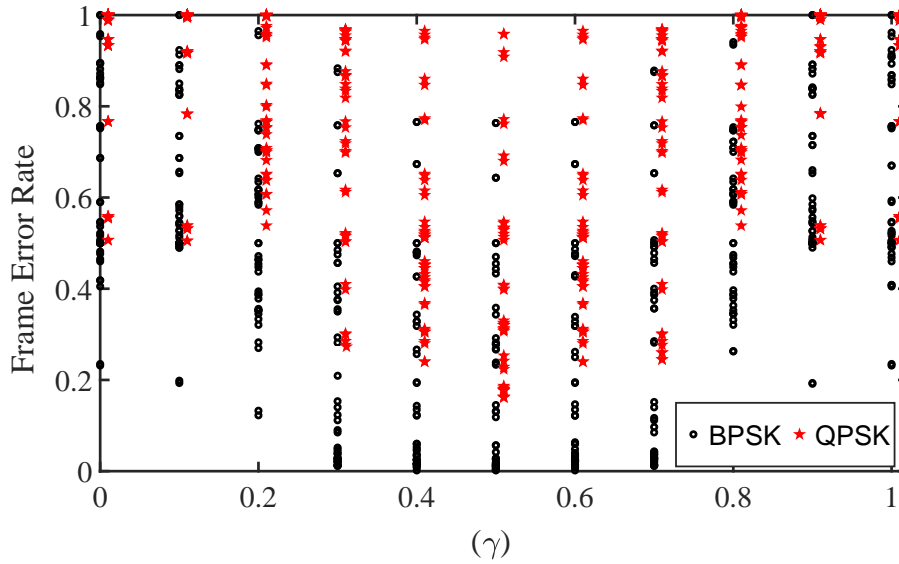
performance of one of the 45 collision cases tested, while the candle bars indicate the highest and lowest FER performance for each case. Such a range of variation for each case is due to differing channel effects, CFO and signal to noise level. The FER performance improvement comes from the nested-loop design which is based on interactions of the inner loop decoder with the backward and coding stages of the outer loop decoder, as described in Section 6.5.1.2. Expectedly, the performance worsens for lower values of  $\gamma$  and/or higher modulation. In all cases there is evidence of error floor indicating values of decoding window size beyond which no further improvement of FER is attained.

**FER versus  $\gamma$ .** Figure 6.26(a) shows FER performance of PSR for different collision cases versus  $\gamma$  values, which is taken from the last stage of the outer loop decoder,  $G = 10$ . Each point in the figure represents the FER of a single collision case (black points are BPSK while red are QPSK). Clearly, the FER performance is almost symmetrical around  $\gamma = 0.5$ , because the FER performance is restricted to the shortest partial symbol duration of the two colliding users (see Section 6.5.1.2).

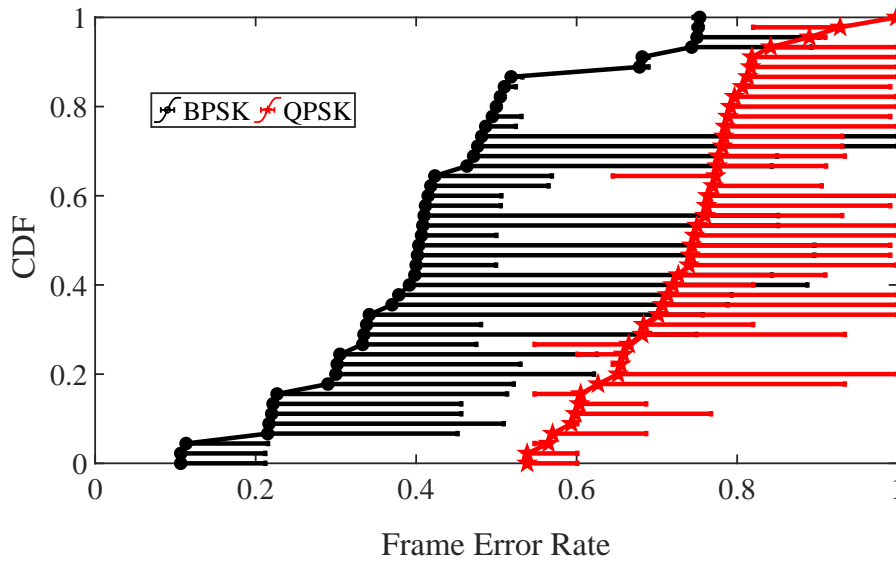
**CDF of FER.** The CDF of the FER performance of each collision case is shown in Figure 6.26(b), where each marker point on the curves indicates average PSR performance over all  $\gamma$  values. The horizontal lines attached to each point represent the difference in performance of the PSR and SIC decoders. On average, PSR achieves 22% and 16% better (lower) FER than SIC using BPSK and QPSK modulation, respectively.

#### 6.7.4 End-to-end performance

In this section, we use the testbed in Figure 6.23 to evaluate the throughput and retransmission rate performance of PSR in intra- and inter-network collisions, described in Section 6.5.2. The two scenarios are implemented in NS-3 driven by our experimental testbed decoding performance.

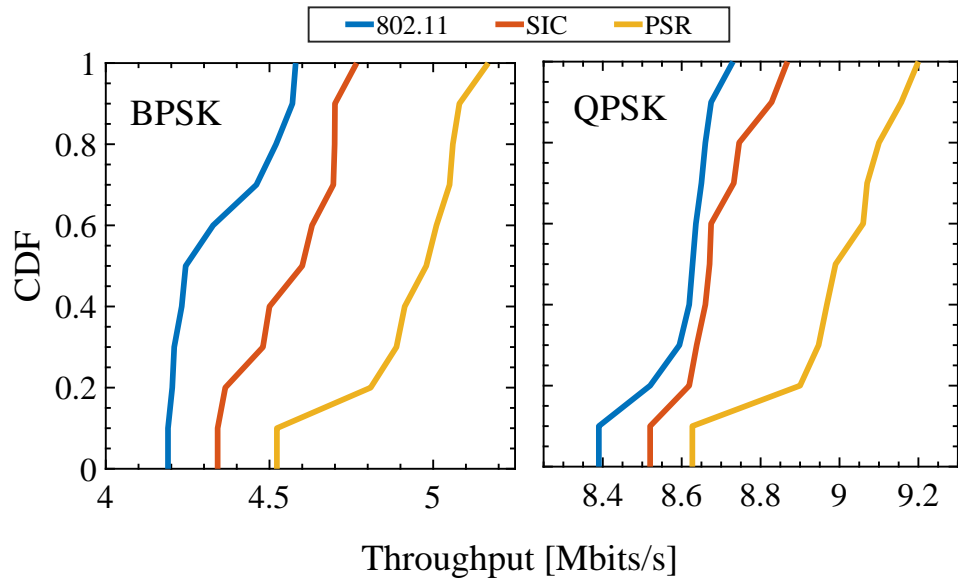


(a) Frame error rates vs  $\gamma$

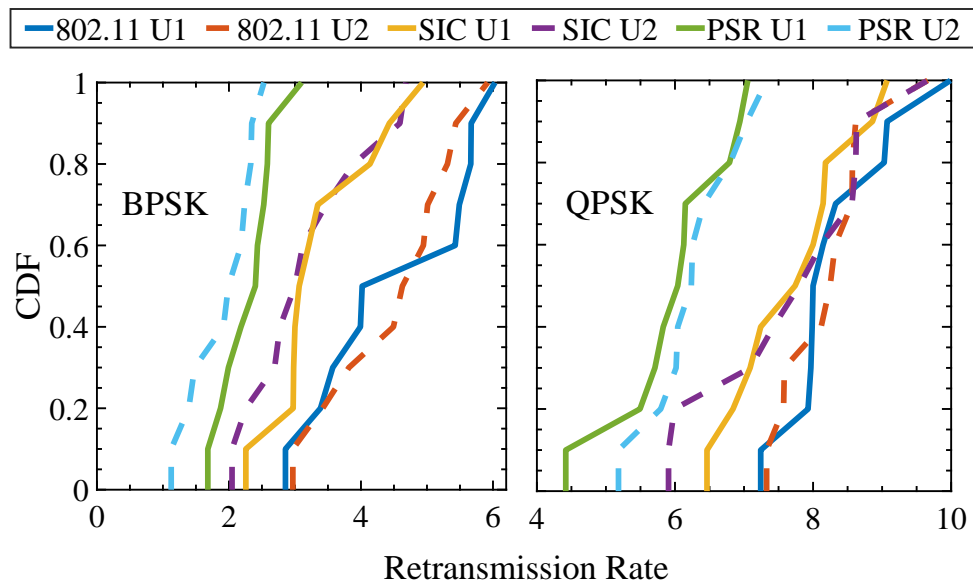


(b) CDF of frame error rates across links

**Figure 6.26:** PSR Frame Error Rates Performance. (a) FER versus  $\gamma$  for different collision cases; (b) CDF of FER across all collision cases (in total 45 cases), each case is a single marker point. The horizontal lines show the difference in FER performance between PSR and SIC



(a) CDF of throughput



(b) CDF of retransmission rate

**Figure 6.27:** CDF of throughput and retransmission rate in intra-network scenario using uplink-UDP transmissions. The legends in figure (b) apply to the following figures

#### 6.7.4.1 Intra-network collisions

In this case study scenario, the performance of PSR, SIC and 802.11n are evaluated for intra-network collisions, such as the collisions from hidden terminal nodes. Network 1 in Figure 6.23 is used as the experimental testbed, providing ten collision cases. Data flow of User Datagram Protocol (UDP) packets using 802.11n frame structure is simulated in NS-3. Request-to-send/clear-to-send (RTS/CTS) is disabled.

**Throughput performance at the transport layer.** Figure 6.27(a) shows the CDF of throughput measured for collision case in network 1. Compared to a baseline 802.11n decoder, PSR improves average throughput by 13.6%, while the average throughput improvement of the SIC decoder is 5.2%. For QPSK modulation, the average throughput improvements of PSR and SIC are 4.7% and 1.2% over the 802.11n baseline. The throughput enhancement comes from the fact that PSR attempts to decode collided frames and recovers their data.

**Retransmission rate performance.** Figure 6.27(b) shows the CDF of retransmission rates measured for each collision case in network 1. PSR and SIC reduce average BPSK retransmission rate by 49.3% and 25.5% respectively. For QPSK modulation, those reduction change to 27.6% and 7.2%, compared to 802.11n.

#### 6.7.4.2 Inter-network collisions

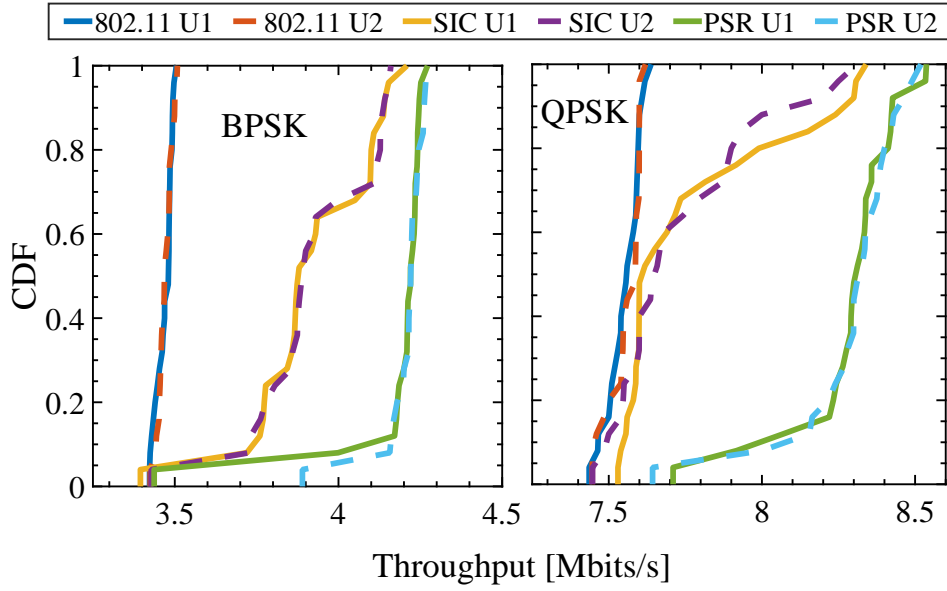
In this section, the PSR performance in a scenario representing a topology, where two stations downloading data using (i) bulk Transmission Control Protocol (TCP) and (ii) video on demand data flows from the AP in their respective networks is evaluated, as shown in Figure 6.2. Since the two data flows require uplink and downlink data, collisions occur when a station is receiving a frame while the other station, in the neighbouring network, is transmitting a frame to its AP.

Under these circumstances, we evaluate the downlink performance of the two networks in Figure 6.23 as the experimental testbed, providing 25 collision cases for each network. In every experimental run, a station from each

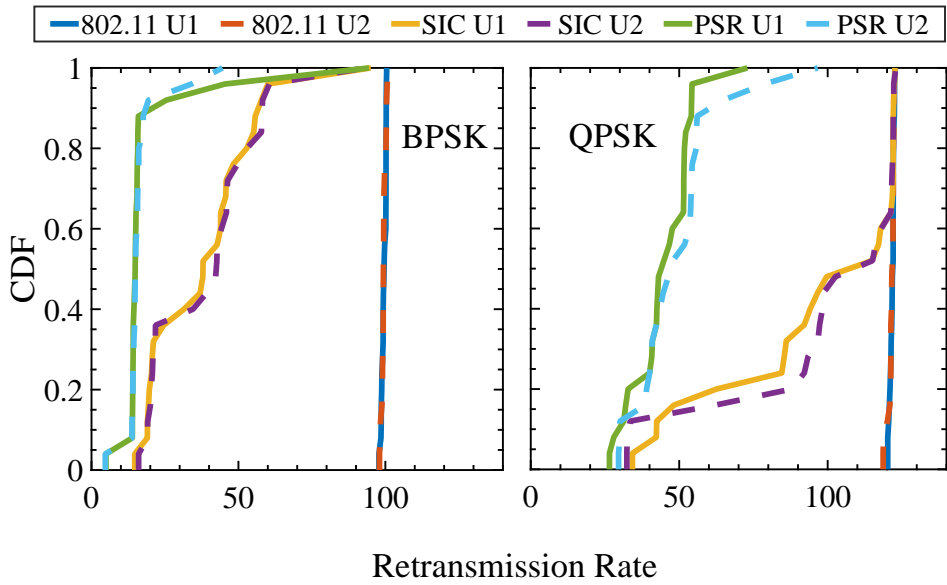
network is involved and its AP, hence, there are two links under test, where the first link is between a network 1 station and AP 1 while the second link is between a network 2 station and AP 2. We measure the throughput at the transport layer of each station, as well as the link layer retransmission rate of AP 1 and AP 2. We plot the CDF of throughput and retransmission rates for both bulk TCP and video on demand using BPSK and QPSK modulation formats in Figure 6.28 and 6.29.

According to our experimental results, the average throughput improvements in comparison to 802.11n, shown in Figure 6.28(a) and 6.29(a), are 21.27% and 21.26% for the downlink bulk TCP and downlink video on demand, respectively, for BPSK modulation. The average throughput enhancement using QPSK modulation are 9.7% and 7.7% for the above respective topology scenarios shown in the same figures.

Moreover, the average retransmission rate in BPSK modulation, shown in Figure 6.28(b) and 6.29(b), is reduced by 81% and 80.8% for the downlink bulk TCP and downlink video on demand, respectively. The reductions for QPSK modulation are 63% and 57% for the above respective topologies shown in the same figures.

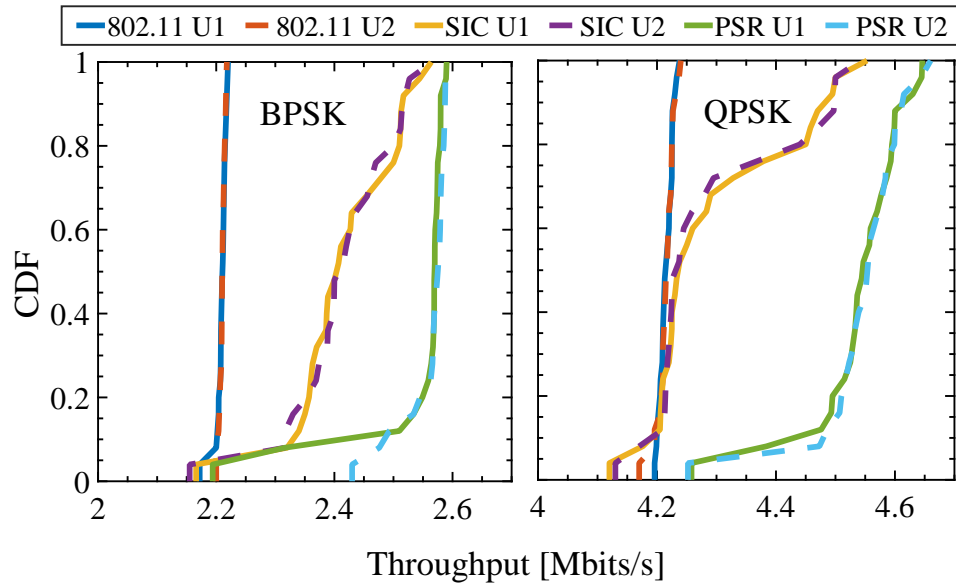


(a) CDF of throughput

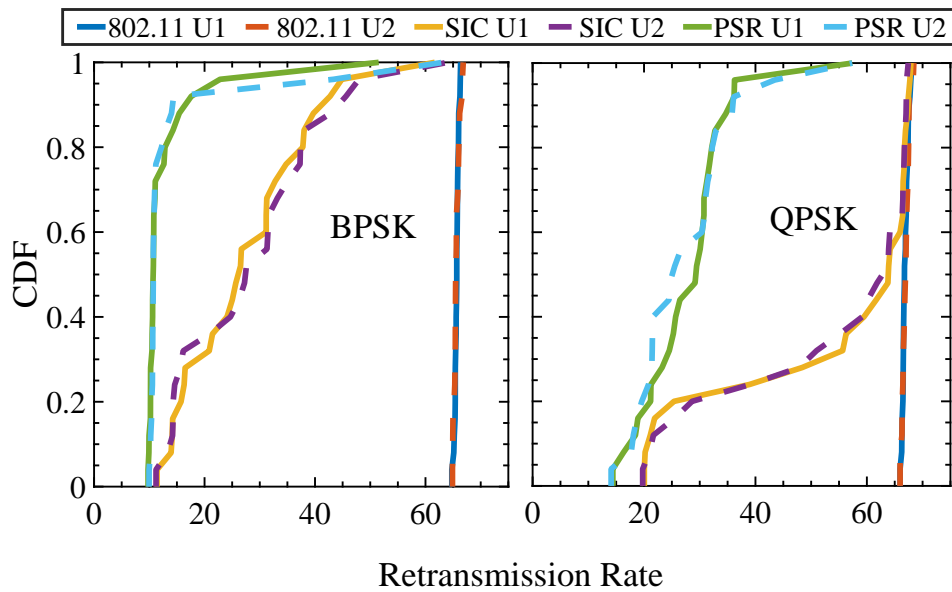


(b) CDF of retransmission rate

**Figure 6.28:** CDF of throughput and retransmission rate in inter-network scenario using bulk TCP transmissions



(a) CDF of throughput



(b) CDF of retransmission rate

**Figure 6.29:** CDF of throughput and retransmission rate in inter-network scenario using video on demand transmissions

## 6.8 Conclusions

The uplink capacity region for interfering transmissions in wireless networks has been characterized and proven, yet its underlying model assumes a complete temporal overlap. Practical unplanned networks, however, adopt packetized transmissions and avoid tight inter-network coordination, resulting in packet collisions that often partially overlap, but rarely ever completely overlap. The work in this chapter presented a new receiving technique and design, termed PSR, that allows efficient operation beyond the capacity region of fully overlapping data in wireless communication systems with collisions. The PSR technique is based on recovery of collision-free partial OFDM symbols, followed by the reconstruction of complete symbols to recover progressively the frames of two users suffering collision. The PSR receiver operates in the physical and data link layers.

In the physical layer, the PSR decoder consists of (i) an inner loop decoder and (ii) an outer loop decoder. The purpose of using the inner loop decoder is to encode the collision-free partial OFDM symbols. The partial symbols have self-created ICI between the subcarriers, due to lose part of the symbols in the collision. Therefore, the inner loop decoder acts on cancelling this ICI iteratively. The design of this decoder is based on TOFDM signals and systems, which was introduced in Chapter 5 of this thesis. The outer loop decoder is added to the receiver to cancel the users interference and hence restricting the inner loop decoding error rate from propagating to the consecutive symbols in a user frame. The operation of the outer loop starts with a decoding window of length equal to one symbols and then increases with the number of stages. At the first stage (the initial stage of decoding) the outer loop decoder employs the inner loop decoder to recover initial estimate of the partial symbol. At the end of the last stage, the outer loop decoder recover the first two symbols in the colliding frames at the receiving station. After that, the decoder resets its window to start with a fresh collision-free partial symbols.

In the data link layer, the system is designed to transmit two consecutive acknowledgements to the two colliding transmitters after successful data re-

covery. The system evaluation presented in this chapter considered different scenarios including collision of various frame types in this system design. In addition, different network topologies were implemented and evaluated.

The system was evaluated in a testbed of 12-nodes using software defined radio platforms and in NS-3 simulator. The extensive experimental results presented in this chapter, show 10–21% throughput enhancement in 802.11n systems when downlink bulk TCP, downlink video-on-demand and uplink UDP are operated in rich collision environment and under different scenarios.

# Chapter 7

## Conclusions

Spectrum is one of most essential resources in any communications system, especially so in wireless networks. Hence, research into spectral saving new signal formats has increased rapidly over the last decade, with several candidate technologies. OFDM modulation format, which was briefly introduced in Chapter 2, is a classic multicarrier technology, which has been widely used in 4G, 5G and several of 802.11x standards due to its ability to mitigate distortion arising from frequency selective fading channels, despite its spectral efficiency limitations. Achieving high spectral efficiency is a recurring key challenge in wireless communications systems, which is generally approached using high order and advanced modulation formats including non-orthogonal ones such as SEFDM, one of the non-orthogonal modulation formats, which saves bandwidth by violating the orthogonality of subcarriers, causing interference in the real and imaginary parts of the signal. SEFDM and other non-orthogonal multicarrier signals, which have been considered as candidates for beyond 5G systems, were described in Chapter 2.

The research reported in Chapter 3 of this thesis explored the design and implementation of SEFDM in a real-time testbed. Thus far, non-practical offline testbeds have been reported in the literature and that is due to two main reasons. Firstly, channel estimation and equalization mechanisms were implemented in the time-domain, which is based on matrix inversion that increases the computational complexity exponentially with number of subcarriers and

can not be done in real-time. Second, latency in detecting SEFDM symbols is a main limitation of SEFDM receivers also preventing real-time SEFDM systems. The latency is introduced through either high computational complexity decoders, such as SD, or due to the number of iterations required to decode SEFDM signals using an ID. Research in this thesis addressed these two issues, leading to practical and implementable systems. Using OFDM pilot symbols to obtain interference-free channel estimates and allowing simple one-tap equalization. In addition, pipeline processing was applied in the iterative decoding receivers to reduce decoding latency, enhance throughput and allow practical real-time operation.

The debate concerning the type of guard interval to be used in multi-carrier systems has been resolved, in favour of cyclic prefix, for orthogonal systems. For non-orthogonal systems this issue was yet to be resolved. This is addressed in Chapter 4, where studies were detailed to assess the impact of CP and CCP on SEFDM systems. Work here started by deriving equations to calculate the added interference in such systems on SEFDM subcarriers (on top of the self-created ICI) rendering channel estimation and equalization inaccurate as interference in fact adds to all subcarriers and all portions of the signal including the cyclic prefix part. Consequently, this work proposed a new channel estimation and equalization technique combining ZP with an orthogonal demodulator and utilizing interference (in the ZP part of the signal) to enhance performance relative to when CP and CCP were used. Furthermore, the research in this chapter investigated the use of OFDM for pilot symbols, while using SEFDM with different guard interval techniques (CP, CCP and ZP) for the data symbols. Computer simulation results showed that using OFDM pilot symbols for channel estimation results in optimum channel estimates. The proposed new designs therefore advantageously combine OFDM pilot symbols with ZP-SEFDM data symbols to improve both channel estimation and equalization and error rates.

In Chapter 5, a new signal termed TOFDM, which enhances the data rate of the current existing multicarrier communication systems, was introduced. TOFDM is generated by transmitting only part of an OFDM symbol and discarding the rest. Thus, within the same bandwidth, more data symbols

can be packed in time relative to OFDM; this improves spectral efficiency and increases data rates. The research presented in this chapter provided two system designs; uncoded and coded TOFDM. The uncoded TOFDM systems utilizes sphere decoding to retrieve the transmitted data. On the other hand, the coded TOFDM systems was implemented on top of 802.11a,g standards by modifying the transmitters to send TOFDM signals. An iterative decoder was designed specifically to cancel the self-induced ICI among the subcarriers iteratively, and recover the transmitted data. Practical/experimental evaluation of the new signals, their properties and performance was carried out using specially designed transceivers implemented using SDR National Instruments USRP-Rio platforms, with realistic RF channels emulated using a Spirent VR5 channel emulator.

Inspired by the ability to decode partial information, i.e. present in only part of a symbol as in the new TOFDM signals, Chapter 6 presented a technique that tackles the collision problem in wireless 802.11 systems; this was named PSR. The basic concept is that when two data frames collide, they never collide fully and part of each frame remains collision free. PSR acts on this collision-free partial symbol of two colliding frames at the receiving station to recover the data of both frames, using the TOFDM decoding concepts discussed in Chapter 5. The PSR technique is designed so it requires no modifications at the transmitters of standard 802.11 systems, thus can be seen as an upgrade to existing systems. The receiver design is a detailed design of two layers; physical layer and data link layer. The physical layer design consisted of two nested loops, (i) an inner loop decoder and (ii) an outer loop decoder. The inner loop decoder is responsible of decoding the collision-free part of the symbols and recovering their data by cancelling the self-created ICI, iteratively. The task of the outer loop decoder is to cancel the two users' interference and restrain error rates propagation. After full recovery of two colliding frames at the receiving station, the data link layer of the PSR sends one or two consecutive acknowledgements, depending on the collision scenario, to prevent retransmission, which would be otherwise encountered in traditional systems. This results in substantial improvement in effective data rate and system capacity. The system was evaluated in a testbed of 12-nodes

using experimental SDR platform for signal generation and reception and NS-3 for network layer throughput measurements. The system performance was assessed and compared to the well known SIC technique. Extensive experiments were run for different physical signal parameters, different collision environment parameters, various network scenarios and for a number of nodes and links. Results, shown in a set of figures studying performance statistics, indicated PSR system performance improvement over existing systems in terms of error rates, retransmission rates and throughput.

To sum up, this thesis has reported the world's first real-time SEFDM system implemented in SDR. Analytical modelling expression for different guard interval techniques for SEFDM was mathematically derived and reported. In addition, a new signal modulation format termed TOFDM was proposed and demonstrated. Finally, a new receiving technique termed PSR was proposed, designed and implemented, for successful operation of 802.11 systems in collision environments.

## 7.1 Future Work

The topics explored in this thesis leave several open questions and may lead to new areas of research into signals and systems with the ultimate aim of improving data rates and spectral efficiency whilst having no (or only limited) performance degradation. The five headline areas below make an attempt at broadly specifying such areas of work.

- **SEFDM signals and systems for 802.11 systems.** In 802.11 standards, OFDM has been chosen as the signal modulation for many of its variants. The goal of this thesis work was to upgrade the 802.11 systems by employing TOFDM signals and design appropriate transceivers. Potentially, SEFDM will have similar advantages in 802.11 systems but such, although may be based on the work of Chapters 5 and 6, requires research into specific aspects, not covered in this thesis, such as: (i) a new preamble signal, which is used for frequency offset and channel estimation (full details provided in Section 6.3), should be designed for

SEFDM systems, (*ii*) the pilot signals, which are used for channel and phase tracking (full details provided in Section 6.3), will suffer from interference and hence a new method of phase and channel tracking should be considered, (*ii*) integrate SEFDM signals with ZP into the current existing frame and symbols structure of 802.11.

- **MIMO-SEFDM using ZP guard interval.** In Chapter 4 of this thesis, ZP is found to be the optimum choice to serve as a guard interval in SEFDM systems. This is because using ZP with SEFDM signals allows the wideband channel of the medium to be divided to a set of orthogonal narrowband sub-channels. Therefore, this work may be extended to MIMO-SEFDM systems using ZP. To achieve this and to prove the applicability of this work, mathematical derivations of MIMO-SEFDM should be derived to find the analytical expression of channel estimation and equalization for different guard interval techniques. After that, experimental validation of this proposal should be implemented using SDR platform and tested using a channel emulator.
- **Advanced secure TOFDM systems.** In Chapter 5 of this thesis, TOFDM was reported as a new system to enhance the data rate of existing communication systems. Recently, building on publications of this research, researchers in [143] proposed to use TOFDM systems for security enhancement. This is achieved by truncating different parts of the symbols at the transmitter, which leads to the generation of different interference coefficients in the correlation matrix, where the latter is required at the receiver for signal recovery. Moreover, researchers in [144] proposed using machine learning to classify non-orthogonal signals and to identify signal parameters, such as compression factor. Therefore, the current concept of secure TOFDM may no longer hold. In order to increase the immunity of secure TOFDM, a new truncation algorithm should be designed, resulting in an enhanced, secure TOFDM that is less susceptible to classification by machine learning detectors. To achieve this, a complete study of all possible truncated symbols may be evaluated in terms of interference coefficient and signal

classification error when machine learning tools are applied.

- **Ultra dense FDM for NB-IoT.** In appendix B, repetition time coding with self-ICI cancellation were proposed to enable the use of complex symbols in Fast-OFDM and to save 3 dB in SNR [145]. The concept of self-ICI cancellation is based on transmitting a precoded image of an original Fast-OFDM signal with complex data symbols; where combining the Fast-OFDM signal and its image at the receiver results in self-ICI cancellation. This is the methodology that allows the extension of the modulation format to complex-valued signals for Fast-OFDM. This work may be extended to use the repetition time coding with self-ICI cancellation for the original Fast-OFDM with BPSK modulation format for NB-IoT systems. Therefore, the new system may compress the spectrum by up to 75% (this system is termed Ultra Dense-Frequency Division Multiplexing (UD-FDM)). In addition, researchers in [51] claim that the higher the bandwidth compression, the better the PAPR performance. Hence, the UD-FDM system should show advantage in PAPR because the bandwidth is compressed by up to 75% which makes the system a very good candidate for NB-IoT systems.
- **Fast-OFDM for 802.11ah.** In 802.11ah [146], a new mode has been designed and introduced which is the 1 MHz MCS10 mode, which is designed for narrowband modes of Internet of Things (IoT) systems. The new mode uses BPSK-OFDM as the signal modulation format. In Chapters 5 and 6 of this thesis, TOFDM signal was employed in 802.11 systems to enhance their spectral efficiency. Potentially, Fast-OFDM, which is a subset of SEFDM systems, will have similar advantages in 802.11 systems and more specifically in the 1 MHz MCS10 mode of 802.11ah systems. This is because Fast-OFDM, presented in Section 2.3.1 of this thesis, has the ability to save 50% of the signal bandwidth, however, it is only applicable for one-dimensional modulation formats, such as BPSK. Therefore, the 1 MHz MCS10 mode can be enhanced by adopting Fast-OFDM instead of using OFDM. This can

lead to 50% bandwidth enhancement and hence double the number of the IoT devices.

# Appendix A

## SEFDM LabVIEW Code

The SEFDM LabVIEW code is the complete transceiver with system controller built in LabVIEW Communications System Design Suite and it consists of the panel and the diagram platforms. This code is available for the community of National Instruments software defined radio developers, and a description of the system is available in an article on: [The SEFDM article](#). This article appears in Appendix A.3.

### A.1 The Panel Platform

The panel platform represents the system monitoring and the parameters controller. The panel system monitoring is used to monitor: frequency spectrum, constellation diagrams of the received, equalized and detected SEFDM symbols and the BER measurements.

The parameters controller can be classified into two groups, (*i*) the RF system configuration parameters and (*ii*) the transceiver signal processing parameters. The RF system parameters are responsible of enabling/disabling the transmitters/receivers and setting the centre frequency, the sampling rate and the number of transmitted complex samples. The signal processing parameters are responsible of setting the transmitted signals parameters, such parameters are FFT size, CP length and the compression factor ( $\alpha$ ).

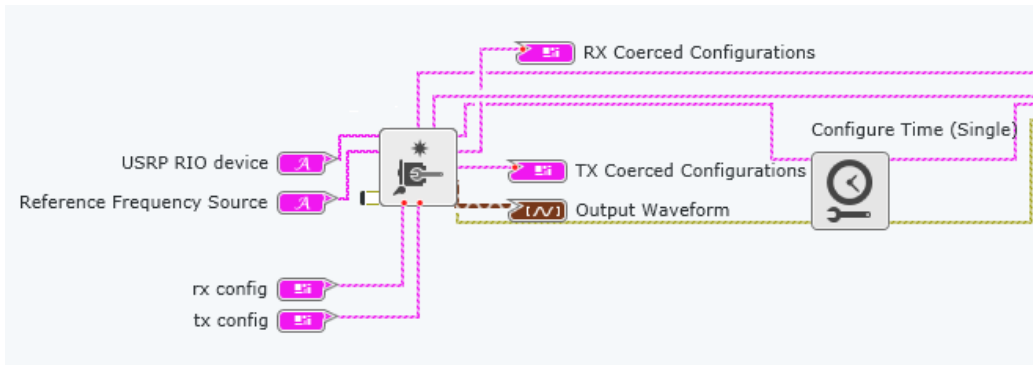


**Figure A.1:** The USRP setting configurations blocks

## A.2 The Diagram Platform

The diagram platform has the LabVIEW code, which is the complete transceiver system code. The code has two parts, (i) the USRP settings part and (ii) the main loop transceiver. The USRP settings, which is shown in Figure A.1, is responsible of enabling the RF transceivers in the connected USRPs. The RF system parameters must be set before running the code. The main loop transceiver is responsible of all the signal processing steps required to transmit and receive the data. The system transmitter and receiver codes are shown in Figures A.2 and A.3, respectively.

It is worth noting that the LabVIEW codes enabling communications between the USRPs and the computers, converting the signal from digital to analogue or analogue to digital and sampling the signals are all build-in functions in LabVIEW. However, the SEFDM LabVIEW code functions, such as SEFDM signal generation and detection, are newly developed functions. The complete SEFDM system LabVIEW code is available in the National Instrument website and can be found in the following link:

[The SEFDM LabVIEW code link](#)

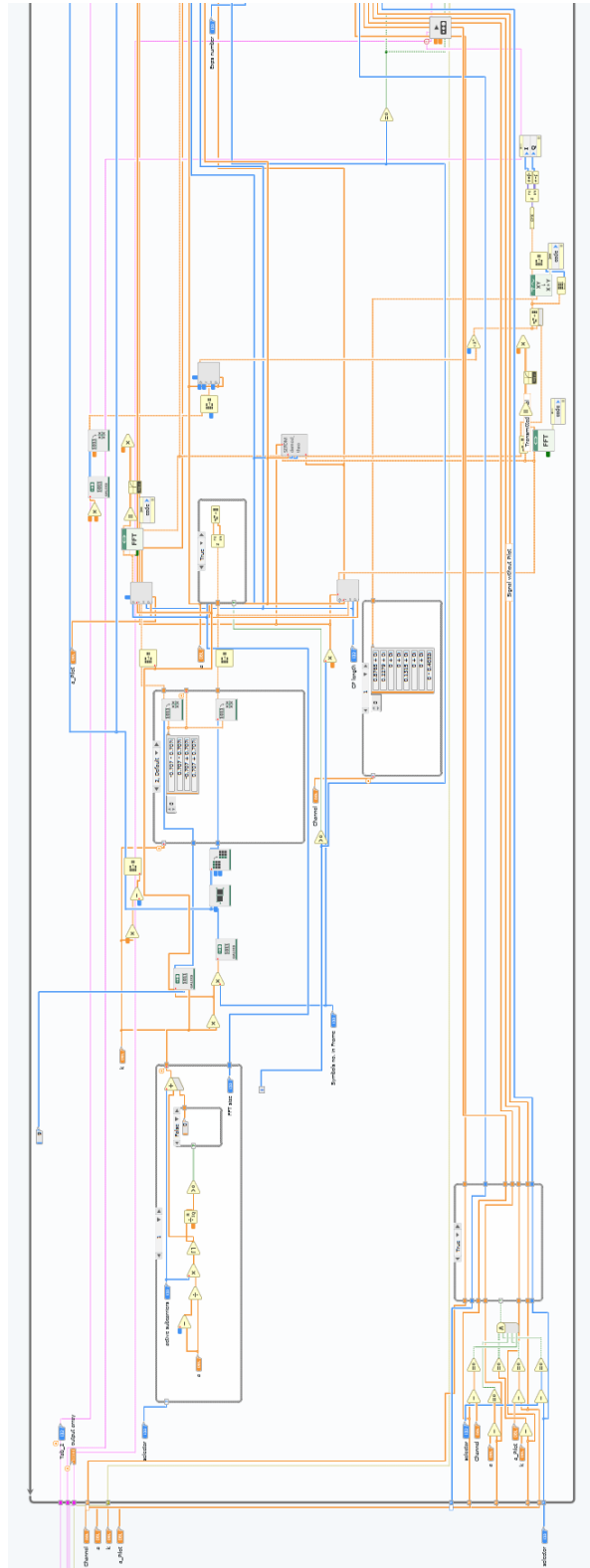


Figure A.2: The LabVIEW code of the SEFDM transmitter



### **A.3 Implementation of the First SEFDM 5G Transceiver Prototype Using LabVIEW Communications System Design Suite and USRP RIO**

## Implementation of the First SEFDM 5G Transceiver Prototype Using LabVIEW Communications System Design Suite and USRP RIO

Waseem Ozan, [University College London](#)



"We estimate that using LabVIEW with the USRP RIO saved us approximately six months in comparison to using the FPGA toolkits for MATLAB."  
- **Waseem Ozan, University College London**

### The Challenge:

Billions of devices will soon be connected to the Internet in line with the vision of the Internet of Things (IoT). This means 5G must make highly efficient use of the wireless spectrum. Spectrally efficient frequency division multiplexing (SEFDM) has the potential to make better use of the spectrum through bandwidth compression, however at the cost of a higher level of interference. Our challenge was to create a real-time testbed, on an industrial platform, to allow the world to investigate SEFDM.

### The Solution:

We demonstrated the world's first real-time SEFDM system using USRP RIO and the LabVIEW Communications System Design Suite. The key innovation is in the deployment of a novel real-time channel estimation and equalisation algorithm, combined with a real-time iterative detector. Our system compresses transmitted signal bandwidths up to 60% (for BPSK) and 30% (for QPSK), offering significant bandwidth savings, thereby satisfying one of the key challenges of 5G deployment.

### Author(s):

Waseem Ozan - [University College London](#)  
Ryan Grammenos - [University College London](#)  
Hedaia Ghannam - [University College London](#)  
Paul Anthony Haigh - [University College London](#)  
Izzat Darwazeh - [Find this author in the NI Developer Community](#)



**Figure 1.** Our SEFDM System Created With LabVIEW Communications System Design Suite and USRP RIO

### Introduction

Our proposed SEFDM system saves bandwidth by compressing traditional orthogonal frequency division multiplexed (OFDM) subcarrier spacing beyond the orthogonality limit, thus increasing spectral efficiency. This enhancement in spectral efficiency translates directly into a gain in capacity, which is of paramount importance to network operators who could use this technique to add an additional 30 to 60 percent number of subscribers (depending on the modulation format) without higher spectrum licensing costs. Hence, SEFDM becomes a timely and key technique for future 5G communication systems and beyond.

SEFDM, originally developed at University College London (UCL) in 2003, has been the focus of increased interest. Over the last decade, SEFDM systems have been demonstrated through many research publications and laboratory experiments. However, only offline systems have been demonstrated, which simplifies the problem and avoids system-level development at the FPGA level. In this work, we created a real-time system implementation for the first time. This is an important milestone, since the literature typically argues that real-time implementation of SEFDM systems is difficult due to the high level of complexity at the receiver.

Testbed Software and Hardware

To prove the SEFDM concept in real hardware transceivers and test the signals in realistic channels, we carried out two steps. First, we developed and implemented the software design using the LabVIEW Communications System Design Suite, which enabled the rapid development, test and deployment of a system prototype. Subsequently, we synthesised the code for an FPGA using a USRP-2953R software defined radio, to generate the radio frequency signals and modulate them into the SEFDM format. The LabVIEW Suite does this automatically, which was a great advantage because it meant that we only needed to work with the FPGA hardware at a high level.

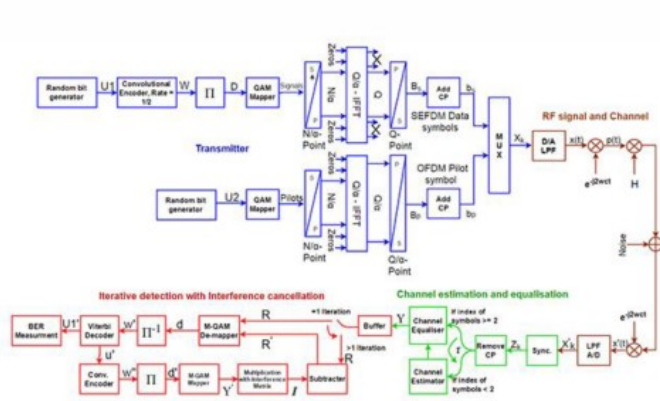


**Figure 1.** Schematic Block Diagram of SEFDM System (blue shows the transmitter; brown shows the RF signal transmission, reception, and channel; green shows channel estimation and equalisation; and red shows the iterative detection with interference cancellation)

The second step was deploying the hardware in a real-world mobile environment over a realistic channel where we employed the Spirent-VR5 channel emulator. We used the LTE EPA5 wireless channel model in this work (others are applicable and have been tested but are not shown here). The USRP RIO devices operate over the 1.2 GHz-6 GHz frequency range, meaning we can use standards

such as IEEE 802.11 and LTE, without loss of generality. The device operates with a 120 MHz sampling frequency that can support video transmission and reception. We also demonstrated over-the-air transmission using two 2.4 GHz antennas as shown in the video.

### Testbed Description

The software design consists of three parts: SEFDM generation and transmission, channel estimation and equalisation, and signal detection.

At the transmitter, we generated a stream of pseudorandom bits, which are encoded by a recursive convolutional coder of code rate  $R_c=1/2$ , where the forward polynomial (G1) is  $G1=1+D+D^2$  and the feedback polynomial (G2) is  $G2=1+D^2$ . The coded bits are interleaved by a block interleaver before being mapped onto the appropriate constellation. We can test binary phase shift keying (BPSK), quadrature phase shift keying (QPSK), 8-phase shift keying (8-PSK) and 16-quadrature amplitude modulation (16-QAM).

Next, we converted the serial symbols into parallel streams and then used an inverse fast Fourier transform (IFFT) for modulation into SEFDM symbols, where the distance between subcarriers is compressed by a factor  $\alpha \leq 1$ , relative to OFDM signals, where  $\alpha=1$ .

In the final stage of the transmitter, the complex signal is fed into the FPGA inside the USRP RIO, which then feeds the signal to the necessary D/A converter, before up-conversion of the signal by a local oscillator to the 2 GHz band.

### World First

In our application, we used a novel method to estimate the channel effect for the SEFDM system. One of the key challenges previously established is that when using bandwidth-compressed pilots (that is, using an SEFDM symbol as a pilot) they are not only impaired by the channel, but also by the inter-carrier interference between the subcarriers, which seriously degrades the channel estimate. In this work, the pilot is sent as an OFDM symbol, but at a lower rate compared to SEFDM symbols. This is because in SEFDM the separation between subcarriers is reduced compared to conventional OFDM. Therefore, we design our OFDM pilot so that the frequencies of the subcarriers equal those of SEFDM but without the inter-carrier interference, which makes these pilots orthogonal. This does not impact the system performance since the pilot carries no user information. This results in clean pilots, allowing the use of a simple one-tap equaliser in the frequency domain to mitigate the effect of the channel.

### Recovering the Signal

To recover the transmitted signal, we developed an iterative detector based on a turbo equalisation technique with an interference canceller (shown in red in Figure 1), which depicts the process of recovering the transmitted signal. The equalised data is de-mapped and de-interleaved at the beginning of each iteration before Viterbi decoding. The correlation matrix has information about the interference generated between the self-interfering SEFDM subcarriers. We can use the estimated correlation matrix and the decoded data to estimate the interference generated between the SEFDM subcarriers.

After subtracting the estimated interference from the received signal, the resulting signal passes back into the decoding process to enhance the interference cancellation; repetition of this process leads to a better estimate of the transmitted data.

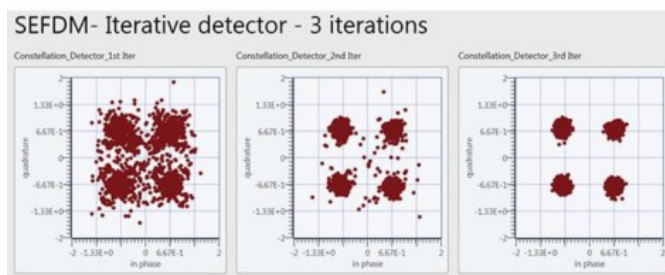


**Figure 2.** SEFDM Iterative Detector Showing Perfect Signal Recovery After Three Iterations While Saving 30 Percent Bandwidth

Figure 2 shows the detected signal after each iteration, where we used a compression factor of 30 percent ( $\alpha=0.7$ ) QPSK-SEFDM. It is clear that the symbols are recovered, error free, using our new channel estimation and equalisation method in combination with an iterative detector.

### Worldwide Benefits

We plan to make the code open source and available online so that the research, industrial and equipment manufacturer communities anywhere in the world can experiment with and develop the system and consider it for future standards. The designed and implemented system is fully interactive for different parameters, such as number of subcarriers, type of pilot symbols, and the compression factor ( $\alpha$ ) so that users can fully appreciate how the parameters will affect their designs. This will impact 5G research and other wireless systems, powering high-quality and high-bit-rate services in a reduced wireless spectrum, which can lower the cost of future systems.

### Working With NI

We chose the USRP RIO and LabVIEW Communications System Design Suite together as they provide a powerful and flexible technology platform to build and prototype our system. We ran the original simulation using The MathWorks, Inc. MATLAB® software. However, when it came to implementing the code on the FPGA, we found it to be significantly faster to use LabVIEW. This is thanks to the LabVIEW Suite handling the minute details of FPGA programming, which would otherwise require a steep learning curve if dealt with by the user. We estimate that using LabVIEW with the USRP RIO saved us approximately six months in comparison to using the FPGA toolkits for MATLAB.

Since this was our first time using NI hardware and software, we sat a three-day LabVIEW Communications training course to get us up and running quickly. We also had one day of support from an NI systems engineer to could answer our questions and to help us progress even faster with our work. Our initial link with NI was with the sales teams in the UK. We have recently extended our links to their research teams (in Dresden, Germany) as well as their educational training teams (in Austin, Texas) and have regular virtual meetings to enhance the system design. This has been very valuable in helping us complete this project in a reasonable time period.

### Conclusion

This work introduces a world-first, experimental, real-time implementation of baseband generation, signal assembly, signal decoding, and a novel frequency domain channel estimation and equalisation method.

Using USRP-2953R with LabVIEW Communications System Design Suite was the right choice to build and rapidly prototype a communication system, in order to realise a real-time SEFDM demonstrator along with the associated software.

### Acknowledgements

This work was part funded by the Engineering and Physical Sciences Research Council (EPSRC) "Discovery to Use Impact Acceleration" award for the development of a pre-commercialisation 5G transceiver prototype. The work was also supported by National Instruments and by a generous donation of the LTE FPGA core through the Xilinx University Program (XUP).

### Author Information:

Waseem Ozan  
University College London  
[w.ozan@ucl.ac.uk](mailto:w.ozan@ucl.ac.uk)

## Next Steps

[Download the Code for the Case Study](#)

[Learn More About the NI SDR Platform](#)

[Read How NI Helped Set the 5G Wireless Spectral Efficiency Record](#)

[Download Your Free Evaluation of LabVIEW to Design a Wireless Communications System Now](#)

## Appendix B

# Time Precoding Enabled Non-Orthogonal Frequency Division Multiplexing

This is a recent work presented at the IEEE International Symposium on Personal, Indoor and Mobile Radio Communications (PIMRC) in September 2019 in Turkey. This work has not been included in the main text of the thesis, but is added in the appendix as reference.

# Time Precoding Enabled Non-Orthogonal Frequency Division Multiplexing

Waseem Ozan\*, Paul Anthony Haigh†, Bo Tan‡ and Izzat Darwazeh\*

\*Department of Electronic and Electrical Engineering, University College London, Gower Street, UK

†Intelligent Sensing and Communications Group, Newcastle University, Newcastle-upon-Tyne, UK

‡Faculty of Information Technology and Communication Sciences, Tampere University, Finland

i.darwazeh@ucl.ac.uk

**Abstract**—In this paper, we propose a time precoding scheme for cancelling inter-carrier interference in non-orthogonal frequency division multiplexing for the first time. Achieving high spectral efficiencies is a recurring and key challenge in wireless communications systems and researchers generally use high order and advanced modulation formats to approach this problem, in particular, non-orthogonal modulation formats are a topic of particular interest. Fast orthogonal frequency division multiplexing (F-OFDM) doubles the throughput of conventional OFDM by violating orthogonality of the quadrature carrier, causing interference in the real and imaginary domains. Here, we propose a precoding scheme that enables self-interference cancellation without the need of the interference level calculation. The proposed scheme is implemented in the context of a narrowband internet-of-things (NB-IoT) system and verified on a software define radio (SDR) testbed with realistic AWGN and multiple path channels from channel emulator for concept proving. By comparing with the standard OFDM transmission, the time precoded F-OFDM outperforms around 3dB by BER with same signal-to-ratio (SNR) level.

**Index Terms**—Time precoding, non-orthogonal, Fast OFDM, spectrally efficient, NB-IoT waveform.

## I. INTRODUCTION

Spectrum is one of most essential resources in any communications system, but even more so in wireless networks. Orthogonal frequency-division multiplexing (OFDM) [1] is one of the classic FDM technologies and has been widely used in 4G/5G and several of 802.11x standards due to its ability to manage spectral nulls and maintain high throughput. Taking advantage of orthogonality between subcarriers (i.e. subcarrier separation of  $1/T$ , where  $T$  is the symbol period), OFDM successfully controls the inter-carrier interference (ICI). However, should this condition be violated, i.e. subcarrier separation  $< 1/T$ , orthogonality is violated and ICI is introduced.

Driven by increasing user density and high data rate applications, such as real time video and audio streaming, researchers have been exploring new solutions for compressing the spectrum. Fast orthogonal frequency-division multiplexing (F-OFDM) [2, 3] is a subset of spectrally efficient frequency division multiplexing (SEFDM) [4, 5]. F-OFDM is one important and widely discussed approach in which the spacing between subcarriers is compressed below the Nyquist limit to  $1/2T$ .

This work was supported by the UK EPSRC grant EP/P006280/1: Multi-functional Polymer Light-Emitting Diodes with Visible Light Communications (MARVEL). WO acknowledges a UCL studentship for his PhD studies.

Unlike OFDM, F-OFDM is a non-orthogonal scheme, which packs twice as many subcarriers into the same spectrum as OFDM, thereby doubling the spectral efficiency [2]. F-OFDM's ability to save spectrum makes it a topic of increased research interest, as exemplified by the wide-ranging work that is being carried out [6–14]. However, the compression in the frequency domain causes interference exclusively in the real portion of the signal to the imaginary portion and vice versa, thus limiting the modulation to one dimension formats, such as binary phase shift keying (BPSK). Though a spectrally efficient system has been demonstrated to use a zero-forcing strategy [9] to estimate the channel, there is still strong ICI components remaining in the received signal. Thus, an effective ICI cancellation method is key to utilise fully the bandwidth saving at the same time for both the real and quadrature components of the signal. In [9], zero-forcing based waveform precoding for ICI suppression and orthogonal space precoding was used to avoid interference between antennas. Zero-forcing is a well established method to cancel out the interference, however, it results in noise-enhancement. In addition, the work in [15] implements self interference cancellation by sending a complex symbol with its precoded copy onto two neighbouring subcarriers, however, the data rate is halved.

In this paper, we propose a precoding scheme that tackles the ICI problem in the quadrature part of the signal. Inspired by Alamouti space-time block code [16] in multiple-input and multiple-output (MIMO), we leverage on the fact that F-OFDM utilises half the bandwidth of OFDM signals to counterpart the ICI in frequency domain, by generation of the image of the interference matrix. The detailed coding scheme is described in Section IV. By application of our precoding method, we demonstrate that quadrature amplitude modulation (QAM) constellations can be supported using F-OFDM whilst maintaining equivalent data rate to that of OFDM with the same order QAM. The contributions of the paper are:

- A new precoding scheme is proposed to cancel the ICI in F-OFDM without noise-enhancement.
- The ICI cancellation level is derived in analytic form.
- The time precoding non-orthogonal FDM is implemented and verified on software define radio (SDR) test-bed with realistic signal propagation environment.
- The new design demonstrates ICI cancellation in F-OFDM

enabling QAM constellation transmission for the first time.

The rest of the paper is organised by following order: Section II introduces the signal model of traditional F-OFDM; ICI of F-OFDM is modelled in Section III; We described the time precoding in detail in Section IV; In Section V, the ICI cancelling performance of time precoding F-OFDM and final BER performance are shown with comparison with OFDM; At last the conclusion and future work are given in Section VI.

## II. FAST-OFDM SIGNAL MODEL

In F-OFDM, thus far, symbols have been parallelised into  $N$  real-valued data streams for modulation onto  $N$  subcarriers spaced at  $1/2T$ . For the same value of  $N$ , F-OFDM offers 50% bandwidth saving compared to OFDM at the same transmission speed and for the same number of bits/symbol. The discrete time-sampled F-OFDM symbol is, in general, expressed as [2, 3, 11]:

$$x(k) = \frac{1}{\sqrt{Q}} \sum_{n=0}^{Q-1} S_n \cos \left[ \frac{2\pi nk}{2Q} \right] \quad (1)$$

where  $k = \{0, 1, 2, \dots, Q-1\}$  is the index of the time samples in an F-OFDM symbol,  $\rho$  is the oversampling rate,  $Q = \rho N$  and  $S_n$  is the input symbol modulated on the  $n^{\text{th}}$  subcarrier. Note, we include the factor of two on the numerator and denominator to highlight the factor-of-two difference with conventional OFDM [2, 3].

One of the issues with this transformation is that it neglects the quadrature portion of the Fourier transform and hence imposes the limitation for one dimensional, normally real-valued modulation formats. If one considers the quadrature part, and modulates a complex-valued signal, the transform becomes [11, 12]:

$$x(k) = \frac{1}{\sqrt{Q}} \sum_{n=0}^{Q-1} S_n \exp \left[ \frac{j2\pi nk}{2Q} \right] \quad (2)$$

Note, it is expected at this stage that the signal will contain significant inter-carrier interference due to the obvious loss of orthogonality.

An equivalent method for representing the discrete F-OFDM symbol is the matrix form:

$$X = \mathbf{F}S \quad (3)$$

where  $X$  represents a  $Q$ -dimensional vector of a sampled F-OFDM symbol in the time-domain,  $S$  is an  $Q$ -dimensional vector of a complex-valued sampled input signal in the frequency-domain and  $\mathbf{F}$  is a  $Q \times Q$  matrix representing the sampled carrier matrix. The matrix elements of  $\mathbf{F}$  are given by  $\mathbf{F}_{k,n} = \frac{1}{\sqrt{Q}} e^{j2\pi nk/2Q}$ .

Consider that the transmitted F-OFDM symbols pass through an additive white Gaussian noise channel (AWGN), which leads to a signal contaminated by noise  $Z$ , and hence, the received signal is expressed as follows:

$$\begin{aligned} R &= \mathbf{F}^H X + \mathbf{F}^H Z = \mathbf{F}^H \mathbf{F} S + \mathbf{F}^H Z \\ &= \mathbf{C} S + Z_{FH} \end{aligned} \quad (4)$$

where  $R$  is the demodulated signal vector that consists of symbols and has length  $Q$ ,  $\mathbf{C}$  is the correlation matrix [17],  $Z_{FH}$  is a vector of AWGN samples correlated with the conjugate subcarriers, and  $(\cdot)^H$  is the transpose conjugate operation.

## III. CHARACTERISING ICI IN F-OFDM SYSTEMS

The correlation matrix  $\mathbf{C}$  quantifies the interference contribution on each subcarrier from its neighbouring subcarriers [17]. Its components can be found as:

$$\begin{aligned} \mathbf{C}_{(l,n)} &= \mathbf{F}_{(l,p)}^H \mathbf{F}_{(p,n)} \\ &= \frac{1}{Q} \sum_{p=0}^{Q-1} \exp \left[ \frac{-j2\pi lp}{2Q} \right] \exp \left[ \frac{j2\pi pn}{2Q} \right] \\ &= \frac{1}{Q} \sum_{p=0}^{Q-1} \exp \left[ \frac{-j\pi(l-n)p}{Q} \right] \\ &= \begin{cases} 1, & l = n \\ \frac{1}{Q} \sum_{p=0}^{Q-1} \exp \left[ \frac{-j\pi(l-n)p}{Q} \right], & l \neq n \end{cases} \quad (5) \\ &= \begin{cases} 1, & l = n \\ \frac{1}{Q} \left[ \frac{1 - \exp[-j\pi(l-n)]}{1 - \exp\left[\frac{-j\pi(l-n)}{Q}\right]} \right], & l \neq n \end{cases} \end{aligned}$$

The final derivation in (5) is based on the sum of geometric series:  $\sum_{k=0}^{Q-1} r^k = \frac{1-r^Q}{1-r}$ . From (5), we can represent the correlation matrix in summation form of two matrices as:

$$\mathbf{C} = \mathbf{I} + \mathbf{\Lambda} \quad (6)$$

where the matrix  $\mathbf{I}$  is a  $Q \times Q$  identity matrix and the matrix  $\mathbf{\Lambda}$  carries the interference contribution on each subcarrier and is given as:

$$\mathbf{\Lambda} = \begin{cases} 0, & l = n \\ 0, & l \neq n \ \& \ |l \pm n| \text{ is even} \\ \frac{1}{Q} \left[ \frac{1 - \exp[-j\pi(l-n)]}{1 - \exp\left[\frac{-j\pi(l-n)}{Q}\right]} \right], & l \neq n \ \& \ |l \pm n| \text{ is odd} \end{cases} \quad (7)$$

After substituting (6) in (4), the demodulated signal is represented as:

$$\begin{aligned} R &= \mathbf{C} S + Z_{FH} = (\mathbf{I} + \mathbf{\Lambda}) S + Z_{FH} \\ &= \mathbf{I} S + \mathbf{\Lambda} S + Z_{FH} = S + \mathbf{\Lambda} S + Z_{FH} \end{aligned} \quad (8)$$

where the term  $\mathbf{\Lambda} S$  indicates the additional ICI components that are added to each subcarrier.

## IV. TIME PRECODING SELF-INTERFERENCE CANCELLATION

The concept of self-ICI cancellation is based on transmitting a precoded image of an original F-OFDM signal; where combining the F-OFDM signal and its image at the receiver results in self-ICI cancellation. This is the methodology that allows us to extend the modulation format to complex-valued signals for the first time.

### A. Generating a precoded image

The precoded image of the signal is generated by multiplication of the complex data symbols ( $S$ ) with the column vector  $\Gamma$  before F-OFDM modulation using (2). At the receiver, the signal is once again multiplied with the same vector  $\Gamma$ , which is given as:

$$\Gamma_{(n,1)} = \begin{cases} 1, & |n| \text{ is even} \\ -1, & |n| \text{ is odd} \end{cases} \quad (9)$$

The received image signal of the original signal that is given in (4) is re-written and represented as:

$$\begin{aligned} R' &= \Gamma \mathbf{F}^H X' + \mathbf{F}^H Z = \Gamma \mathbf{F}^H \mathbf{F} \Gamma S + \mathbf{F}^H Z \\ &= \mathbf{C}' S + Z_{FH} \end{aligned} \quad (10)$$

### B. Characterizing the ICI of the precoded F-OFDM image

In this design, we derive the F-OFDM image and its correlation matrix as follows:

$$\begin{aligned} \mathbf{C}'_{(l,n)} &= \Gamma_{(l,1)} \mathbf{F}_{(l,p)}^H \mathbf{F}_{(p,n)} \Gamma_{(n,1)} \\ &= \frac{1}{Q} \left[ \sum_{l=0}^{Q-1} (-1)^l \exp \left[ \frac{-j2\pi lp}{2Q} \right] \sum_{n=0}^{Q-1} \exp \left[ \frac{j2\pi pn}{2Q} \right] (-1)^n \right] \\ &= \frac{1}{Q} \sum_{p=0}^{Q-1} (-1)^l e^{\left(\frac{-j\pi lp}{Q}\right)} e^{\left(\frac{j\pi pn}{Q}\right)} (-1)^n \\ &= \frac{1}{Q} (-1)^{1+n} \sum_{p=0}^{Q-1} e^{\left(\frac{-j\pi(l-n)p}{Q}\right)} \\ &= \begin{cases} 1, & l = n \\ 1/Q (-1)^{1+n} \sum_{p=0}^{Q-1} e^{(-j\pi(l-n)p/Q)}, & l \neq n \end{cases} \\ &= \begin{cases} 1, & l = n \\ 0, & l \neq n \ \& \ |l \pm n| \text{ is even} \\ -1/Q \left[ \frac{1 - e^{-j\pi(l-n)}}{1 - e^{-j\pi(l-n)/Q}} \right], & l \neq n \ \& \ |l \pm n| \text{ is odd} \end{cases} \\ &= \mathbf{I} - \mathbf{\Lambda} \end{aligned} \quad (11)$$

Thus, (10) is formulated as:

$$\begin{aligned} R' &= \mathbf{C}' S + Z'_{FH} = (\mathbf{I} - \mathbf{\Lambda}) S + Z_{FH} \\ &= \mathbf{I} S - \mathbf{\Lambda} S + Z'_{FH} = S - \mathbf{\Lambda} S + Z'_{FH} \end{aligned} \quad (12)$$

### C. Self-interference mechanism

After obtaining the original F-OFDM symbol and its precoded image, we add the two symbols together. The resulting signal is therefore given as:

$$\begin{aligned} A &= R + R' = S + \mathbf{\Lambda} S + Z_{FH} + S - \mathbf{\Lambda} S + Z'_{FH} \\ &= 2S + Z_{FH} + Z'_{FH} \end{aligned} \quad (13)$$

It should be noted that the proposed precoding ICI scheme stands based on the assumption that the channel remains invariant during one pair of original F-OFDM and its precoding image transmission period.

## V. TESTBED DESCRIPTIONS

In this section we present the software and hardware designs of the real-time experiment of the proposed F-OFDM with the self-ICI cancellation mechanism. The experimental testbed contains a universal software radio peripheral (USRP) reconfigurable input-output (RIO) transceiver (National Instruments USRP-RIO 2953) programmed using LabVIEW, an Anritsu MS2830A signal analyser and a Spirent VR5 channel emulator for realistic frequency selective channels and noise generation within the analogue radio frequency (RF) domain. All of the digital signal processing blocks including the generation and detection of the signals as well as the proposed self-ISI cancellation methods are implemented in real-time. A photograph of the experimental testbed is shown in Fig. 1.

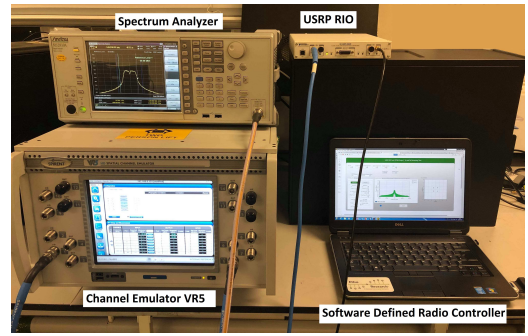


Fig. 1. Time precoding F-OFDM testbed.

### A. Signal generation and transmission

At the transmitter, a pseudorandom binary sequence is generated and mapped onto the QAM constellation, with order  $M$ . In this experiment, we test both 4- and 16-QAM without loss of generality. Afterwards, the symbols are converted to an  $N$ -width parallel stream via a serial-to-parallel ( $S/P$ ) converter which feeds an inverse fast Fourier transform (IFFT), thus generating the F-OFDM signal as depicted in Fig. 2 (the blocks at the top surrounded by the dotted green line). The frequency spacing between the subcarriers in the generated F-OFDM signal is halved in comparison to that of conventional OFDM. A precoding image of the same signal is generated following the method described in section IV as shown in Fig. 2 (the blocks in the middle surrounded by dashed red line), and then the F-OFDM and its precoding image are sent using time-division multiplexing. Next, following parallel-to-serial conversion ( $P/S$ ), and to limit the effect of inter-symbol interference (ISI) between adjacent symbols in the wireless frequency selective channel, a cyclic prefix is added at the beginning of the transmitted F-OFDM symbol. In the final transmission stage, the complex F-OFDM signal is fed into the field-programmable gate array (FPGA) that drives the USRP-RIO device, to perform digital-to-analogue conversion (DAC) and up-conversion to a 2 GHz RF carrier via a local oscillator. The signal generation processes are in Fig. 2, and system parameters, which follow the narrowband internet-of-things (NB-IoT) specifications [18], are in Table I.

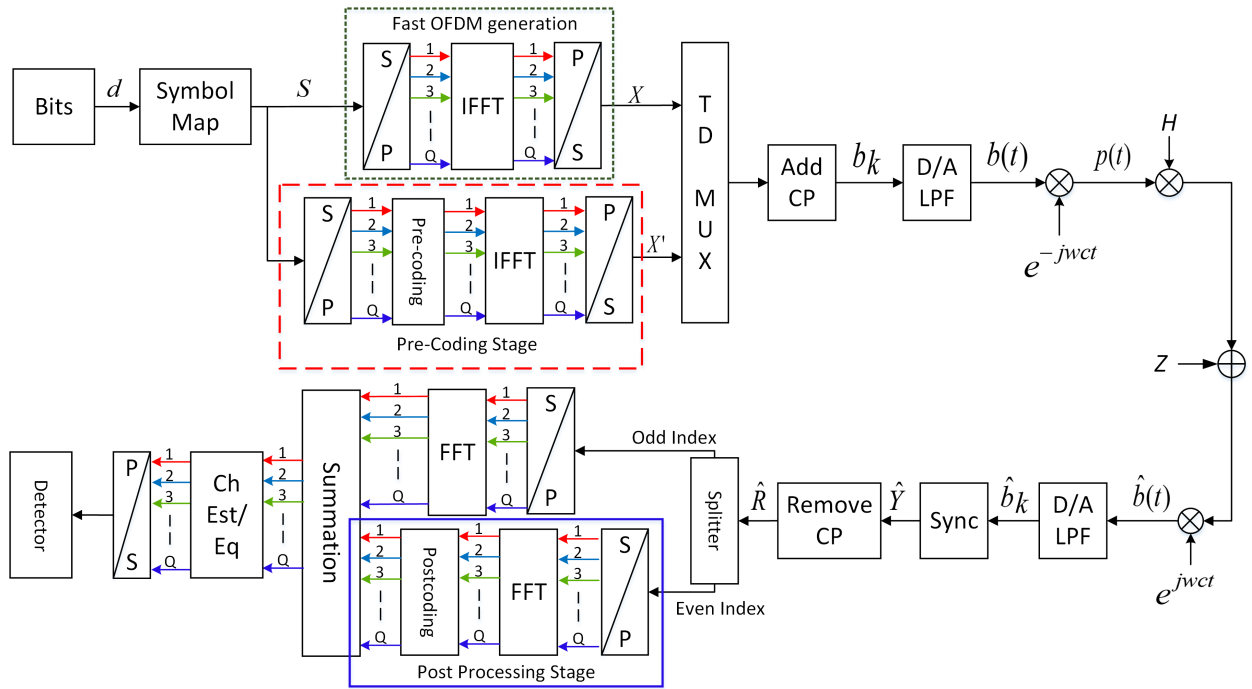


Fig. 2. Schematic block diagram of time precoding F-OFDM system.

TABLE I  
EXPERIMENTAL SYSTEM SPECIFICATIONS

Parameters	OFDM	F - OFDM
Central carrier frequency (GHz)	2	2
Sampling frequency (MHz)	1.92	1.92
Signal bandwidth (KHz)	180	90
Subcarrier baseband bandwidth (KHz)	15	15
Subcarrier spacing (KHz)	15	7.5
IFFT/FFT size	128	256
Number of cyclic prefix samples	10	10
Number of data samples	128	128
Number of data subcarriers	12	12
Modulation scheme	4-QAM 16-QAM	4-QAM 16-QAM

### B. Frame structure

We use a system with frame similar to those of Long-Term Evolution (LTE) [18] where every radio frame of length 10 ms consists of ten equally sized subframes, each of which contains  $2 \times 0.5$  ms time slots. In every time slot, there are seven F-OFDM symbols; thus, every subframe contains 14 symbols. Of these 14 symbols, two carry a pilot that is used for channel estimation and the other 12 symbols carry data signals. Fig. 3 depicts the frame structure of the transmitted signal.

### C. Frequency selective channel and signal synchronisation

The RF frames are transmitted over a mobile environment implemented using the VR5 channel emulator. We used the LTE EPA5 wireless channel model in this work [19] (although others are applicable and have been tested but not shown here). The output of the channel emulator is fed into the USRP-RIO

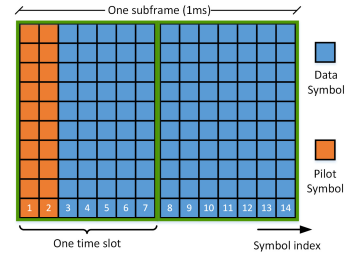


Fig. 3. Radio frame structure.

device, which down-converts the RF signal to baseband before analogue-to-digital conversion (ADC). For frame synchronisation, the popular and effective Schmidl & Cox technique [20] is applied where two identical time sequences are attached to each radio frame.

### D. Channel estimation/equalisation and signal detection

After CP removal, the even indexed symbols are processed as in Eq. 10 as depicted in Fig. 2 (the blocks at the bottom surrounded by the solid blue line) and then every two data symbols (i.e. the odd and the following even indexed symbol pairs) are summed to cancel the ICI between subcarriers. This summation process of the odd and even indexed symbols is given in Eq. 13. Then, channel estimation (using zero-forcing estimator in frequency domain [21]) and signal equalisation (using a one-tap equaliser in the frequency domain [21]) are applied to mitigate the channel effects. The resulting signal is free of ICI and channel effects, however, it is contaminated with

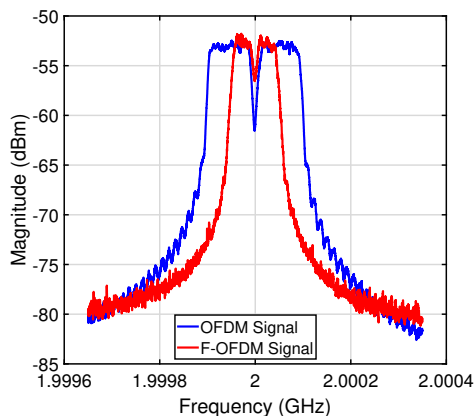


Fig. 4. Measured spectra for OFDM and F-OFDM.

the noise generated at the receiver. Therefore, a hard decision decoder is applied to recover the transmitted data.

## VI. SYSTEM PERFORMANCE

The frequency spectra of the two received signals, F-OFDM and OFDM, are shown in Fig. 4. In the case of using F-OFDM, only 50% of the bandwidth is required to transmit data with the same bit rate as OFDM. However, in this self-ICI cancellation F-OFDM method, we transmit the signal twice, which leads to loss of the standard F-OFDM 50% bandwidth saving.

In Fig. 5, constellations for 4- and 16-QAM using the proposed self-ICI cancellation system are shown. From left to right, the first two constellations show the received F-OFDM signal and its precoded image, respectively. It is clear that the two signals in the constellations are highly distorted by the ICI generated between the subcarriers due to the 50% reduction in the frequency spacing between subcarriers. The third constellations indicate the results of the summation of the two constellations (i.e. the summation of F-OFDM and its precoded signal). It is evident that the ICI generated among subcarriers is cancelled in the summation process, which leads to self-ICI cancellation. Clearly, at this stage the data cannot be recovered successfully because of the channel effects and system hardware impairments, therefore, an equalisation process is required to cancel these effects. The signal after equalisation (right-most constellations) can then simply be detected using a hard decision decoder.

Finally, we measure bit error rate (BER) for a range of signal-to-noise ratios (SNRs) as a metric to evaluate the performance of the proposed self-ICI cancellation scheme and use the BER performance of conventional OFDM as a benchmark. First, we evaluate the performance in an AWGN channel. In the experimental system noise is accurately generated and added to the RF signal by the channel emulator. The 4- and 16-QAM BER comparisons of OFDM and self-ICI cancellation F-OFDM are shown in Fig. 6. Second, we test the system performance across the (frequency selective, multi-path) LTE EPA5 channel contaminated with AWGN noise. The 4- and 16-QAM BER performances of both OFDM and F-OFDM

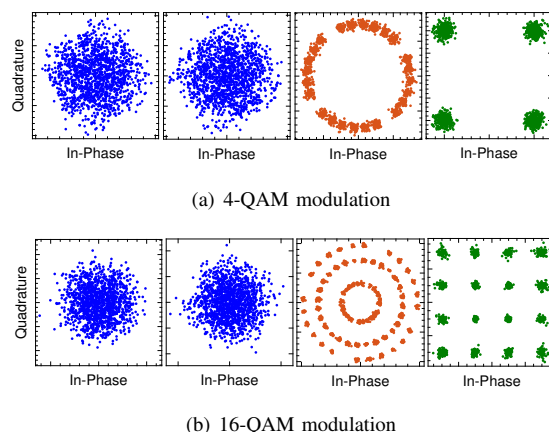


Fig. 5. Received constellations for 4-QAM and 16-QAM signals. For both row (a) and (b), from left to right, the first two constellations show the received F-OFDM and precoded signals; the third shows the summation of the two signals; and the most right constellation shows the signal after equalisation process.

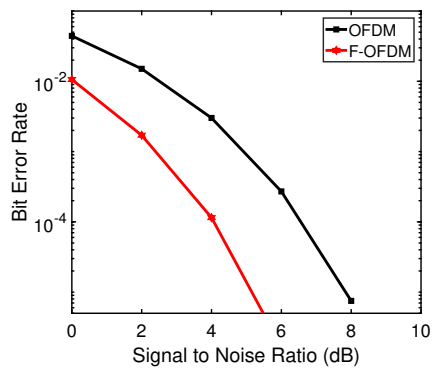
with self-ICI cancellation are shown in Fig. 7. The results in Fig. 6, prove that the simple addition process of the original F-OFDM signal and its precoding image at the receiver is sufficient to cancel the ICI between the subcarriers caused by the compression in signal bandwidth, and hence enable data recovery when using complex modulation formats for the first time. The BER performance shown in Fig. 7 indicates that the multi-path effects degrade the performance of both systems under test, where the  $\sim 3$  dB performance gap (i.e. in SNR) is maintained for either the AWGN or noisy multi-path channel. The reason for this SNR gap is simply that the time precoding F-OFDM transmits the signal twice. The first transmission is the original F-OFDM signal and the second is the precoding copy of the same signal. Therefore, the signal power at the receiver adds up, while the ICI of the two signals is mutually cancelled. Hence, the proposed F-OFDM method demonstrates a 3 dB SNR advantage over OFDM.

## VII. CONCLUSION

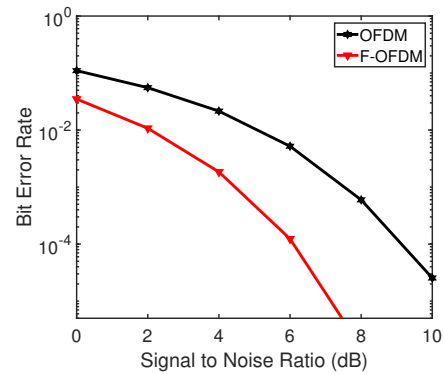
In this work, we proposed a time precoding method for cancelling out the ICI in F-OFDM transmission. The analytic ICI cancelling process of the proposed method is provided and the performance is assessed with experimental SDR system and BER measurements. The proposed time precoding and self ICI cancelling method is experimentally shown to be effective in both AWGN and frequency selective multi-path channels, thus paving the way for the practical use of F-OFDM in wireless data transmission. Furthermore, this work will hopefully inspire future exploration of spatial and joint time-space precoding for non-orthogonal multicarrier system, which may improve the spectral and energy efficiency of wireless communication standards.

## REFERENCES

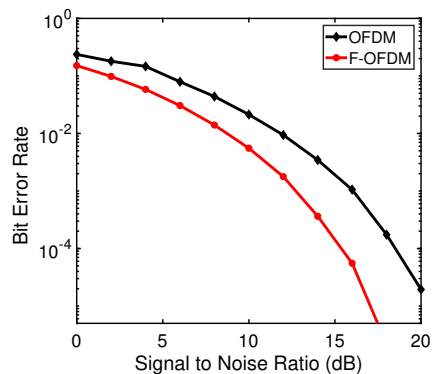
- [1] Y. S. Cho; J. Kim; W. Y. Yang; C. G. Kang, "Introduction to OFDM," in *MIMO-OFDM Wireless Communications with MATLAB*, , IEEE, 2010.



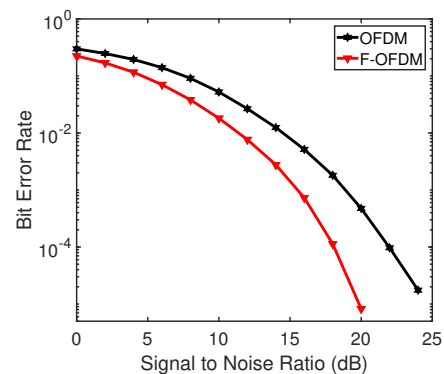
(a) 4-QAM modulation



(a) 4-QAM modulation



(b) 16-QAM modulation



(b) 16-QAM modulation

Fig. 6. Experimental BER of 4-QAM and 16-QAM for OFDM and F-OFDM signals in AWGN channel.

Fig. 7. Experimental BER of 4-QAM and 16-QAM for OFDM and F-OFDM signals in LTE EPA5 channel.

- [2] M. Rodrigues and I. Darwazeh, "Fast OFDM: a proposal for doubling the data rate of OFDM schemes," in *International conference on Telecommunications*, vol. 3, 2002.
- [3] K. Li "Fast orthogonal frequency division multiplexing (Fast-OFDM) for wireless communications", PhD Thesis, UCL, 2008.
- [4] I. Kanaras, A. Chorti, M. R. D. Rodrigues and I. Darwazeh, "Spectrally Efficient FDM Signals: Bandwidth Gain at the Expense of Receiver Complexity," *Communications, 2009. ICC '09. IEEE International Conference on*, Dresden, 2009, pp. 1-6.
- [5] I. Darwazeh, H. Ghannam and T. Xu, "The First 15 Years of SEFDM: A Brief Survey," 2018 11th International Symposium on Communication Systems, Networks & Digital Signal Processing (CSNDSP), Budapest.
- [6] T. Xu and I. Darwazeh, "Non-Orthogonal Narrowband Internet of Things: A Design for Saving Bandwidth and Doubling the Number of Connected Devices," in *IEEE Internet of Things Journal*, vol. 5, no. 3, pp. 2120-2129, June 2018.
- [7] T. Xu and I. Darwazeh, "Non-Orthogonal Waveform Scheduling for Next Generation Narrowband IoT," 2018 *IEEE Globecom Workshops (GC Wkshps)*, Abu Dhabi, United Arab Emirates, 2018, pp. 1-6.
- [8] S. K. Ibrahim, J. Zhao, D. Rafique, J. A. O'Dowd and A. D. Ellis, "Demonstration of world-first experimental optical Fast OFDM system at 7.174Gbit/s and 14.348Gbit/s," *36th European Conference and Exhibition on Optical Communication*, Torino, 2010, pp. 1-3.
- [9] T. Xu, C. Masouros and I. Darwazeh, "Waveform and Space Precoding for Next Generation Downlink Narrowband IoT," in *IEEE Internet of Things Journal*.
- [10] Z. Hu and C. Chan, "A 7-D Hyperchaotic System-Based Encryption Scheme for Secure Fast-OFDM-PON," in *Journal of Lightwave Technology*, vol. 36, no. 16, pp. 3373-3381, 15 Aug. 2018.
- [11] P. Anthony Haigh and I. Darwazeh, "Visible light communications: Fast-orthogonal frequency division multiplexing in highly band limited conditions," *2017 IEEE/CIC International Conference on Communications in China (ICCC Workshops)*, Qingdao, 2017, pp. 1-8.
- [12] Z. Hu, J. Zhao, Y. Hong, S. Gao, C. Chan and L. Chen, "Set-Partitioned QAM Fast-OFDM with Real-Valued Orthogonal Circulant Matrix Transform Pre-Coding," *2018 Conference on Lasers and Electro-Optics (CLEO)*, San Jose, CA, 2018, pp. 1-2.
- [13] W. Ozan, P. A. Haigh, B. Tan and I. Darwazeh, "Experimental SEFDM Pipelined Iterative Detection Architecture with Improved Throughput," *IEEE 87th Vehicular Technology Conference (VTC Spring)*, Porto, 2018.
- [14] F.-L. Luo and C. Zhang, *Signal Processing for 5G: Algorithms and Implementations*. Wiley, 2016.
- [15] T. Xu and I. Darwazeh, "Experimental Validations on Self Interference Cancelled Non-Orthogonal SEFDM Signals," *2018 IEEE 87th Vehicular Technology Conference (VTC Spring)*, Porto, 2018, pp. 1-5.
- [16] S. Alamouti, "A simple transmit diversity technique for wireless communications," *IEEE J. Sel. Areas Commun.*, vol. 16, no. 8, Oct. 1998.
- [17] S. Isam and I. Darwazeh, "Characterizing the intercarrier interference of non-orthogonal Spectrally Efficient FDM system," *2012 8th International Symposium on Communication Systems, Networks & Digital Signal Processing (CSNDSP)*, Poznan, 2012, pp. 1-5.
- [18] LTE; Evolved Universal Terrestrial Radio Access (E-UTRA); Physical Layer Procedures, Rel. 14, 3GPP Standard v.14.2.0, Apr. 2017.
- [19] Evolved Universal Terrestrial Radio Access (E-UTRA); Base station radio transmission and reception, 3GPP TS 36.104 V10.2.0, May 2011.
- [20] T. M. Schmidl and D. C. Cox, "Robust frequency and timing synchronization for OFDM," in *IEEE Transactions on Communications*, vol. 45, no. 12, pp. 1613-1621, Dec 1997.
- [21] S. Boumard and A. Mammela, "Channel estimation versus equalization in an OFDM WLAN system," *IEEE Vehicular Technology Conference, Spring 2001*. Proceedings (Cat. No.01CH37202), Rhodes, Greece, 2001.

# Appendix C

## Partial Symbol Recovery Paper

The work presented in Chapter 6 of this thesis has been prepared for submission to the IEEE/ACM Transactions on Networking. The final draft of this journal paper, titled “Shifting perspective to operate interfering wireless networks beyond capacity”, is presented in this appendix.

# PSR: Partial Symbol Recovery to Operate Interfering Wireless Networks in Collision Environments

Waseem Ozan, Izzat Darwazeh, Kyle Jamieson

The uplink data rate region for interfering transmissions in wireless networks has been characterized and proven, yet its underlying model assumes a complete temporal overlap. Practical unplanned networks, however, adopt packetized transmissions and eschew tight inter-network coordination, resulting in packet collisions that often partially overlap, but rarely ever completely overlap. In this work, we report a new design that allows Partial Symbol Recovery (PSR), based on specially designed receiver that specifically targets the parts of data symbols that experience no interference during a packet collision. PSR bootstraps a successive interference cancellation (SIC) like decoder from these strong signals, thus operating beyond the uplink data rate region, as our performance evaluation shows. We have implemented PSR on the WARP software-defined radio platform and in trace-based simulations. Our performance evaluation presents experimental results from this implementation operating in a 12-node software network testbed spread over two rooms in a non-line-of-sight indoor office environment. Experimental results confirm that the PSR decoder is capable of decoding up to nearly 60% of collided frames depending on the type of data and modulation used. This consistently leads to throughput enhancement under different scenarios and for the various data types tested, namely downlink bulk TCP, downlink video-on-demand and uplink UDP.

**Index Terms**—Partial Symbol Recovery, wireless communications, 802.11, collision environments, hidden terminals, interference cancellation.

## I. INTRODUCTION

In densely populated urban areas, wireless networks that exist in unlicensed spectrum (such as 802.11) routinely contend with vast numbers of users operating nearby, causing uncontrolled amounts of interference, with transmissions overlapping in both time and frequency. While medium access protocols can avoid some collisions, packet collisions due to hidden terminal nodes and inter-network collisions are still prevalent and harm throughput [1], [2]. Roughly speaking, the likelihood of a bit error is positively correlated with the ratio of signal power to noise plus interference power (SINR), measured at the receiver. The result is that in such unplanned networks, problems of interference from neighboring networks combine with the problems of range and reliability these networks already experience, resulting in degradation of application performance.

W. Ozan is with the Department of Electronic and Electrical Engineering, University College London (UCL), London WC1E 7JE, U.K. and was also with the Department of Computer Science, Princeton University, NJ 08540, USA (e-mail: w.ozan@ucl.ac.uk).

I. Darwazeh is with the Department of Electronic and Electrical Engineering, UCL, London WC1E 7JE, U.K. (e-mail: i.darwazeh@ucl.ac.uk).

K. Jamieson is with the Department of Computer Science, Princeton University, NJ 08540, USA and is also with the Department of Computer Science, UCL, London WC1E 7JE, U.K. (e-mail: kylej@cs.princeton.edu).

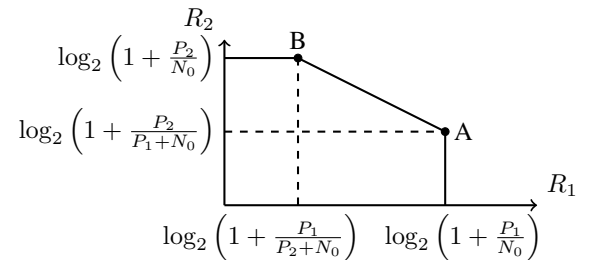


Fig. 1: Capacity region of the two-user uplink Gaussian noise interference channel [3].

From an information-theoretic standpoint, Ahlswede [4] and Liao [5] characterized the *capacity region* of the general multiple access channel, *i.e.*, the set of tuples (each entry in the tuple containing the rate of each user) such that there exists a receiver design that achieves an arbitrarily low bit error rate provided that the users transmit at rates within that set. Fig. 1 shows the capacity region for the two-user uplink Gaussian noise channel [3]. This line of work proved that in such a channel, the rate of each user cannot exceed that in the Shannon capacity of interference-free links (leading to the constraints that  $R_{1,2} < \log(1 + P_{1,2}/N_0)$ , where  $P_{1,2}$  are the transmit powers of users one and two respectively, and  $N_0$  is the Gaussian noise power) and that the total rate cannot exceed the Shannon capacity of a Gaussian noise channel with power equal to the sum of the two users' powers.

The receiver that achieves Pareto-optimal points in the capacity region is the *successive interference cancellation* (SIC) receiver [3], which achieves point A or B in the capacity region by first treating one transmission as noise while decoding the other transmission, then re-modulating and subtracting the first transmission from the received signal.

For years, work in this area took the above model—which treats every bit in two interfering transmissions equally—as the best fit to the reality of interfering data transmissions in wireless networks. Thus, this concept of capacity was treated as a given for single antenna communication and effort instead expended in other promising directions to increase capacity (such as the use of multiple antennas), which we survey in Section II.

However, in practical unplanned wireless networks, such as 802.11 there are many opportunities for collisions both within (Fig. 2 (A)) and between (Fig. 2 (B–D)) networks. Our insight begins with the observation that in a practical unplanned wireless network such as 802.11, or uncoordinated mobile cellular networks, the interference channel model is not necessarily exhaustively applicable to every bit in the colliding packets, as Fig. 3 illustrates. From two colliding

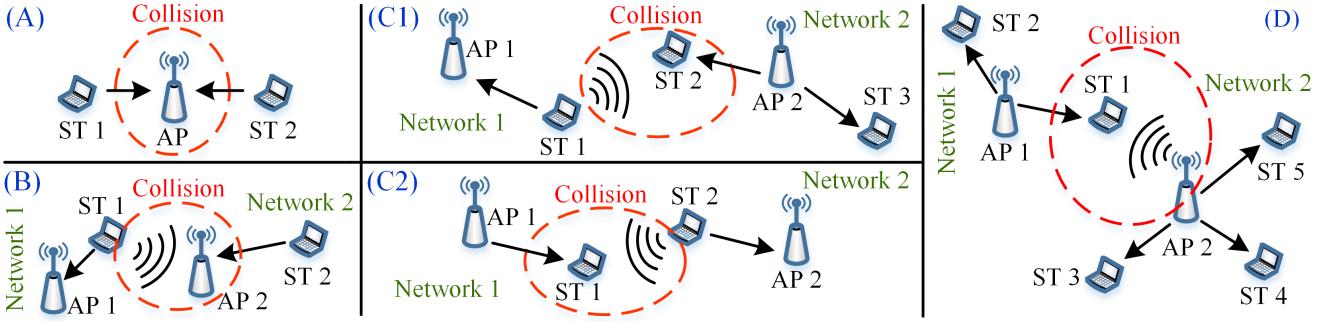


Fig. 2: PSR applies to different collision scenarios. The scenario (A) is hidden terminal nodes which causes collisions within a network; the scenarios (B, C1, C2 and D) depict the inter-network collision scenarios that occur in two existing neighbouring networks. The nodes surrounded with dashed line are the nodes that experience collisions.

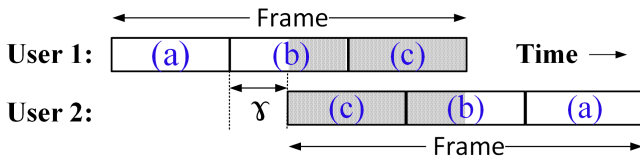


Fig. 3: Stations 1 and 2 transmit concurrently, leading to a collision at a receiver. Different data symbols experience differing degrees of overlap (a)–(c).

packet transmissions, we note **(a)** a head of some data symbols “in the clear” of the collision, **(b)** two partially-overlapping symbols of each colliding packet, and finally **(c)** the remainder of the wholly-overlapping symbols in the body of the packet overlap. Crucially, out of these three regions of packet data involved in the collision, region **(c)** and the collided part of region **(b)** are subject to the Ahlswede-Liao capacity region of multi-user. Therefore, there is an opportunity to tailor a receiver to operate beyond the optimum rate region of multi-user by utilizing the collision-free part of region **(b)** to fully recover region **(b)**, then exploiting that to decode and recover region **(c)**. Achieving this, however, requires that two challenges be overcome:

- 1) First, for the symbols in region **(b)** that are partially overlapped by interference, a decode attempt on just the interference-free region of these symbols results in interference across different orthogonal frequency division multiplexing (OFDM) subcarriers in frequency. While the sphere decoder (SD) [6], [7] can take this interference into account, it quickly becomes computationally prohibitive as the number of OFDM subcarriers increases past 20 or so, and so to make Partial Symbol Recovery practical, we need to develop a computationally-efficient receiver whose performance approaches that of the SD.
- 2) Second, channel coding is employed with the symbol-by-symbol modulation shown in Fig. 3, and this channel coding spreads information across the symbols in time, blurring the boundaries between the three regions noted above. Thus any receiver that leverages our observation for increased capacity must be co-designed with the channel coding in use.

This paper presents a new technique termed Partial Symbol

Recovery (PSR), a physical-layer and data link layer wireless receiver design that explicitly treats non- and partially-overlapping OFDM symbols differently from completely-overlapping OFDM symbols involved in a collision. The PSR algorithm first decodes the non-overlapping part of one user’s overlapping OFDM symbol sent from one of the users, using a novel *interference modeling* step that models and cancels the intercarrier interference that results from truncation of the OFDM symbol in time. Our design also applies the SD to small blocks of OFDM subcarriers in order to precisely cancel this intercarrier interference, while relying on linear methods to cancel the interference across blocks, thus bounding the computational complexity required by SD utilization in the design. Furthermore, our design jointly integrates the functions of intercarrier interference cancellation, channel equalization, carrier frequency offset (CFO) and phase offset compensation, and inter-symbol interference (ISI) mitigation, co-designing this functionality with the remainder of the system. This functionality comprises the *inner loop decoder*, which is described fully in Section III-A1.

After using the inner loop decoder to make an estimate of the interference-free portion of an OFDM symbol, PSR re-modulates the resulting bits to a full-length OFDM symbol and cancels the interference (user interference) from the originally received signal, allowing it to make a decoding attempt on a complete symbol lacking interference from the other user, provided the partially-received symbol was decoded correctly: this allows for a *window* of two symbols to be decoded jointly, and another symbol from the first user to be rendered interference-free. This process continues, expanding the window until the number of bit errors falls to an error floor (determined by power and noise levels, and modulation/coding rates) that are determined empirically. The window then slides along the entire length of the collision, comprising the *outer loop decoder* of the PSR decoding algorithm. This algorithm adapts, with minor modification, to various collision patterns resulting from different lengths of colliding frames.

Our PSR performance results, presented in Section V, reveal and confirm the following findings:

- **Two-user rate region**, PSR operates in a two-user rate region beyond the Ahlswede-Liao rate region, where the latter is found using SIC decoder;

- **Decoding capability**, experimentally proved that PSR decoder is capable of decoding on average 59% and 25% of collided frames, carrying 12,000 bits each, for BPSK and QPSK modulation formats, respectively;
- **Throughput performance**, results confirms an average throughput improvement over 802.11n of 10–21%, 8–21% and 5–14% for downlink bulk TCP, downlink video-on-demand and uplink UDP, respectively, depending on modulation used;
- **Retransmission performance**, PSR reduces the average rate of retransmissions by 63–81%, 57–81% and 28–49% in the above scenarios, respectively.

The rest of this paper is structured as follows. We outline related work in Section II, placing our contributions in further context of the many ideas for coping with interference in wireless networks. Partial symbols are characterized in Section III-A1. We detail the design of the PSR link and physical layers in Section III. Our testbed implementation is given in Section IV. PSR system performance is extensively evaluated in Section V. At last, the conclusion is given in Section VI.

## II. RELATED WORK

A prior work on exploiting packet overlaps in partial packet recovery (PPR) [2] aims to recover the collision free part of colliding packets but does not attempt to recover their colliding parts, hence it requires retransmission and suffers reduced throughput. Other work for decoding collisions from hidden terminal nodes, termed Zigzag Decoding [1], requires two successive collisions of the same packets. In contrast, Partial Symbol Recovery is the first work we are aware of, besides the classical SIC algorithm (against which we benchmark in Section V), that recovers full packets from a single collision and requires no retransmission to operate.

a) *Faster than Nyquist (FTN) Modulation.*: Most data transmission is linear: the result of summing a sequence of pulses. These pulses are almost always orthogonal (*i.e.*, invisible) to each other, meaning that if the current symbol is viewed at a symbol duration later in time, it is zero—this is the *Nyquist criterion* [8]. If the criterion is not met, the pulses interfere, but in 1975 Mazo showed that for a simple linear modulation the data pulses could in fact be compressed in time by a multiplicative factor of 0.802 [9], a speedup of approximately 25%, without a loss in performance. Follow-on work has generalized this concept to OFDM modulation, compressing the OFDM signal in frequency [10]–[12] and both time and frequency [13]–[15]. Partial Symbol Recovery’s inner partial OFDM symbol decoder can be viewed as a type of FTN modulation that differs from previous work because of its time truncation. Partial Symbol Recovery leverages a refined version of the truncated-OFDM (T-OFDM) decoder [16] for its inner partial OFDM symbol decoder, but builds atop T-OFDM to develop the outer decoder in its entirety.

Massive MIMO base stations [17]–[21] leverage large numbers of antennas to increase spectral efficiency. In multi-user communication networks, a coordination scheme utilizing machine learning is applied to minimize the collisions [22]. Interference alignment [23] (IA) techniques use multiple antennas to align different interfering transmissions, and have

been realized in both wireless LAN [24], [25] and cellular [26] settings. For the physical layer cross-technology communication (CTC), the work of ZigFi [27] leverages the channel state information of the received frames to enable WiFi receivers to decode data from ZigBee senders, while the work of TwinBee [28] enables direct communication from WiFi to ZigBee.

Bit rate adaptation based on acknowledgements [29], [30] and SINR [31]–[34] and rateless codes [35]–[43] attempts to maximize utilization of individual links, but still does not exploit the partial overlap concept. Other influential link-centric approaches include full-duplex wireless links [44]–[47], which are also independent of PSR contribution.

## III. DESIGN

PSR is implemented jointly in the physical and data link layers. In this section, the physical layer (L1) design of PSR is discussed in Section III-A; the data link layer (L2) design is described in Section III-B, and Section III-C addresses experimental design considerations for our choices of key system parameters.

### A. Physical layer design

PSR uses the 802.11a standard for preamble and data generation in the physical frame. Our modifications to the current existing physical layer involve adding the PSR decoder design and a triggering mechanism to a current 802.11 receiver. The PSR decoder is a nested-loop decoder, consisting of (i) an *inner loop decoder* and (ii) an *outer loop decoder*. The inner loop decoder is designed to decode a partial symbol, depicted in the collision-free part of region (b) in Fig. 3, and recover its full symbol, depicted in the full region (b) in Fig. 3, as explained next in Section III-A1. The outer loop decoder is designed to cancel users interference, and to constrain error propagation between symbols in a user frame. Its design is detailed in Section III-A2.

#### 1) Inner loop decoder

The *partial symbol*, which has no interference coming from the other user as depicted in region (b) in Fig. 3, is contaminated with interference resulting from truncation in time. Therefore, we characterize the predictable interference between OFDM subcarriers that occurs when the receiver observes just the beginning fraction  $\gamma$  of an OFDM symbol, in time. This *partial symbol* can be analyzed by the inverse discrete Fourier transform (IDFT) as:

$$x(m) = \frac{1}{\sqrt{\gamma Q}} \sum_{l=0}^{Q-1} d_l \exp\left(\frac{j2\pi lm}{Q}\right) \quad (1)$$

where  $m = [0, 1, \dots, \gamma Q - 1]$  is the index of the time samples and  $l$  is the subcarrier index;  $d_l$  is the complex input data;  $Q$  is the size of the IDFT, used to generate the signal;  $\gamma Q$  is the number of time samples in a partial symbol, where  $\gamma \leq 1$  is the fractional symbol proportion observed. We observe that each time sample is a summation of sampled input symbols, each modulated on an individual complex subcarrier. This observation is significant because a symbol may be decoded even when only a fraction of its time samples has been received [16].

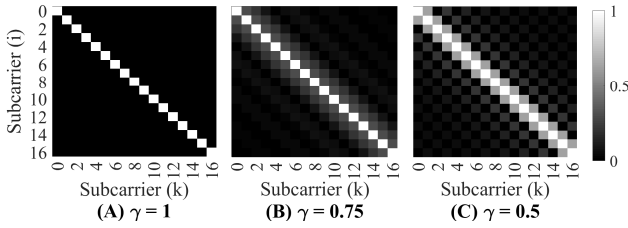


Fig. 4: Heatmap of the covariance matrix that depicts the interference between neighboring subcarriers. (A) is for orthogonal symbols; (B) and (C) are for partial symbols with  $\gamma = 0.75$  and  $0.5$ , respectively.

Orthogonality in time and frequency in OFDM (*i.e.*  $T = 1/\Delta f$ , where  $T$  is the symbol period and  $\Delta f$  is the subcarrier separation), is a crucial factor in its successful operation. However, should this condition be violated, *i.e.* the observed symbol period  $< T$ , orthogonality is violated and inter-carrier interference (ICI) is introduced. The analytical description of the interference resulting from the lost portion of the partial symbols due to the collision, is given by the covariance matrix ( $\Gamma$ ), which quantifies the interference contribution on each subcarrier from its neighboring subcarriers [16]. The covariance matrix components are derived and given in Appendix VI-A.

To visualize the effect of interference, resulting from the truncation in time, on the received partial symbols, Fig. 4 (A) shows that all the subcarriers are orthogonal with no interference while (B) and (C) in the same figure show that the interference caused on a specific subcarrier (represented on the main diagonal) stems from the neighboring subcarriers (on the secondary diagonals) when  $\gamma$  is smaller than 1.

After characterizing the interference of the partial symbol, which resulted due to the lost symbol portion in the collision, the *inner loop decoder* utilizes the covariance matrix to decode a partial symbol and recover its data to reconstruct a full symbol. The inner loop decoder comprises of two steps; (i) ISI cancellation and cyclic prefix (CP) part utilization; and (ii) joint iterative decoder. The first step is to eliminate the ISI, which appear in the CP part, hence the interference-free CP part is used to increase the number of samples in the partial symbol, as explained next in Section III-A1a. The second step is to iteratively equalize the channel effect, compensate the phase offset, cancel the interference resulting from the truncation in the end of a symbol, and decode the partial symbol to recover its data, thus, this step is termed *joint iterative decoder*. Its design is detailed in Section III-A1b.

*a) ISI cancellation and CP part utilization:* In the 802.11a frame, each OFDM symbol starts with a CP, which is generated by copying the last  $\mu$  samples of a symbol to the start of the symbol (see Fig. 5), and is used to mitigate the ISI stemming from the prior OFDM symbol and reduce sensitivity to symbol timing estimation error. Hence, in conventional 802.11a systems, the CP is discarded at the receiver because it is distorted with ISI and carries redundant data.

In the PSR receiver, each collision-free partial symbol consists of a CP portion and a part of the OFDM symbol, as shown in Fig. 5. When the tail of the symbol is overlapped by the other user, as in  $s_{1p}$ , we use the CP in the decoding

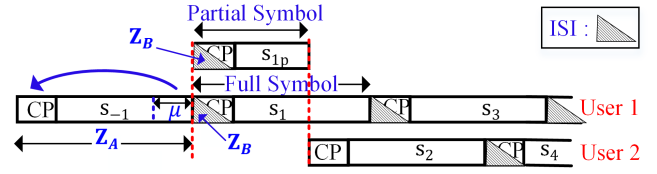


Fig. 5: A partial and full symbol in received colliding frames. The partial symbol,  $s_{1p}$ , consists of a CP and a part of a symbol. Symbols with odd indices belong to user 1 and the symbols with even indices belong to user 2. Each CP is contaminated with ISI.

process to compensate for the portion lost due to the collision. This results in increase in the number of time samples in the partial symbol by the number of samples in the CP part, and an increase in the energy contained in the partial symbol, thus resulting in reduced error rate. However, the CP in the partial symbol ( $s_{1p} \in \mathbb{C}^{(\gamma Q) \times 1}$ ) is distorted due to ISI from the preceding symbol ( $s_{-1} \in \mathbb{C}^{Q \times 1}$ ), hence, we estimate the ISI and subtract it from the partial symbol. This is achieved by convolving the channel impulse response (CIR,  $\mathbf{h} \in \mathbb{C}^{(\mu+1) \times 1}$ ), with the estimated prior symbol,  $\hat{s}_{-1}$ , as:

$$\mathbf{z}_{-1} = \mathbf{h} * \hat{s}_{-1} = \begin{cases} \mathbf{z}_A, & 1 \leq k \leq Q \\ \mathbf{z}_B, & Q+1 \leq k \leq Q+\mu \end{cases} \quad (2)$$

where  $\mathbf{z}_{-1} \in \mathbb{C}^{(Q+\mu) \times 1}$  is the symbol after the convolution process, and  $(*)$  is the convolution process. The output of the convolution comprises of  $\mathbf{z}_A$  and  $\mathbf{z}_B$ . The  $\mathbf{z}_A$  part is the preceding symbol after traversing the multi-path channel, and the  $\mathbf{z}_B$  part is the ISI components, as shown in Fig. 5. Next, we subtract the ISI ( $\mathbf{z}_B$ ) from the partial symbol,  $s_{1p}$  before passing it to our joint iterative decoder.

*b) Joint iterative decoder:* The received partial symbols, after eliminating the ISI and including the CP in the partial symbol, is passed to the next decoding stage to recover its data. The partial symbols suffer from (i) multi-path effects from the wireless channel; (ii) phase offsets; and (iii) the interference between the subcarriers, which is created when the tail part is lost in the overlap with the other user. We design an iterative receiver that jointly equalizes channel effects and the phase offset, and then cancels the interference in every iteration, thus recovering the overall data from the partially received symbols. Then, re-encodes the recovered data bits to generate a full symbol to estimate and add missing multi-path components to enhance the channel equalization and phase compensation process, as detailed in the following paragraph. After that, using the full symbol to estimate and subtract the interference from the original partial symbol before being passed to the next iteration. Repetition of these joint processes in each iteration leads to the enhancement of the error rate performance of the decoding process. Fig. 6 depicts the inner loop decoder including the joint iterative decoder process.

*Partial symbol equalization and phase compensation.* The multi-path effects and the phase offset are combined with the interference, resulting from truncation in time, among the partial symbol subcarriers. Therefore, partial symbol equalization and phase compensation become more challenging. To

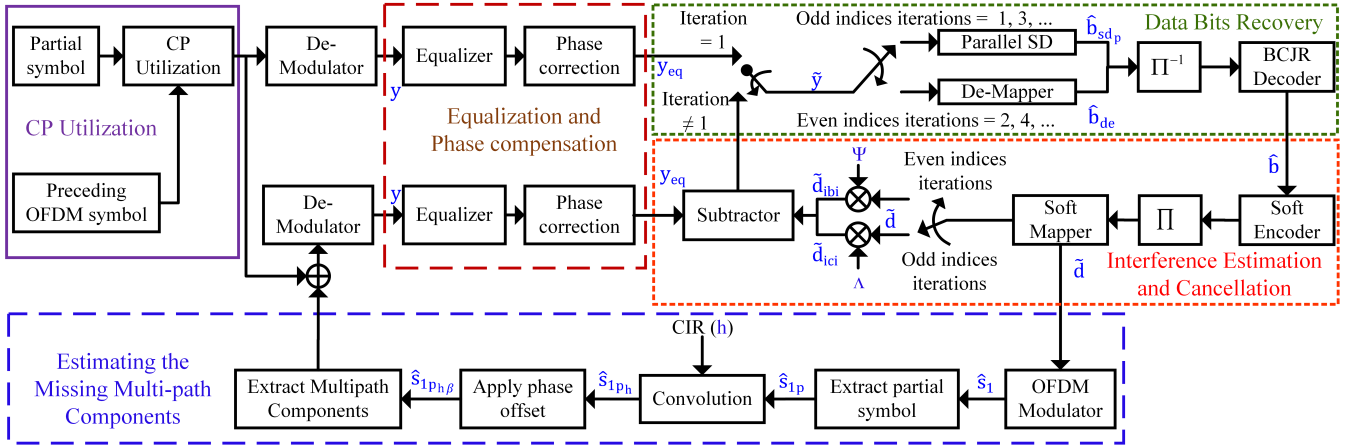


Fig. 6: Inner Loop Decoder concept illustration: Eliminates ISI and uses information in the CP then equalizes and phase corrects; recovers the bits from partial symbols; re-encodes the symbols to estimate and subtract the interference of the original signal before being passed to the next iteration.

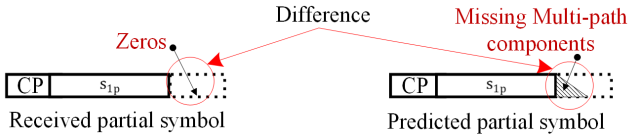


Fig. 7: A truncated partial symbol lacks certain multi-path components. The triangle depicts these estimated, missing multi-path components.

illustrate, we compare, in Fig. 7, a received partial symbol with what such symbol would “hypothetically” be after traversing a multi-path wireless channel. The missing multi-path components, in received partial symbols, result in increased interference levels and consequently inaccurate equalization and phase correction. Dealing with this problem requires the estimation of the missing multi-path components and then adding the estimates to the partial symbols (the dashed-blue line box of Fig. 6 depicts the processes). The processes are detailed in the following paragraph.

- **Estimating the missing multi-path components process.** The process requires knowledge of two key parameters; namely the CIR and phase offset, the estimation of these is detailed in Section III-C3. Two stages are required, firstly, we convolve the recovered partial symbol 1,  $\hat{s}_{1p}$ , at the end of every iteration with the CIR:

$$\hat{s}_{1p_h} = \mathbf{h} * \hat{s}_{1p} \quad (3)$$

where  $\hat{s}_{1p_h}$  is the estimated partial symbol 1 with channel effects. Secondly we add the effects the phase offset to the resulting signal from the first step:

$$\hat{s}_{1p_{h\beta}} = \hat{s}_{1p_h} \cdot e^{-j\beta_1}, \quad (4)$$

where  $\hat{s}_{1p_{h\beta}}$  is the estimated partial symbol 1 after applying phase offset ( $\beta_1$ ). The last  $\mu$  samples of the resulting signal, as shown in Fig. 7, represent the required multi-path components, which are added to the partial symbol before being passed to the next iteration. It should be noted that, for the first iteration, the partial symbol

is passed to the equalization and phase compensation process with no addition of the missing multi-path components. The processes of equalizing the channel effects and compensating the phase offset are detailed in the following paragraph.

- **Channel equalization and phase compensation processes.** The partial symbol is passed to the equalization and phase compensation processes in each iteration (the dashed-brown part of Fig. 6 depicts the processes). The channel equalization and the phase compensation are applied in the frequency domain. The multi-path channel effects at each subcarrier are equalized using zero forcing equalization process. The phase offset is compensated by multiplying the complex data symbol of each subcarriers with  $e^{j\beta_1}$ . Repetition of these processes during the joint channel equalization, phase compensation and decoding iterations, leads to a better estimate of the missing multi-path components and hence, improves the equalization and phase compensation processes.

*The interference cancellation mechanism.* In order to cancel the resulting interference due to the symbol truncation in time, the interference cancellation mechanism comprises of two main stages.

- **Data bits recovery.** The complex symbols for each subcarrier of the partial symbol is converted to bits given as log-likelihood ratio (LLR) values, where the sign of LLR values indicates the sign of the bits and its magnitude determines the reliability of the bits. After that, the output of all the subcarriers is de-interleaved and decoded using soft-output BCJR decoder [48]. The process is depicted in the dashed-green line box of Fig. 6.
- **Interference estimation and cancellation.** In this stage the interference in the partial symbol is estimated and then subtracted from received partial symbol after the equalization process. The process is illustrated in the dotted-red line box of Fig. 6.

**Data bit recovery design and discussion.** In order to recover the bits of a partial symbol, the covariance matrix,

$\Gamma$ , is used in a sphere decoder [49] [50], to retrieve the data of a partial symbol. The sphere decoder mathematical representation is given as:

$$\hat{\mathbf{b}}_{\text{sd}} = \arg \min_{\mathbf{d} \in M^N, \|\tilde{\mathbf{y}} - \Gamma \mathbf{d}\|^2 \leq g} \|\tilde{\mathbf{y}} - \Gamma \mathbf{d}\|^2 \quad (5)$$

where  $\hat{\mathbf{b}}_{\text{sd}} \in \mathbb{C}^{Q \times 1}$  is the estimated data bits vector in the partial symbol,  $M^N$  is the number of all possible signal combinations in a symbol,  $M$  is the cardinality of the constellation diagram,  $N$  is the number of subcarriers and  $g$  is the radius of the hypersphere search area that is centered at  $\tilde{\mathbf{y}} \in \mathbb{C}^{Q \times 1}$  which is the demodulated partial symbol after equalization and phase compensation,  $\mathbf{d} \in \mathbb{C}^{Q \times 1}$  is the complex input data vector that has the highest probability of being transmitted. The solution is found by finding the minimum Euclidean distance from all the possible vector combinations which take place inside the multi-dimensional hypersphere searching area. This results in data recovery of the partial symbol.

However, we note that using a single sphere decoder, to recover the data in all subcarriers, leads to high computational complexity, hence we adapt the method of [51], in which the subcarriers are divided into sets of blocks, each is operated on by a smaller sphere decoder. For 802.11a signals, there is a natural division into such blocks and separation of these (5 blocks) by the four pilot tones, which are placed between the data subcarriers [52]. Thus, the interference of the known pilot tones onto subcarrier blocks is measured and canceled by subtraction from each subset at the receiver.

Nevertheless, the interference from subcarriers in one block to adjacent blocks (inter block interference, IBI) has also to be considered. Therefore, in our design, the iterations with odd indices eliminate interference within a block of subcarriers; while the iterations with even indices eliminate the IBI among the blocks.

- **The odd indices iterations.** In order to recover the data in each block of subcarriers, we use the covariance matrix of each block ( $\tilde{\Gamma}$ ), in a small-size sphere decoder set following equation (5). The output of the small-size sphere decoder set ( $\hat{\mathbf{b}}_{\text{sd,p}}$ ) is de-interleaved and decoded using soft-output BCJR decoder (see Fig. 6). Next, the soft-bits ( $\hat{\mathbf{b}}$ ) are encoded using soft-encoder where its output bits are interleaved and mapped ( $\tilde{\mathbf{d}}$ ). Then, the interference in each block ( $\tilde{\mathbf{d}}_{\text{ici}}$ ) is estimated and subtracted. Where the covariance matrix characterizes the data and the interference in the partial symbols, hence, it can be decomposed into two matrices as:

$$\tilde{\Gamma} = \mathbf{I} + \mathbf{\Lambda} \quad (6)$$

where  $\mathbf{I}$  is an identity matrix that represents the data coefficients matrix and the  $\mathbf{\Lambda}$  is the ICI coefficients matrix of each block. The components of the covariance matrix in a block of subcarriers is given in Appendix VI-B. Now, using  $\tilde{\mathbf{d}}$ , and the interference coefficients matrix,  $\mathbf{\Lambda}$  of each block, the interference is found as:

$$\tilde{\mathbf{d}}_{\text{ici}} = \mathbf{\Lambda} \tilde{\mathbf{d}} \quad (7)$$

After that, the interference components are subtracted from the equalized partial symbol ( $\mathbf{y}_{\text{eq}}$ ) before the symbol being passed to the next iteration (see Fig. 6).

- **The even indices iterations.** After canceling the interference within the blocks in the odd indices iterations, here in the even indices iterations, the decoder cancels the IBI among the blocks. To achieve this, the received signal from the previous iteration is fed to a soft-output demapper, which translates the distorted received constellation into LLR values ( $\hat{\mathbf{b}}_{\text{de}}$ ). Then, the output is de-interleaved and decoded using soft-output BCJR to get soft-bits,  $\hat{\mathbf{b}}$ . Next, we find and subtract the interference between the blocks. To achieve this, the  $\hat{\mathbf{b}}$  are encoded and interleaved to get  $\tilde{\mathbf{d}}$ , as shown in Fig. 6. Then, the latter is multiplied with the IBI coefficient matrix ( $\Psi$ ), which is given in Appendix VI-C, to estimate the IBI components, as:

$$\tilde{\mathbf{d}}_{\text{ibi}} = \Psi \tilde{\mathbf{d}} \quad (8)$$

After that, the IBI is estimated and subtracted before the symbol is being passed to the next iteration. Repetition of these processes results in decoding efficiency enhancement.

## 2) Outer loop decoder

Fig. 8 illustrates the operation of the outer loop decoder. Starting with the received ( $R_r$ ) signal, distorted by interference from user 2, and comprises the two overlapped signals of the two users; each one of these signals is composed of a set of OFDM symbols, represented by the numbered elementary rectangles in the figure, where those with odd indices belong to user 1. The partial symbol 1 ( $s_{1p}$ ) of user 1 is the collision-free partial symbol, while the rest of the symbols (of both users) are overlapped interfered symbols. The role of the outer decoder is to follow the inner decoder, which has already recovered the data of  $s_{1p}$ , to reconstruct a full symbol 1 ( $s_1$ ). Then, the outer decoder acts on  $s_1$  and the rest of the symbols, so that all symbols are recovered even those with severe interference.

The outer loop operation starts with a decoding window of a length equal to one symbol as shown in Fig. 8 in step #I. Then, the decoding window size is increased linearly, with the number of stages, until it reaches the size of  $G$  symbols. For this work, the value of  $G$  was selected empirically following an extensive number of experiments (Section V-C). The outer loop decoding algorithm operates to detect data only of the first two symbols in the window of size  $G$ . After that, these two symbols are subtracted from the received overlapped signal and the result is passed to the next decoding window.

a) *Initial stage of decoding:* Here, the outer loop decoder uses the inner loop (described in Section III-A1) to decode the partial symbol,  $s_{1p}$ . After that, the outer loop fully reconstructs  $s_1$ .

b) *Backward stage of decoding:* The decoding window is set to two, where  $s_1$  and the partial symbol 2 ( $s_{2p}$ ) are part of the decoding process (stage #IIa, b in Fig. 8). This stage is divided into five steps: (i) the outer loop implements basic interference cancellation by subtracting the reconstructed  $s_1$  from the received signal to estimate  $s_{2p}$ ; (ii) in a manner similar to that of the initial decoding stage, the receiver decodes  $s_{2p}$  using the inner loop, then reconstructs the full symbol 2 ( $s_2$ ); (iii) next,  $s_2$  is subtracted from the received signal to get  $s_1$  without interference as shown in stage #IIb in Fig. 8; (iv) then  $s_1$  is fully decoded to recover its data and

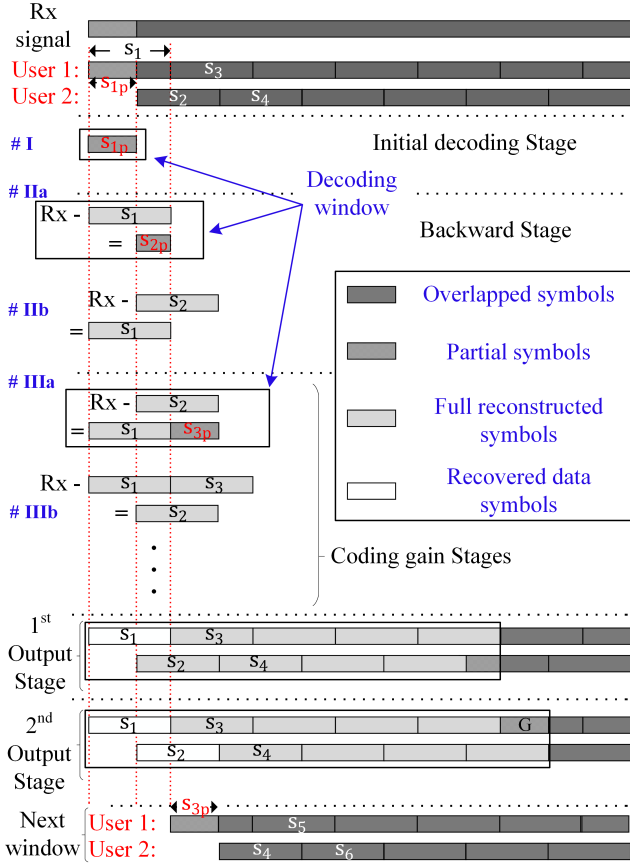


Fig. 8: The outer loop decoding algorithm recovers the received ( $R_x$ ) signal, which comprises the overlapped user 1 and 2 signals. The algorithm uses the inner loop decoder to recover the data in the collision-free portion of symbol 1 ( $s_{1p}$ ) in the first stage #I. In the backward stage, the reconstructed symbol 1 ( $s_1$ ) is subtracted from the  $R_x$  signal to obtain partial symbol 2 ( $s_{2p}$ ) in stage #IIa, which is reconstructed to symbol 2 ( $s_2$ ). The reconstructed symbol 2 ( $s_2$ ) is subtracted from the  $R_x$  signal to obtain symbol 1 ( $s_1$ ) as an interference-free symbol as in stage #IIb. In the coding gain stages, the partial symbol 3 ( $s_{3p}$ ) is extracted as in stage #IIIa, then  $s_1$  and  $s_{3p}$  are decoded together to increase the coding gain. After that, the reconstructed symbols 1 and 3 are subtracted from the  $R_x$  to yield  $s_2$  as if it was received with no interference, this is depicted in stage #IIIb. Then, the algorithm increases the decoding window size in every additional stage up to stage  $G$  in this example, where decisions on symbol 1 and 2 are made. After that, the decoding algorithm starts a fresh decoding window from symbol 3. The symbols with odd indices belong to user 1 and the ones with even indices belong to user 2.

then reconstructed to yield a received  $s_1$ , as if there were no interference; finally, (v) the outer loop repeats the first and second steps to reconstruct an interference-free version of  $s_2$  to be passed to the next stage.

The reason for stage #IIa, b is that the partial decoder results in higher error rates relative to a conventional OFDM decoder, because partial symbols contain fewer samples, which means each has lower energy than the full symbol. Therefore, stage #IIa, b cancels the interference effects of  $s_{2p}$  to obtain a full interference-free symbol,  $s_1$ , yielding a better error rate performance.

It should be noted that the partial symbol length of user 1 ( $s_{1p}$  in stage #I in Fig. 8) is different to the partial symbol length of user 2 ( $s_{2p}$  in stage #IIa in Fig. 8), where the duration of the partial symbols of the two users in total is equal to the duration of a full symbol.

c) *Middle (coding gain) stages of decoding:* In the same way as the backward stage, the decoding window increases its size by one symbol for every additional stage until the stage preceding the hard decision, in which, all the symbols in the decoding window are full symbols except for the last symbol, which is the partial symbol. For instance, when the decoding window size is equal to six symbols, there will be five full symbols and one partial symbol. Through these stages, the symbols of each user go through the appropriate convolutional decoder, to increase the coding gain.

d) *Hard decision on symbol 1:* The outer loop decoder gives the first output, which is the recovered data of  $s_1$ .

e) *Final stage of decoding:* The PSR decoder produces the second output that is the recovered data of  $s_2$ .

f) *Reset the decoding window:* Recovered  $s_1$  and  $s_2$  are subtracted completely from the overlapped received signal before being passed to the next decoding window, also of size  $G$ . The above processes are repeated again but now starting with a fresh decoding window, of size equal to one, to decode partial symbol 3 ( $s_{3p}$ ) and ending with a decoding of full symbols 3 and 4 ( $s_3$  and  $s_4$ , respectively). This carries on to the end of the frame, making hard decision on two symbols only per decoding window.

### B. Link layer design

In the current 802.11 receivers, the receiving station transmits an acknowledgment (ACK) after a data frame is successfully decoded and passes the cyclic redundancy check (CRC), as shown in Fig. 9. Otherwise, the received frame is dropped and no ACK is sent. The solid-black lines of Fig. 9 depict this process, in the existing 802.11 receivers. On the other hand, our design modifies the data link layer by adding a new acknowledgment scheme, which allows the receiving station to acknowledge successfully recovered frames of the two users, as shown by the added dotted-red blocks in Fig. 9. In this system design, we use delayed block acknowledgment (BA) mechanism from 802.11n to delay sending the BA to the transmitting users until PSR fully decodes the two colliding frames. This is because one of the colliding users could finish transmitting data frames while the other user has not yet completed its transmission.

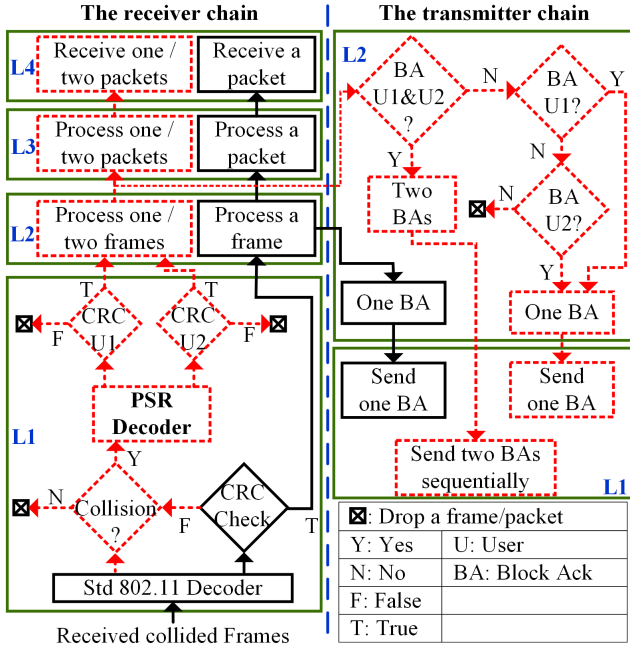


Fig. 9: Schematic chart of Partial Symbol Recovery system. The solid-black lines depict the existing 802.11 receivers, while the dot-red lines represent the additional PSR functions in each layer. U 1 and U 2 are user 1 and user 2, respectively.

Decoding overlapped frames necessitates two different designs; (i) for intra-network collision (the scenario in Fig. 2 (A) and (B)) and (ii) for collisions in two co-existing networks (the scenarios in Fig. 2 (C)). We note that, at the physical layer, the two designs are identical.

#### 1) Intra-network collisions

When two users are transmitting concurrently, the receiving station of the two users decodes the overlapping data frames using PSR as explained in Section III-A. However, the acknowledgment mechanism differs according to whether the collisions occur (i) between data frames of two users or (ii) between data and control frames.

##### a) Collision between data frames of two users:

Fig. 10 (A) depicts the operation of the AP using standard 802.11 and PSR receivers. The 802.11 receiver sends a BA indicating indices of successfully recovered frames. On the other hand, after successful recovery of the overlapping frames using PSR, the AP sends two separate BAs, one for each user. Each BA indicates the indices of the recovered frames of each transmitter, as shown in Fig. 10 (A).

##### b) Collision of data frames with control frames:

In this case, exemplified by Fig. 10 (B), user 2 sends control frames to the AP, which collides and hence no ACK is received. Then user 2 re-sends the control frame after a random wait, in the worst case and under heavy traffic from user 1, further collisions may occur. In the 802.11 receiver, the affected data frames of user 1 are dropped and a single BA is sent for the recovered frames. In contrast, for the PSR case, overlapped frames are recovered for both users and the receiver waits

until no transmission is detected, then an Ack is sent for the control of user 2 and a BA for the data frames of user 1.

#### 2) Inter-network collisions

In this case of inter-network scenarios, the overlapped frames at the recipient station have different destination addresses. Therefore, after decoding the overlapped frames, the receiving station only takes the frames that have its address in the destination field. Hence, sending only a single BA after a complete reception. Fig. 10 (C) depicts the process of sending a single BA. The advantage of using PSR over standard 802.11 receivers, is the ability to recover overlapped frames. This enhances the throughput and reduces the retransmission rate.

### C. Experimental parameters estimation

#### 1) Collision detection

We follow a technique similar to Zigzag Decoding [1], where the known preamble is correlated with the received signal. When the two preambles are properly aligned, a correlation peak results. A single incoming frame results in a single correlation peak at the start of that frame. The generation of a second peak within the duration of the first frame indicates that a colliding/interfering frame is present, since the second peak is a result of correlation with the colliding frame's preamble. This identifies the cause of CRC failure as a collision and hence the receiving station activates PSR to decode the colliding frames.

#### 2) $\gamma$ estimation

It is important to find the value of  $\gamma$ , defined in Section III-A1, and hence the inter-carrier interference levels as these are required for the detection process in the inner loop as explained in Section III-A1 and Section III-A1.  $\gamma$  can simply be estimated (see Fig. 3) by finding the time delay between the starting sample, of the colliding user transmission using the first correlation peak, and the second correlation peak.

#### 3) User identification, CFO, and CIR estimation and compensation

The received signals are distorted by the wireless multi-path channels and the CFO effects and contaminated with AWGN noise. In order to mitigate the multi-path channel and CFO effects, the receiving station estimates the CIR and CFO for each user. In 802.11 standards, such is estimated using the received preamble attached to each frame.

a) *Colliding user ID and initial CFO and CIR:* For user 1, the CIR and CFO are estimated using its preamble signal, which is received within the collision-free region. Unfortunately, this can not be done for user 2, since its received preamble is corrupted by the collision with the signal of user 1. To resolve this problem, we introduce a new technique to define the colliding user ID, and the corresponding CIR and CFO. The technique, implemented in two stages, is based on the premise that the combination of CIR and CFO for each station will be unique. The first stage, the receiving station keeps a record of user IDs and associated most recent CIR and CFO of users stations in its vicinity, whenever user data is received with no collision. The second stage is to define which set of CIR and CFO is the correct

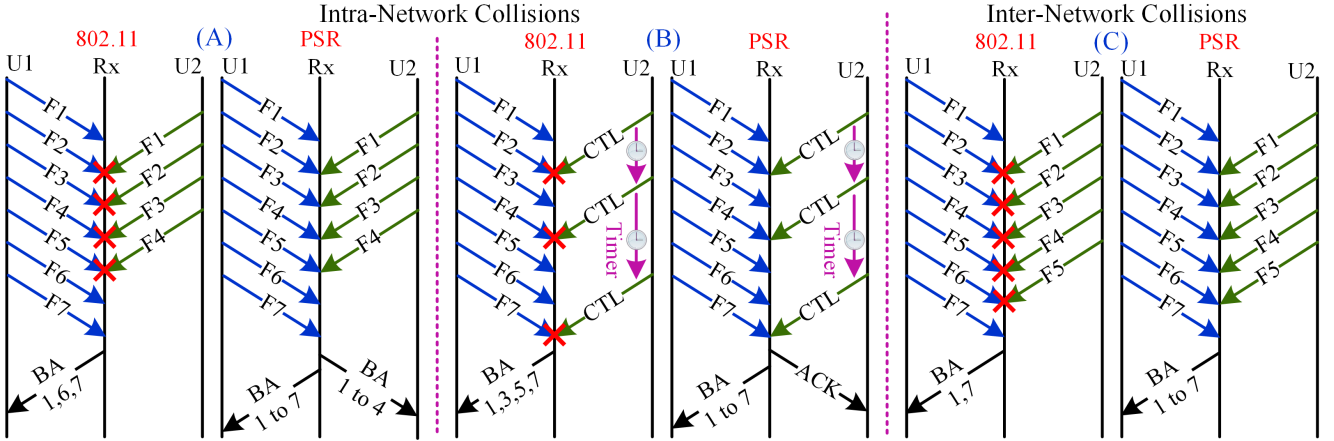


Fig. 10: Message sequence chart of intra- and inter-network collision scenarios. User 1 and user 2 cause collisions at the receiving station when they have concurrent transmissions. (A) collisions of data frames of two users at the AP; (B) collisions between data and control frames at the AP; (C) collisions are the inter-network collision scenario. The character F refers to the data frames, while the CTL refers to the control frames.

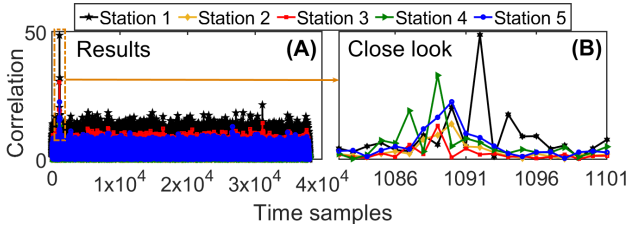


Fig. 11: Our technique ability to identify a colliding user from its recent CFO and CIR. (B) shows that station 1 has the highest peak, which indicates the colliding user.

match to the colliding user. To achieve this, our decoder sequentially convolves all the saved CIR with the known preamble signal and then applies CFO. After that, the decoder correlates the resulting convolution values with the received signal and compares the results of all correlation processes. This comparison identifies the colliding station ID through its most recent CFO and CIR, which are used as an initial estimate to decode the signal of the colliding user. Fig. 11 shows the correlation values resulting from using five saved pairs of CFO and CIR measured in our experimental testbed. The result with highest peak represents the right CFO and CIR of the colliding station, which is station 1 in this example.

*b) Updating CFO and CIR information:* After identifying the initial CFO and CIR information as mentioned earlier, the decoder uses this information to decode the colliding signal until the preamble of the user 2 (the colliding signal) is fully recovered. Then, the extracted/recovered preamble signal of user 2 is used to get a new estimate of the CFO and CIR. In general, any residual error in estimating the CFO will result in a phase offset, which is estimated using the pilot tones inserted in 802.11 OFDM symbols.

*c) CFO compensation:* We correct CFO for a partial symbol before it is passed to the inner loop decoder by

applying a frequency shift to the signal in the time domain:

$$s_{xp} = s_{xp_{cfo}} \cdot e^{-j2\pi\delta f n} \quad (9)$$

where  $s_{xp}$  and  $s_{xp_{cfo}}$  are the partial symbol (with sub index  $x$ ) after and before compensating CFO, respectively, and the exponential term represents the applied correction of the frequency shift,  $\delta f$ , which is estimated using the preamble, and  $n$  the time index from the beginning of the frame.

#### IV. IMPLEMENTATION

The 802.11 devices for both transmitters and receivers are WARP V3 devices software defined radios (SDRs). The WARP devices operate on channel 17 at 5660 MHz and use TP-link antennas with 5 dBi gain. We set the sampling rate in the WARP device to be 20 MHz. The WARP devices connect to a Linksys SE4008 WRT 8-port gigabit Ethernet switch through Ethernet cables. The network topology is shown in Fig. 12.

##### A. Physical layer

The SDR testbed is driven by MATLAB R2017b for 802.11a signal generation, following the 802.11a OFDM physical frame structure. A 64-point IFFT generates the symbols, and uses 48 inputs for data, 4 for pilots and the rest are padded with zeros. A preamble is attached at the beginning of each frame.

Automatic gain control is applied to the received signals, then the received overlapped signal is saved to disk to be processed in off-line decoding. The PSR and SIC decoders are written in Matlab. The decoders save the decoded bits to disk for performance evaluation.

##### B. Link layer to transport layer

We build the network topology scenario shown in Fig. 12 in NS-3 [53] with the 802.11n standard system specifications. First, we evaluate standard 802.11, in which an ACK is sent to the transmitter only when a frame is decoded correctly. On

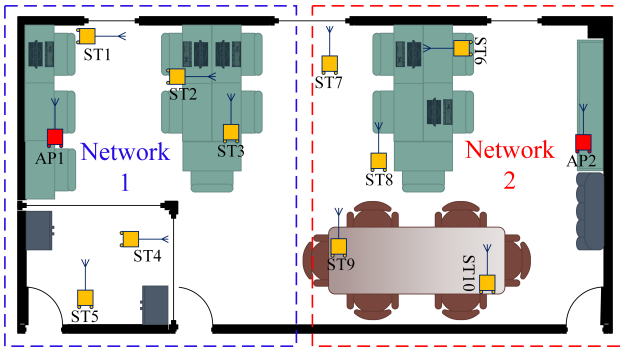


Fig. 12: Indoor experimental testbed map. The testbed consists of ten nodes operate as user stations and two nodes operate as APs. The nodes are distributed across two rooms for two networks in non-line-of-sight and line-of-sight indoor environment.

the other hand, SIC and PSR are built on top of 802.11n, and so act exactly as 802.11n unless there is a collision, in which case, the frame that could not be decoded by the 802.11n receiver is examined to detect if it experiences collision event as explained in Section III-C1. When a collision event is detected, trace driven data of the decoder under evaluation (either SIC or PSR), which contains details of the decoding performance, is used by the receiver to make a decision on the success or otherwise of frame decoding. The use of NS-3 in our evaluations, is to achieve almost real life collision environment where transmissions are not synchronized, the frame length is variable and the  $\gamma$  variable is not set.

## V. EVALUATION

In this section, we evaluate the PSR system versus the 802.11 and SIC systems. In Section V-A we describe the methodology and in Section V-B we evaluate the PSR versus SIC in terms of rate region. Experimental evaluation of the PSR system in the link layer is given in Section V-C and of the end-to-end throughput performance of the transport layer in Section V-D.

### A. Methodology

We evaluate PSR with 12-nodes using our SDRs testbed. Physically, each node is a WARP device connected to a computer. The network topology, shown in Fig. 12, contains both non-line-of-sight and line-of-sight links. In order to evaluate PSR with real traffic, which includes realistic collision environment (*i.e.* collisions occurrence are not manually set), in a complete network that covers up to the transport layer, the network testbed is implemented in two steps: (*i*) the physical frames collisions intentionally occur in a realistic RF environment experimented in a two-room office, as shown in Fig. 12, to capture the effect of various real channels in PSR decoding capability between two colliding frames, (*ii*) the data traffic is implemented following a realistic network topology of the 12-node testbed using the experimental collision decoding success for end-to-end evaluation.

### 1) Experimental collision traces

In our application, we focus on decoding two 802.11 frames that have collided. Two nodes simultaneously transmit data to another node to intentionally cause a collision. For example, ST 1 and ST 2, shown in Fig. 12, both transmit data to AP 1, and the received collision data are saved in files to be decoded later.

For each experimental run, we vary the experiment parameters, which are the modulation formats and  $\gamma$  variable. We experiment for BPSK and QPSK modulation formats and for ten values of the fractional overlap,  $\gamma = 0, 0.1, \dots, 0.9$ . In each experiment we send 600 physical frames from two nodes and collect 600 collision traces. Every frame carries 12,000 bits (1,500 bytes) and the measured SNR at the receivers is within the range of 13-25 dB. The wide range in SNR arises from the variation in the channel environment, as the two-room office was occupied by eight people. Also, two of the stations, ST 4 and ST 5 as shown in Fig. 12, were positioned in a storage area partitioned with glass walls.

### 2) Schemes compared for end-to-end evaluation

Using our 12-node testbed and the trace driven simulations, we evaluate three schemes end-to-end: (*i*) PSR, (*ii*) SIC, and (*iii*) 802.11n. We evaluate with the following metrics:

- **Rate region comparison**, which compares the rate region of the two user uplink in AWGN channel using SIC and PSR receivers.
- **Frame error rate (FER)**, which is the percentage of incorrectly decoded colliding frames to the total collided frames. In this evaluation, a frame is considered successfully decoded if it passes the CRC.
- **Throughput**, this is the data throughput-per-second measured at the transport layer.
- **Frame retransmission rate**, this is the number of physical frame retransmissions-per-second measured at L2.

### B. Rate region comparison

In this section, we compare the rate region of the two users uplink AWGN channel, using SIC and PSR. Fig. 13 (A) shows the rate region of both SIC and PSR systems using a data rate range of 3-6 Mbps, where the first modulation and coding scheme 0 (MCS0) of 802.11a systems is used in this evaluation. The data rate of users is varied by changing the signal power of a user, while the signal power of the other user and the noise power level is kept constant. The SNR for this test is equal to 2.3 dB, which is the lowest SNR that achieves the optimum rate region using SIC receivers.

The current maximum rate region of a communication system, for a two-user scenario, can be achieved using SIC receivers [3]. In 802.11a systems, this is depicted by the black curve in Fig. 13 (A). The maximum rate of a user in this rate region is constrained by the rate of the other user who shares the same link. This is because a SIC decoder considers the interfering signal of a user as noise in order to decode the signal of the other user [3]. Interestingly, this role does not apply to the PSR system. This is because the PSR exploits the collision-free partial symbol to bootstrap the colliding frames in a collision, where such a partial symbol is not constrained

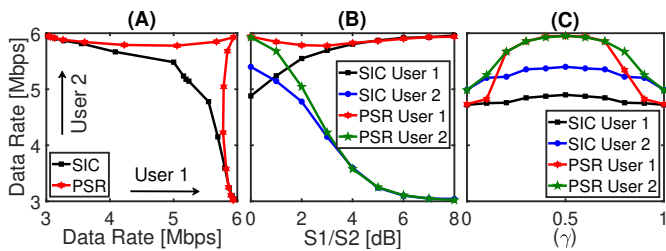


Fig. 13: Rate region comparisons. (A) the rate region of the two user uplink AWGN channel. (B) The data rate of user 1 and 2 using SIC and PSR. (C) Rate performance versus different values of  $\gamma$ .

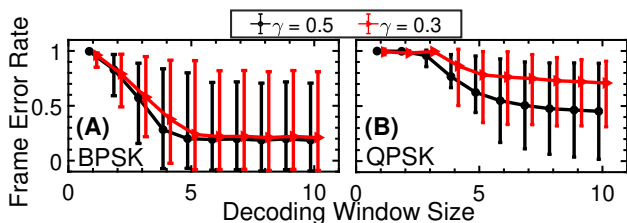


Fig. 14: Average FER of all collision cases versus decoding window size of the outer loop decoder. Maximum and minimum FER values, due to variation of channel conditions and noise, indicated by the vertical lines. (A) using BPSK modulation; (B) using QPSK modulation.

by the rate of the interfering user. Therefore, the rate region achieved by the PSR receiver for two users is beyond that of the SIC receivers, *i.e.* the PSR has a larger two-user rate region than that of the SIC receivers, as shown by the red curve in Fig. 13 (A).

To investigate further how the PSR decoder can “break” the rate region, we provide the rate performance of the two users, using SIC and PSR with  $\gamma = 0.5$ , versus the difference between their signal powers. This is depicted in Fig. 13 (B). As expected, using SIC decoder, the rate of a user decreases as the power difference between the two received signals decreases (*i.e.* the signal power of the interfering user increases). On the other hand, the PSR decoder outperforms the SIC decoder, where the rate performance of a user is maintained at almost the same level regardless of the difference in power between the two received signals.

However, the performance of the PSR is not without limitation, where the PSR decoder depends on the duration of the partial symbols in time; such duration is represented by the  $\gamma$  ratio factor, defined in Section III-A1. Fig. 13 (C), shows the rate performance of the two users using the PSR and the SIC decoders versus different values of  $\gamma$  measured at SINR = 0 dB. The figure shows that the PSR performance outperforms the SIC decoder for most of the  $\gamma$  values and then converges to the SIC performance level at the edges of  $\gamma$  values. Moreover, from the figure, we note that the PSR performance is constrained by the lowest value of  $\gamma$ , this is because the shorter the period the partial symbols have, the fewer time samples used, and hence, the lower the amount of energy per symbol, leading to more errors and lower rate.

### C. FER measurements in link layer

As mentioned in Section III-C1, using conventional 802.11 receivers the physical frames are declared successfully decoded if they pass the CRC. However, for the unsuccessfully decoded frames, which are tested with CRC failure, retransmission is required for these frames. This is not the case for the SIC and PSR receivers, where these techniques are activated in this testbed after a frame fails to pass the CRC. This means that the SIC and PSR act only on the unsuccessfully decoded frames. To investigate which technique, SIC or PSR, has a higher decoding capability of these undecoded frames the two techniques are evaluated using the FER as the frame decoding capability metric.

In this section, we evaluate SIC and PSR in terms of FER performance using all permutations of two nodes transmitting simultaneously to another node in our testbed (this is called collision cases). In total our indoor testbed, shown in Fig. 12, provides 45 collision cases. The evaluation metrics are (i) FER versus the decoding window size of the outer loop decoder, where the decoder is described in §III-A2; (ii) FER versus different values of  $\gamma$ ; and (iii) the CDF of the FER for PSR and compared to SIC for all the collision cases.

#### a) Performance evaluation of the outer loop decoder:

As mentioned in Section III-A2, the PSR makes a decoding decision when its outer loop decoder reaches the maximum decoding window. In this experiment, the decoding window size is set to  $G = 10$ ,  $G$  defined in Section III-A2. Fig. 14 shows the FER performance of different stages of the outer loop decoder. Each marker point in the curve represents the average FER performance of one of the 45 collision cases tested, while the candle bars indicate the highest and lowest FER performance for each case. Such a range of variation for each case is due to differing channel effects, CFO and signal to noise level. The FER performance improvement comes from the nested-loop design which is based on interactions of the inner loop decoder with the backward and coding stages of the outer loop decoder, as described in Section III-A2. As expected, the performance worsens for lower values of  $\gamma$  and/or higher modulation.

From the figure, it is clear that PSR with BPSK modulation format is better than that of using QPSK modulation. This is because having only a partial symbol causes self-induced ICI exclusively from the real part of the signal to the imaginary part and vice versa, as well as, ICI from the real and imaginary parts to themselves. Thus, a one-dimensional modulation format, such as BPSK, will be decoded with lower error rate, using the inner loop decoder, in comparison to a two-dimensional modulation, such as QPSK. In general, in all cases there is evidence of error floor, indicating values of decoding window size beyond which no further improvement of FER can be obtained.

b) FER versus  $\gamma$ : Fig. 15(a) shows FER performance of PSR for different collision cases versus  $\gamma$  values, which is taken from the last stage of the outer loop decoder,  $G = 10$ . Each point in the figure represents the FER of a single collision case (black points are BPSK while red are QPSK). Clearly, the FER performance is almost symmetrical around  $\gamma = 0.5$ , because the FER performance is restricted to the

TABLE I: Performance summary of PSR, SIC and 802.11a decoding capability of colliding frames.

Experimental set	802.11a		SIC		PSR	
	BPSK	QPSK	BPSK	QPSK	BPSK	QPSK
Decoding capability of colliding frames	0%	0%	37%	9%	59%	25%

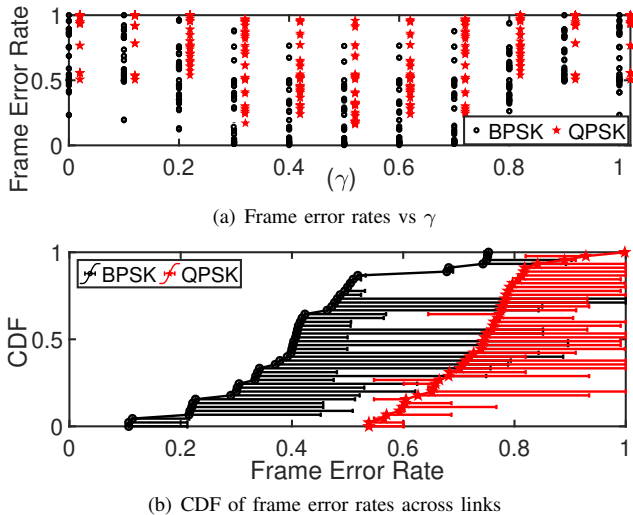


Fig. 15: PSR FER performance. (a) FER versus  $\gamma$  for different collision cases; (b) CDF of FER across all collision cases (in total 45 cases), each case is a single marker point. The horizontal lines show the difference in FER performance between PSR and SIC.

shortest partial symbol duration of the two colliding users (see Section III-A2).

*c) CDF of FER:* The CDF of the FER performance of each collision case is shown in Fig. 15(b), where each marker point on the curves indicates average PSR performance over all  $\gamma$  values. The horizontal lines attached to each point represent the difference in performance of the PSR and SIC decoders. On average, PSR achieves 22% and 16% better (lower) FER than SIC, using BPSK and QPSK modulation, respectively.

To sum up, Table I shows the decoding capability of colliding frames, which the ability of decoding frames with 12,000 bits, using 802.11a, SIC and PSR receivers. From these results, the PSR receiver is experimentally shown to be effective for non-line-of-sight and line-of-sight indoor environment, thus paving the way for practical implementation of PSR in wireless LAN systems. In addition, the results make PSR an attractive technique for low data rate networks that suffer from collisions. An example of such low data rate networks is the 802.11ah internet-of-things (IoT), which is a low rate and long range network [54], [55]. Using PSR in the uplink of 802.11ah systems can enhance the spectrum utilization by decoding up to 59% of the collided frames.

#### D. End-to-end performance

In this section, we use the testbed in Fig. 12 to evaluate the throughput and retransmission rate performance of PSR in intra- and inter-network collisions, described in Section III-B. The two scenarios are implemented in NS-3, driven by our experimental testbed decoding performance.

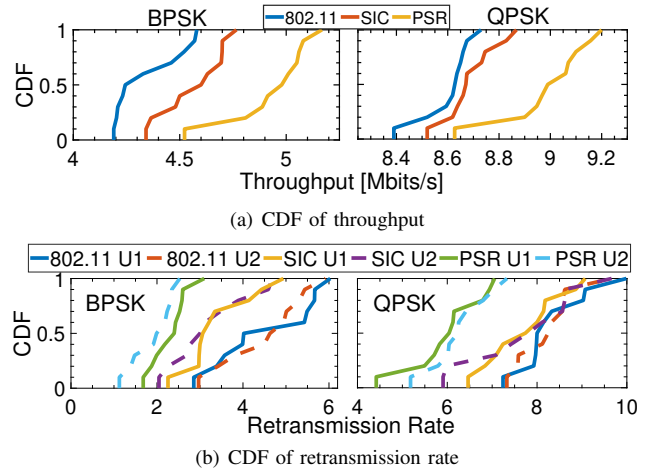


Fig. 16: CDF of throughput and retransmission rate in intra-network scenario using uplink-UDP transmissions. The legends in figure (b) apply to the following figures.

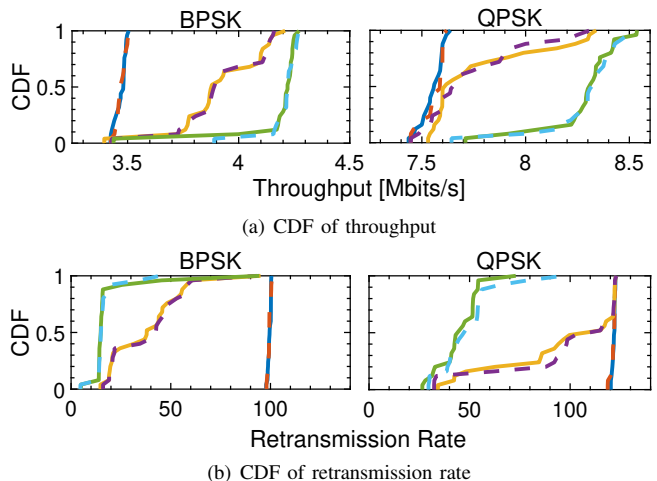


Fig. 17: CDF of throughput and retransmission rate in inter-network scenario using bulk TCP transmissions.

##### 1) Intra-network collisions

We use this case study scenario to evaluate the performance of PSR, SIC and 802.11n for intra-network collisions, such as the collisions from hidden terminal nodes. We use Network 1 in Fig. 12 as the experimental testbed, providing ten collision cases. Data flow of UDP packets using 802.11n frame structure is simulated in NS-3. Request-to-send/clear-to-send (RTS/CTS) is disabled. The network performance is evaluated using throughput and retransmission rate.

*a) Throughput performance at the transport layer:* We start by comparing the throughput of each decoder. Fig. 16(a) shows the CDF of throughput measured for collision cases in Network 1. Compared to a baseline 802.11n decoder, PSR improves average throughput by 13.6%, while the average

TABLE II: Summary of PSR performance enhancement in comparison to 802.11n.

Experimental set	Uplink UDP		Bulk TCP		Video on demand	
	BPSK	QPSK	BPSK	QPSK	BPSK	QPSK
Throughput enhancement	13.6%	4.7%	21.27%	9.7%	21.26%	7.7%
Retransmission rate reduction	49.3%	27.6%	81%	63%	80.8%	57%

throughput improvement of the SIC decoder is 5.2%. For QPSK modulation, the average throughput improvements of PSR and SIC are 4.7% and 1.2% over the 802.11n baseline. The throughput enhancement comes from the fact that PSR attempts to decode collided frames and recovers their data.

*b) Retransmission rate performance:* Fig. 16(b) shows the CDF of retransmission rates measured for each collision case in Network 1. PSR and SIC reduce average BPSK retransmission rate by 49.3% and 25.5% respectively. For QPSK modulation, those reduction change to 27.6% and 7.2%, compared to 802.11n.

The retransmission enhancements can be translated into two types of gain: *(i)* frame loss reduction and *(ii)* power consumption enhancements. PSR reduces the frame loss, which occurs in the uplink regime of 802.11n, from 4.6 to 2 and from 8.3 to 6 measured in *frame/s* for BPSK and QPSK, respectively. The reason for the higher enhancement in frame loss for BPSK compared to QPSK is due to the PSR capability in recovering higher percentage of the collided frames for low rate schemes, such as BPSK.

In terms of power consumption, the work in [56] shows that the impact of retransmission on power consumption is directly proportional. Hence, implementing PSR in the current 802.11 systems will decrease the power consumption, occurs in the retransmission scenarios, in the user station by the factor of the retransmission reduction rate, which are 49.3% and 27.6% for BPSK and QPSK modulation formats, respectively, compared to the baseline 802.11n. Furthermore, these results will hopefully inspire the future exploration of the adoption of PSR in the uplink regime of the 802.11ah IoT networks. Thus, the power consumption in the IoT devices can be reduced, due to the reduction in the frames retransmission, and hence, maximizing battery and saving costs.

## 2) Inter-network collisions

We evaluate the PSR performance in a scenario representing a topology, where two stations downloading data using *(i)* bulk TCP and *(ii)* video on demand data flows from the AP in their respective networks, as shown in Fig. 2. Since the two data flows require uplink and downlink data, collisions occur when a station is receiving a frame while the other station, in the neighbouring network, is transmitting a frame to its AP.

Under these circumstances, we evaluate the downlink performance of the two networks in Fig. 12 as the experimental testbed, providing 25 collision cases for each network. In every experimental run, a station from each network is involved, as well as its AP, hence, there are two links under test: the first link is between a Network 1 station and AP 1 while the second link is between a Network 2 station and AP 2. We measure the throughput at the transport layer of each station, as well as the link layer retransmission rate of AP 1 and AP 2. We plot the CDF of throughput and retransmission rates for both bulk

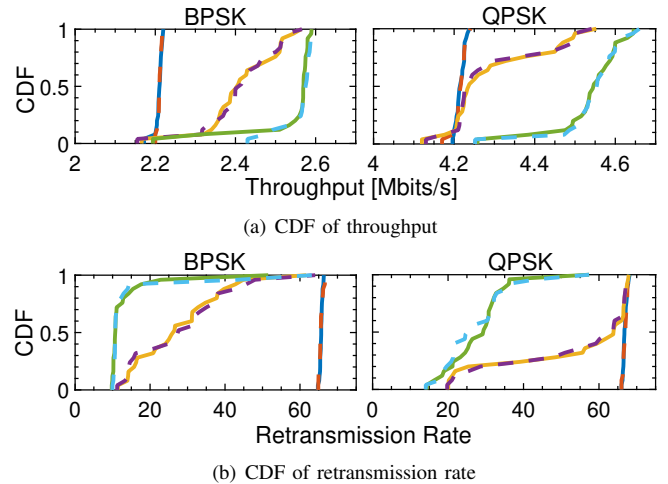


Fig. 18: CDF of throughput and retransmission rate in inter-network scenario using video on demand transmissions.

TCP and video on demand using BPSK and QPSK modulation formats in Fig. 17 and 18.

*a) Throughput performance:* According to our experimental results, the average throughput improvements in comparison to 802.11n, shown in Fig. 17(a) and 18(a), are 21.27% and 21.26% for the downlink bulk TCP and downlink video on demand, respectively, for BPSK modulation. The average throughput enhancement using QPSK modulation are 9.7% and 7.7% for the above respective topology scenarios shown in the same figures.

The throughput enhancement, in PSR systems, is due to the fact that PSR acts only on the collided frames with decoding capability of 59% and 25% of the collided frames for BPSK and QPSK, respectively, as mentioned in Section V-C. Thus, PSR always has potential for the throughput improvement but never degrades the system performance. This makes PSR an attractive potential system in highly dense user environment, such as massive offices that has multiple 802.11 networks operating close to each other and suffer from inter-network collisions.

*b) Retransmission rate performance:* Moreover, the average retransmission rate in BPSK modulation, shown in Fig. 17(b) and 18(b), is reduced by 81% and 80.8% for the downlink bulk TCP and downlink video on demand, respectively. The reductions for QPSK modulation are 63% and 57% for the above respective topologies shown in the same figures.

As mentioned earlier, the retransmission rate enhancement can be translated to frame-loss reduction and power consumption enhancement. Using PSR in networks suffering from inter-network collisions leads to reduction in the frame-loss of the downlink bulk TCP in 802.11n networks from 99.6 to 19.3

and from 121.7 to 45.1 measured in *frame/s* for BPSK and QPSK modulation formats, respectively. Using the downlink video on demand, the frame loss in 802.11n networks from 65.6 to 13.4 and from 66.9 to 28.3 measured in *frame/s* for BPSK and QPSK modulation formats, respectively. In addition, PSR has the potential to reduce the power consumption that occurs due to frames retransmission by acting on the collided frames to recover their data.

To summarize the results of PSR system, Table II shows a summary of the performance enhancement in terms of throughput and retransmission rate compared to the baseline 802.11n systems.

## VI. CONCLUSION

This work presents a new receiving technique and design, termed Partial Symbol Recovery (PSR), that allows efficient operation beyond the capacity region of fully overlapping data in wireless communication systems with collisions. The PSR technique is based on recovery of the parts of OFDM symbols, which are collision-free, followed by the reconstruction of complete symbols to recover progressively the frames of two users suffering collision. The system is evaluated in a testbed of 12-nodes using software defined radio platforms. Extensive experimental results show 10–21% throughput enhancement in 802.11n systems when downlink bulk TCP, downlink video-on-demand and uplink UDP are operated in a collision-rich environment and under different scenarios.

## REFERENCES

- [1] S. Gollakota and D. Katabi, "Zigzag decoding: Combating hidden terminals in wireless networks," in *Proc. of the ACM SIGCOMM Conf.*, Aug. 2008, pp. 159–170.
- [2] K. Jamieson and H. Balakrishnan, "PPR: Partial packet recovery for wireless networks," in *SIGCOMM*, 2007.
- [3] D. Tse and P. Viswanath, *Fundamentals of Wireless Communication*. Cambridge University Press, 2005.
- [4] R. Ahlswede, "Multi-way communication channels," in *IEEE ISIT Symp.*, 1971, pp. 103–135.
- [5] H. Liao, "A coding theorem for multiple access communications," in *IEEE ISIT Symp.*, 1972.
- [6] M. Damen, H. El Gamal, and G. Caire, "On maximum likelihood detection and the search for the closest lattice point," *IEEE Trans. on Information Theory*, vol. 49, no. 10, pp. 2389–2402, 2003.
- [7] E. Agrell, T. Eriksson, A. Vardy, and K. Zeger, "Closest point search in lattices," *IEEE Trans. on Information Theory*, vol. 48, no. 8, pp. 2201–2214, Aug. 2002.
- [8] D. Barry, E. Lee, and D. Messerschmitt, *Digital Communication*, 3rd ed. New York, NY: Springer, 2003.
- [9] J. Mazo, "Faster-than-Nyquist signalling," *Bell Syst. Tech. J.*, vol. 54, pp. 1451–1462, Oct. 1975.
- [10] I. Kanaras, A. Chorti, M. Rodrigues, and I. Darwazeh, "Spectrally efficient FDM signals: Bandwidth gain at the expense of receiver complexity," in *ICC*, 2009.
- [11] S. Ahmed, "Spectrally efficient FDM communication signals and transceivers: Design, mathematical modeling and system optimization," Ph.D. dissertation, Univ. College London, 2011.
- [12] S. Isam and I. Darwazeh, "Characterizing the intercarrier interference of a non-orthogonal spectrally efficient FDM system," in *CSNDSP*, 2012.
- [13] F. Rusek and J. Anderson, "The two dimensional Mazo limit," in *ISIT*, 2005.
- [14] —, "Multi-stream faster than Nyquist signaling," *IEEE Trans. on Comms.*, vol. 57, no. 5, pp. 1329–1340, 2009.
- [15] J. Anderson, F. Rusek, and V. Öwall, "Faster-than Nyquist signaling," *Proc. of the IEEE*, vol. 101, no. 8, pp. 1817–1830, Aug. 2013.
- [16] W. Ozan, K. Jamieson, and I. Darwazeh, "Truncating and oversampling OFDM signals in white Gaussian noise channels," in *CSNDSP*, 2016.
- [17] H. Rahul, S. Kumar, and D. Katabi, "JMB: Scaling Wireless Capacity with User Demands," in *SIGCOMM*, 2012.
- [18] E. Hamed, H. Rahul, M. A. Abdelghany, and D. Katabi, "Real-time Distributed MIMO Systems," in *SIGCOMM*, 2016.
- [19] E. Hamed, H. Rahul, and B. Partov, "Chorus: Truly distributed distributed-MIMO," in *SIGCOMM*, 2018.
- [20] Q. Yang, X. Li, H. Yao, J. Fang, K. Tan, W. Hu, J. Zhang, and Y. Zhang, "BigStation: Enabling Scalable Real-time Signal Processing in Large MU-MIMO systems," in *SIGCOMM*, 2013.
- [21] C. Shepard, H. Yu, N. Anand, L. Li, T. Marzetta, R. Yang, and L. Zhong, "Argos: Practical many-antenna base stations," in *MobiCom*, 2012.
- [22] O. Avner and S. Manner, "Multi-user communication networks: A coordinated multi-armed bandit approach," *IEEE/ACM Transactions on Networking*, vol. 27, no. 6, pp. 2192–2207, 2019.
- [23] S. Jafar and S. Shamai, "Degrees of freedom of the MIMO X channel," *IEEE Trans. on Information Theory*, vol. 54, no. 1, pp. 151–170, Jan. 2008.
- [24] S. Gollakota, S. Perli, and D. Katabi, "Interference Alignment and Cancellation," in *SIGCOMM*, 2009.
- [25] K. Lin, S. Gollakota, and D. Katabi, "Random access heterogeneous MIMO networks," in *SIGCOMM*, 2011.
- [26] C. Suh and D. Tse, "Interference alignment for cellular networks," in *Allerton*, 2008.
- [27] X. Guo, Y. He, X. Zheng, L. Yu, and O. Gnowali, "Zigfi: Harnessing channel state information for cross-technology communication," *IEEE/ACM Transactions on Networking*, 2020.
- [28] Y. Chen, S. Wang, Z. Li, and T. He, "Reliable Physical-Layer Cross-Technology Communication With Emulation Error Correction," *IEEE/ACM Transactions on Networking*, 2020.
- [29] S. Wong, H. Yang, S. Lu, and V. Bharghavan, "Robust rate adaptation for 802.11 wireless networks," in *MobiCom*, 2006.
- [30] J. Bicket, "Bit-Rate Selection in Wireless Networks," Master's thesis, Massachusetts Inst. of Technology, Feb. 2005.
- [31] J. Zhang, K. Tan, J. Zhao, H. Wu, and Y. Zhang, "A practical SNR-guided rate adaptation," in *Infocom*, 2008.
- [32] J. Camp and E. Knightly, "Modulation Rate Adaptation in Urban and Vehicular Environments: Cross-Layer Implementation and Experimental Evaluation," in *MobiCom*, 2008.
- [33] D. Halperin, W. Hu, A. Sheth, and D. Wetherall, "Predictable 802.11 packet delivery from wireless channel measurements," in *SIGCOMM*, 2010.
- [34] M. Vutukuru, H. Balakrishnan, and K. Jamieson, "Cross-layer wireless bit rate adaptation," in *SIGCOMM*, 2009.
- [35] H. Jin, A. Khandekar, and R. McEliece, "Irregular repeat-accumulate codes," in *Proc. Symp. Turbo Codes Related Topics*, 2000.
- [36] M. Luby, "LT codes," in *Proc. of the Symp. on Foundations of Computer Science*, 2002, p. 271.
- [37] J. Byers, M. Luby, and M. Mitzenmacher, "A digital fountain approach to asynchronous reliable multicast," *IEEE J. Sel. Areas in Comm.*, vol. 20, no. 10, pp. 1528–1540, Oct. 2002.
- [38] J. Byers, M. Luby, M. Mitzenmacher, and A. Rege, "A digital fountain approach to reliable distribution of bulk data," in *SIGCOMM*, 1998.
- [39] A. Shokrollahi, "Raptor codes," *IEEE transactions on information theory*, vol. 52, no. 6, pp. 2551–2567, 2006.
- [40] O. Etesami and A. Shokrollahi, "Raptor codes on binary memoryless symmetric channels," *IEEE Trans. on Information Theory*, vol. 52, no. 5, pp. 2033–2051, 2006.
- [41] J. Perry, P. Iannucci, K. Fleming, H. Balakrishnan, and D. Shah, "Spinal codes," in *SIGCOMM*, 2012.
- [42] J. Perry, H. Balakrishnan, and D. Shah, "Rateless spinal codes," in *HotNets Workshop*, 2011.
- [43] K. C. Lin, N. Kushman, and D. Katabi, "ZipTx: Exploiting the gap between bit errors and packet loss," in *MobiCom*, 2008, pp. 351–362.
- [44] J. Choi, M. Jain, K. Srinivasan, P. Levis, and S. Katti, "Achieving single channel, full duplex wireless communication," in *MobiCom*, 2010.
- [45] M. Jain, J. Choi, T. Kim, D. Bharadia, K. Srinivasan, S. Seth, P. Levis, S. Katti, and P. Sinha, "Practical, real-time, full duplex wireless," in *MobiCom*, 2011.
- [46] D. Bharadia, E. McMillin, and S. Katti, "Full duplex radios," in *SIGCOMM*, 2013.
- [47] D. Bharadia and S. Katti, "Full duplex MIMO radios," in *NSDI*, 2014.
- [48] L. Bahl, J. Cocke, F. Jelinek, and J. Raviv, "Optimal decoding of linear codes for minimizing symbol error rate (corresp.)," *IEEE Transactions on Information Theory*, vol. 20, no. 2, pp. 284–287, March 1974.
- [49] E. Agrell, T. Eriksson, A. Vardy, and K. Zeger, "Closest point search in lattices," *IEEE transactions on information theory*, vol. 48, no. 8, pp. 2201–2214, 2002.

- [50] M. O. Damen, H. El Gamal, and G. Caire, "On maximum-likelihood detection and the search for the closest lattice point," *IEEE Transactions on information theory*, vol. 49, no. 10, pp. 2389–2402, 2003.
- [51] T. Xu and I. Darwazeh, "Multi-band reduced complexity spectrally efficient fdm systems," in *Communication Systems, Networks & Digital Signal Processing (CSNDSP), 2014 9th International Symposium on*. IEEE, 2014, pp. 982–987.
- [52] "IEEE Standard for Information technology–Telecommunications and information exchange between systems Local and metropolitan area networks–Specific requirements - Part 11: Wireless LAN Medium Access Control (MAC) and Physical Layer (PHY) Specifications," *IEEE Std 802.11-2016 (Revision of IEEE Std 802.11-2012)*, pp. 1–3534, Dec 2016.
- [53] G. F. Riley and T. R. Henderson, "The ns-3 network simulator," in *Modeling and tools for network simulation*. Springer, 2010, pp. 15–34.
- [54] M. Park, "IEEE 802.11 ah: sub-1-GHz license-exempt operation for the internet of things," *IEEE Communications Magazine*, vol. 53, no. 9, pp. 145–151, 2015.
- [55] "IEEE Standard for Information technology–Telecommunications and information exchange between systems - Local and metropolitan area networks–Specific requirements - Part 11: Wireless LAN Medium Access Control (MAC) and Physical Layer (PHY) Specifications Amendment 2: Sub 1 GHz License Exempt Operation," *IEEE Std 802.11ah-2016 (Amendment to IEEE Std 802.11-2016, as amended by IEEE Std 802.11ai-2016)*, pp. 1–594, May 2017.
- [56] P. Serrano, A. Garcia-Saavedra, G. Bianchi, A. Banchs, and A. Azcorra, "Per-frame energy consumption in 802.11 devices and its implication on modeling and design," *IEEE/ACM Transactions on networking*, vol. 23, no. 4, pp. 1243–1256, 2014.

## APPENDIX

### A. Modelling the covariance matrix of a partial symbol

The matrix components can be found as:

$$\begin{aligned} \mathbf{\Gamma} &= \mathbf{F}_{(l,m)}^H \mathbf{F}_{(m,n)} \\ &= \frac{1}{\gamma Q} \sum_{m=0}^{\gamma Q-1} \exp \left[ \frac{-j2\pi lm}{Q} \right] \exp \left[ \frac{j2\pi mn}{Q} \right] \\ &= \begin{cases} 1, & l = n \\ \frac{1}{\gamma Q} \left[ \frac{1 - \exp[-j2\pi(l-n)\gamma]}{1 - \exp\left[\frac{-j2\pi(l-n)}{Q}\right]} \right], & l \neq n \end{cases} \quad (10) \end{aligned}$$

where  $\mathbf{\Gamma} \in \mathbb{C}^{Q \times Q}$  is the covariance matrix,  $l = n = [0, 1, \dots, Q-1]$  are the subcarriers row and column indices, respectively,  $(\cdot)^H$  is the transpose conjugate operation. The final derivation in (10) is based on the sum of geometric series:  $\sum_{k=0}^{Q-1} r^k = \frac{1-r^Q}{1-r}$ . From (10), it should be noted that the covariance matrix coefficients change according to the duration of the partial symbol, which is identified by the  $\gamma$  factor.

### B. Modelling the covariance matrix in a block of subcarriers

We follow the same method that we used to derive the covariance matrix for the all subcarriers, which is given in equation (10). Thus, the covariance matrix,  $\tilde{\mathbf{\Gamma}} \in \mathbb{C}^{N \times N}$ , of each block is given as:

$$\begin{aligned} \tilde{\mathbf{\Gamma}} &= \begin{cases} 1, & m = q \\ \frac{1}{\gamma Q} \left[ \frac{1 - \exp[-j2\pi(m-q)\gamma]}{1 - \exp\left[\frac{-j2\pi(m-q)}{Q}\right]} \right], & m \neq q \end{cases} \quad (11) \\ &= \mathbf{I} + \mathbf{\Lambda} \end{aligned}$$

where  $m = q = [0, 1, \dots, N-1]$  are the subcarriers row and column indices, respectively,  $N$  is the number of subcarrier in

a block,  $\mathbf{I} \in \mathbb{C}^{N \times N}$  is an identity matrix and the  $\mathbf{\Lambda} \in \mathbb{C}^{N \times N}$  is the interference coefficients matrix of each block.

### C. Modelling the covariance matrix between the blocks of sucarrriers

In order to quantify the interference between the blocks, we derive the interference matrix using equation (10). Thus, the IBI interference matrix is given as:

$$\begin{aligned} \mathbf{\Gamma}_{\text{IBI}} &= \begin{cases} 1, & l = n \\ 0, & l \neq n \ \& \\ & N_1 \leq l \leq N_2, \\ & N_1 \leq n \leq N_2 \end{cases} \\ &= \frac{1}{\gamma Q} \left[ \frac{1 - \exp[-j2\pi(l-n)\gamma]}{1 - \exp\left[\frac{-j2\pi(l-n)}{Q}\right]} \right], \quad \text{else} \\ &= \mathbf{I}_{\text{IBI}} + \mathbf{\Psi} \end{aligned} \quad (12)$$

where  $l = n = [0, 1, \dots, Q-1]$  are the subcarriers row and column indices, respectively,  $N_1$  is the index of the first subcarrier in a block, while  $N_2$  is the index of the last subcarrier in a block,  $\mathbf{I}_{\text{IBI}} \in \mathbb{C}^{Q \times Q}$  is an identity matrix and the matrix  $\mathbf{\Psi} \in \mathbb{C}^{Q \times Q}$  is the interference coefficients matrix.

# References

- [1] 3GPP TS 36.300 version 8.12.0 Release 8. Evolved universal terrestrial radio access (E-UTRA) and evolved universal terrestrial radio access network (EUTRAN); overall description; stage 2 (release 8), April 2010.
- [2] 3GPP TS 23.502 version 15.2.0 Release 15. 5G; Procedures for the 5G System, June 2018.
- [3] Jeffrey G Andrews, Stefano Buzzi, Wan Choi, Stephen V Hanly, Angel Lozano, Anthony CK Soong, and Jianzhong Charlie Zhang. What will 5G be? *IEEE Journal on selected areas in communications*, 32(6):1065–1082, 2014.
- [4] I Darwazeh, RC Grammenos, and T Xu. Key Enabling Technologies for 5G Mobile Communications. In *ch. Spectrally Efficient Frequency Division Multiplexing for 5G*. Springer, 2016.
- [5] Fa-Long Luo and Charlie Zhang. *Signal processing for 5G: algorithms and implementations*. John Wiley & Sons, 2016.
- [6] Visual Networking Index Cisco. Cisco Annual Internet Report (2018–2023) White Paper. 2018.
- [7] Erik Dahlman, Stefan Parkvall, and Johan Skold. *4G: LTE/LTE-advanced for mobile broadband*. Academic press, 2013.
- [8] Ioannis Kanaras, Arsenia Chorti, Miguel RD Rodrigues, and Izzat Darwazeh. Spectrally efficient FDM signals: Bandwidth gain at the expense of receiver complexity. In *Communications, 2009. ICC'09. IEEE International Conference on*, pages 1–6. IEEE, 2009.

- 
- [9] Sergey V Zavjalov, Sergey V Volvenko, and Sergey B Makarov. A method for increasing the spectral and energy efficiency SEFDM signals. *IEEE Communications Letters*, 20(12):2382–2385, 2016.
- [10] Kyeongwon Park, Haeun Kim, Arim Lee, Donghoon Kang, and Wangrok Oh. Iterative frequency-domain inter-carrier interference cancellation for coded SEFDM. *Electronics Letters*, 53(19):1333–1335, 2017.
- [11] Yiguang Wang, Yingjun Zhou, Tao Gui, Kangping Zhong, Xian Zhou, Liang Wang, Alan Pak Tao Lau, Chao Lu, and Nan Chi. SEFDM based spectrum compressed VLC system using RLS time-domain channel estimation and ID-FSD hybrid decoder. In *ECOC 2016; 42nd European Conference on Optical Communication; Proceedings of*, pages 1–3. VDE, 2016.
- [12] Tongyang Xu and Izzat Darwazeh. Transmission experiment of bandwidth compressed carrier aggregation in a realistic fading channel. *IEEE Transactions on Vehicular Technology*, 66(5):4087–4097, 2017.
- [13] Jiancun Fan, Shengjie Guo, Xiangwei Zhou, Yajie Ren, Geoffrey Ye Li, and Xi Chen. Faster-than-Nyquist signaling: An overview. *IEEE Access*, 5:1925–1940, 2017.
- [14] Waseem Ozan, Paul Anthony Haigh, Bo Tan, and Izzat Darwazeh. Experimental SEFDM pipelined iterative detection architecture with improved throughput. In *2018 IEEE 87th Vehicular Technology Conference (VTC Spring)*, pages 1–5. IEEE, 2018.
- [15] Safa Isam and Izzat Darwazeh. Robust channel estimation for spectrally efficient FDM system. In *Telecommunications (ICT), 2012 19th International Conference on*, pages 1–6. IEEE, 2012.
- [16] John B Anderson, Fredrik Rusek, and Viktor Öwall. Faster-than-Nyquist signaling. *Proceedings of the IEEE*, 101(8):1817–1830, 2013.

- 
- [17] Yi Feng and Jan Bajcsy. Improving throughput of faster-than-Nyquist signaling over multiple-access channels. In *Vehicular Technology Conference (VTC Spring), 2015 IEEE 81st*, pages 1–5. IEEE, 2015.
- [18] Yi Feng and Jan Bajcsy. On faster-than-Nyquist transmission over a multiple-access channel. In *Military Communications Conference (MILCOM), 2014 IEEE*, pages 824–829. IEEE, 2014.
- [19] Masanori Hamamura and Shinichi Tachikawa. Bandwidth efficiency improvement for multi-carrier systems. In *Personal, Indoor and Mobile Radio Communications, 2004. PIMRC 2004. 15th IEEE International Symposium on*, volume 1, pages 48–52. IEEE, 2004.
- [20] Waseem Ozan, Kyle Jamieson, and Izzat Darwazeh. Truncating and oversampling OFDM signals in white Gaussian noise channels. In *Communication Systems, Networks and Digital Signal Processing (CSNDSP), 2016 10th International Symposium on*, pages 1–6. IEEE, 2016.
- [21] Ryan Costadinos Grammenos. *Spectrum Optimisation in Wireless Communication Systems: Technology Evaluation, System Design and Practical Implementation*. PhD thesis, UCL (University College London), 2013.
- [22] Taewon Hwang, Chenyang Yang, Gang Wu, Shaoqian Li, and Geoffrey Ye Li. OFDM and its wireless applications: A survey. *IEEE transactions on Vehicular Technology*, 58(4):1673–1694, 2008.
- [23] 3GPP. LTE; Evolved Universal Terrestrial Radio Access (E-UTRA) and Evolved Universal Terrestrial Radio Access Network (E-UTRAN); Overall description; Stage 2 . 3GPP TS 36.300, Rel. 11, v.11.6.0, 3GPP, July 2013.
- [24] Eldad Perahia and Robert Stacey. *Next generation wireless LANs: 802.11 n and 802.11 ac*. Cambridge university press, 2013.

- 
- [25] M. Shafi, A. F. Molisch, P. J. Smith, T. Haustein, P. Zhu, P. De Silva, F. Tufvesson, A. Benjebbour, and G. Wunder. 5G: A Tutorial Overview of Standards, Trials, Challenges, Deployment, and Practice. *IEEE Journal on Selected Areas in Communications*, 35(6):1201–1221, June 2017.
- [26] G. Wunder, P. Jung, M. Kasparick, T. Wild, F. Schaich, Y. Chen, S. T. Brink, I. Gaspar, N. Michailow, A. Festag, L. Mendes, N. Cas-siau, D. Ktenas, M. Dryjanski, S. Pietrzyk, B. Eged, P. Vago, and F. Wiedmann. 5GNOW: non-orthogonal, asynchronous waveforms for future mobile applications. *IEEE Commun. Mag.*, 52(2):97–105, February 2014.
- [27] Mojtaba Vaezi, Zhiguo Ding, and H Vincent Poor. *Multiple access techniques for 5G wireless networks and beyond*. Springer, 2019.
- [28] M Rodrigues and Izzat Darwazeh. A spectrally efficient frequency division multiplexing based communications system. In *Proc. 8th Int. OFDM Workshop*, pages 48–49, 2003.
- [29] Izzat Darwazeh, Hedaia Ghannam, and Tongyang Xu. The First 15 Years of SEFDM: A Brief Survey. In *2018 11th International Symposium on Communication Systems, Networks & Digital Signal Processing (CSNDSP)*, pages 1–7. IEEE, 2018.
- [30] MRD Rodrigues and Izzat Darwazeh. Fast OFDM: A proposal for doubling the data rate of OFDM schemes. 2002.
- [31] Nicola Michailow, Maximilian Matthé, Ivan Simões Gaspar, Ainoa Navarro Caldevilla, Luciano Leonel Mendes, Andreas Festag, and Gerhard Fettweis. Generalized frequency division multiplexing for 5th generation cellular networks. *IEEE Transactions on Communica-tions*, 62(9):3045–3061, 2014.
- [32] Behrouz Farhang-Boroujeny. OFDM versus filter bank multicarrier. *IEEE signal processing magazine*, 28(3):92–112, 2011.

- 
- [33] Kai Li. *Fast orthogonal frequency division multiplexing (Fast-OFDM) for wireless communications*. University of London, University College London (United Kingdom), 2008.
- [34] Tongyang Xu and Izzat Darwazeh. Non-orthogonal narrowband internet of things: A design for saving bandwidth and doubling the number of connected devices. *IEEE Internet of Things Journal*, 5(3):2120–2129, 2018.
- [35] Fuqin Xiong. M-ary amplitude shift keying OFDM system. *IEEE Transactions on Communications*, 51(10):1638–1642, 2003.
- [36] Tongyang Xu. *Bandwidth compressed waveform and system design for wireless and optical communications: Theory and practice*. PhD thesis, UCL (University College London), 2017.
- [37] Wang Jian, Yang Xun, Zhang Xi-lin, and Daoben Li. The prefix design and performance analysis of DFT-based overlapped frequency division multiplexing (OvFDM-DFT) system. In *2007 3rd International Workshop on Signal Design and Its Applications in Communications*, pages 361–364. IEEE, 2007.
- [38] Yafei Hou and Masanori Hamamura. Bandwidth efficiency of PC-OFDM systems with high compaction multi-carrier modulation. In *Proceedings. 2005 International Conference on Wireless Communications, Networking and Mobile Computing, 2005.*, volume 1, pages 197–200. IEEE, 2005.
- [39] Ryuji Hayashi and Masanori Hamamura. Performance of Continuous-Phase, Unmodulated Parallel-Combinatory High-Compaction Multi-carrier Modulation. In *2008 International Wireless Communications and Mobile Computing Conference*, pages 195–199. IEEE, 2008.
- [40] Ryuji Hayashi and Masanori Hamamura. Complexity-reduced decoding algorithm for unmodulated parallel-combinatory high-compaction multicarrier modulation signals. In *2008 International Conference on Innovations in Information Technology*, pages 49–53. IEEE, 2008.

- 
- [41] J Mazo. Faster-than-Nyquist signalling. *Bell Syst. Tech. J.*, 54:1451–1462, October 1975.
- [42] Fredrik Rusek and John B Anderson. Multistream Faster than Nyquist Signaling. *IEEE Trans. Communications*, 57(5):1329–1340, 2009.
- [43] Deepak Dasalukunte, Fredrik Rusek, and Viktor Owall. An iterative decoder for multicarrier faster-than-Nyquist signaling systems. In *2010 IEEE International Conference on Communications*, pages 1–5. IEEE, 2010.
- [44] Deepak Dasalukunte, Fredrik Rusek, and Viktor Owall. Multicarrier faster-than-Nyquist transceivers: Hardware architecture and performance analysis. *IEEE Transactions on Circuits and Systems I: Regular Papers*, 58(4):827–838, 2010.
- [45] Alan Barbieri, Dario Fertonani, and Giulio Colavolpe. Time-frequency packing for linear modulations: spectral efficiency and practical detection schemes. *IEEE Transactions on Communications*, 57(10), 2009.
- [46] Vida Vakilian, Thorsten Wild, Frank Schaich, Stephan ten Brink, and Jean-Francois Frigon. Universal-filtered multi-carrier technique for wireless systems beyond LTE. In *Globecom Workshops (GC Wkshps), 2013 IEEE*, pages 223–228. IEEE, 2013.
- [47] Safa Isam and Izzat Darwazeh. Simple DSP-IDFT techniques for generating spectrally efficient FDM signals. In *Communication Systems Networks and Digital Signal Processing (CSNDSP), 2010 7th International Symposium on*, pages 20–24. IEEE, 2010.
- [48] Marcus R Perrett and Izzat Darwazeh. Flexible hardware architecture of SEFDM transmitters with real-time non-orthogonal adjustment. In *Telecommunications (ICT), 2011 18th International Conference on*, pages 369–374. IEEE, 2011.
- [49] Paul N Whatmough, Marcus R Perrett, Safa Isam, and Izzat Darwazeh. VLSI architecture for a reconfigurable spectrally efficient FDM

- 
- baseband transmitter. *IEEE Transactions on Circuits and Systems I: Regular Papers*, 59(5):1107–1118, 2012.
- [50] Tongyang Xu and Izzat Darwazeh. Nyquist-SEFDM: Pulse shaped multicarrier communication with sub-carrier spacing below the symbol rate. In *Communication Systems, Networks and Digital Signal Processing (CSNDSP), 2016 10th International Symposium on*, pages 1–6. IEEE, 2016.
- [51] Safa Isam and Izzat Darwazeh. Peak to average power ratio reduction in spectrally efficient FDM systems. In *Telecommunications (ICT), 2011 18th International Conference on*, pages 363–368. IEEE, 2011.
- [52] Evgeny O Antonov, Andrey V Rashich, Dmitrii K Fadeev, and Ngoc Tan. Reduced complexity tone reservation peak-to-average power ratio reduction algorithm for SEFDM signals. In *Telecommunications and Signal Processing (TSP), 2016 39th International Conference on*, pages 445–448. IEEE, 2016.
- [53] Safa Isam and Izzat Darwazeh. Precoded spectrally efficient FDM system. In *Personal Indoor and Mobile Radio Communications (PIMRC), 2010 IEEE 21st International Symposium on*, pages 99–104. IEEE, 2010.
- [54] Safa Isam and Izzat Darwazeh. Characterizing the intercarrier interference of non-orthogonal spectrally efficient FDM system. In *Communication Systems, Networks & Digital Signal Processing (CSNDSP), 2012 8th International Symposium on*, pages 1–5. IEEE, 2012.
- [55] D. Nopchinda et al. Dual Polarization Coherent Optical Spectrally Efficient Frequency Division Multiplexing. *IEEE Photonics Tech. Lett.*, 28(1):83–86, Jan 2016.
- [56] Hedaia Ghannam and Izzat Darwazeh. Robust channel estimation methods for spectrally efficient FDM systems. In *2018 IEEE 87th Vehicular Technology Conference (VTC Spring)*, pages 1–6. IEEE, 2018.

- 
- [57] Safa Isam, Ioannis Kanaras, and Izzat Darwazeh. A truncated SVD approach for fixed complexity spectrally efficient FDM receivers. In *2011 IEEE Wireless Communications and Networking Conference*, pages 1584–1589. IEEE, 2011.
- [58] Safa Isam and Izzat Darwazeh. Design and performance assessment of fixed complexity spectrally efficient FDM receivers. In *Vehicular Technology Conference (VTC Spring), 2011 IEEE 73rd*, pages 1–5. IEEE, 2011.
- [59] Tongyang Xu, Ryan C Grammenos, Farokh Marvasti, and Izzat Darwazeh. An improved fixed sphere decoder employing soft decision for the detection of non-orthogonal signals. *IEEE Communications Letters*, 17(10):1964–1967, 2013.
- [60] Izzat Darwazeh, Tongyang Xu, Tao Gui, Yuan Bao, and Zhaohui Li. Optical spectrally efficient FDM system for electrical and optical bandwidth saving. In *Communications (ICC), 2014 IEEE International Conference on*, pages 3432–3437. IEEE, 2014.
- [61] Ioannis Kanaras, Arsenia Chorti, Miguel Rodrigues, and Izzat Darwazeh. Investigation of a Semidefinite Programming detection for a spectrally efficient FDM system. In *Personal, Indoor and Mobile Radio Communications, 2009 IEEE 20th International Symposium on*, pages 2827–2832. IEEE, 2009.
- [62] Ioannis Kanaras, Arsenia Chorti, Miguel RD Rodrigues, and Izzat Darwazeh. A combined MMSE-ML detection for a spectrally efficient non orthogonal FDM signal. 2008.
- [63] Ioannis Kanaras, Arsenia Chorti, Miguel Rodrigues, and Izzat Darwazeh. A new quasi-optimal detection algorithm for a non orthogonal spectrally efficient FDM. In *Communications and Information Technology, 2009. ISCIT 2009. 9th International Symposium on*, pages 460–465. IEEE, 2009.

- 
- [64] Tongyang Xu, Tianhua Xu, and Izzat Darwazeh. Deep learning for interference cancellation in non-orthogonal signal based optical communication systems. In *2018 Progress In Electromagnetics Research Symposium-Spring (PIERS)*, 2018.
- [65] Tongyang Xu and Izzat Darwazeh. A soft detector for spectrally efficient systems with non-orthogonal overlapped sub-carriers. *IEEE Communications Letters*, 18(10):1847–1850, 2014.
- [66] Hedaia Ghannam and Izzat Darwazeh. Comparison of turbo decoder and turbo equalizer for spectrally efficient FDM system. In *Communication Systems, Networks and Digital Signal Processing (CSNDSP), 2016 10th International Symposium on*, pages 1–6. IEEE, 2016.
- [67] Hedaia Ghannam and Izzat Darwazeh. Signal coding and interference cancellation of spectrally efficient FDM systems for 5G cellular networks. In *Telecommunications (ICT), 2017 24th International Conference on*, pages 1–6. IEEE, 2017.
- [68] Hedaia Ghannam and Izzat Darwazeh. SEFDM over satellite systems with advanced interference cancellation. *IET Communications*, 12(1):59–66, 2017.
- [69] Spiros Mikroulis, Tongyang Xu, John E Mitchell, and Izzat Darwazeh. First demonstration of a spectrally efficient FDM radio over fiber system topology for beyond 4G cellular networking. In *Networks and Optical Communications-(NOC), 2015 20th European Conference on*, pages 1–5. IEEE, 2015.
- [70] Tongyang Xu, Spiros Mikroulis, John E Mitchell, and Izzat Darwazeh. Bandwidth compressed waveform for 60-GHz millimeter-wave radio over fiber experiment. *Journal of Lightwave Technology*, 34(14):3458–3465, 2016.
- [71] Ryan C Grammenos, Safa Isam, and Izzat Darwazeh. FPGA design of a truncated SVD based receiver for the detection of SEFDM signals.

- 
- In *Personal Indoor and Mobile Radio Communications (PIMRC), 2011 IEEE 22nd International Symposium on*, pages 2085–2090. IEEE, 2011.
- [72] Tongyang Xu, Ryan C Grammenos, and Izzat Darwazeh. FPGA implementations of real-time detectors for a spectrally efficient FDM system. In *Telecommunications (ICT), 2013 20th International Conference on*, pages 1–5. IEEE, 2013.
- [73] Johnson, Charles R and Horn, Roger A. *Matrix analysis*. Cambridge university press Cambridge, 1985.
- [74] W. Ozan, H. Ghannam, T. Xu, P. A. Haigh, and I. Darwazeh. Experimental Evaluation of Channel Estimation and Equalisation in Non-Orthogonal FDM Systems. In *2018 11th International Symposium on Communication Systems, Networks Digital Signal Processing (CSNDSP)*, pages 1–6, July 2018.
- [75] H. Ghannam and I. Darwazeh. A Proposal for Scalable 5G New Radio Frames with Enhanced Throughput. In *2019 IEEE 89th Vehicular Technology Conference (VTC2019-Spring)*, pages 1–6, April 2019.
- [76] Timothy M Schmidl and Donald C Cox. Robust frequency and timing synchronization for OFDM. *IEEE transactions on communications*, 45(12):1613–1621, 1997.
- [77] Bo Tan, Karl Woodbridge, and Kevin Chetty. A real-time high resolution passive WiFi Doppler-radar and its applications. In *Radar Conference (Radar), 2014 International*, pages 1–6. IEEE, 2014.
- [78] Luis G Barbero and John S Thompson. Rapid prototyping of a fixed-throughput sphere decoder for MIMO systems. In *Proc. of IEEE ICC*, 2006.
- [79] 3GPP. LTE; Evolved Universal Terrestrial Radio Access (E-UTRA); Base Station (BS) conformance testing. ETSI TS 36.141, Rel. 10, v.10.8.0, 3GPP, October 2012.

- 
- [80] Bertrand Muquet, Zhengdao Wang, Georgios B Giannakis, Marc De Courville, and Pierre Duhamel. Cyclic prefixing or zero padding for wireless multicarrier transmissions? *IEEE Transactions on communications*, 50(12):2136–2148, 2002.
- [81] S. Venkatesan and R. A. Valenzuela. OFDM for 5G: Cyclic prefix versus zero postfix, and filtering versus windowing. In *Proc. IEEE Int. Conf. Commun. (ICC)*, pages 1–5, May 2016.
- [82] M. Nakao and S. Sugiura. Spectrally Efficient Frequency Division Multiplexing With Index-Modulated Non-Orthogonal Subcarriers. *IEEE Wireless Commun. Lett.*, 8(1):233–236, Feb 2019.
- [83] W. Ozan, R. Grammenos, and I. Darwazeh. Zero Padding or Cyclic Prefix: Evaluation for Non-Orthogonal Signals. *IEEE Communications Letters*, pages 1–1, 2019.
- [84] Andrea Goldsmith. *Wireless communications*. Cambridge university press, 2005.
- [85] Robert M Gray et al. Toeplitz and circulant matrices: A review. *Foundations Trends® Commun. Inf. Theory*, 2(3):155–239, 2006.
- [86] Xianbin Wang, Paul Ho, and Yiyan Wu. Robust channel estimation and ISI cancellation for OFDM systems with suppressed features. *IEEE Journal on Selected Areas in communications*, 23(5):963–972, 2005.
- [87] LTE ETSI. LTE; Evolved Universal Terrestrial Radio Access (E-UTRA); Physical layer procedures (3GPP TS 36.213 version 14.2.0 Release 14), 2017.
- [88] Tongyang Xu, Christos Masouros, and Izzat Darwazeh. Waveform and space precoding for next generation downlink narrowband IoT. *IEEE Internet of Things Journal*, 2019.
- [89] 3GPP. 5G; Study on channel model for frequencies from 0.5 to 100 GHz. ETSI TR 38.901, Rel. 14, v.14.0.0, 3GPP, May 2017.

- 
- [90] 3GPP. NR; Physical channels and modulation. ETSI TR 38.211, Rel. 15, v.15.2.0, 3GPP, July 2018.
- [91] Gilbert Strang. Introduction to Linear Algebra, 4th edn. Wellesley, MA: Wellesley, 2009.
- [92] S. Isam. *Spectrally Efficient FDM Communication Signals and Transceivers: Design, Mathematical Modeling and System Optimization*. PhD thesis, University College London - Department of Electronic and Electrical Engineering, October 2011.
- [93] Ieee standard for information technology–telecommunications and information exchange between systems local and metropolitan area networks–specific requirements - part 11: Wireless lan medium access control (mac) and physical layer (phy) specifications. *IEEE Std 802.11-2016 (Revision of IEEE Std 802.11-2012)*, pages 1–3534, Dec 2016.
- [94] L. Bahl, J. Cocke, F. Jelinek, and J. Raviv. Optimal decoding of linear codes for minimizing symbol error rate (Corresp.). *IEEE Transactions on Information Theory*, 20(2):284–287, March 1974.
- [95] S Gollakota and D Katabi. Zigzag decoding: Combating hidden terminals in wireless networks. In *Proc. of the ACM SIGCOMM Conf.*, pages 159–170, August 2008.
- [96] R Ahlswede. Multi-way communication channels. In *IEEE ISIT Symp.*, pages 103–135, 1971.
- [97] H Liao. A coding theorem for multiple access communications. In *IEEE ISIT Symp.*, 1972.
- [98] David Tse and P Viswanath. *Fundamentals of Wireless Communication*. Cambridge University Press, 2005.
- [99] M Damen, H El Gamal, and G Caire. On maximum likelihood detection and the search for the closest lattice point. *IEEE Trans. on Information Theory*, 49(10):2389–2402, 2003.

- 
- [100] E. Agrell, T. Eriksson, A. Vardy, and K. Zeger. Closest point search in lattices. *IEEE Trans. on Information Theory*, 48(8):2201–2214, Aug. 2002.
- [101] Kyle Jamieson and Hari Balakrishnan. PPR: Partial packet recovery for wireless networks. In *SIGCOMM*, 2007.
- [102] David Barry, Edward Lee, and David Messerschmitt. *Digital Communication*. Springer, New York, NY, 3rd. edition, 2003.
- [103] F Rusek and J Anderson. The two dimensional Mazo limit. In *ISIT*, 2005.
- [104] F Rusek and J Anderson. Multi-stream Faster than Nyquist Signaling. *IEEE Trans. on Comms.*, 57(5):1329–1340, 2009.
- [105] J Anderson, F Rusek, and V Öwall. Faster-Than Nyquist Signaling. *Proc. of the IEEE*, 101(8):1817–1830, August 2013.
- [106] T Xu and I Darwazeh. M-QAM Signal Detection for a Non-Orthogonal System Using an Improved Fixed Sphere Decoder. In *CSNDSP*, 2014.
- [107] I Kanaras, A Chorti, M Rodrigues, and I Darwazeh. Investigation of a Semidefinite Programming Detection for a Spectrally Efficient FDM System. In *PIMRC*, 2009.
- [108] S Isam and I Darwazeh. Design and Performance Assessment of Fixed Complexity Spectrally Efficient FDM Receivers. In *VTC*, 2011.
- [109] A. Goldsmith, M. Effros, R. Koetter, M. Medard, A. Ozdaglar, and L. Zheng. Beyond shannon: the quest for fundamental performance limits of wireless ad hoc networks. *IEEE Communications Magazine*, 49(5):195–205, May 2011.
- [110] Hariharan Rahul, Swarun Kumar, and Dina Katabi. JMB: Scaling Wireless Capacity with User Demands. In *SIGCOMM*, 2012.

- 
- [111] Ezzeldin Hamed, Hariharan Rahul, Mohammed A. Abdelghany, and Dina Katabi. Real-time Distributed MIMO Systems. In *SIGCOMM*, 2016.
- [112] Ezzeldin Hamed, Hariharan Rahul, and Bahar Partov. Chorus: Truly distributed distributed-MIMO. In *SIGCOMM*, 2018.
- [113] Q Yang, X Li, H Yao, J Fang, K Tan, W Hu, J Zhang, and Y Zhang. BigStation: Enabling Scalable Real-time Signal Processing in Large MU-MIMO systems. In *SIGCOMM*, 2013.
- [114] C Shepard, H Yu, N Anand, L Li, T Marzetta, R Yang, and L Zhong. Argos: Practical many-antenna base stations. In *MobiCom*, 2012.
- [115] S Jafar and S Shamai. Degrees of freedom of the MIMO X channel. *IEEE Trans. on Information Theory*, 54(1):151–170, January 2008.
- [116] S Gollakota, S Perli, and D Katabi. Interference Alignment and Cancellation. In *SIGCOMM*, 2009.
- [117] K Lin, S Gollakota, and D Katabi. Random access heterogeneous MIMO networks. In *SIGCOMM*, 2011.
- [118] C Suh and D Tse. Interference alignment for cellular networks. In *Allerton*, 2008.
- [119] S Wong, H Yang, S Lu, and V Bharghavan. Robust rate adaptation for 802.11 wireless networks. In *MobiCom*, 2006.
- [120] John Bicket. Bit-Rate Selection in Wireless Networks. Master’s thesis, Massachusetts Inst. of Technology, February 2005.
- [121] J Zhang, K Tan, J Zhao, H Wu, and Y Zhang. A practical SNR-guided rate adaptation. In *Infocom*, 2008.
- [122] J Camp and E Knightly. Modulation Rate Adaptation in Urban and Vehicular Environments: Cross-Layer Implementation and Experimental Evaluation. In *MobiCom*, 2008.

- [123] D Halperin, W Hu, A Sheth, and D Wetherall. Predictable 802.11 packet delivery from wireless channel measurements. In *SIGCOMM*, 2010.
- [124] M Vutukuru, H Balakrishnan, and K Jamieson. Cross-layer wireless bit rate adaptation. In *SIGCOMM*, 2009.
- [125] H Jin, A Khandekar, and R McEliece. Irregular Repeat-Accumulate Codes. In *Proc. Symp. Turbo Codes Related Topics*, 2000.
- [126] M Luby. LT Codes. In *Proc. of the Symp. on Foundations of Computer Science*, page 271, 2002.
- [127] J Byers, M Luby, and M Mitzenmacher. A Digital Fountain Approach to Asynchronous Reliable Multicast. *IEEE J. Sel. Areas in Comm.*, 20(10):1528–1540, October 2002.
- [128] J Byers, M Luby, M Mitzenmacher, and A Rege. A Digital Fountain Approach to Reliable Distribution of Bulk Data. In *SIGCOMM*, 1998.
- [129] A Shokrollahi. Raptor Codes. *IEEE/ACM Trans. on Networking*, 14(SI):2551–2567, June 2006.
- [130] O Etesami and A Shokrollahi. Raptor Codes on Binary Memoryless Symmetric Channels. *IEEE Trans. on Information Theory*, 52(5):2033–2051, 2006.
- [131] J Perry, P Iannucci, K Fleming, H Balakrishnan, and D Shah. Spinal codes. In *SIGCOMM*, 2012.
- [132] Jonathan Perry, Hari Balakrishnan, and Devavrat Shah. Rateless Spinal Codes. In *HotNets Workshop*, 2011.
- [133] K C Lin, N Kushman, and D Katabi. ZipTx: Exploiting the Gap Between Bit Errors and Packet Loss. In *MobiCom*, pages 351–362, 2008.

- 
- [134] J Choi, M Jain, K Srinivasan, P Levis, and S Katti. Achieving Single Channel, Full Duplex Wireless Communication. In *MobiCom*, 2010.
- [135] M Jain, J Choi, T Kim, D Bharadia, K Srinivasan, S Seth, P Levis, S Katti, and P Sinha. Practical, Real-Time, Full Duplex Wireless. In *MobiCom*, 2011.
- [136] D Bharadia, E McMillin, and S Katti. Full Duplex Radios. In *SIGCOMM*, 2013.
- [137] D Bharadia and S Katti. Full Duplex MIMO Radios. In *NSDI*, 2014.
- [138] Erik Agrell, Thomas Eriksson, Alexander Vardy, and Kenneth Zeger. Closest point search in lattices. *IEEE transactions on information theory*, 48(8):2201–2214, 2002.
- [139] Mohamed Oussama Damen, Hesham El Gamal, and Giuseppe Caire. On maximum-likelihood detection and the search for the closest lattice point. *IEEE Transactions on information theory*, 49(10):2389–2402, 2003.
- [140] Tongyang Xu and Izzat Darwazeh. Multi-band reduced complexity spectrally efficient fdm systems. In *Communication Systems, Networks & Digital Signal Processing (CSNDSP), 2014 9th International Symposium on*, pages 982–987. IEEE, 2014.
- [141] E. Sourour, H. El-Ghoroury, and D. McNeill. Frequency offset estimation and correction in the IEEE 802.11a WLAN. In *IEEE 60th Vehicular Technology Conference, 2004. VTC2004-Fall. 2004*, volume 7, pages 4923–4927 Vol. 7, Sep. 2004.
- [142] George F Riley and Thomas R Henderson. The ns-3 network simulator. In *Modeling and tools for network simulation*, pages 15–34. Springer, 2010.
- [143] M. Jia, Z. Yin, D. Li, Q. Guo, and X. Gu. Toward Improved Offloading Efficiency of Data Transmission in the IoT-Cloud by Leveraging Secure

- Truncating OFDM. *IEEE Internet of Things Journal*, 6(3):4252–4261, June 2019.
- [144] Tongyang Xu and Izzat Darwazeh. Deep Learning for Over-the-Air Non-Orthogonal Signal Classification. *arXiv preprint arXiv:1911.06174*, 2019.
- [145] Waseem Ozan, Paul Anthony Haigh, Bo Tan, and Izzat Darwazeh. Time Precoding Enabled Non-Orthogonal Frequency Division Multiplexing. In *2019 IEEE 30th Annual International Symposium on Personal, Indoor and Mobile Radio Communications (PIMRC)*, pages 1–6. IEEE, 2019.
- [146] Minyoung Park. IEEE 802.11 ah: sub-1-GHz license-exempt operation for the internet of things. *IEEE Communications Magazine*, 53(9):145–151, 2015.